Lead Optimization of an N-type Calcium Channel Blocker for a General Neuroprotection Approach

Inaugural dissertation

for the attainment of the jointly awarded title of doctor in the

Faculty of Mathematics and Natural Sciences
at the Heinrich Heine University Düsseldorf

&

Faculty of Medicine, Dentistry and Health Sciences
at the University of Melbourne

presented by

Esther Katharina Wollert
from Troisdorf, Germany

Troisdorf, June 2024

from the „Institut für Physikalische Biologie“
at the Heinrich Heine University Düsseldorf

Published by permission of the
Faculty of Mathematics and Natural Sciences at
Heinrich-Heine-Universität Düsseldorf

Supervisor: Prof. Dr. Dieter Willbold
Co-supervisor: Prof. Dr. Colin L. Masters

Date of the oral examination: 27th August 2024

Affidavit

I declare under oath that I have produced my thesis independently and without any undue assistance by third parties under consideration of the 'Principles for the Safeguarding of Good Scientific Practice at Heinrich Heine University Düsseldorf'. Due acknowledgement has been made in the text to all other material used.

I also declare that this thesis was not presented to another faculty, besides the Faculty of Medicine, Dentistry and Health Sciences at the University of Melbourne, and the Faculty of Mathematics and Natural Sciences at the Heinrich Heine University Düsseldorf for the attainment of the jointly awarded degree.

I further declare that the thesis is fewer than the maximum word limit in length, as defined in the Graduate Research Theses Rules from the University of Melbourne, exclusive of tables, maps, bibliographies and appendices.

Düsseldorf,

_____

(Esther Katharina Wollert)

“Our greatest weakness lies in giving up.

The most certain way to succeed is always to try just one more time.”

- Thomas Edison

Table of Contents

List of Tables

List of Figures

List of Abbreviations

$(NH_4)_2SO_4$	Ammonium sulfate
AD	Alzheimer's disease
AIEX	Anion exchange chromatography
ALS	Amyotrophic lateral sclerosis
APP	Amyloid precursor protein
APS	Ammonium peroxodisulphate
AUC	Area under the curve
Aβ	Amyloid-beta
$BaCl_2$	Barium chloride
BBB	Blood brain barrier
BCA	Bicinchoninic acid
BG	Binding groove
BSA	Bovine serum albumin
Ca^{2+}	Calcium ion
$CaCl_2$	Calcium chloride
CaMKII	Ca^{2+} calmodulin activated kinase II
CARP	Cationic arginine-rich peptide
CCB	Calcium channel blocker
$CdCl_2$	Cadmium chloride
CDI	Calcium-dependent inactivation
CDK5	Cyclin-dependent kinase 5
CFA	Complete Freund's adjuvant
CHS	Cholesteryl hemisuccinate
CIEX	Cation exchange chromatography
CNS	Central nervous system
$CsCl_2$	Cesium chloride
CSF	Cerebrospinal fluid
$CsMeSO_3$	Cesium methanesulfonate
CsOH	Cesium hydroxide
CSP	Cysteine string protein
CV	Column volume
DAPI	4′,6-diamidino-2-phenylindole

DC	Direct control
ddH_2O	Double-distilled water
DDM	n-Dodecyl-β-D-maltopyranoside
DGC	Density gradient centrifugation
DHP	Dihydropyridines
DMEM	Dulbecco's modified eagle medium
DMSO	Dimethyl sulfoxide
dNTP	Deoxynucleotide
DRG	Dorsal root ganglia
ECL	Enhanced chemiluminescence
EDC	N-ethyl-N'-(dimethylaminopropyl)carbodiimide
EDTA	Ethylenediaminetetraacetic acid
EGFP	Enhanced green fluorescent protein
EGTA	Egtazic acid
EM	Electron microscopy
EmS	Empty score
EnS	Enrichment score
EOAD	Early-onset AD
ER	Endoplasmic reticulum
ES	Empty selection
EtBr	Ethidium bromide
FCS	Feta calf serum
$FeSO_4$	Iron(II) sulfate
F_{Norm}	Normalized change in fluorescence
FPLC	Fast protein liquid chromatography
GDN	Glyco-diosgenin
GPCR	G-protein coupled receptor
GSR	Global signal regression
HAC	Hydroxyapatite chromatography
HB	Hydrogen bonds
HCl	Hydrogen chloride
HD	Huntington's disease
HIC	Hydrophobic interaction chromatography
His6	Hexa-histidine

HPLC	High-performance liquid chromatography
HRP	Horse-radish peroxidase
HVA	High-voltage-activated
i.p.	intraperitoneal
IEX	Ion exchange chromatography
Il-1β	Interleukin-1β
Il-10	Interleukin-10
IMAC	Immobilized metal affinity chromatography
IP	Immunoprecipitation
IP_3R	Inositol triphosphate receptor
IPTG	Isopropyl β-D-thiogalactopyranoside
k_a	Association rate constant
KCl	Potassium chloride
K_D	Dissociation constant
k_d	Dissociation rate constant
KH_2PO_4	Potassium dihydrogen phosphate
KO	Knock-out
LB	Luria-Bertani
LTP	Long-term potentiation
LVA	Low-voltage-activated
mABs	monoclonal antibodies
MD	Myoclonus dystonia
MEMα	Alpha minimal essential medium
MgATP	Magnesium adenosine triphosphate
$MgCl_2$	Magnesium chloride
MS	Multiple sclerosis
MST	Microscale thermophoresis
MTT	(3-(4,5-Dimethylthiazol-2-yl)-2,5-diphenyl-tetrazolium bromide)
Na_2GTP	Sodium guanosine triphosphate
Na_2HPO_4	Disodium hydrogen phosphate
Na_3PO_4	Trisodium phosphate
NaCl	Sodium chloride
NaH_2PO_4	Sodium dihydrogen phosphate

NaOH	Sodium hydroxide
NBC	Non-bonded contacts
NFT	Neurofibrillary tangles
NF-κB	Nuclear factor kappa B
NGS	Next-generation sequencing
NHS	N-hydroxysuccinimide
NMDAR	N-methyl-D-aspartate receptor
NTA	Nitrilotriacetic acid
ORF	Open reading frame
PBS	Phosphate buffered saline
PCC	Pearson's correlation coefficient
PCR	Polymerase chain reaction
PD	Parkinson's disease
PEG	Polyethylene glycol
PFU	Plaque-forming unit
pI	Isoelectric point
PIP_2	Phosphatidylinositol-4,5-bisphosphate
PKC	Protein kinase C
PMSF	Phenyl-methyl-sulfonyl-fluoride
PNS	Peripheral nervous system
PPI	Protein-protein interaction
PSEN1	Presenilin 1
PSEN2	Presenilin 2
PTM	Post-translational modification
ROC	Receptor-operated calcium channel
ROI	Region of interest
RT	Room temperature
RU	Resonance unit
RyR	Ryanodine receptor
SB	Salt bridges
SDS	Sodium dodecyl sulfate
SDS-PAGE	SDS-polyacrylamide gel electrophoresis
SEC	Size exclusion chromatography
SEM	Standard error of the mean

SNAP-25	Synaptosome-associated protein, 25kDa
SNARE	Soluble N-ethylmaleimide-sensitive factor attachment protein receptor
SOC	Store-operated calcium channel
SPR	Surface plasmon resonance
ssDNA	Single-stranded DNA
synprint	Synaptic protein interaction
TAE	Tris acetate EDTA buffer
TBI	Traumatic brain injury
TBS	Tris buffered saline
TCE	2,2,2-trichloro-ethanol
TEA-$MeSO_3$	Triethylammonium methanesulfonate
TEA-OH	Triethylammonium hydroxide
TEMED	Tetramethylethylenediamine
TFA	Trifluoroacetic acid
TMB	3,3′,5,5′-tetramethylbenzidine
TROX-1	Triazole oxindole
TRP	Transient receptor potential
TS	Target selection
TSAT	Target sequencing analysis tool
UPS	Ubiquitin proteasome system
V_{act}	Activation potential
VDI	Voltage-dependent inactivation
VGCC	Voltage-gated calcium channel
V_{half}	Half-activation voltage
VSD	Voltage sensing domain
WT	Wild-type
X-Gal	5-bromo-4-chloro-3-indolyl-beta-D-galacto-pyranoside
ω-Aga IVA	Omega-Agatoxin IVA
ω-CgTx GVIA	Omega-Conotoxin GVIA
ω-CgTx MVIIA	Omega-Conotoxin MVIIA

Three and One Letter Code of Naturally Occurring Amino Acids

Ala	A	Alanine
Arg	R	Arginine
Asn	N	Asparagine
Asp	D	Aspartic acid
Cys	C	Cysteine
Gln	Q	Glutamine
Glu	E	Glutamic acid
Gly	G	Glycine
His	H	Histidine
Ile	I	Isoleucine
Leu	L	Leucine
Lys	K	Lysine
Met	M	Methionine
Phe	F	Phenylalanine
Pro	P	Proline
Ser	S	Serine
Thr	T	Threonine
Trp	W	Tryptophan
Tyr	Y	Tyrosine
Val	V	Valine

Contributions

Statement of contributions by others to the thesis:

Invaluable input in study design, establishing of research projects, designing experiments, interpreting results and providing feedback has been given by my supervisory team Professor Dieter Willbold, Professor Colin L. Masters and Dr. Janine Kutzsche.

Ian Gering assisted in method development for purification approaches and in binding experiments (SPR and MST).

In vivo Ca^{2+} imaging experiments were performed in collaboration with Professor Lucy Palmer.

Dr. Luke Miles has contributed with assisting in the modeling process.

Overall, I contributed to the here presented work to over 90%.

Contributions by others to results:

Chapter 3.1: $Ca_V2.2$ Channel Levels are Increased in a Mouse Model of AD (Figures 3.1 and 3.2): Mice were provided by Dr. Sarah Schemmert.

Chapter 3.3.2.2: Purification of $Ca_V2.2$ via Ion Exchange Chromatography: Purification experiments via ion exchange chromatography using beads as column material were performed by Ian Gering (Fig. 3.11). Contribution in study design, data analysis and interpretation, as well as writing.

Chapter 3.3.2.5: Purification of $Ca_V2.2$ via Immobilized Metal Affinity Chromatography: Purification of $Ca_V2.2$ via Fe^{2+}-NTA and experimental replicates of purification via Ni^{2+}-NTA (Fig. 3.14) were performed by Ian Gering. Contribution through methodic idea, study design, data analysis and interpretation, as well as writing.

Chapter 3.3.2.7: Purification of $Ca_V2.2$ via Centrifugation-Based Separation: Separation of $Ca_V2.2$ from complex samples via differential centrifugation (Fig. 3.16) was performed by Ian Gering. Contribution in study design, data analysis and interpretation, as well as writing.

Chapter 3.4.2: Kinetics of RD2 Binding to Partially Purified $Ca_V2.2$ Measured by Microscale Thermophoresis: Part of published paper (Kutzsche, Guzman et al. 2023). Contribution in study design, experiment conduct, data analysis, writing and interpretation.

Chapter 3.5: *In Vivo* Ca^{2+} Imaging of Neuronal Activity in Response to a Sensory Stimulus Before and After RD2 Application: Lucy Palmer and Rosie Firth assisted with the study design. Surgical preparation of mice was performed by Rosie Firth. Experiments and data analysis were performed by Rosie Firth and me. Data interpretation and writing was performed by me.

Chapter 3.7.1.1-3: VGCC subtype-specific inhibition property of RD2-derivatives: Electrophysiological recordings and subsequent data analysis were performed by Dr. Gustavo Guzman. Contribution in data analysis and interpretation, as well as writing.

Chapter 3.7.1.4: Toxicity of RD2-derivative RD2C *in vitro*: MTT assays and subsequent data analysis were performed by Markus Tusche. Contribution in data analysis and interpretation, as well as writing.

Abstract

Calcium (Ca^{2+}) signaling plays a central role in numerous cellular processes, especially in excitatory cells, such as neurons, creating the necessity for tight regulation and homeostasis to facilitate normal cellular function. In part, this neuronal Ca^{2+} influx is mediated by ion channels from the family of Voltage-Gated Calcium Channels (VGCCs), which regulate Ca^{2+} transmembrane fluxes into the cell in response to membrane depolarization.

Previously, it was shown that cytosolic Ca^{2+} levels are affected in numerous neurodegenerative diseases, subsequently followed by excitotoxicity-induced neurodegeneration. In this context, we aimed to identify putative key proteins mediating excitotoxic Ca^{2+} fluxes and found the N-type VGCC ($Ca_V2.2$) as promising target, as we could show a disease progression-associated upregulation of the protein in a mouse model of Alzheimer's disease (AD). We were previously able to show the inhibitory capacity of the all D-enantiomeric peptide RD2 on $Ca_V2.2$ channels, making RD2 a promising lead candidate for the treatment of putative $Ca_V2.2$-mediated neurodegeneration for a general neuroprotection approach. One central aim of this study was to understand the interaction of RD2 with $Ca_V2.2$ channels more in detail to subsequently improve the lead candidate with regard to its inhibitory capacity and specificity.

In addition to previously obtained *in vitro* proof of concept of the inhibitory capacity of RD2 on Ca^{2+} fluxes mediated by $Ca_V2.2$, we were able to further confirm this effect in *in vivo* experiments using a wide-field Ca^{2+} imaging-based approach in awake mice. We could show that RD2 not only inhibits signal transmission from the periphery to the brain, but was further observed to influence intracortical signaling, which is thought to be involved in signal processing.

Another objective of this study was to functionally express and purify the channel in its native three-dimensional conformation as basis for subsequent binding assays for the optimization of the lead compound. A first protocol was developed, that achieved partial separation of $Ca_V2.2$ protein from complex cell lysates. This paved the way for the analysis of binding kinetics of RD2 in complex with $Ca_V2.2$, showing an overall strong association with a respective dissociation coefficient in the low nanomolar range.

Using rational design, a first lead-derived candidate, namely RD2C, was identified that demonstrates improved inhibitory effects on $Ca_V2.2$ currents. RD2C was able to inhibit $Ca_V2.2$-mediated currents significantly stronger than RD2, while showing a similar dose-dependent and fully reversible inhibition manner.

In addition, we used peptide docking modeling to assess the underlying mode of action of the inhibition of $Ca_V2.2$ by RD2 or RD2C more in detail. Results suggested a flexible binding mode of RD2 and RD2C on $Ca_V2.2$ channels inside the electronegative cavity associated with the Ca^{2+}-permeable pore, which was mainly mediated through electrostatic interactions. These results point towards a pore-blocking mechanism of RD2 and RD2-derived D-peptides, mainly mediated through their overall positive net charge and the arginine-rich C-terminal region. Here obtained findings will subsequently provide an interesting basis for the ongoing optimization of $Ca_V2.2$-inhibiting D-peptides using rational design.

Taken together, in this study we present the $Ca_V2.2$ as a potential new therapeutic target for the treatment of neurodegenerative diseases in a general neuroprotective approach, and a corresponding D-peptide as lead compound for subsequent inhibition.

Zusammenfassung

Ca^{2+} Ionen stellen einen der wichtigsten Botenstoffe im Körper dar und spielen eine zentrale Rolle in einer Vielzahl von zellulären Prozessen, vor allem in erregbaren Zellen wie Neuronen. Dies bedingt die Notwendigkeit einer entsprechend strikten Kontrolle der homöostatischen Prozesse als Grundlage für die normale physiologische Funktion aller Zellen. Ein zentraler Kontrollmechanismus ist der kontrollierte Ca^{2+} Einstrom in die Zelle, der zu einem Großteil durch spannungsgesteuerte Ca^{2+} Kanäle (VGCCs) reguliert wird, die einen Ca^{2+} Einstrom als Folge einer Membran-Depolarisation bedingen.

Es wurde bereits mehrfach nachgewiesen, dass abweichende zytosolische Ca^{2+} Konzentrationen eine kausale Rolle in einer Vielzahl von neurodegenerativen Erkrankungen spielen, indem durch toxische Übererregung der Neuronen final der neuronale Zelltod verursacht wird. In diesem Kontext war eines der Ziele dieser Arbeit neue interessante zentrale krankheitsassoziierte Proteine zu identifizieren, die potentiell toxische Ca^{2+} Ströme vermitteln. Durch semi-quantitative Analyse der Proteinkonzentration von VGCCs in verschiedenen Hirnarealen eines Mausmodells der Alzheimer Demenz (AD) konnten wir den VGCC des N-Typs ($Ca_V2.2$) identifizieren, der eine progressive Überexpression im Krankheitsverlauf zeigte.

Für das D-enantiomere Peptid RD2 konnte in vorangegangenen Studien bereits eine inhibitorische Wirkung auf $Ca_V2.2$-vermittelte Ca^{2+} Ströme gezeigt werden, weshalb RD2 als vielversprechende Leitstruktur für die Behandlung von vermeintlich $Ca_V2.2$-bedingter Neurodegeneration gewählt wurde. Eines der Hauptziele dieser Arbeit war die Analyse der Interaktion von RD2 mit $Ca_V2.2$ Kanälen, um auf Basis hiervon nachfolgend die Leitstruktur im Hinblick auf Effizienz und Spezifität ihrer inhibitorischen Wirkung auf $Ca_V2.2$ Kanäle zu optimieren.

In Übereinstimmung mit dem zuvor erbrachten *in vitro* Nachweis der inhibitorischen Wirkung von RD2 auf durch $Ca_V2.2$ vermittelte Ca^{2+} Ströme konnten wir diese Wirkung in *in vivo* Experimenten mit Ca^{2+} Bildgebungsverfahren in wachen Mäusen weiter bestätigen. Wir konnten hierbei zeigen, dass RD2 nicht nur die Signalübertragung von der Peripherie zum Gehirn geringfügig hemmt, sondern auch die intrakortikale Kommunikation beeinflusst, die vermeintlich an der Signalverarbeitung beteiligt ist.

Ein weiterer Schwerpunkt dieser Studie war die funktionelle Expression und Reinigung des Kanals in seiner nativen, dreidimensionalen Konformation als Basis für nachfolgende Bindungstests zur Optimierung der Leitstruktur. Hierfür konnte ein Protokoll entwickelt werden, das eine partielle Reinigung des $Ca_V2.2$ Proteins aus komplexem Zelllysat ermöglicht. Dies stellte die Basis für Analysen der Bindungskinetik von RD2 in Komplex mit $Ca_V2.2$ dar, in denen eine starke Assoziation mit einem entsprechenden Dissoziationskoeffizienten im niedrigen nanomolaren Bereich gezeigt werden konnte.

Mit Hilfe von rationalem Design wurde ein erster, von der Leitstruktur RD2 abgeleiteter Kandidat, namentlich RD2C, entwickelt, der eine verbesserte inhibitorische Wirkung auf $Ca_V2.2$-vermittelte Ca^{2+} Ströme zeigte. Es konnte beobachtet werden, dass RD2C $Ca_V2.2$-vermittelte Ca^{2+} Ströme deutlich stärker als RD2 hemmt, dabei jedoch ähnlich dosisabhängig und vollständig reversibel wirkt.

Weitergehend haben wir Peptid-Rezeptor-Docking-Modellierung verwendet, um die zugrunde liegende Wirkungsweise der Hemmung von $Ca_V2.2$ durch RD2 oder RD2C genauer zu untersuchen. Die Ergebnisse deuten auf einen flexiblen Bindungsmodus von RD2 und RD2C an $Ca_V2.2$ Kanälen hin, der innerhalb der elektronegativen Tasche lokalisiert ist, die den Eingang der Ca^{2+}-permeablen Pore bildet. Zudem konnte festgestellt werden, dass diese Interaktion hauptsächlich durch elektrostatische Wechselwirkungen stabilisiert wird. Diese Ergebnisse deuten auf einen Porenblockierungsmechanismus von RD2 und RD2C hin, der hauptsächlich durch die positive Gesamtladung und den Arginin-reichen C-Terminus vermittelt wird. Die hier gewonnenen Erkenntnisse bilden eine interessante Grundlage für die laufende Optimierung von $Ca_V2.2$-hemmenden D-enantiomeren Peptiden mittels rationalen Designs.

Insgesamt konnte in dieser Arbeit der $Ca_V2.2$ Kanal als potenzielles neues therapeutisches Ziel für die Behandlung neurodegenerativer Erkrankungen identifiziert werden, wofür zusätzlich ein entsprechendes D-Peptid als Leitstruktur für die anschließende Hemmung dieser Kanäle charakterisiert und erste erfolgreiche Optimierungsprozesse durchgeführt wurden.

1 Introduction

1.1 Calcium Signaling

Ca^{2+} functions as the main intracellular secondary messenger in the body. As this, it is involved in a variety of cellular processes and mediates transmission of different extracellular signals in order to regulate physiological cellular function, mainly mediated through its electrogenic properties. The versatility of the role of Ca^{2+} in signaling is crucial for controlling diverse processes, and many signaling pathways rely on activation by Ca^{2+} (Cheung 1980; Berridge, Lipp et al. 2000; Greer and Greenberg 2008; Brini, Cali et al. 2014). In its role as cellular messenger, Ca^{2+} was found to be involved in various processes mediating cell viability, such as regulation of cytoskeleton stability and dynamics (Schlaepfer and Zimmerman 1985; Trifaro and Vitale 1993), regulating gene expression (Bading 2013; Puri 2020), as well as membrane depolarization (Schwartzkroin and Stafstrom 1980; Krnjevic and Xu 1989) and subsequent excitability of cells (Smith and Augustine 1988; Llinas, Sugimori et al. 1992; Robitaille, Garcia et al. 1993). At the resting state of cells, the intracellular concentration of Ca^{2+} is maintained at low levels in the range of 75 nM to 200 nM, in order to achieve significant changes in concentration at low energy costs. During signal transmission, intracellular Ca^{2+} concentrations will increase in a local and transient way up to a concentration of 1 µM to 10 µM, resulting in a 20,000-fold gradient between Ca^{2+} concentrations at resting and activated state. Because the role of Ca^{2+} is so universal, tight regulation and homeostasis is crucial for normal cellular function (Berridge, Bootman et al. 2003).

1.1.1 Physiological Functions of Calcium in the Brain

In the peripheral nervous system (PNS) and the central nervous system (CNS) neurons are highly specialized cells that form the major unit for signal transduction. By coupling electrical and chemical signals, neurons are able to transmit information throughout the entire body. The underlying process, the generation of action potentials, is highly dependent on Ca^{2+} signaling and its tight regulation. Ca^{2+} links excitability of membranes with the process of signal transduction, forming the base for neuronal activity.

In the CNS, Ca^{2+} is involved in various physiological and pathological processes. Throughout development of the CNS, Ca^{2+} functions as an important messenger during neurogenesis and synapse formation, a crucial step for establishment of a functional and stable neuronal network and normal function of the CNS (Scheiffele 2003; Rash, Ackman et al. 2016). Furthermore, Ca^{2+} signaling mediates neuronal differentiation and plasticity as well as apoptosis of neurons and is therefore a key player in learning and memory formation (Berridge, Bootman et al. 1998; Emptage, Reid et al. 2001; Rash, Ackman et al. 2016). In a functional neuronal network, Ca^{2+} signaling regulates synaptic transmission by controlling the release of neurotransmitters from synaptic vesicles at the pre-synapse into the synaptic cleft which initiates signal transmission to the post-synaptic neuron (Katz and Miledi 1967; Sudhof 2012). Chemical and electrical stimulation of neurons induce a local increase in the intracellular Ca^{2+} concentration by influx through different ion channels, subsequently triggering the fusion of synaptic vesicles with the plasma membrane (Stanley 1993). This process is tightly compartmentalized to specific signaling microdomains and highly controlled and regulated. A multitude of calcium sensor proteins as well as calcium channels are important for tight regulation of the underlying processes and strict regulation of intracellular Ca^{2+} concentrations is crucial for the normal neuronal function.

Different families of calcium channels are involved in controlling Ca^{2+}-mediated signaling. Channel gating properties regulate the Ca^{2+} fluxes through the membrane in response to different stimuli and thereby modulating intracellular Ca^{2+} concentrations. These channels can be grouped in families of VGCCs and receptor-operated calcium channels (ROC), both mediating Ca^{2+} influx from the extracellular space, as well as store-operated calcium channels (SOC), which control the release of Ca^{2+} from intracellular stores in the ER. SOCs comprise inositol triphosphate receptor (IP_3R) and ryanodine receptor (RyR) channels, whereas ROCs mainly comprise ligand-dependent ionotropic receptors like N-methyl-D-aspartate receptors (NMDAR), that regulate signal transmission at the post-synapse in response to glutamate, as well as transient receptor potential (TRP) channels.

VGCCs open and shuttle Ca^{2+} across the membrane in response to a membrane depolarizing stimulus, for example in the context of an action potential. Multiple types of VGCCs are expressed differentially in CNS neurons, comprising P/Q-type and N-type VGCCs, localized at the pre-synapse that are responsible for vesicle release, as well as L-type calcium channels that indirectly mediate Ca^{2+} fluxes in response to signal transmission at the post-synapse. VGCCs function as a crucial mediator in synaptic transmission and neuronal activity and survival. Therefore, their dysfunction is associated with numerous pathological features.

As a consequence of Ca^{2+} dysregulation, various cellular compartments can be affected, comprising the endoplasmic reticulum (ER), mitochondria and other organelles, as well as the cytoskeleton. For this reason, Ca^{2+}-induced dysfunction can lead to significant cellular damage (Young 1992; Stys and Jiang 2002).

1.1.2 Calcium Dysregulation in Neurodegeneration

Neurodegenerative diseases are characterized by the progressive loss of neurons in the PNS and CNS, associated with subsequent cognitive and functional decline in patients. Millions of people worldwide are affected and, to date, there is still a lack of therapy options for the treatment of symptoms. The most common neurodegenerative diseases, beyond others, comprise AD, Parkinson's disease (PD), amyotrophic lateral sclerosis (ALS), Huntington's disease (HD) as well as prion diseases. The underlying pathological hallmark in all of these diseases is the process of neurodegeneration, which is characterized by changes in the structure and function of neuronal cells, subsequently resulting in cell death.

Ca^{2+} signaling is a tightly controlled process, that includes regulation at the transcriptional, as well as at post-transcriptional levels and may even include self-regulation (Mellstrom, Savignac et al. 2008). It is well described that dysregulation of Ca^{2+} homeostasis is occurring as part of normal brain aging (Mattson and Magnus 2006; Murchison and Griffith 2007; Camandola and Mattson 2011). During normal aging, several Ca^{2+}-associated processes like synaptic plasticity, long-term potentiation, as well as depression, and neuronal excitability are differentially regulated (Foster 2007). There is further evidence that Ca^{2+} dyshomeostasis during normal brain aging is associated with age-related deficits in learning and memory (Thibault, Gant et al. 2007). In addition, it was reported that the capability of ER and mitochondria to maintain Ca^{2+} homeostasis is linked to cellular aging (Toescu, Verkhratsky et al. 2004; Puzianowska-Kuznicka and Kuznicki 2009). Persistently elevated intracellular Ca^{2+} levels can subsequently lead to neurodegeneration in a process termed excitotoxicity. In line with this, Ca^{2+} was found to be at least in part responsible for neuronal injury and subsequent cell death (Choi 1988; Tymianski 1996; Bano and Ankarcrona 2018). Different processes associated with Ca^{2+} dyshomeostasis are found to be responsible for a variety of pathological changes, including perturbations in various signaling pathways, alterations in synaptic transmission and impairment in Ca^{2+} buffering capacity, as well as Ca^{2+}-dependent neuronal cell death.

In the context of this, a variety of neurodegenerative diseases was previously reported to be associated with perturbations in Ca^{2+} regulation (Mattson 2007), including HD (Raymond 2017), PD (Zaichick, McGrath et al. 2017), multiple sclerosis (MS) (Kurnellas, Donahue et al. 2007; Enders, Heider et al. 2020) and AD (Bezprozvanny and Mattson 2008; Camandola and Mattson 2011). Dysregulation of Ca^{2+} is associated with alterations in the cellular buffering capacity for Ca^{2+}, excitotoxicity and oxidative stress. Remarkably, in familiar forms of AD, PD, ALS, and HD, mutations in respective disease-associated genes are strongly related to pathological Ca^{2+} dyshomeostasis. In HD, huntingtin was previously described as the link between Ca^{2+} dysregulation and neuronal cell death (Sun, Savanenin et al. 2001; Tang, Slow et al. 2005; Fan and Raymond 2007; Lim, Fedrizzi et al. 2008). Huntingtin is directly involved in inducing mitochondrial dysfunction, as well as Ca^{2+} release from the ER (Tang, Slow et al. 2005; Lim, Fedrizzi et al. 2008). In a similar fashion, α-synuclein in PD is involved in Ca^{2+} control through interactions with the Ca^{2+}-binding and modulating protein calmodulin, or by enhancing Ca^{2+} fluxes across the plasma membrane (Martinez, Moeller et al. 2003; Furukawa, Matsuzaki-Kobayashi et al. 2006; Hettiarachchi, Parker et al. 2009; Melachroinou, Xilouri et al. 2013). Ca^{2+} dyshomeostasis was further proposed to play a causative role in selective neuronal vulnerability in PD (Mattson, Pedersen et al. 1999; Chan, Gertler et al. 2009). In the context of MS, Ca^{2+} dysregulation and subsequent activation of Ca^{2+}-dependent proteases may increase neuronal vulnerability by destabilizing cytoskeletal components and, therefore, subsequently cause neuronal degeneration (Kurnellas, Donahue et al. 2007; Meuth, Melzer et al. 2009). Furthermore, in ALS, malfunction of Ca^{2+} signaling regulation was observed to have a causative role in vulnerability of motor neurons (Smith, Kimura et al. 1995; Rowland and Shneider 2001; von Lewinski and Keller 2005). In AD, known associated mutations, affecting the gene encoding presenilin 1 (PSEN1), cause an increase in intracellular Ca^{2+} concentrations (Guo, Fu et al. 1999; Schneider, Reverse et al. 2001). Furthermore, the central player amyloid-beta (Aβ) is thought to induce cellular Ca^{2+} dysregulation in disease context (Mattson 2007; Thibault, Gant et al. 2007). Therefore, understanding the role of Ca^{2+} dyshomeostasis in the context of neurodegenerative diseases is of high interest (Brini, Cali et al. 2014). Finally, the causative role of Ca^{2+} dysregulation in neuronal cell death in various neurodegenerative diseases provides an interesting target for treatment strategies (Zundorf and Reiser 2011).

1.1.3 Calcium Dysregulation in Alzheimer's Disease

AD, a multifactorial neurodegenerative disease, is the most common cause of dementia in the elderly. Pathological hallmarks comprise the accumulation of Aβ, a 40 aa to 43 aa long cleavage product of the amyloid precursor protein (APP) into extracellular plaques, followed by an irreversible and progressive loss of neurons (Selkoe 2000; Mattson 2004). So far, many therapeutic strategies have targeted the early accumulation of Aβ. As there is currently no treatment available that could cure Alzheimer's Disease or stop the development of symptoms, other therapeutic strategies are tackled. As an alternative to very early intervention strategies, "downstream" targets could be of specific interest, such as dysregulation of Ca^{2+} homeostasis observed to follow Aβ accumulation which can subsequently lead to cell damage and neuronal cell death (LaFerla 2002; Demuro, Mina et al. 2005). In particular, increased cytoplasmic Ca^{2+} levels are thought to be responsible for over-excitation and cellular stress of neurons, followed by apoptosis.

A connection between AD and Ca^{2+} dysregulation was first postulated by Khachaturian in the 1980s in the 'Calcium hypothesis' (Khachaturian 1989; Khachaturian 1994). In AD pathology, a delay between Aβ pathology onset and cognitive decline has been described, which could in part be explained by the calcium hypothesis (Berridge 2010). In different mouse models of AD, disease pathology was found to be correlated with elevated resting cytosolic Ca^{2+} levels, locally associated with amyloid plaques (Kuchibhotla, Goldman et al. 2008; Lopez, Lyckman et al. 2008). Those increased intracellular levels of Ca^{2+} could be accounted for by perturbations in different underlying processes. Different studies in AD patients further reported alterations in genes and proteins that are involved in Ca^{2+} regulation (Emilsson, Saetre et al. 2006) and several typical AD-related genes, like PSEN1 and presenilin 2 (PSEN2), were previously described to function as Ca^{2+} regulators (LaFerla 2002). In particular, PSEN1 is thought to control Ca^{2+} release from intracellular stores via modulation of different SOCs (Guo, Furukawa et al. 1996; Tu, Nelson et al. 2006; Chakroborty, Briggs et al. 2012). Several studies also reported PSEN-dependent regulation of RyR channels (Chan, Mayne et al. 2000; Lee, Hwang et al. 2006; Stutzmann, Smith et al. 2006) and IP3 receptors (Leissring, Parker et al. 1999; Cheung, Shineman et al. 2008; Cheung, Mei et al. 2010) in the context of Ca^{2+} dysregulation in AD. Moreover, homeostasis of Ca^{2+} is hypothesized to further be disrupted by an Aβ-dependent increase in plasma membrane permeability for Ca^{2+} by either a direct pore formation through Aβ (Kawahara and Kuroda 2000; Kagan, Hirakura et al. 2002) or modulation of different calcium channels

(NMDA or VGC channels) (Mattson, Cheng et al. 1992; Price, Held et al. 1998) and thereby increasing intracellular Ca^{2+} from extracellular sources. One putative underlying mechanism is the increase in Ca^{2+} influx at the pre-synapse through pre-synaptic VGCCs which triggers the release of neurotransmitters like glutamate. Excessive glutamate-mediated activation of NMDA receptors will subsequently lead to post-synaptic dyshomeostasis, activating intracellular Ca^{2+}-dependent signaling pathways, subsequently leading to neuronal cell death.

1.2 Voltage-Gated Calcium Channels

Together with voltage-gated potassium channels and voltage-gated sodium channels, VGCCs form the superfamily of voltage-dependent ion channels. Those channels mediate the transport of their respective ions across the plasma membrane in response to a voltage-dependent stimulus. In general, following a local membrane depolarization event, voltage-gated ion channels undergo a conformational change to open the aqueous channel pore to enable ions to pass down their electrochemical gradient.

VGCCs are the main mediator of Ca^{2+} fluxes in response to membrane stimulation and were first discovered and described in the 1950s (Fatt and Katz 1953; Fatt and Ginsborg 1958). Besides voltage-gated ion channels, the main family of ion channels further comprise ligand-operated ion channels, that require the binding of a specific ligand for a subsequent opening conformational change.

1.2.1 Classification

Various closely related and highly homologous channels that are part of the voltage-gated calcium channel (VGCC) family have been identified. These channels can be subdivided with regard to their electrophysiological properties into low- and high-voltage-activated channels. Furthermore, the channels are distinguished and grouped based on their biophysical and pharmacological properties. Based on their primary sequence, the channels were grouped and named Ca_V1, Ca_V2 and Ca_V3 (Birnbaumer, Campbell et al. 1994). These channels are further divided into five main categories of VGCCs: T-type, L-type, N-type, P/Q-type and R-type channels (McCleskey, Fox et al. 1986; Dunlap, Luebke et al. 1995) (Fig. 1.1). The nomenclature of the different channel subtypes was defined as $Ca_VX.Y$, with X describing the number of the channel group and Y determining the position of the subtype within its group (Catterall, Perez-Reyes et al. 2005).

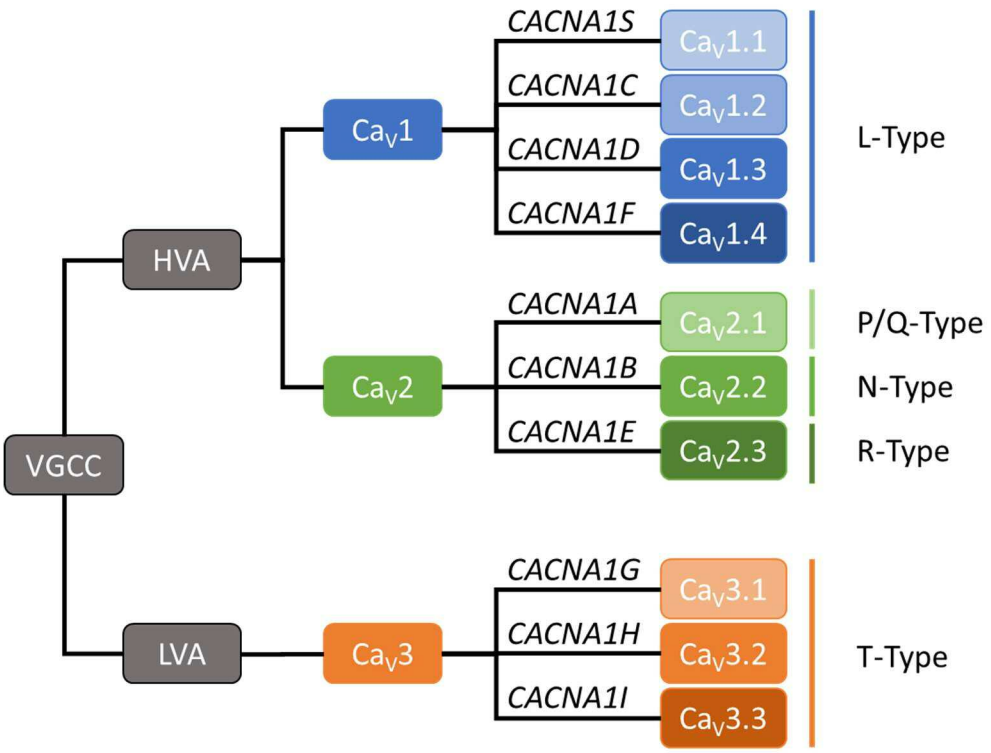

Figure 1.1: Dendrogram of the voltage-gated calcium channel (VGCC) family Calcium channels of the VGCC family can be subdivided in high-voltage-activate (HVA) and low-voltage-activated (LVA) channels. The group of HVA channels is further subdivided into Ca_V1 channels, that comprise four L-type channels ($Ca_V1.1$-1.4) encoded by four different genes (CACNA1-C, -D, -F, -S). The second group of HVA channels includes Ca_V2 channels of P/Q-, N- and R-type, encoded by three distinct CACNA1 genes. LVA channels are subdivided into three T-type channels ($Ca_V3.1$-3.3), encoded by three different genes (CACNA1G-I).

Low-voltage-activated (LVA) channels comprise T-type channels $Ca_V3.1$, $Ca_V3.2$ and $Ca_V3.3$. Those channels are characterized by activation at low voltage membrane depolarizations and their fast inactivation kinetics, resulting in transient ("T"-type) currents (Carbone and Lux 1984; Fedulova, Kostyuk et al. 1985). In contrast to this, high-voltage-activated (HVA) VGCCs are activated at more positive membrane potentials. This group comprises all "long-lasting" L-type Ca_V1 channels, including $Ca_V1.1$, $Ca_V1.2$, $Ca_V1.3$ and $Ca_V1.4$, that are expressed in a wide range of excitatory cells in the skeletal and smooth muscle, as well as in cardiac myocytes. Those channels are characterized by sensitivity to blocking through dihydropyridines (DHP). On the contrary, HVA Ca_V2 VGC channels are insensitive to DHPs. Channels belonging to the Ca_V2 family are mainly expressed at the pre-synapse of neurons where they are involved in neurotransmitter release in the context of signal transduction. P-type Ca_V2 channels ($Ca_V2.1$) were originally named after their discovery in Purkinje cells and are blocked by the funnel web spider (*Agelenopsis aperta*)-derived venom omega-Agatoxin IVA (ω-Aga IVA) (Hillman, Chen et al. 1991; Mintz, Venema et al. 1992). A less ω-Aga IVA-sensitive Q-type channel was additionally discovered, and later described as an alternative splice variant of P-type channels, for what

reason both channels are now referred to as one P/Q-type channel category (Bourinet, Soong et al. 1999). The “neuronal” N-type channel was described as $Ca_V2.2$ channel and is specifically inhibited by the cone snail (*Conus geographus*/ *Conus magus*) toxins omega-Conotoxin GVIA and MVIIA (ω-CgTx GVIA and ω-CgTx MVIIA) (Olivera, McIntosh et al. 1984; Nowycky, Fox et al. 1985; Olivera, Cruz et al. 1987). After blocking of all Ca^{2+} currents mediated through the other subtypes of VGCCs, residual currents were assigned to the R-type VGCC, $Ca_V2.3$, also known as E-type VGCC, which is known to be specifically inhibited by the compound SNX-482 (Niidome, Kim et al. 1992; Newcomb, Szoke et al. 1998).

1.2.2 Structure

VGCCs are multiprotein complexes, originally described based on studies of $Ca_V1.1$ to consist of a pore-forming domain of about 175 kDa, and three auxiliary subunits, with respective sizes of 150 kDa, 50 kDa and 30 kDa. Later, the structure of the VGCC complex was described more in detail as comprising the pore-forming α_1-domain with a size of 190 kDa to 250 kDa depending on the channel subtype, that is associated with an auxiliary β-subunit of 50 kDa, an extracellular di-sulfide-connected and membrane-anchored $\alpha_2\delta$- subunit of around 150 kDa, as well as additional association with a membrane-spanning γ-subunit in some channels (Ruth, Rohrkasten et al. 1989; Dolphin 2012; Dolphin 2013; Dolphin 2016).

1.2.2.1 α_1-Subunit

The α_1-subunit is the main pore-forming structure of all VGCCs and exhibits a similar topology for all different subtypes. Its structure was first described in detail based on a cryo- electron microscopy (EM) structure model of the $Ca_V1.1$ channel (Wu, Yan et al. 2016). The α_1-subunit is not only the pore-forming unit, but also contains the voltage sensor in the voltage sensor domain (VSD) and is responsible for ion selectivity. Structurally, the α_1-subunit is composed of four homologous domains, termed domain I, II, III and IV, which each consist of six transmembrane helices, S1-S6, that are connected via intra- or extracellular loops of differing length and sequence (Fig. 1.2).

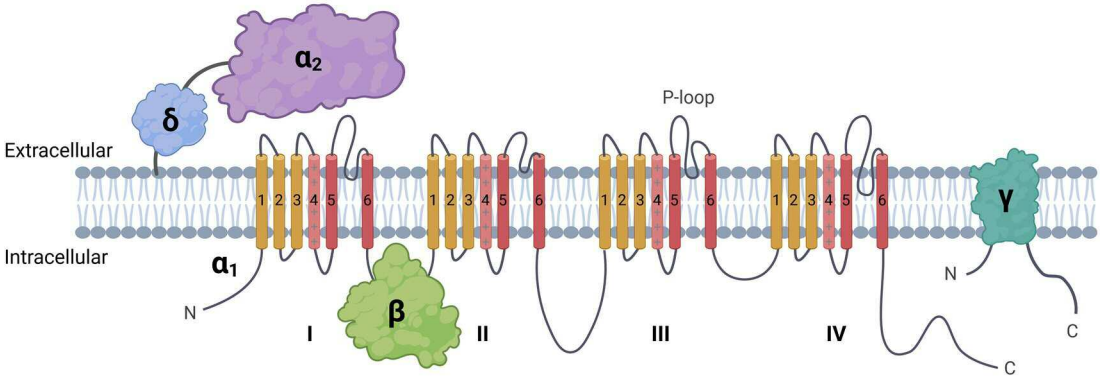

Figure 1.2: Schematic representation of the structure of the α_1-subunit of voltage-gated calcium channels (VGCCs) The pore forming α1-subunit (cyan) is composed of four homologous domains (I-IV), each comprising six transmembrane helices (S1-S6) connected via loops. The Ca^{2+}-permeable pore is formed by S5/S6 helix regions (teal) and the P-loops, latter containing the ion selectivity filter. Helices S4 contain the voltage sensor (+), responsible for mediating channel opening and closing processes of the S5/S6 activation gate. Auxiliary subunits $\alpha_2\delta$ (pink/purple), β (green) and γ (orange) are associated further with the α_1-domain. Figure created with BioRender.com

The central Ca^{2+}-permeable pore is formed by membrane spanning residues of helices S5 and S6 of all domains, as well as their connecting reentrant P-loops. The P-loops are located at the extracellular part of the channel and are partially integrated in the membrane portion. Each P-loop contains a conserved negatively charged glutamic acid residue, which together form an EEEE-motif that is mainly responsible for Ca^{2+} ion selectivity (Ellinor, Yang et al. 1995; Tang, Gamal El-Din et al. 2019).

Helices S4 contain the voltage sensor domain in all VGCCs. At resting membrane potentials, positively charged amino acids of S4, either arginine or lysine residues, form electrostatic interactions with negatively charged residues of neighboring helix regions, so the channel conformation is remained in a 'closed' and inactive state at negative internal resting membrane potentials. Depolarization of the membrane as response to an action potential reduces electrostatic forces which subsequently enables the S4 segment to undergo a conformational change, resulting in a spiral-like outward movement of the gating charges (Catterall 2010). In the 'closed' state of the channel, the aqueous Ca^{2+}-permeable pore of the channel is blocked by intracellular regions of the S6 helix that protrudes into the channel pore. In response to the physical displacement of the S4 helix after membrane depolarization, a mechanical force is put on the S4-S5 linker, which triggers a conformational change in the S6 helix resulting in an opening movement of the S6 segment. As a result, helices S5 and S6 form the so-called 'activation gate' (Domene, Doyle et al. 2005). Channel opening enables the influx of hydrated Ca^{2+} ions, which exhibit an uni-directional movement across the membrane in an extra- to intracellular direction following a step-wise process (Wu, Yan et al. 2016; Tang, Gamal El-Din et al. 2019).

1.2.2.2 Auxiliary Subunits

Multiple auxiliary subunits are associated with the pore-forming α_1-subunit, namely an extracellular $\alpha_2\delta$-subunit, an intracellular β-subunit, and in some VGC channels an additional associated transmembrane γ-subunit.

The **$\alpha_2\delta$-subunit** is encoded by a single gene as this subunit is produced as one pre-polypeptide. Subsequently, the protein undergoes post-translational cleavage into two disulfide-linked domains of approximately 150 kDa (α_2) and 17 kDa to 25 kDa (δ) (Dolphin 2013). Four different gene variants of the *CACNA2D* gene have been identified so far (*CACNA2D1-4*), and transcripts further undergo alternative splicing. *CACNA2D1* encodes for the $\alpha_2\delta_1$-domain, which is ubiquitously expressed in muscle cells as well as in the CNS. In contrast, $\alpha_2\delta_2$ and $\alpha_2\delta_3$, encoded by *CACNA2D2* and *CACNA2D3*, respectively, show expression only in neurons of the CNS and the PNS (Cole, Lechner et al. 2005). The *CACNA2D4* gene encodes the $\alpha_2\delta_4$-subunit, that is mainly expressed in endocrine tissue and retinal neurons (Wycisk, Zeitz et al. 2006).

The $\alpha_2\delta$-subunit is located extracellularly, but remains membrane-anchored via a C-terminal GPI anchor at the δ-portion. This particular subunit is mainly involved in facilitating the trafficking of Ca_V channels to allow for their proper expression and localization at the plasma membrane for functional activity (Canti, Nieto-Rostro et al. 2005; Cassidy, Ferron et al. 2014; Kadurin, Ferron et al. 2016). Furthermore, the $\alpha_2\delta$-subunit is involved in regulation of channel function by promoting channel activation (Davies, Hendrich et al. 2007; Hoppa, Lana et al. 2012; Kadurin, Ferron et al. 2016). Expression of auxiliary $\alpha_2\delta$-subunits leads to increased channel density in the plasma membrane and association of α_1-subunits with $\alpha_2\delta$-subunits shifted the activation current to more hyperpolarized values and increases macroscopic Ca^{2+} currents (Shistik, Ivanina et al. 1995; Gurnett, De Waard et al. 1996; Felix, Gurnett et al. 1997; Davies, Hendrich et al. 2007; Dolphin 2018). Interestingly, the $\alpha_2\delta$-domain provides a binding site for drugs like pregabalin and gabapentin that target epilepsy and neuropathic pain, respectively (Field, Cox et al. 2006).

β-subunits are 50 kDa to 65 kDa large domains that are associated with the α_1-subunit by interacting at the intracellular loop region connecting domains I and II. Four different genes encode for mammalian β-subunits, *CACNB1-4*, with additional variation during post-transcriptional alternative splicing events. Thus, they give rise to different forms of $\beta_{1\text{-}4}$-subunits that vary in their tissue distribution (Powers, Liu et al. 1992; Tanaka, Sakagami et al. 1995; Chu, Larsen et al. 2004; Buraei and Yang 2010). Association of VGC channels

with β-subunits promotes channel expression by modulating proteasome-dependent degradation processes (Altier, Garcia-Caballero et al. 2011; Waithe, Ferron et al. 2011). Furthermore, β-subunits increase the current density of Ca_V channels by mediating channel trafficking to the plasma membrane as well as by increasing channel opening probability through shifting channel kinetics and voltage dependence of the channel in a subunit-dependent way (Singer, Biel et al. 1991; Hofmann, Lacinova et al. 1999; Dolphin 2003; Dalton, Takahashi et al. 2005).

L-type calcium channels were originally thought to be the only VGCC subtype to additionally associate with an auxiliary **γ-subunit** in skeletal muscle cells, but more recently the γ-subunit was found to also associate with Ca_V channels in the brain (Letts, Felix et al. 1998; Kang, Chen et al. 2001; Yang, Katchman et al. 2011). So far, eight different γ-subunit, encoded by the CACNG gene family have been identified (Catterall 2000). All γ-subunits are composed of four transmembrane spanning helices connected by loops, as well as intracellular N- and C-terminal regions with an overall corresponding molecular weight of approximately 30 kDa (Chen, Deng et al. 2007). It is hypothesized that γ-subunits are involved in regulation of Ca^{2+} influx by functioning as an endogenous Ca^{2+} antagonist (Andronache, Ursu et al. 2007). Association of Ca_V channels with γ-subunits has been reported to reduce macroscopic Ca^{2+} currents, whereby affected channel subtypes and the extent of regulation was dependent on the γ-subunit isoform (Sharp, Black et al. 2001; Moss, Viard et al. 2002; Sandoval, Arikkath et al. 2007; Ferron, Davies et al. 2008).

1.2.3 Expression and Function

VGC channels are expressed in a variety of tissues throughout the body, including skeletal and cardiac muscle cells, endocrine and immune cells, as well as neurons of the CNS and PNS.

L-type **Cav1** channels were reported to be expressed in all excitable cells of the body and, thus, play an important role in various physiological and pathophysiological functions (Tsien, Ellinor et al. 1991; Striessnig and Koschak 2008; Striessnig, Pinggera et al. 2014). In neurons, Cav1 channels are mainly localized at the post-synapse and the soma, although pre-synaptic expression was observed as well (Zhang, Maximov et al. 2005; Tippens, Pare et al. 2008). A differential expression pattern is observed for the different channel subtypes: Cav1.1 channels are primarily found in skeletal muscle cells, where they exhibit a key role in excitation-contraction coupling (Tanabe, Takeshima et al. 1987; Numa, Tanabe et al. 1990; Tuluc, Molenda et al. 2009). As cells of the skeletal muscle are not reliant on Ca^{2+} influx from external stores, it is thought that L-type channels regulate the release of Ca^{2+} ions from internal stores in response to membrane depolarization by modulating RYRs (Nakai, Sekiguchi et al. 1998). Cav1.2 and Cav1.3 channels are equally expressed in skeletal muscle cells, but are further found in cardiomyocytes, sensory and endocrine cells, as well as neurons in the CNS (Hell, Westenbroek et al. 1993). They exhibit a large variability through post-transcriptional alternative splicing events and differential association with β-subunits (Pichler, Cassidy et al. 1997; Link, Meissner et al. 2009). The heterogeneity of Cav1.2 and Cav1.3 channels is overall attributed to their large functional diversity through modulation of protein-protein interactions (PPI) and channel gating properties (Koschak, Reimer et al. 2001; Bock, Gebhart et al. 2011). Their main function is excitation-contraction coupling, but Cav1.2 and Cav1.3 channels are further involved in Ca^{2+} homeostasis, regulation of gene expression as well as hormone secretion (Tanabe, Beam et al. 1988; Artalejo, Adams et al. 1994; Bers 2002; Lipscombe, Helton et al. 2004; Felizola, Maekawa et al. 2014), with a specific role for Cav1.2 channels in signaling in the heart (Harvey and Hell 2013) and Cav1.3 in heart pacemaker activity (Mangoni, Couette et al. 2003). In contrast, Cav1.4 channels are expressed in cells of the immune system, in sensory cells and in retinal neurons, where they are mainly involved in mediating neurotransmitter release (Xu, Zhao et al. 2002; Berntson, Taylor et al. 2003; Singh, Hamedinger et al. 2006; Pangrsic, Singer et al. 2018; Koschak, Fernandez-Quintero et al. 2021).

In contrast to the predominant post-synaptic expression of Cav1 channels, **Cav2** channels exhibit a pre-synaptic localization. They are expressed in neurons and endocrine cells, where they function as mediators of membrane depolarization-induced release of neurotransmitters, supporting synaptic transmission, and are further involved in gene regulation. In the brain, expression of Cav2 channels is found in different regions, like the hippocampus, in cortical neurons and also in the thalamus (Schlick, Flucher et al. 2010). Cav2.1 P/Q-type channels and Cav2.2 N-type channels are key mediators of fast synaptic transduction, as they trigger the release of neurotransmitter like acetylcholine or glutamate in response to a depolarizing stimulus in a rapid fashion (Wheeler, Randall et al. 1994; Kitano, Nishida et al. 2003; Pardo, Hajela et al. 2006). The effective coupling of neuron excitation to neurotransmitter release is enabled by close proximity of the channels to synaptic vesicles facilitated via a syntaxin interaction site present in Cav2.1 and Cav2.2, but not in Cav2.3 (Sheng, Rettig et al. 1994; Rettig, Sheng et al. 1996; Sheng, Rettig et al. 1996). Furthermore, Cav2.1 and Cav2.2 channels were reported to play a role in potassium-dependent cellular signaling (Berkefeld, Sailer et al. 2006; Loane, Lima et al. 2007). Cav2.3 R-type channels are similarly involved in mediation of neurotransmitter release and further function in secretory cell control (Albillos, Neher et al. 2000). In addition, Cav2 channels exhibit regulatory function in gene expression for a variety of proteins in a CREB-dependent manner (Wheeler, Groth et al. 2012).

Cav3 T-type LVA-VGC channels are widely expressed in neurons of the CNS (Soong, Stea et al. 1993; Perez-Reyes, Cribbs et al. 1998; Perez-Reyes, Lee et al. 1999), but their expression pattern has been reported to change during CNS development (Aguado, Garcia-Madrona et al. 2016). Cav3 channels mainly regulate neuronal excitability, as the resting membrane potential of neurons keeps them in a partially inactivated state, but already small depolarizing stimuli may activate channels, which allows for Cav3-mediated Ca^{2+} influx facilitating subsequent membrane depolarization (Chevalier, Lory et al. 2006; Dreyfus, Tscherter et al. 2010). They are further associated with neuronal potassium channels and thus additionally regulate neuronal firing activity (Turner and Zamponi 2014). Besides this, T-type channels are also involved in mediation of hormone secretion as well as regulation of gene expression (Carabelli, Marcantoni et al. 2007).

1.3 N-type Voltage-Gated Calcium Channels ($Ca_V2.2$)

After the first discovery of membrane depolarization-induced Ca^{2+} fluxes mediated by the L-type VGCC, additional non-L-type neuronal currents were observed to persist after blocking of Ca_V1 channels. Channels mediating these currents exhibited different channel activation and inactivation kinetics and were termed N-type VGCC ($Ca_V2.2$) (Nowycky, Fox et al. 1985). Later, the discovery of ω-CgTx GVIA as potent $Ca_V2.2$ channel blocker paved the way for the isolation and more detailed analysis of those channels via specific pharmacological blocking of N-type-mediated Ca^{2+} currents (Kerr and Yoshikami 1984; Olivera, McIntosh et al. 1984; Dooley, Lupp et al. 1987; Kasai, Aosaki et al. 1987). In surrounding medium containing 5 mM calcium chloride ($CaCl_2$), $Ca_V2.2$ channels were observed to get activated at membrane potentials of -20 mV and more depolarized potentials, showing a peak in activation at around 10 mV (Bleakman, Bowman et al. 1995). Thus, it could be demonstrated that N-type channels feature an intermediate activation potential, compared with other VGCC subtypes.

Initially, a hierarchy of VGCC conductance was postulated based on their activation potential, with $Ca_V1 > Ca_V2 > Ca_V3$. In contrast, under physiological Ca^{2+} gradients, $Ca_V2.2$ was identified to carry the largest Ca^{2+} currents, suggesting that in pre-synaptic terminals intermediate conductance $Ca_V2.2$ channels are favored (Weber, Wong et al. 2010). This identified $Ca_V2.2$ as the primary mediator of Ca^{2+} influx at pre-synaptic terminals, triggering subsequent neurotransmitter release, suggesting a main function for $Ca_V2.2$ channels in coupling of neuronal excitability with signal transduction (Hirning, Fox et al. 1988; Maggi, Tramontana et al. 1990; Wheeler, Randall et al. 1994; Weber, Wong et al. 2010).

1.3.1 Structure, Expression and Function

The first structure of the $Ca_V2.2$ channel was published in 1992, but more recently higher resolution structures of the channel complex were obtained by analysis using cryo-EM (Williams, Brust et al. 1992; Dong, Gao et al. 2021; Gao, Yao et al. 2021). In general, $Ca_V2.2$ has a similar structure and complex assembly like all VGCCs, comprising a pore-forming α_1-subunit, that is associated with auxiliary subunits β and $\alpha_2\delta$ (for more details, see chapter 1.2.2).

The $Ca_V2.2$ channel is encoded by the *CACNA1B* gene that comprises 46 exons. During protein expression, alternative splicing events create various $Ca_V2.2$ isoforms with differential distribution and function (Lipscombe, Pan et al. 2002). Expression and alternative splicing events are dependent on the respective tissue and cell type, and were observed to further vary during development (Gray, Raingo et al. 2007). So far, at least four cell-specific 5' and 3' splicing sites are known. In addition, different cassette exons were reported (exons 18a, 20a, 24a, 31a), which are either included or not included, as well as one mutually spliced exon (exon 37a/b), that is incorporated as isoform a or b (Lipscombe, Andrade et al. 2013).

Exons 24a and 31a encode amino acids localized in extracellular regions of the S3-S4 connecting loop of domain III and IV, respectively. Exon 24a is mainly incorporated in the brain, whereas inclusion of exon 31a is primarily observed in cells of the PNS. As the insertion occurs in the VSD, overall channel kinetics are modulated. Insertion of glutamate and threonine residues (exon 31a) results in alteration of channel kinetics with reduced channel activation and inactivation, while leaving the voltage dependence of the channel unaltered (Lin, McDonough et al. 2004).

In contrast, exon 18a and 20a are located in the intracellular region linking domain II and III. Incorporation of exon 20a leads to the insertion of a premature stop codon, resulting in expression of an incomplete and malfunctioning channel, which is thought to be involved in regulation of $Ca_V2.2$ protein expression by premature degradation of truncated proteins (Raghib, Bertaso et al. 2001). In contrast, exon 18a encodes a short stretch of serine and threonine-rich sequences in the synaptic protein interaction (synprint) binding region, influencing protein interaction capacity in this region, which suggests a potential regulatory role in neuronal excitability (Catterall 1999; Harkins, Cahill et al. 2004). Channels expressing exon 18a have been observed to exhibit reduced cumulative and closed-state inactivation, as well as a shift of steady-state inactivation to more depolarized potentials in a β-subunit-dependent way (Pan and Lipscombe 2000; Lipscombe, Pan et al. 2002; Thaler, Gray et al. 2004). Furthermore, $Ca_V2.2$ channels containing exon 18a were observed to carry increased Ca^{2+} current densities (Allen, Toro et al. 2017). In the same region, deletions in the intracellular II-III loop were reported at position ΔR756-L1139 and ΔK737-A1001. This creates deletions in the synprint interaction site, resulting in the lack of ability of $Ca_V2.2$ channels to organize in clusters at the pre-synapse, reducing the neurotransmitter release probability in response to membrane depolarization (Szabo, Obermair et al. 2006).

In addition to cassette exons, the best studied alternatively spliced exon is exon 37 that undergoes mutually exclusive splicing into 37a or 37b. These exons encode amino acids that are located in the intracellular C-terminal region of the channel. Exon 37a is predominantly expressed in dorsal root ganglia (DRG) and nociceptors, where the channel is thought to be involved in pain perception (Bell, Thaler et al. 2004; Jiang, Andrade et al. 2013). For $Ca_V2.2$ channels expressing exon 37a, an increased amplitude and longer lasting currents have been reported, partially mediated by changing G-protein-dependent inhibition (Castiglioni, Raingo et al. 2006; Raingo, Castiglioni et al. 2007). These channels were observed to be involved in basal nociception and further linked to thermal and mechanical hyperalgesia in the context of inflammation or neuropathic pain (Altier, Dale et al. 2007). On the other hand, $Ca_V2.2$ channels expressing exon 37b are widely expressed in neurons in the CNS and PNS. Incorporation of exon 37b increases ubiquitination of $Ca_V2.2$ channels, which subsequently enhances degradation through the ubiquitin proteasome system (UPS) resulting in reduced overall $Ca_V2.2$-mediated current density compared with $Ca_V2.2$ e37a channels (Marangoudakis, Andrade et al. 2012).

In general, $Ca_V2.2$ channels are found widely expressed in cells of the CNS and in the PNS, first determined in immunostaining approaches (Westenbroek, Hell et al. 1992). N-type channels were observed to be predominantly expressed in dendrites, along axons and in synapses, but were also found in high density on large mossy fiber terminals of dentate gyrus granule neurons. Predominant expression is found in dendrites and nerve terminals as well as in the soma of central neurons, further highlighting its role in synaptic transmission (Westenbroek, Hoskins et al. 1998). In addition, $Ca_V2.2$ channels have been reported to be the primary VGCC subtype in sympathetic and sensory neurons (Fox, Nowycky et al. 1987; Hirning, Fox et al. 1988; Murakami, Nakagawasai et al. 2001; Mori, Nishida et al. 2002).

The main function reported for $Ca_V2.2$ channels is the regulation of cellular excitability and synaptic signal transduction. Ca^{2+} influx through N-type channels triggers a rapid (< 100 µs) release of neurotransmitters from synaptic vesicles in response to membrane depolarization, which is achieved by coupling $Ca_V2.2$ channels, located in the pre-synaptic membrane, to the release machinery of synaptic vesicles (Muller, Haupt et al. 2010). This organization in nano- and microdomains enables close proximity of channels with synaptic vesicles. This proximity is essential in effectively triggering neurotransmitter release, as tight coupling is required for fast synaptic transmission (Bucurenciu, Kulik et al. 2008; Eggermann, Bucurenciu et al. 2011). On the other hand, it was reported that the coupling intensity changes during brain development, as loose coupling is important for synaptic plasticity

(Vyleta and Jonas 2014). During synaptic maturation, a decrease in channel density is observed, accompanied by a reorganization of the channels to allow for tighter coupling (Nakamura, Harada et al. 2015; Bornschein, Eilers et al. 2019).

For rapid synaptic transmission, most synapses rely on a combination of Ca^{2+} fluxes through pre-synaptic $Ca_V2.1$ as well as $Ca_V2.2$ channels, and only to a lesser extent through $Ca_V2.3$ channels (Takahashi and Momiyama 1993; Wheeler, Randall et al. 1996; Ariel, Hoppa et al. 2012). Although the N-type channel is thought to be the dominant VGCC at the pre-synapse during neurotransmitter release, overlapping function with the P/Q-type channel has been observed in the pre-synapse of various neuronal cell types in the CNS (Meir, Ginsburg et al. 1999; Wu, Westenbroek et al. 1999; Reid, Bekkers et al. 2003). In the PNS, $Ca_V2.2$ channels are the main contributor of vesicle release in DRG neurons (Murali, Napier et al. 2015). N-type Ca^{2+} channels were previously reported to be involved in regulation of release of various neurotransmitters (Turner, Adams et al. 1993; Wheeler, Randall et al. 1994). Those comprise neurotransmitters such as noradrenaline, dopamine, acetylcholine, GABA, glutamate as well as serotonin (Dooley, Lupp et al. 1988; Woodward, Rezazadeh et al. 1988; Herdon and Nahorski 1989; Wessler, Dooley et al. 1990; Horne and Kemp 1991; Li and Duckles 1991; Luebke, Dunlap et al. 1993; Foehring 1996; Pardo, Hajela et al. 2006).

In summary, $Ca_V2.2$ channels are involved in neurotransmitter release in response to membrane depolarization in various regions of the CNS and PNS. High variability in expression patterns and contribution of different pre-synaptic Ca_V channels allows for tight and specific regulation of synaptic function, highlighting the important role of $Ca_V2.2$ channels in the CNS as well as in the periphery.

1.3.2 Modulation of $Ca_V2.2$

Ca^{2+} fluxes through $Ca_V2.2$ channels are functionally versatile as well as highly plastic, and are mainly dependent on the gating properties of these channels. Therefore, tight control of channel expression and activation is crucial for normal physiological cellular functions. Regulatory mechanisms comprise direct modulation at the translational and post-translational level, and also indirect modulation via PPI. The major regulatory mechanisms comprise inactivation of $Ca_V2.2$ channels either by voltage-dependent inactivation (VDI) or calcium-dependent inactivation (CDI), modulation by secondary proteins like auxiliary subunits or other associated proteins, and also by direct modulation through post-translational modification (PTM) of the channel.

1.3.2.1 Regulatory Effect of Auxiliary Subunits

The auxiliary subunits associated with the pore-forming α_1-subunit exhibit a main regulatory function with regard to channel expression, trafficking as well as opening and gating properties.

The auxiliary subunit $\alpha_2\delta$ is involved in mediating trafficking of VGC channels and thus regulates the channel density in the plasma membrane at the pre-synapse. Furthermore, it was reported, that association with $\alpha_2\delta$ subunits changes the biophysical properties of VGC channels (Dolphin 2013). In line with this, $\alpha_2\delta$ subunits have been observed to regulate the function of $Ca_V2.2$ channels, as association with $\alpha_2\delta_1$ reduced the opening probability of the channel (Wakamori, Mikala et al. 1999). Nevertheless, the main $\alpha_2\delta$-dependent regulation on $Ca_V2.2$ function is mediated through regulation of channel trafficking. Association of α_1-subunits with $\alpha_2\delta$-subunits was observed to mediate the transport of channels from the *trans*-golgi network to membrane regions located at the pre-synapse of neurons (Patel, Bauer et al. 2013; Cassidy, Ferron et al. 2014; Nieto-Rostro, Ramgoolam et al. 2018). The importance of this regulatory mechanism becomes apparent when considering the wide range of pathophysiological processes related to pain in which dysregulation of $\alpha_1/\alpha_2\delta$-association is implicated. This highlights the potential of targeting this process as an interesting therapeutic strategy in treating neuropathic pain (Field, Cox et al. 2006).

VGCC regulation by β-subunits has been demonstrated to be mediated by influencing channel trafficking as well as regulation of biophysical properties of the channel (Neely, Garcia-Olivares et al. 2004; Buraei and Yang 2013). Association of $Ca_V2.2$ α_1-subunits with different β-subunits enhanced their cell surface expression, rather by protecting it from proteasomal degradation by inhibition of ubiquitination, than, as initially hypothesized, through ER retention (Bichet, Cornet et al. 2000; Waithe, Ferron et al. 2011). Furthermore, association with β-subunits is essential for G-protein-dependent inhibitory mechanisms (explained in 1.3.2.2) (Meir, Bell et al. 2000; Leroy, Richards et al. 2005).

Although the exact regulatory effect of γ-subunits remains to be elucidated, it is known that association of $Ca_V2.2$ channels with different γ-subunit isoforms has a regulatory effect on channel expression and activity (Moss, Viard et al. 2002; Ferron, Davies et al. 2008).

1.3.2.2 Protein-Protein Interaction-Dependent Regulation

Besides regulation through interaction with auxiliary subunits, $Ca_V2.2$ channel expression and activity are also mediated by interaction with other secondary proteins via direct and indirect interactions. Direct interaction of $Ca_V2.2$ α_1-subunits with soluble N-ethylmaleimide-sensitive factor attachment protein receptor (SNARE) proteins, as well as with G-protein coupled receptors (GPCR) has been reported.

Previously, a negative feedback inhibition of $Ca_V2.2$ channels mediated by **GPCRs** could be observed. GPCRs get activated in response to $Ca_V2.2$-dependent neurotransmitter release, which induces activation of heterotrimeric G-proteins that will bind directly to different regions on the $Ca_V2.2$ α_1-subunit, subsequently leading to channel inhibition (Furukawa, Miura et al. 1998; Simen, Lee et al. 2001). Association of the G-protein βγ-dimer with the linker region between domain I and II induced a conformational change that stabilized the channel in closed conformation, resulting in slowed activation kinetics (De Waard, Liu et al. 1997; Qin, Platano et al. 1997; Furukawa, Miura et al. 1998; Page, Canti et al. 1998; Stephens, Brice et al. 1998; Canti, Page et al. 1999; Tedford and Zamponi 2006; Pan, Wu et al. 2008). This interaction is less prominent at more depolarized membrane potentials, which led to characterization of channel regulation by direct binding of the G-protein βγ-dimer as voltage-dependent inhibition (Bean 1989). In contrast to this, G-proteins further mediate $Ca_V2.2$ channel activity through an indirect voltage-independent inhibitory regulation mechanism via phosphatidylinositol-4,5-bisphosphate (PIP_2) hydrolysis (Vivas, Castro et al. 2013). Furthermore, G-proteins are able to indirectly regulate channel activity by second messenger activation resulting in phosphorylation of $Ca_V2.2$, which affects the biophysical properties of the channel (Arnot, Stotz et al. 2000; Herlitze, Zhong et al. 2001; Pan, Wu et al. 2008). In addition, direct interaction of $Ca_V2.2$ α_1-subunits with different GPCRs was found to mediate channel expression at the plasma membrane, as well as channel internalization (Kisilevsky, Mulligan et al. 2008; Heinke, Gingl et al. 2011).

A direct interaction of $Ca_V2.2$ α_1-subunits was also observed with different **SNARE** proteins such as syntaxin 1A, synaptosome-associated protein, 25 kDa (SNAP-25), synaptotagmin and cysteine string protein (CSP) (Leveque, Hoshino et al. 1992; Leveque, el Far et al. 1994). The predominant interacting region of SNARE proteins on α_1-subunits of $Ca_V2.2$ is the synprint region located in the cytoplasmic loop connecting domain II and III (Sheng, Rettig et al. 1994; Sheng, Yokoyama et al. 1997). Direct interaction of SNARE proteins with $Ca_V2.2$ resulted in clustering of $Ca_V2.2$ channels in close proximity to the synaptic vesicle

release machinery and poses an important basis for rapid neurotransmission (Mochida, Sheng et al. 1996; Rettig, Heinemann et al. 1997; Bezprozvanny, Zhong et al. 2000; Degtiar, Scheller et al. 2000). The binding of SNARE proteins to the synprint region was previously reported to be Ca^{2+}-dependent with a maximal binding near Ca^{2+} concentrations required for vesicle release, providing an important regulatory feedback mechanism in response to increased intracellular Ca^{2+} levels (Sheng, Rettig et al. 1996). In addition, direct binding of SNARE proteins has been observed to regulate channel modulation by G-proteins (Jarvis, Magga et al. 2000; Magga, Jarvis et al. 2000; Jarvis and Zamponi 2001; Lu, AtKisson et al. 2001).

1.3.2.3 Post-Translational Modification-Dependent Regulation

PTMs are key regulators in a wide range of protein functions throughout the whole body and are also observed to regulate the activity and expression of VGCCs. Most important regulatory PTMs on VGCCs comprise channel phosphorylation, glycosylation, S-palmitoylation as well as ubiquitination.

Direct regulatory **phosphorylation** of $Ca_V2.2$ at the α_1-subunit occurs at several phosphorylation sites mediated by different kinases such as protein kinase C (PKC), cyclin-dependent kinase 5 (CDK5) or Ca^{2+} calmodulin activated kinase II (CaMKII) (Chad and Eckert 1986; Zhu and Ikeda 1994). Phosphorylation of the C-terminal region of the α_1-subunit by CDK5 recruits $Ca_V2.2$ channels to active zones of the pre-synapse which facilitates neurotransmitter release. This was further accompanied by increased channel opening probability (Su, Seo et al. 2012). In addition, PKC-dependent phosphorylation of auxiliary subunits increased Ca^{2+} current amplitudes and total Ca^{2+} entry, while also resulting in faster channel inactivation (Rajagopal, Fang et al. 2011; Rajagopal, Fields et al. 2014). This effect was at least partially mediated by reducing G-protein-dependent inhibitory regulation mechanisms (Zhu and Ikeda 1994; Zamponi, Bourinet et al. 1997; Hamid, Nelson et al. 1999). In addition, activation of a PKC-dependent signaling cascade was observed to increase channel density in the pre-synaptic plasma membrane (Zhang, Helm et al. 2008). In contrast to that, a negative regulatory mechanism was further reported for phosphorylation of the α_1-subunit by PKC and also CaMKII in the synprint region, which subsequently inhibits the binding of SNARE proteins (Yokoyama, Sheng et al. 1997).

All subtypes of VGCCs undergo extensive post-translational **glycosylation** at several glycosylation sites (Lazniewska and Weiss 2014; Lazniewska and Weiss 2017). In general, regulatory glycosylation is found more frequently in channels of Ca_V1 and Ca_V3 families.

Nevertheless, indirect modulation of $Ca_V2.2$ was reported via glycosylation of $\alpha_2\delta$-subunits, which subsequently was found to increase the functional expression of $Ca_V2.2$ channels in the pre-synaptic plasma membrane (Sandoval, Oviedo et al. 2004).

S-palmitoylation predominantly occurs as a regulatory PTM for VGCCs at sites on auxiliary subunits, mainly on the β-subunit (Chien, Carr et al. 1996; Chien, Gao et al. 1998; Miranda-Laferte, Ewers et al. 2014; Cassinelli, Vinola-Renart et al. 2022). In N-type as well as P/Q-type channels palmitoylation of the associated β_{2a}-subunit was correlated with slowed channel inactivation (Hurley, Cahill et al. 2000).

Ubiquitination is a key regulatory mechanism in proteasome-mediated degradation of different proteins and is also implicated in regulation of VGCC turn-over. Association of $Ca_V2.2$ with the auxiliary β-subunit was observed to reduce the level of ubiquitination and prevented subsequent proteasome-dependent degradation of channels. As a consequence, the lack of ubiquitination and subsequent proteolysis indirectly increased channel density in the plasma membrane (Waithe, Ferron et al. 2011; Felix and Weiss 2017). This mechanism is mediated by interaction of β-subunits with poly-ubiquitination sites located in the cytoplasmic loop connecting domains I and II. Furthermore, ubiquitination-dependent degradation of $Ca_V2.2$ is highly isoform-dependent, heavily facilitated through expression of exon 37b resulting from alternative splicing events (see 1.3.1) (Marangoudakis, Andrade et al. 2012).

1.3.2.4 Voltage-Dependent and Calcium-Dependent Channel Inactivation

Following channel activation in response to a membrane depolarization stimulus, VGCCs will transit into a short phase of inactivation after closing of the channel. This mechanism prevents excitotoxicity caused by prolonged membrane depolarization or by increased intracellular Ca^{2+} levels. The main regulatory mechanisms controlling channel inactivation are VDI and CDI.

VDI is the inactivation of the channel in response to prolonged membrane depolarization, and is therefore defined as voltage-dependent. After continuing channel activation induced by a prolonged depolarizing stimulus, a conformational change in the cytoplasmic linker loop between domain I and II occludes the Ca^{2+}-permeable pore and creates a physical barrier for Ca^{2+} influx. This is mediated by a conformational change in the S6 domain, which leads to exposure of a binding site for the linker structure to allow docking of the domain I-II linker at the cytoplasmic S6 site, stabilizing the pore-blocking “hinged-lid” conformation (Stotz, Hamid et al. 2000; Stotz, Jarvis et al. 2004).

In contrast to this, **CDI** provides a negative feedback loop for increased intracellular Ca^{2+} concentrations (Brehm and Eckert 1978). The pore-forming α_1-subunit is associated with the Ca^{2+} sensor calmodulin at its C-terminal region (Lee, Wong et al. 1999; Liu, Yang et al. 2010; Chi, Tang et al. 2017). After binding of Ca^{2+}, the $Ca_V2.2$-calmodulin complex undergoes a conformational change, subsequently resulting in channel inhibition (Peterson, Lee et al. 2000). CDI as regulatory mechanism is mainly found in Ca_V1 channels where it occurs in response to local increases of the Ca^{2+} concentration, whereas in Ca_V2 a global increase in Ca^{2+} levels is necessary for CDI, and Ca_V3 channels are not regulated by CDI (Budde, Meuth et al. 2002; Zamponi 2003; Dick, Tadross et al. 2008).

1.3.2.5 Pharmacological Inhibition

The first identified and best characterized specific inhibitor for $Ca_V2.2$ channels is ω-CgTx GVIA, derived from the venomous marine cone snail *Conus geographus* (Olivera, McIntosh et al. 1984). ω-CgTx GVIA is a 27 amino acid long peptide, that contains three structure-determining cysteine-mediated di-sulfide bonds. It specifically and irreversibly inhibits the $Ca_V2.2$ channel via a pore-blocking mechanism by interacting with the extracellular loop region of the $Ca_V2.2$ α_1-subunit domain III between helices S5 and S6 (Ellinor, Zhang et al. 1994). In connection with this, more peptides from cone snails and spiders were identified to block VGCCs (Olivera, Miljanich et al. 1994). Several VGCC-inhibiting peptides were observed to exhibit a similar pore-blocking mechanism on VGCCs (Catterall, Perez-Reyes et al. 2005; Zamponi, Striessnig et al. 2015). Although several small molecule inhibitors like triazole oxindole (TROX-1) or other chemical structures have been identified for the inhibition of $Ca_V2.2$ channels, so far, only peptide-based compounds did exhibit subtype specificity (Hu, Ryder et al. 1999; Hu, Ryder et al. 1999; Hu, Ryder et al. 2000; Lukyanetz, Shkryl et al. 2002; Abbadie, McManus et al. 2010; Swensen, Herrington et al. 2012).

A related cone snail-derived peptide with high homology to ω-CgTx GVIA, namely ω-CgTx MVIIA, was found to selectively and, in contrast to ω-CgTx GVIA, reversibly block $Ca_V2.2$ channels (Yoshikami, Bagabaldo et al. 1989). A recombinant form of ω-CgTx MVIIA, ziconotide (SNX-111, Prialt), was developed for the specific pharmacological inhibition of $Ca_V2.2$ channels for the treatment of neuropathic pain (McGivern 2007; Schmidtko, Lotsch et al. 2010). The drug has to be administered intrathecally as it exhibits extremely low blood brain barrier (BBB) permeability and several adverse side effects like nausea, vomiting or confusion have been reported (Newcomb, Abbruscato et al. 2000; Smith and Deer 2009).

Nevertheless, to this day, ziconotide is the only drug approved for the specific block of $Ca_V2.2$ channels. More recently, in cryo-EM-based structural analysis of ziconotide in complex with $Ca_V2.2$ channels the binding mode and inhibition mechanism has been elucidated more in detail (Fig. 1.3) (Gao, Yao et al. 2021). Ziconotide was reported to be complexed in an electronegative cavity on the $Ca_V2.2$ α_1-subunit, coordinated by helices P1 and P2 of the P-loop connecting transmembrane helices S5 and S6 of domain II, III and IV, while sitting in close proximity above the Ca^{2+} selectivity filter. Binding to this site prevents movement of the VSD in response to membrane depolarization, keeping the VSD_{II} in resting-state conformation (Dong, Gao et al. 2021).

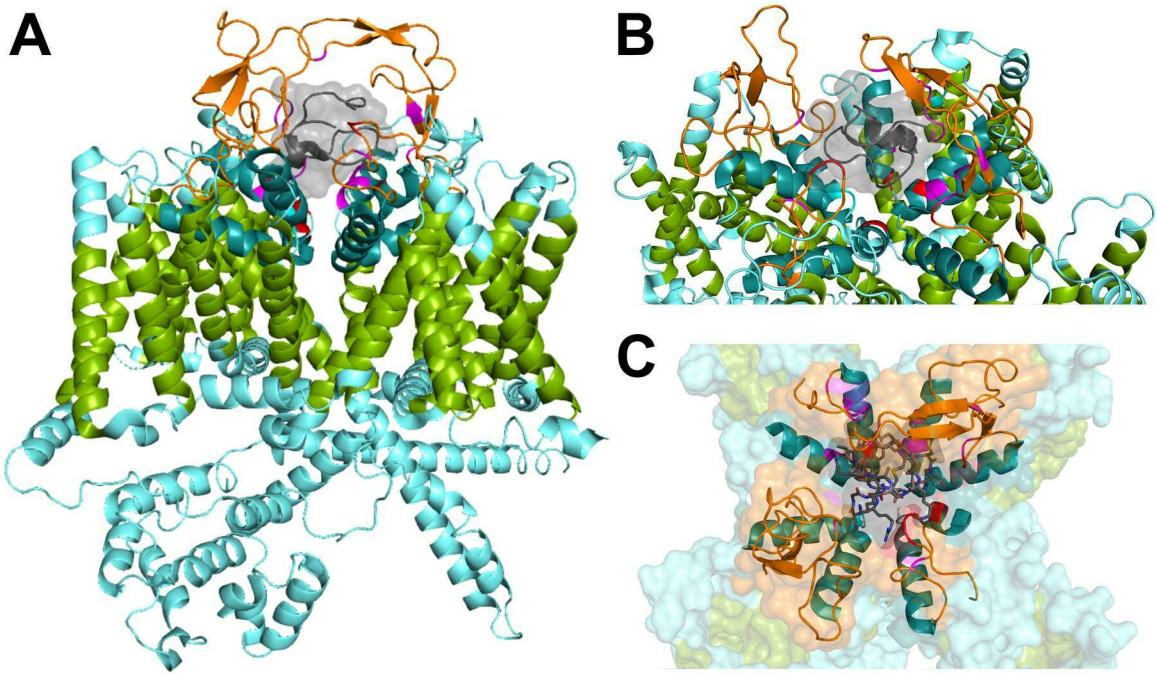

Figure 1.3: Ziconotide in complex with $Ca_V2.2$ The model is based on the cryo-EM structure of $Ca_V2.2$ in the presence of ziconotide at 3.0 Å resolution (PDB code 7MIX, (Gao, Yao et al. 2021)). All structure figures were prepared in PyMol. **A** shows the overall structure of $Ca_V2.2$ (cyan) with its membrane spanning regions highlighted in green, in complex with ziconotide (grey). **B** represents a close-up view of the pore-forming residues of $Ca_V2.2$ associated with ziconotide in a pore-blocking mechanism. The Ca^{2+}-permeable pore is mainly formed by helices of the P-loop (teal), which coordinate binding to ziconotide over several amino acids of the P1 and P2 helices and extracellular loop regions (orange) that are involved in electrostatic interactions (red), as well as amino acids associated with ziconotide via hydrophobic interactions (pink). **C** Top view of the pore-blocking mechanism of ziconotide on the $Ca_V2.2$ channel.

Indirectly, $Ca_V2.2$ channels are further modulated by drugs that target auxiliary subunits. Gabapentin (Neurontin) and pregabalin (Lyrica), developed for the treatment of epilepsy and neuropathic pain, target $\alpha_2\delta$-subunits and subsequently reduce channel density by decreasing channel trafficking activity (Tran-Van-Minh and Dolphin 2010).

1.3.3 Neuropathophysiology of $Ca_V2.2$

As previously described, $Ca_V2.2$ channels have implications in a diverse range of cellular functions and are mainly important in regulation of neuronal signal transduction. Therefore, malfunctions of $Ca_V2.2$ channels are associated with a wide range of pathological phenotypes exhibiting disrupted neuronal signal transmission or Ca^{2+} dysregulation.

$Ca_V2.2$-associated channelopathies have been reported to be caused by mutations in the gene encoding the α_{1B}-subunit. A disruptive missense mutation in the $Ca_V2.2$-encoding gene *CACNA1B* was observed to cause myoclonus dystonia (MD) syndrome and cardiac arrhythmias in a family over three generations (Groen, Andrade et al. 2015). An associated point mutation in the *CACNA1B* sequence (c.4166G>A) leads to an arginine to histidine exchange (R1389H). The respective arginine residue (R1389) is highly conserved between different VGCC subtypes and located at the end of the P-loop between helices S5 and S6 in domain III, where it is implicated in regulation of ion conductivity. The mutation was found to result in decreased single channel Ca^{2+} conductance without altering voltage-dependent activation and inactivation or ion selectivity, while overall increasing whole cell Ca^{2+} currents. Latter was proposed to be caused by increased opening duration. In contrast, no causative relationship of this mutation and MD was observed in another study (Mencacci, R'Bibo et al. 2015).

In six unrelated children, bi-allelic loss-of-function of *CACAN1B* was reported to cause progressive epilepsy-dyskinesia (Gorman, Meyer et al. 2019). Patients displayed delays in neurodevelopmental processes, epileptic encephalopathy, hyperkinetic movement disorder and finally death before reaching adulthood. This was hypothesized to be caused by an impairment in signal transmission through disruption of Ca^{2+} influx through $Ca_V2.2$ channels.

In a few cases, an aberrant autoimmune response led to the production of autoantibodies targeting $Ca_V2.2$ channels. These antibodies were found to play a causative role in Lambert-Eaton myasthenic syndrome (Motomura, Lang et al. 1997), cause severe autonomic dysfunction (Kimpinski, Iodice et al. 2009), autoimmune encephalitis (Finkel and Koh 2013; Simutis, Brosch et al. 2020) and were observed to mimic frontotemporal dementia (Younes, Lepow et al. 2018). Overall, $Ca_V2.2$-targeting antibodies were found to be implicated in oncological, neurological, as well as serological pathophysiological effects (Zalewski, Lennon et al. 2016).

Neuropathic pain is a usually chronic condition which is defined as an aberrant pain sensitization after an injury or a disease affecting the somatosensory system (Jensen, Baron et al. 2011). It can be differentiated between *allodynia*, which describes the circumstance in which a nociceptive sensation, usually not associated with pain, causes an aberrant painful sensation, and *hyperalgesia*, which is characterized by an increased pain sensation in response to a painful stimulus. Dysfunction and dysregulation of $Ca_V2.2$ channels are known to be common hallmarks in the pathophysiology of pain. $Ca_V2.2$ channels show subcellular distribution in sensory neurons and spinal dorsal horn neurons and are expressed in DRGs in the cell body, as well as in central terminals (Westenbroek, Hoskins et al. 1998; Wu, Chen et al. 2004). Mediated through their respective expression pattern, $Ca_V2.2$ channels are main contributors in nociceptive signaling in the dorsal horn and spinal cord. Malfunctions of $Ca_V2.2$ channels or associated $\alpha_2\delta$-subunits have been extensively linked to neuropathic pain, being observed to facilitate neuronal firing and neurotransmitter release (McGivern and McDonough 2004; Bourinet and Zamponi 2005; Snutch 2005; Gribkoff 2006; Schroeder, Doering et al. 2006; Yaksh 2006; Zamponi, Lewis et al. 2009). In line with this, although $Ca_V2.2$ knock-out (KO) mouse models exhibit a relatively mild phenotype, most probably caused by compensatory upregulation of $Ca_V2.1$ or $Ca_V2.3$ channels, reduced sensitivity to pain, especially inflammatory pain, was reported (Ino, Yoshinaga et al. 2001; Kim, Jun et al. 2001; Saegusa, Kurihara et al. 2001). In addition, upregulation of $Ca_V2.2$ channels in the dorsal horn was observed after sciatic nerve ligation and associated neuropathic pain was subsequently reduced by specific inhibition of $Ca_V2.2$ channels (Cizkova, Marsala et al. 2002; Saegusa, Matsuda et al. 2002). Specific inhibition of $Ca_V2.2$ with ω-CgTx GVIA blocked neurotransmitter release in sensory neurons and spinal nerve terminals, which shed light on their physiological and pathophysiological roles in the context of nociception and pain sensation (Maggi, Giuliani et al. 1990; Maggi, Tramontana et al. 1990; Gruner and Silva 1994; Ramirez, Gonzalez et al. 2017).

1.4 Voltage-Gated Calcium Channels in Disease

1.4.1 Voltage-Gated Calcium Channels in Neurological Disorders

Different members of the VGCC family are known to be implicated in various psychiatric as well as neurological disorders (Schampel and Kuerten 2017). Underlying pathological mechanisms of channelopathies in general comprise channel malfunction due to mutation, mainly in the α_1-subunit, but are also associated with differences in expression, turn-over rates as well as activation and inactivation kinetics. A general pathological hallmark underlying channelopathies is the disruption of synaptic transmission by modulation of Ca_V expression and activity (Pietrobon 2005; Pietrobon 2010). Furthermore, age-dependent alternative splicing and PTM events may also regulate channel function in healthy and diseased brain during aging (Davare and Hell 2003; Chang, Yong et al. 2007; Michailidis, Abele-Henckels et al. 2014; Qian, Patriarchi et al. 2017).

The best described group of VGCC-associated diseases is caused by malfunctions of L-type calcium channels. These calcium channel dysfunctions are involved in different diseases affecting behavioral performance. For example, it was previously described that L-type calcium channels may play a role in autism, in fear conditioning and also in mental disorders like depression or schizophrenia (Busquet, Hetzenauer et al. 2008; Dao, Mahon et al. 2010; Ripke, O'Dushlaine et al. 2013; Ostacher, Iosifescu et al. 2014; Ortner and Striessnig 2016). In addition, they are associated with disorders involving abnormal pain sensitization and blocking of Ca_V1 channels exhibits an analgesic effect (Gadotti, Bladen et al. 2015; Radwani, Lopez-Gonzalez et al. 2016).

Similarly, Ca_V2 channels are involved in a broad spectrum of neurological disorders. Mutations in the α_1-subunit of P/Q-type channels are long known to be associated with human diseases like familial hemiplegic migraine, spinocerebellar ataxia type 6, as well as episodic ataxia type 1 (Fletcher, Lutz et al. 1996; Ophoff, Terwindt et al. 1996; Zhuchenko, Bailey et al. 1997). These diseases are accompanied by cell death of Purkinje neurons, granule neurons and Golgi neurons, hypothesized to be mediated by abnormal intracellular Ca^{2+} levels. In contrast to $Ca_V2.1$ channels, $Ca_V2.2$ and $Ca_V2.3$ channels are mainly observed to be involved in pain sensation and related disorders (Saegusa, Kurihara et al. 2000; Cataldi 2013; Shan, Cai et al. 2019; DuBreuil, Lopez Soto et al. 2021). This characteristic makes the N- and R-type channels an interesting therapeutic target for the treatment of pain.

Furthermore, they also play a role in behavioral processes, as $Ca_V2.2$ inhibition was effective in reducing alcohol consumption providing a target for alcohol abuse disorder (Newton, Orr et al. 2004; Newton and Messing 2009), and $Ca_V2.3$ was previously observed to be involved in regulation of anxiety and in epileptic disorders (Zaman, Lee et al. 2011).

Channels of the Ca_V3 family are involved in similar pathologic processes. It was previously reported that malfunctions of T-type channels are implicated in various neurological diseases such as epilepsy, autism and in neuropathic pain (Ernst, Zhang et al. 2009; Lu, Dai et al. 2012; Bourinet, Francois et al. 2016). In addition, in a mouse model of PD, increased Ca^{2+}-dependent neuronal firing was mediated by T-type VGCC and blocking of the channel rescued locomotor deficits (Tai, Yang et al. 2011).

Taken together, as Ca^{2+} fluxes mediated through different VGC channels are involved in a variety of cellular processes, channel malfunctions are thought to play a causative role in a variety of different neurological disorders. Specifically targeting VGCC subtypes may therefore provide an interesting target for the treatment of various diseases (Zundorf and Reiser 2011; Heyes, Pratt et al. 2015; Schampel and Kuerten 2017).

1.4.2 $Ca_V2.2$ in Different Neurological and Neurodegenerative Diseases

Although $Ca_V2.2$ channels are thought to play a role in inflammation, excitotoxicity, as well as neuropathic pain, a limited number of studies evaluates the role of N-type VGCCs in various neurodegenerative diseases.

Interestingly, it was previously reported that inhibition of Ca^{2+} fluxes through N-type VGCCs exhibits neuroprotective effects after **ischemic injury** and in **traumatic brain injury (TBI)** (Valentino, Newcomb et al. 1993; Buchan, Gertler et al. 1994; Yenari, Palmer et al. 1996; Perez-Pinzon, Yenari et al. 1997; Berman, Verweij et al. 2000). Furthermore, blocking of N-type VGCC-dependent Ca^{2+} currents was able to resolve chronic headaches in the context of **migraine** (Narain, Al-Khoury et al. 2015; Holden, Chauhan et al. 2022).

As described in 1.1.2, in **HD**, Ca^{2+} dysregulation is found as a pathological hallmark of this disease (Oikonomou, Donzis et al. 2021). In the same study, application of a VGCC inhibitor was able to abolish Ca^{2+} dysregulation, proposing a role of VGCC in the pathological mechanism underlying HD. In line with this, it was reported that pre-synaptic Ca^{2+} influx and subsequent increased synaptic neurotransmitter release and neurodegeneration in HD was mediated through $Ca_V2.2$ channels (Chen, Yu et al. 2018). In addition, a direct

regulatory mechanism of huntingtin, one of the key players in HD, on $Ca_V2.2$ channels was reported (Silva, Miranda et al. 2017). This process is thought to be mediated by huntingtin via enhancement of the $Ca_V2.2$-mediated Ca^{2+} influx by blocking syntaxin-dependent channel inhibition (Swayne, Chen et al. 2005). An increase in channel current density and expression levels was additionally reported, which varied during disease progression. Phα1β and its recombinant version CTK 01512-2 are known to inhibit VGCCs from the Ca_V2 family. These compounds were observed to exhibit neuroprotective effects in a mouse model of HD, which is thought to be mediated by reducing Ca^{2+} dysregulation-induced excitotoxicity (Antunes, de Souza et al. 2021; Joviano-Santos, Valadao et al. 2021; Joviano-Santos, Valadao et al. 2022).

In **MS**, upregulated levels of glutamate are found in the cerebrospinal fluid (CSF) of patients (Sarchielli, Greco et al. 2003). This may in part be caused by Ca^{2+} influx through ectopically expressed VGCCs in the axonal membrane that are involved in regulating glutamate release at the pre-synapse (Kukley, Capetillo-Zarate et al. 2007). Interestingly, application of the Ca_V2 VGCC-specific inhibitor CTK 01512-2 had a beneficial effect on disease progression and improved neuroinflammation in a mouse model of MS (Silva, Greggio et al. 2018).

PD is characterized by the progressive loss of dopaminergic neurons, mainly in the substantia nigra, with α-synuclein-induced neurotoxicity as a major pathological hallmark. It could be shown that activation of N-type VGCCs and subsequently increased intracellular Ca^{2+} levels were induced by an α-synuclein-dependent regulatory mechanism on the channel. In addition, subsequently modulated neurotransmitter (dopamine) release was rescued by specifically blocking the N-type VGCC (Bergquist, Jonason et al. 1998; Melachroinou, Xilouri et al. 2013; Ronzitti, Bucci et al. 2014). Blocking of N-type as well as L-type VGCCs was previously proposed as a therapeutic strategy for the treatment of excitotoxicity in the context of PD (Koutsilieri and Riederer 2007; Ortner 2021).

Pathological changes in the context of **ALS** mainly affect motor neurons. It was previously reported that increased putative neurotoxic Ca^{2+} fluxes in motor neurons of a $SOD1^{G93A}$ mouse model of ALS were mainly mediated through N- and L-type VGCCs, which subsequently leads to hyperexcitability of cells. In part, this was mediated by upregulation of gene expression and increased channel density in the plasma membrane (Chang and Martin 2016). In fact, in the same mouse model of ALS, overexpression of pre-synaptic N-type channels was reported, whereas other pre-synaptic P/Q-type channels remained unaffected (Pieri, Caioli et al. 2013).

AD is the most common form of dementia and characterized by the progressive loss of neurons. It was previously hypothesized that specific inhibition of N-type VGCCs may be effective in rescuing memory impairments in AD, as memory enhancing effects have previously been reported for the $Ca_V2.2$ inhibitor ziconotide (Bozorgi, Budde et al. 2020). In addition, direct effects of Aβ, one of the key players in AD, have been observed on N-type channel function (discussed in chapter 1.4.3), which could trigger intracellular Ca^{2+} overload and subsequent excitotoxicity (Koutsilieri and Riederer 2007). One of the proposed underlying mechanism was $Ca_V2.2$-dependent activation of NMDA receptors and subsequent Ca^{2+} overload in the post-synaptic cell (Sinor, Du et al. 2000; Dong, Wang et al. 2009). In fact, blocking of N-type-mediated Ca^{2+} currents by a specific inhibitor prevented glutamate-dependent excitotoxicity and rescued associated cognitive decline in a rat model of glutamate-induced excitotoxicity (Keimasi, Salehifard et al. 2023). This was further confirmed by findings that modulation of N-type- as well as P/Q-type-mediated Ca^{2+} fluxes in the hippocampus improved memory and cognitive function after glutamate-induced neuronal excitotoxic dysfunction (Keimasi, Salehifard et al. 2023).

Another disease-contributing mechanism besides excitotoxicity may additionally be found in the implication of N-type VGCCs in **neuroinflammatory processes**. In the context of hyperalgesia, N-type VGCCs were observed to be involved in inflammatory processes, as seen by an associated modulation of firing rates in sensory neurons, as well as induced neurite outgrowth (Pitake, Middleton et al. 2019). In line with this is the observation that $Ca_V2.2$ KO mice exhibit reduced inflammation in a model of neuropathic pain (Saegusa, Kurihara et al. 2001). Interestingly, reduced contribution of N-type channel-mediated Ca^{2+} currents in synaptic transmission has been observed during inflammation in a specific subtype of neurons in the rat dorsal horn (Rycroft, Vikman et al. 2007). Furthermore, in the context of AD, Aβ was reported to regulate N-type channel function which was observed to be directly modulated by the pro-inflammatory cytokine interleukin-1β (Il-1β) (MacManus, Ramsden et al. 2000).

1.4.3 Voltage-Gated Calcium Channels in Alzheimer's Disease

In AD, increased intracellular Ca^{2+} levels are thought to subsequently cause neuronal cell death in the context of neurodegeneration (Hartley, Kurth et al. 1993; Marambaud, Dreses-Werringloer et al. 2009; Zundorf and Reiser 2011). Therefore, it is of high interest to identify mechanisms and sources of abnormal Ca^{2+} influx to subsequently target them in a therapeutic treatment strategy. It was previously hypothesized, that not all sources of Ca^{2+} influx into neurons are equally toxic for the cell (Tymianski, Charlton et al. 1993; Sattler, Charlton et al. 1998). This effect is mainly mediated through the proximity of different Ca^{2+}-gating molecules to cell death controlling signaling cascades (Forder and Tymianski 2009). Originally, it was though that VGCCs would not carry lethal Ca^{2+} fluxes (Tymianski, Charlton et al. 1993; Sattler, Charlton et al. 1998). In contrast, more recent evidence suggested, that VGCC may become effective in triggering excitotoxicity in certain disease states or in a specific population of neuronal cells (Stanika, Villanueva et al. 2012). In this study, neuronal vulnerability was associated with modulated intracellular Ca^{2+} levels in a subset of neurons showing increased VGCC expression and activity, subsequently leading to cell death. In this context, the Ca^{2+}-dependent toxicity was hypothesized to be mediated through mitochondrial dysfunction. For those reasons, alterations in the expression level, plasma membrane density or activity of certain VGCCs may become harmful in disease context by causing Ca^{2+}-dependent toxicity.

Two underlying Ca^{2+}-dependent mechanisms can be hypothesized for VGCC-mediated neuronal cell death (Cataldi 2013): As previously described, the expression or the activity of VGCCs may change, and channel malfunction will subsequently induce cell death. In fact, during aging, increased Ca^{2+} currents, mediated by the L-type VGCC, have been observed (Thibault and Landfield 1996; Brewer, Thibault et al. 2007; Thibault, Gant et al. 2007), which was only in part mediated by upregulated expression and more by increased activity (Herman, Chen et al. 1998; Norris, Blalock et al. 2010). Furthermore, increased levels of L-type VGCCs have been reported in the hippocampus and the cerebellum in brains of AD patients (Coon, Wallace et al. 1999). In addition, a causative role of VGCCs, especially L-type channels, in synaptic dysfunction was shown before (Moyer, Thompson et al. 1992; Norris, Halpain et al. 1998). Besides changes in channel expression or activity, neurons may also become more vulnerable to VGCC-mediated toxicity, or could be affected in a Ca^{2+}-independent way (Cataldi 2013).

In AD, one of the main protagonists is the Aβ polypeptide, that gets cleaved from APP via different secretase-dependent cleavage processes and is known to be the main toxic species in AD since the last century (Beyreuther and Masters 1991; Hardy and Allsop 1991; Selkoe and Hardy 2016). A multitude of studies has shown a causative link between Aβ and increased intracellular Ca^{2+} levels and subsequent excitotoxicity, further found to be dependent on its aggregation state (Walsh, Klyubin et al. 2002; Demuro, Mina et al. 2005; Deshpande, Mina et al. 2006; Kuchibhotla, Goldman et al. 2008; Demuro, Parker et al. 2010; Demuro and Parker 2013). Aβ was previously observed to form Ca^{2+}-permeable pores in the plasma membrane on its own (Arispe, Rojas et al. 1993). Furthermore, Aβ targets the post-synaptic neuronal NMDA receptor and triggers Ca^{2+} overload by mediating activation of NMDAR (Texido, Martin-Satue et al. 2011; Mota, Ferreira et al. 2014; Zhang, Li et al. 2016; Foster, Kyritsopoulos et al. 2017; Liu, Chang et al. 2019). In the last years, a growing body of evidence also suggests a mediating role of Aβ on VGCC expression and activity and subsequent Ca^{2+} overload-dependent neurodegeneration:

Modulation of VGCC by Aβ was reported to occur at different stages. Transcription and expression levels of L-type channels, as well as N- and P/Q-type channels were observed to be upregulated after incubating human S K-N-SH neuroblastoma with high concentrations (20 µM) of aggregated $Aβ_{25-35}$ (Chiou 2006). A similar effect was observed for expression of L-type channels $Ca_V1.2$ and $Ca_V1.3$ with physiological concentrations (25 nM) of $Aβ_{25-35}$ in rat primary hippocampal neurons (Kim and Rhim 2011). Inducing endogenous expression of Aβ oligomers in a culture of human neuroblastoma MC65 cells also resulted in increased expression levels of $Ca_V1.2$ (Anekonda, Quinn et al. 2011). In addition, increased $Ca_V1.2$ expression was locally associated with amyloid plaques in reactive astrocytes in hAβPP751 mice (Daschil, Obermair et al. 2013).

Besides influencing expression and membrane density of VGCCs, Aβ was previously reported to modulate channel activity. Different concentrations of oligomeric and aggregated $Aβ_{25-35}$, ranging from low physiological relevant concentrations of 25 nM to high concentrations of 40 µM, were observed to increase Ca^{2+} influx through the L-type VGCC in different *in vitro* models (Ueda, Shinohara et al. 1997; Silei, Fabrizi et al. 1999; Rovira, Arbez et al. 2002; Yagami, Ueda et al. 2002; Yagami, Ueda et al. 2004; Fu, Li et al. 2006; Kim and Rhim 2011). The Aβ-induced increase in Ca^{2+} fluxes was inhibited by L-type-specific calcium channel blockers (CCB) nifedipine, nimodipine, S-312-d, verapamil and diltiazem. Interestingly, monomeric $Aβ_{25-35}$ failed to modulate L-type VGCC Ca^{2+} current amplitude or respective kinetics at high concentrations (23 µM) in N1E-115

neuroblastoma cells (Davidson, Shajenko et al. 1994). In the same study, similar concentrations of monomeric $A\beta_{1-40}$ increased L-type VGCC-dependent Ca^{2+} influx and shifted the activation potential (V_{act}) to more positive potentials (Davidson, Shajenko et al. 1994). A similar increase in L-type channel activity was observed after incubating rat cortical synaptosomes with 1 µM of $A\beta_{1-40}$ (MacManus, Ramsden et al. 2000). In contrast, oligomeric species of $A\beta_{1-40}$ did not change L-type VGCC activity, whereas an overall increase in Ca^{2+} influx was found, suggesting a role of non-L-type VGCC in Aβ-mediated intracellular Ca^{2+} overload (Rovira, Arbez et al. 2002). In primary rat cortical neurons, fibrillar as well as soluble oligomeric species of $A\beta_{1-42}$ were reported to increase Ca^{2+} influx in an L-type VGCC-mediated way (Fu, Li et al. 2006).

In contrast to L-type channels, no modulation of channel activity by aggregated $A\beta_{25-35}$ was observed for P/Q-type or N-type channels (Yagami, Ueda et al. 2004). On the other hand, monomeric assemblies of $A\beta_{1-40}$ increased total Ca^{2+} currents in primary rat cortical neurons, which was prevented by the P/Q-type-specific CCB ω-Aga IVA (MacManus, Ramsden et al. 2000; Ramsden, Henderson et al. 2002). Different effects were observed after incubation with preparation of so called $A\beta_{1-42}$ globulomers, a water-soluble globular 60 kDa oligomer of $A\beta_{1-42}$, in various *in vitro* systems (Barghorn, Nimmrich et al. 2005). Incubation of primary rat hippocampal neurons at low physiological concentrations (8 nM) of $A\beta_{1-42}$ globulomer inhibited Ca^{2+} currents, which was reversed by specifically activating P/Q-type channels via roscovitine (Nimmrich, Grimm et al. 2008). In contrast to this, P/Q-type channels in *Xenopus laevis* oocytes, as well as in transfected HEK293 cells showed an $A\beta_{1-42}$ globulomer-dependent reduction in channel opening threshold, caused by a shift in the current-voltage curve to more hyperpolarized values, which was further accompanied by an increased amplitude, reversible by application of specific P/Q-type CCBs (Mezler, Barghorn et al. 2012; Hermann, Mezler et al. 2013).

Similar effects of $A\beta_{1-40}$ have been observed on N-type VGCCs: An Aβ-induced increase in channel deactivation rates, a positive shift in the current-activation curve, as well as an increase in Ca^{2+} currents, specifically blocked by the N-type-specific CCB ω-CgTx GVIA, could be seen in rat cerebellar granule neurons, cortical synaptosomes and cortical neurons (Price, Held et al. 1998; MacManus, Ramsden et al. 2000). Remarkably, in primary rat cortical neurons, an aggregation state-dependent effect of $A\beta_{1-40}$ on N-type VGCCs was reported, where monomeric $A\beta_{1-40}$ increased currents, whereas similar concentrations of aggregated $A\beta_{1-40}$ exhibited a contrary inhibitory effect (Ramsden, Henderson et al. 2002). In addition, $A\beta_{1-42}$ globulomers, but not unaggregated forms of $A\beta_{1-42}$, caused a shift in

half-activation voltage (V_{half}) to more hyperpolarized values, overall increasing the Ca^{2+} current amplitude (Hermann, Mezler et al. 2013). In contrast to this, in a similar *in vitro* model system, high concentrations of protofibrillar assemblies of $A\beta_{1-42}$ caused an inhibitory decrease in N-type VGCC current density, accompanied by a decrease in maximal channel conductance (Kaisis, Thei et al. 2022). Chronic exposure to $A\beta_{1-42}$ leave N-type channels unresponsive to their respective CCBs, further suggesting an $A\beta_{1-42}$-mediated blocking effect on $Ca_V2.2$ channels (Kasparova, Lisa et al. 2001).

It was further reported that oligomeric (4-6-mer) $A\beta_{1-40}$ as well as oligomeric (6-8-mer) $A\beta_{25-35}$ induced an increase in the Ca^{2+} current amplitude of HVA VGCCs in CA1 hippocampal neurons in slice culture (Rovira, Arbez et al. 2002). Also, a general effect of fibrillar $A\beta_{25-35}$ on HVA and LVA VGCCs was observed in rat dorsal root ganglion neurons, where increased Ca^{2+} influx and subsequent increased intracellular Ca^{2+} levels were reported, reversible by the general CCB cadmium chloride ($CdCl_2$) (He, Chen et al. 2002).

CCBs were furthermore reported to have a beneficial effect on Aβ-induced cytotoxicity. L-type inhibition by verapamil, diltiazem, isradipine and nimodipine was effective in increasing survival after endogenously expressed Aβ-oligomer-induced cytotoxicity by decreasing intracellular Ca^{2+} levels (Anekonda, Quinn et al. 2011). Blocking of L-type VGCCs further rescued decreased cellular proliferation and apoptosis, induced by oligomeric, aggregated and fibrillar Aβ species $A\beta_{25-35}$ and $A\beta_{1-42}$ in primary rodent cortical neurons and human microglial cells (Weiss, Pike et al. 1994; Ueda, Shinohara et al. 1997; Silei, Fabrizi et al. 1999; Yagami, Ueda et al. 2004; Fu, Li et al. 2006). Contrary to this, another study reported no change in $A\beta_{1-40}$-induced cytotoxicity by blocking L-type or N-type VGCCs (Whitson and Appel 1995).

On a functional level, blocking of L-type VGCCs further reversed Aβ-induced deficits in long-term potentiation (LTP) *in vivo* (Freir, Costello et al. 2003). In addition, inhibition of L-type channels diminished Aβ-induced behavioral dysfunction in rats (Gholamipour-Badie, Naderi et al. 2013). Interestingly, although different CCBs were able to block Aβ-mediated modulation of Ca_V2 channels, specifically blocking P/Q-type, N-type or R-type channels did not alter cell death induced by aggregated or fibrillar $A\beta_{25-35}$, $A\beta_{1-40}$ or by soluble oligomeric forms of $A\beta_{1-42}$ (Whitson and Appel 1995; Ueda, Shinohara et al. 1997; Yagami, Ueda et al. 2004; Fu, Li et al. 2006). Despite the lack of beneficial effects on neuronal survival, it could be shown that inhibition of N-type, as well as P/Q-type channels prevented $A\beta_{1–42}$ globulomer-induced deficits in excitatory synaptic transmission (Hermann, Mezler et al.

2013). In line with this is the observation that oligomeric $A\beta_{1-42}$, rather than monomers or fibrils, facilitates glutamate and noradrenaline release, which was inhibited by blocking N-type VGCCs, whereas no similar effect could be observed for P/Q- or L-type channels (Bobich, Zheng et al. 2004).

Overall, contradictory findings are reported on Aβ-induced modulation of VGCCs (for a detailed overview of all studies see Appendix Tab. I.1). In general, it can be stated that Aβ exhibits modulatory function on VGCCs on different levels ranging from transcriptional to expressional and functional, while displaying a VGCC subtype-specific modulation. Furthermore, Aβ-induced effects are dependent on the species of Aβ, its aggregation state as well as the respective concentration. More work has to be undertaken to elucidate the exact regulatory mechanism that Aβ exhibits on VGCCs, in particular during different disease states. Nevertheless, due to its involvement in Aβ-induced excitotoxicity, targeting VGCCs may be an interesting treatment strategy in AD and other neurodegenerative diseases.

1.4.4 Voltage-Gated Calcium Channels as Therapeutic Targets for the Treatment of Neurodegenerative Diseases

As VGCCs are implicated in a variety of neurological disorders, the use of specific CCBs has been an interesting strategy for the treatment of various diseases. In different animal models of neurodegeneration it could be proven that Ca^{2+} channel antagonists exhibit neuroprotective effects (Hunter 1997). Blocking of L-type VGCCs not only exhibited neuroprotective function in a rodent model of ischemia (Hosaka, Yamamoto et al. 1991), but was further effective in reducing age-related cognitive decline (Deyo, Straube et al. 1989). In line with this, specific inhibition of P/Q-type channels via application of ω-Aga IVA was also observed to be neuroprotective after ischemic stroke (Asakura, Matsuo et al. 1997). Various studies further reported neuroprotection after ischemic strokes by blocking N-type VGCCs (Valentino, Newcomb et al. 1993; Buchan, Gertler et al. 1994; Yenari, Palmer et al. 1996; Perez-Pinzon, Yenari et al. 1997; Colbourne, Li et al. 1999). In addition, application of an N-type-specific CCB exhibited beneficial effects on neuroprotection in a mouse model of TBI (Berman, Verweij et al. 2000). The underlying mechanism behind the neuroprotective effect was later identified to be the rescue of mitochondrial dysfunction (Verweij, Muizelaar et al. 2000).

In patients with different neurodegenerative diseases, treatment with CCBs resulted in reduced dementia and cognitive decline (Hanyu, Hirao et al. 2007; Hanyu, Hirao et al. 2007; Hussain, Singh et al. 2018). On the other hand, neither DHP, nor non-DHP CCBs caused a significant reduction in the risk of AD (Yasar, Corrada et al. 2005). In addition, CCB application in patients was also not efficient in neuroprotection in the context of stroke (Zhang, Yang et al. 2012).

The best analyzed and described beneficial effect of CCBs in neurodegeneration is observed to be mediated via inhibition of L-type channels. Originally developed for the treatment of hypertension, respective substances were recently identified as promising therapeutic strategy for neurodegenerative diseases (Yagami, Kohma et al. 2012). Various already known drugs with L-type inhibition property have been analyzed in the context of different neurodegenerative diseases. Nimodipine was observed to rescue cognitive decline and behavioral deficits in patients with dementia and in AD patients (Davidson and Stern 1991; Lopez and Birks 2001; Eckert 2005; Baskys and Cheng 2012). Similarly, L-type CCBs nitrendipine, as well as nilvadipine, have previously been reported to reduce cognitive decline (Forette, Seux et al. 1998; Forette, Seux et al. 2002; Hanyu, Hirao et al. 2007; Trompet, Westendorp et al. 2008). Furthermore, in the context of PD, blocking of L-type VGCCs reduced the risk for PD and additionally exhibited neuroprotective effects (Ritz, Rhodes et al. 2010). For this reason, it was proposed as treatment strategy in PD (Ortner 2021). On the other hand, treatment with L-type VGCC-specific CCBs did not reduce the risk of developing AD (Yasar, Corrada et al. 2005), although a reduction in amyloid deposition was observed after L-type VGCC block (Paris, Bachmeier et al. 2011). In addition, isradipine, an L-type specific CCB, was suggested for the treatment of AD based on its neuroprotective effects (Copenhaver, Anekonda et al. 2011). Although the literature suggests blocking of L-type channels as the main treatment strategy, it has to be noted that several of the described CCBs with L-type VGCC blocking properties are not exclusively specific for channels from the Cav1 family (Diochot, Richard et al. 1995). Significant blocking events could be observed for known DHP drugs like nimodipine, verapamil and diltiazem on other HVA channels as P/Q-type, N-type, as well as R-type VGCCs. This suggests, that the reported beneficial effects of CCBs may also be mediated by inhibition of non-L-type VGC channels.

In the last years, non-L-type HVA VGC channels have been overlooked in the development of potential treatment strategies in neurodegenerative diseases. Especially in AD, N-type VGCCs are interesting targets as there is a major link between AD pathology and chronic pain, and symptoms of pain even precede first cognitive decline (Cao, Fisher et al. 2019; Kumaradev, Fayosse et al. 2021). Based on this, new treatment strategies have to be developed to target specific components involved in neuronal Ca^{2+} regulation. This may comprise the development of substances targeting different VGC channels. Hereby, it is important to not only target VGCCs, but specifically and state-dependently target certain channel subtypes or specific subunits. The specificity of CCBs in treatment of neurodegenerative diseases is further important, as DHP-mediated inhibition of L-type VGCCs lowers the systemic blood pressure and, as a result this, may even exacerbate cerebral hypoperfusion and rather impair cognition further (Link, Meissner et al. 2009).

Here, we propose the N-type VGCC as interesting novel therapeutic target for the treatment of neurodegenerative diseases, in particular AD. Due to its pre-synaptic neuronal expression pattern and its previously reported role in neuroprotection, it may provide a safe and effective target to reduce neurodegeneration induced by Ca^{2+}-dependent excitotoxicity.

1.5 Background and Aim of the Thesis

A range of evidence, summarized here, points towards a role for $Ca_V2.2$-dependent Ca^{2+} dysregulation in a variety of neurodegenerative diseases. As millions of people worldwide are affected by diseases characterized by neurodegeneration and, to this day, no effective treatment option is available, it is of high interest to develop therapeutics targeting new molecular sites presenting a promising approach for the treatment of neurodegenerative diseases. Therefore, one of the main aims of this study was the targeted inhibition of $Ca_V2.2$-mediated Ca^{2+} fluxes for a putative general neuroprotection approach in the context of various neurodegenerative diseases.

We recently have identified a compound, namely RD2, that selectively inhibits $Ca_V2.2$-mediated Ca^{2+} fluxes. This compound is a fully D-enantiomeric peptide which is, in contrast to known $Ca_V2.2$-inhibitors (Deer, Pope et al. 2019), orally available, penetrates into the brain across the BBB and has additional favorable pharmacokinetic properties as well as no reported severe adverse effects (Leithold, Jiang et al. 2016; Schartmann, Schemmert et al. 2018). The inhibition of $Ca_V2.2$ by RD2 was already demonstrated previously in *in vitro* patch clamp experiments and additionally, it was found to be effective in reversing neuropathic pain *in vivo*, which is, at least in part, mediated by the $Ca_V2.2$ (Kutzsche, Guzman et al. 2023).

In this study, we focus on the optimization of the $Ca_V2.2$-inhibitor RD2 as lead compound with regard to its affinity and subtype specificity. Additionally, we aim to subsequently show the inhibition capability of RD2 and lead-optimized D-peptides on $Ca_V2.2$ and its effects *in vivo*, to not only show proof of concept of the inhibitory potential *in vivo*, but to also learn more about the involvement of the $Ca_V2.2$ in signal transmission and memory formation in the healthy and diseased brain.

2 Materials and Methods

2.1 Cell culture

2.1.1 Mammalian Cell Lines

CHO-K1 cells were cultivated in standard alpha Minimal Essential Medium (MEMα; Thermo Fisher Scientific, Waltham, Massachusetts, USA), supplemented with 10% (v/v) fetal calf serum (FCS; Sigma-Aldrich, St. Louis, Missouri, USA), 1% (v/v) penicillin/streptomycin (10,000 U/mL penicillin and 10 mg/mL streptomycin; Sigma-Aldrich) and 200 mM L-glutamine (Thermo Fisher Scientific). Medium used for cultivation of stable transfected $Ca_V2.2$-expressing CHO cells, expressing rat $Ca_V\alpha_{1B}$, $Ca_V\alpha_2\delta_1$ and $Ca_V\beta_3$ (kindly provided by Prof. Dr. Bernd Fakler, University Freiburg, Germany) was further supplemented with selection antibiotics 0.7 mg/mL geneticin (Thermo Fisher Scientific), 0.25 mg/mL hygromycin B (Thermo Fisher Scientific) and 0.005 mg/mL blasticidin S hydrochloride (Thermo Fisher Scientific). Medium was changed every two to three days and cells were passaged at a confluency of 90%, approximately every three to five days.

HEK293 and HEK293T cells were cultivated in standard Dulbecco's Modified Eagle Medium (DMEM) (Sigma-Aldrich) supplemented with 10% (v/v) FCS and 1% (v/v) penicillin/streptomycin. For cultivation of stably transfected HEK293 cells, expressing $Ca_V\alpha_{1B\text{-}1}$ ($Ca_V2.2$: M94172.1) splice variant as well as auxiliary subunits $Ca_V\alpha_{2b}\delta_1$ (M76559.1) and $Ca_V\beta_{3a}$ (NM_000725) (kindly provided by David J. Adams, University of Wollongong, Australia), the medium was additionally supplemented with appropriate selection antibiotics 500 µg/mL geneticin, 10 µg/mL blasticidin and 40 µg/µL zeocin (Thermo Fisher Scientific). The culture medium was changed every two to three days and cells were passaged every three to five days when exhibiting approximately 90% confluency.

SH-SY5Y cells (DSMZ, Braunschweig, Germany) were cultivated under standard conditions. Briefly, cells were cultured in DMEM medium supplemented with 20% (v/v) FCS. The medium was changed every two to three days and passaging of cells was performed with regard to their confluency every three to five days.

2.1.1.1 Cell Cultivation and Passaging

Cells were cultivated in different cell culture flasks or plates under standard conditions in a CO_2 incubator at 37°C with 5% CO_2 and saturated humidity. All following steps were performed under sterile conditions using a laminar flow hood. After reaching a confluency of about 90%, cells were passaged by washing once in phosphate-buffered saline (PBS: 13.7 mM sodium chloride (NaCl; AppliChem GmbH, Darmstadt, Germany), 270 µM potassium chloride (KCl; AppliChem), 180 µM potassium dihydrogen phosphate (KH_2PO_4; AppliChem), 1 mM disodium hydrogen phosphate (Na_2HPO_4; AppliChem), pH 6.8) and subsequent detaching of the cells by incubating with Trypsin-ethylenediaminetetraacetic acid (Trypsin-EDTA; Sigma-Aldrich) for 1 min at 37°C. Following detachment, cells were collected by centrifugation for 5 min at 200 × g and room temperature (RT). The supernatant was discarded and cell pellets were washed once with PBS and resuspended in an appropriate volume of fresh medium before seeding in T-75 or T-180 cell culture flasks (VWR International, Radnor, Pennsylvania, USA) at a dilution of approximately 1:10.

For seeding of cells for immunofluorescent staining or electrophysiological experiments, cell pellets were resuspended in 1 mL of fresh medium before determination of viable cell numbers by staining with trypan blue (Invitrogen, Waltham, Massachusetts, USA) and counting of the cells in a Neubauer cell counting chamber. Cells were then plated at required concentrations for the respective experiment.

2.1.1.2 Cryopreservation

For long-term storage of cells, harvesting of the cells was performed as described for passaging of cells (see 2.1.1.1). Cell pellets after centrifugation were resuspended in an appropriate volume of cryopreservation medium comprising the respective medium without antibiotics and supplemented with 50% (v/v) FCS and 10% /(v/v) dimethyl sulfoxide (DMSO, Sigma-Aldrich). After determination of the cell number, cells were diluted to a final concentration of 1×10^6 cells/mL and the cell suspension was transferred to 1.5 mL cryovials. Cells were gradually frozen by placing the vials in an isopropanol-filled Mr. Frosty Freezing Container (Thermo Fisher Scientific) at -80°C for a minimum of 24 h before transferring the cells to a liquid nitrogen container for long-term cryopreservation.

Cells were reintroduced in culture by warming cryovials at 37°C before seeding cells in a T-75 cell culture flask in the appropriate medium to start expansion. One day after seeding, the medium was replaced to remove DMSO and cells were further cultivated.

2.1.1.3 Cell Viability Assay (MTT)

To assess the *in vitro* cytotoxicity of different compounds, MTT (3-(4,5-Dimethylthiazol-2-yl)-2,5-diphenyl-tetrazolium bromide)-based cell viability assays were performed (Mosmann 1983). As the target protein is predominantly expressed in neuronal cells, human neuroblastoma SH-SY5Y cells were chosen as cell model for the toxicity tests.

SH-SY5Y cells were seeded at a density of 1×10^4 cells/well in 96-well surface-treated tissue culture plates (VWR) in standard medium at a total volume of 100 µL/well. Following incubation for 24 h, the culture medium was supplemented with testing compounds to a final concentration of 1 µM, 6 µM or 12 µM, respectively, and incubated for additional 24 h under standard conditions. Evaluation of the cellular toxicity of the compounds was performed using the Cell-Proliferation Kit I (Roche Holding AG, Basel, Switzerland) according to the manufacturer's protocol. In brief, cells were incubated with the MTT labeling reagent and incubated for approximately 4 h under standard conditions. Next, an appropriate volume of solubilization solution was added and the plate was further incubated overnight. Absorbance was measured at 570 nm and 660 nm (reference) in a CLARIOstar Plus Microplate Reader (BMG LABTECH, Ortenberg, Germany) to calculate the cell viability as percentage of MTT reduction, normalized to reference cells grown in regular medium without testing compounds.

2.1.2 *Escherichia coli* (*E. coli*) Cell Culture

For the amplification of plasmid DNA, the competent bacterial strain *Escherichia coli* (*E. coli*) OmniMAX T1 (Genotype: F′ {*pro*AB *lac*I^q *lac*ZΔM15 *Tn*10(Tet^R) Δ(*ccdA*B)}*mcr*A Δ(*mrr hsd*RMS-*mcr*BC)Φ80(*lac*Z)ΔM15 Δ(*lac*ZYA-*arg*F)U169 *end*A1 *rec*A1 *sup*E44 *thi*-1 *gyr*A96 *rel*A1 *ton*A *pan*D; Thermo Fisher Scientific) was used.

2.1.2.1 Cell Cultivation

E. coli cells were cultivated in sterile Luria-Bertani (LB) medium (1% (w/v) tryptone/peptone from casein (Carl Roth GmbH & Co. KG, Karlsruhe, Germany), 0.5% (w/v) yeast extract (Carl Roth), 0.5% (w/v) NaCl), either in liquid culture or on LB-agar-plates containing LB-medium supplemented with 1% (w/v) agar (AppliChem). Cells were cultivated using standard procedures, with liquid cultures incubated overnight at 37°C and 130 rpm and LB-agar-plates overnight at 37°C.

2.1.2.2 Transformation of Competent Cells

For transformation of competent cells, 100 µL of *E. coli* OmniMAX T1 cells was thawed on ice. Approximately 100 ng of DNA was added to the cells and incubated for 30 min on ice. Transformation of the cells was performed using a heat-shock at 42°C in a ThermoMixer comfort 1.5 mL (Eppendorf SE, Hamburg, Germany) for 1 min, followed by subsequent incubation for 2 min on ice. After addition of 900 µL LB-medium, cells were incubated for 1 h under standard conditions. Cells were harvested by centrifugation at 6,000 × g for 5 min and resuspended in 100 µL of fresh LB-medium, which was then spread on LB-agar-plates containing the respective selection antibiotic and incubated overnight at 37°C.

2.2 General Molecular Biological Methods

2.2.1 DNA Amplification and Purification from *E. coli*

For amplification of plasmid DNA, 10 mL (Mini-DNA-preparation) or 100 mL (Midi-DNA-preparation) of LB-medium, supplemented with the respective selection antibiotic, was inoculated with one colony of *E. coli* grown on LB-Agar-plates or 1 mL of a liquid pre-culture of *E. coli*. Overnight cultures of transformed *E. coli* cells were harvested and purified using the innuPREP Plasmid Mini Kit 2.0 (Analytik Jena, Jena, Germany) or the Nucleo-Bond Xtra Midi Kit (Macherey-Nagel, Düren, Germany) following the manufacturer's instructions. DNA pellets were subsequently reconstituted in double-distilled water (ddH_2O) and quantified via spectrophotometric measurements (Nanophotometer P300 with Guard Cell (factor 50); Implen GmbH, Munich, Germany) to further dilute DNA samples to a final stock concentration of 1 µg/µL.

2.2.2 Polymerase Chain Reaction

Polymerase chain reactions (PCR) were performed for specific amplification of DNA fragments in order to achieve restriction site mutagenesis or introducing other mutations using respective primers (see 2.5.1, Tab. 2.2). The reaction mix consisted of 1 ng DNA template, 0.5 µM of each primer (forward/reverse), 200 µM deoxynucleotide (dNTP) Solution Set (New England Biolabs, Ipswich, Massachusetts, USA), 0.02 U/µL of Phusion High-Fidelity DNA polymerase in High-Fidelity buffer (New England Biolabs) and up to 3% (v/v) DMSO, according to the manufacturer's protocol. The reaction was carried out in a

standard heated-lid thermocycler (Thermal Cycler CT1000 Touch; Bio-Rad) following an amplification protocol consisting of 30 s initial denaturation at 98°C, followed by 30 cycles of 10 s denaturation at 98°C, 30 s annealing at 45°C to 72°C and 30 s/kb extension at 72°C, followed by a final extension step for 10 min at 72°C. Modifications to the protocol are indicated for each construct in 2.5.1 and 2.5.2. PCR products were analyzed and purified using agarose gel electrophoresis as described in 2.2.5.

2.2.3 Restriction Digest

For subsequent ligation of constructs, compatible inserts and backbone plasmids were prepared by restriction digest using the respective restriction enzymes. Reactions were carried out according to the FastDigest restriction enzyme protocol (Thermo Fisher Scientific), using 0.5 µg of substrate DNA and 5 U of the respective FastDigest restriction enzymes (Thermo Fisher Scientific) in the recommended buffer system FastDigest Green Buffer (Thermo Fisher Scientific). Reactions were run for 15 min at 37°C and successfully digested DNA fragments were identified and separated using agarose gel electrophoresis (see 2.2.5).

2.2.4 Ligation

Fragments of inserts and plasmid backbones, digested using the same or compatible restriction enzymes, were subsequently ligated following the DNA sticky-end ligation protocol for T4 DNA ligase (Thermo Fisher Scientific). In brief, reactions were performed using 50 ng of digested vector and adding the respective insert at a 3:1 insert to vector molar ratio, followed by incubating for 1 h at RT with 1 U of T4 DNA ligase in T4 DNA ligase buffer (Thermo Fisher Scientific). Ligation reactions were subsequently transformed in *E. coli* OmniMAX T1 cells for amplification (see 2.1.2.2) and purified plasmids were subsequently verified by Sanger sequencing (Microsynth Seqlab GmbH, Göttingen, Germany).

2.2.5 Agarose Gel Electrophoresis and Gel Extraction

Agarose gels were prepared from 1% (w/v) agarose (Biozym Scientific GmbH, Oldendorf, Germany) and 0.5 µg/mL ethidium bromide (EtBr; AppliChem) in TAE (Tris Acetate EDTA) buffer (40 mM Tris (AppliChem), 0.00114% (v/v) glacial acetic acid (AppliChem), 1 mM EDTA (AppliChem)). DNA samples that not already contained FastDigest Green buffer were supplemented with Purple Gel Loading Dye (New England Biolabs) and samples were applied to the gel alongside with either GeneRuler 100 bp Plus DNA Ladder (Thermo Fisher Scientific) or GeneRuler 1 kb DNA Ladder (Thermo Fisher Scientific). Gel electrophoresis was performed in TAE buffer at 85 V for 50 min or until appropriate separation and gels were analyzed on a ChemiDoc Imaging System (Bio-Rad Laboratories, Hercules, California, USA) using the respective protocol for EtBr detection. For separation of DNA fragments from the gel, respective bands were carefully excised from the gel and purified using the Monarch DNA Gel Extraction Kit (New England Biolabs) following the manufacturer's recommendation. The DNA was subsequently eluted twice using ddH_2O.

2.3 General Biochemical Methods

2.3.1 SDS-Polyacrylamide Gel Electrophoresis

For SDS-Polyacrylamide Gel Electrophoresis (SDS-PAGE), samples were supplemented with Laemmli buffer to a final concentration of 56.25 mM Tris, 2% (w/v) sodium dodecyl sulfate (SDS; Carl Roth), 10% (v/v) glycerol (Carl Roth), 2% (v/v) β-mercaptoethanol (Sigma-Aldrich) and 0.005% (w/v) bromophenol blue (Amresco Inc., Solon, Ohio, USA) at pH 6.8. As membrane proteins tend to aggregate under denaturing buffer conditions, preliminary experiments were performed with regard to the effect of initially boiling the samples. Heating for 5 min at 95°C and thus denaturing the sample before SDS-PAGE led to significantly reduced $Ca_V2.2$-specific signals in subsequent immunostaining approaches of western blots (Fig. 2.1). Therefore, all following SDS-PAGE runs, analyzing $Ca_V2.2$ protein, were performed under semi-native conditions without initial boiling of the sample.

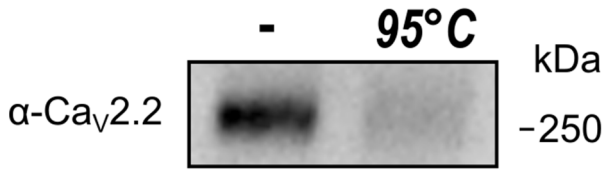

Figure 2.1: Visualization of $Ca_V2.2$ in western blots after SDS-PAGE under semi-native conditions Samples containing $Ca_V2.2$ protein where either run in SDS-PAGE semi-denatured (-) or after denaturing by boiling (95°C).

For quantification of levels of certain proteins in the brain of a mouse model of AD, 15 µL of each sample was run in SDS-PAGE on 7.5% Mini-PROTEAN TGX Stain-Free Precast Gels (Bio-Rad). For analysis of $Ca_V2.2$ levels after transient expression and in protein purification attempts, proteins were separated on 6% SDS-polyacrylamide gels, comprising 6% (v/v) acrylamide (AppliChem), 375 mM Tris pH 8.8, 0.001% (w/v) SDS, 0.001% (w/v) ammonium peroxodisulphate (APS; Fluka, Honeywell International, Inc., Charlotte, North Carolina, USA), 0.001% (v/v) tetramethylethylenediamine (TEMED; AppliChem), supplemented with 0.5% (v/v) 2,2,2-trichloroethanol (TCE; Sigma-Aldrich) for subsequent stain-free imaging technique. In addition, 4% stacking gels, composed of 4% (v/v) acrylamide, 125 mM Tris pH 6.8, 0.001% (w/v) SDS, 0.001% (w/v) APS and 0.001% (v/v) TEMED, were cast overlaying the separation gels. Apparent corresponding molecular weights of respective protein bands were determined with the help of broad range pre- or unstained protein standards (PageRuler; Thermo Fisher Scientific). Gels were run at 200 V, 45 mA per gel and 100 W in SDS-PAGE buffer (25 mM Tris, 250 mM glycine (Carl Roth)) until completed. For visualization, gels were analyzed on a ChemiDoc Imaging System using the stain-free imaging setting in which ultraviolet light-induced reaction of tryptophan moieties allows for subsequent protein visualization at 300 nm (Ladner, Yang et al. 2004; Chopra, Willmore et al. 2019).

2.3.2 Western Blotting

Following SDS-PAGE, proteins were transferred onto PVDF (0.45 µM) membranes (Carl Roth), pre-incubated in methanol (Carl Roth), via semi-dry western blotting. Using the Trans-Blot Turbo Transfer System (Bio-Rad) and an appropriate transfer buffer consisting of 48 mM Tris, 39 mM glycine and 20% (v/v) methanol at pH 9.2, proteins were transferred for 30 min at 25 V and 500 mA. For immunostaining, membranes were blocked through shaking for 1 h in 1% (w/v) bovine serum albumin (BSA, AppliChem) in Tris-buffered

saline (TBS: 19 mM Tris, 137 mM NaCl, 2.7 mM KCl, pH 7.4), supplemented with 0.1% (v/v) Tween-20 (AppliChem) (TBS-T). Primary antibody incubation was performed overnight at 4°C on a tumbling shaker at an appropriate dilution of the antibody in TBS-T (Tab. 2.1). After washing three times for 10 min with TBS-T, membranes were further stained with the respective horse-radish peroxidase (HRP)-coupled secondary antibody diluted in TBS-T (Tab. 2.1). Following three final washing steps for 10 min in TBS-T, blots were probed with Amersham Enhanced Chemiluminescence (ECL) Western Blotting Detection Reagent (Cytiva, Marlborough, Massachusetts, USA) before analyzing signals using the ChemiDoc Imaging System at appropriate exposure times.

Table 2.1: Antibodies used for immunostaining of western blots

Antibody	**Distributor**	**Dilution**
Anti-Calcium Channel (α_{1B} Subunit) (N-type of Voltage-gated Ca^{2+} Channel) antibody produced in rabbit	Sigma-Aldrich; #C1478	1:200
Recombinant anti-Vinculin antibody (rabbit)	Abcam (Cambridge, United Kingdom); #ab219649	1:2000
Goat anti-Rabbit IgG HRP	Dako, Agilent Technologies (Santa Clara, California, USA); #P044801-2	1:3000

2.3.3 BCA Assay

For determination of the overall protein concentration in samples, a Bicinchoninic Acid (BCA) assay was performed (Smith, Krohn et al. 1985). To obtain a reference standard curve BSA samples were prepared at concentrations ranging from 0 mg/mL to 2 mg/mL. Samples from brain homogenates were diluted at a ratio of 1:20 or 1:50 in the respective buffer and 25 µL of each sample was added to a round-bottom 96-well microtiter-plate (Greiner Bio-One, Kremsmünster, Austria). 200 µL of BCA reagent (Thermo Fisher Scientific) was added per well for each sample and the reaction was incubated for 30 min at 37°C before measuring the absorption at 562 nm in a CLARIOstar Plus Microplate Reader. The protein concentration of each sample was subsequently determined with the help of the BSA-standard curve.

2.4 Quantification of $Ca_V2.2$ Protein Levels in Murine Brain

To analyze the protein level of $Ca_V2.2$ in the brain in the context of neurodegenerative diseases, protein levels of $Ca_V2.2$ were assessed in wild-type (WT) mice as well as in a mouse model of AD at different ages. Experiments were performed using the double transgenic mouse line $APP_{swe}/PSEN1^{\Delta E9}$. These mice carry a double mutation in the humanized APP gene located in the γ-secretase cleavage site (K670N and M671L), subsequently leading to increased overall production of Aβ and facilitated Aβ deposition and pathology (Mullan, Crawford et al. 1992; Lambert, Wavrant-De Vrieze et al. 1998; Savonenko, Xu et al. 2003). Furthermore, the sequence encoding PSEN1 lacks exon 9, which is associated with a form of early-onset AD (EOAD) by reducing γ-secretase activity (Crook, Verkkoniemi et al. 1998; Prihar, Verkkoniem et al. 1999; Jankowsky, Fadale et al. 2004; Woodruff, Young et al. 2013). A pathological phenotype, characterized by Aβ deposition into plaques and associated neuroinflammation, can be observed already after 4 months of age, progressively increasing until 12 months of age, which is followed by cognitive decline starting approximately at 12 months of age (Lalonde, Kim et al. 2005; Garcia-Alloza, Robbins et al. 2006; Kamphuis, Mamber et al. 2012).

$APP_{swe}/PSEN1^{\Delta E9}$ mice at age of approximately 15 months, 21 months and 28 months and age-matched WT littermates were analyzed with regard to the $Ca_V2.2$ protein content in the brain. All animal experiments were performed in accordance with the German Law on the protection of animals (TierSchG §§ 7–9) and were approved by a local ethics committee (LANUV, North-Rhine-Westphalia, Germany, AZ 81-02.04.2019A304). The mice were sacrificed by cervical dislocation and brains were removed from the skull. The cortex as well as the cerebellum were separated from the left brain hemisphere, weighed and transferred to Precellys homogenization-tubes (Bertin Technologies, Montigny-le-Bretonneux, France). Each brain tissue sample was supplemented with the nine-fold (v/w) of tissue lysis buffer, containing 25 mM HEPES (AppliChem), 150 mM NaCl, pH 7.4 and freshly supplemented with 1 × cOmplete EDTA-free proteinase inhibitor cocktail (Roche). Mechanical homogenization of the brain tissue was performed using a Precellys Evolution Touch Homogenizer equipped with the Cryolys Evolution cooling system (Bertin Technologies) over two rounds of 20 s at 6500 rpm and 4°C. The homogenate was centrifuged at 1,000 × g for 10 min at 4°C to remove nuclei and cell debris, and membrane proteins were further purified by separation through ultracentrifugation in an Optima MAX-TL ultracentrifuge (Beckman Coulter, Brea, California, USA) at 100,000 × g for 1 h at 4°C. The supernatant

was separated and the pellet was resuspended in 50 µL tissue lysis buffer and used as crude membrane fraction. Total protein concentration of the sample was determined in a BCA assay (see 2.3.3) and approximately 50 µg of total protein was loaded onto 7.5% Mini-PROTEAN TGX Stain-Free Precast Gels (Bio-Rad). After transferring proteins via western blotting, the relative concentration of $Ca_V2.2$ was determined by a semi-quantitative approach. In brief, the total protein concentration was determined by stain-free protein visualization as described previously (see 2.3.1). Membranes were then blocked with 1% (w/v) BSA in TBS-T for 1 h and further stained with a specific anti-$Ca_V2.2$ antibody (1:1,000; OriGene, Rockville, Maryland, USA) overnight at 4°C. Incubation with the HRP-labeled secondary antibody (Goat anti-Rabbit IgG HRP, 1:3000; Dako) was performed in TBS-T for 1 h at RT and the ECL reaction was carried out as described previously (see 2.3.2) and visualized using the ChemiDoc Imaging System. Quantification of the protein band of interest was performed using ImageLab 6.1 software (Bio-Rad) and respective densities were normalized to the determined total protein concentration (Fig. 2.2).

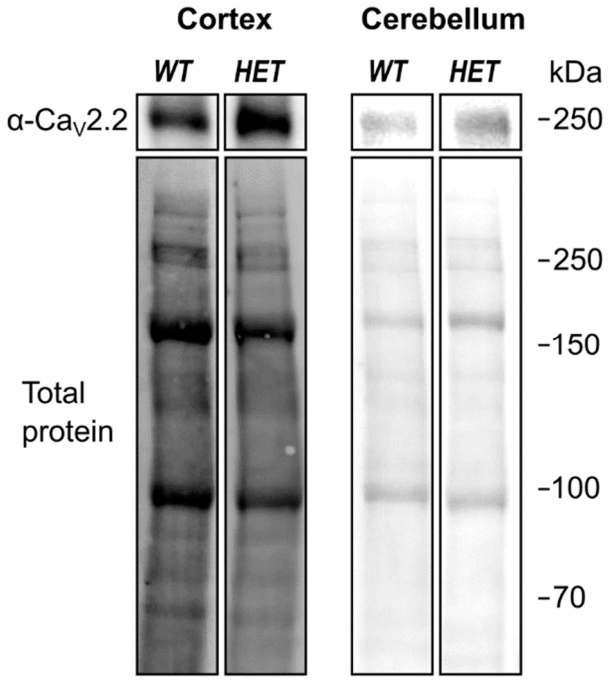

Figure 2.2: $Ca_V2.2$ visualization and quantification in western blots of AD mouse brain homogenate Immunoblot of crude membrane fractions isolated from brain tissue (cortex and cerebellum) from $APP_{swe}/PSEN^{\Delta E9}$ mice (HET) at an age of 28 months and aged-matched WT littermates. The respective brain region-specific $Ca_V2.2$ content was evaluated using an α-$Ca_V2.2$ antibody over ECL-based visualization (upper panel). Total protein content (TCE-based stain-free approach) was included for normalization in a semi-quantitative analysis of $Ca_V2.2$ protein levels (lower panel).

2.5 *In Vitro* Expression of Different $Ca_V2.2$ Constructs

2.5.1 Cloning of $Ca_V2.2$ Constructs

For *in vitro* expression of $Ca_V2.2$ constructs for subsequent protein purification and interaction studies, the human *CACNA1B* gene, encoding for the α_1-subunit of the N-type VGCC was cloned as a fusion construct with additional fluorescence and affinity tags for subsequent transient transfection of mammalian cells. The plasmid pSAD442-1_hu$Ca_V2.2$, containing full length human *CACNA1B* sequence including alternate exons +e10a, +18a, Δ19a, +e31a, +e37b and +e46 in a pcDNA6-vector backbone, was a gift from Diane Lipscombe (Addgene plasmid # 62574; http://n2t.net/addgene:62574; RRID: Addgene_62574) (Groen, Andrade et al. 2015). The construct was further cloned to express a C-terminally fused enhanced green fluorescent protein (EGFP) for visualization during expression as well as a V5 and hexa-histidine (His6) affinity tag for protein purification. As the gene spans approximately 7000 bp, with a GC-content over 80% within the first 150 bp, an adapted strategy for cloning and gene amplification had to be developed.

For C-terminal fusion with EGFP, $Ca_V2.2$-encoding DNA was separated from the vector backbone by restriction digest using NdeI and XbaI restriction sites and was subsequently used as a template for STOP-codon mutagenesis amplification of the C-terminal region of $Ca_V2.2$ DNA by PCR. Subsequent PCR reactions for STOP-codon mutagenesis of *CANCA1B* were prepared using 1 ng digested DNA template, 0.5 µM of each primer (Primer #1/#2, Tab. 2.2), 200 µM dNTPs, 0.02 U/µL of Phusion High-Fidelity DNA polymerase in High-Fidelity buffer and 3% (v/v) DMSO. The reaction was carried out following an amplification protocol consisting of 30 s initial denaturation at 98°C, followed by 30 cycles of 10 s denaturation at 98°C, 30 s annealing at 61°C and 150 s extension at 72°C, finalized by an extension step for 10 min at 72°C. Correctly amplified constructs were purified, quantified via Nanodrop measurement and digested with HindIII and XbaI restriction enzymes. Fragments were subsequently ligated into the similarly digested vector pSAD442-1_$Ca_V2.2$ as described previously (see 2.2.4). Ligated constructs were transformed in *E. coli* OmniMAX T1 cells for amplification and inserts were subsequently verified by Sanger sequencing. In the resulting construct, the C-terminal region of the *CACNA1B* gene is exchanged for a variant lacking the stop codon (ΔSTOP → pSAD442-1_$Ca_V2.2_{\Delta STOP}$).

In addition to this, EGFP was amplified for restriction site mutagenesis using primers that introduce N-terminal XbaI and C-terminal BstBI restriction sites and an additional frame-shift mutation for in-frame expression of C-terminal V5- and His-Tag expression. PCR reactions consisted of 1 ng DNA template (pEGFP_N1), 0.5 µM of each primer (Primer #3/#4, Tab 2.2), 200 µM dNTPs and 0.02 U/µL of Phusion High-Fidelity DNA polymerase in High-Fidelity buffer. The reaction was carried out following a protocol of 30 s initial denaturation at 98°C, followed by 30 cycles of 10 s denaturation at 98°C, 30 s annealing at 62°C and 22 s extension at 72°C, finalized by an extension step for 10 min at 72°C. Correctly amplified constructs were purified as previously described (see 2.2.5) and insert (EGFP) and template (pSAD442-1_$Ca_V2.2_{\Delta STOP}$) were digested and ligated via XbaI and BstBI restriction sites. Ligated constructs were transformed in *E. coli* OmniMAX T1 cells for amplification and constructs were subsequently verified by Sanger sequencing (plasmid map in Appendix Fig. I.1).

Table 2.2: PCR primers used for DNA amplification and mutagenesis Blue regions depict backbone gene homology, grey parts vector homology, orange-colored sequence stretches mark restriction sites and green parts show inserted mutations (* = Stop-codon) or primer overhangs.

#	Sequence	Template	Description
1	GCCAATCAGAAGCTTGCTCTGCAA	pSAD442-1_ $Ca_V2.2$	**Fwd**: Amplification (HindIII)
2	AAGGGCCCTCTAGACCCGCACCAGTGGTCT	pSAD442-1_ $Ca_V2.2$	**Rev**: Mutagenesis (*→Gly; XbaI; Frame)
3	GCTAGCGTCTAGAACCGCCACCATGGTGAGCAA	pEGFP_N1	**Fwd**: Mutagenesis (XbaI)
4	TCTGAGTTCGAACAACTTGTACAGCTCGTCCATGC	pEGFP_N1	**Rev**: Mutagenesis (BstBI)
5	CATTTCTCGAGATGGTGAGCAAGGGCGAG	pTR3G_ mCherry	**Fwd**: Mutagenesis (XhoI)
6	CCGTCTAGACTACTTGTACAGCTCGTCCATG	pTR3G_ mCherry	**Rev**: Mutagenesis (XbaI)
7	AGCGCGCGGAATTCATG	*CACNA2D1*	**Fwd**: Amplification (EcoRI)
8	AGCTCGTCGACTCCGAGCAGTCTA	*CACNA2D1*	**Rev**: Mutagenesis (* → Gly; Sal I)

2.5.2 Cloning of Auxiliary Subunits

As functional expression of $Ca_V2.2$ channels is also dependent on co-expression of auxiliary subunits, constructs containing Ca_V auxiliary subunit-encoding genes *CACNA2D1* ($\alpha_2\delta_1$-subunit) and *CACNB3* (β_3-subunit) in combination with a C-terminally fused fluorescent mCherry-Tag were generated and introduced in a pCDNA3 vector backbone.

To begin, the gene encoding the C-terminal mCherry-tag was inserted into a pCDNA3 vector backbone by designing primer for restriction site cloning (Tab. 2.2, Primer #5/#6). XhoI and XbaI sites were introduced into the sequence of mCherry at the N- and C-terminus, respectively, followed by performing PCR reactions as previously described (see 2.2.2), using primer #5 and #6 (Tab. 2.2), an annealing temperature of 71°C and 22 s extension time. The correctly amplified construct was inserted into the pCDNA3 vector. The vector was prepared for subsequent insertion of *CACNA2D1* or *CACNB3* by digesting with restriction enzymes EcoRI and XhoI.

The template for *CACNA2D1* cloning was designed based on the human open reading frame (ORF) NM_000722.4, codon-optimized for expression in mammalian cells and sourced as recombinant gene with EcoRI and SalI restriction sites at the N- and C-terminus, respectively, using GeneArt Gene Synthesis (Thermo Fisher Scientific). For a non-tagged construct of the $\alpha_2\delta_1$-subunit, the gene was digested via EcoRI and SalI and ligated into the pACEMam1 vector (Geneva Biotech, Pregny-Chambésy, Switzerland) as previously described (see 2.2.4). In addition, the *CACNA2D1* insert was amplified by PCR to introduce a mutation in the stop codon for subsequent fusion with a C-terminal fluorescent protein tag. PCR reactions were carried out as previously described (see 2.2.2), using primer #7 and #8 (Tab. 2.2), an annealing temperature of 64°C and 100 s extension time. Correctly amplified constructs were ligated using EcoRI and SalI restriction sites in a previously prepared pCDNA3 vector backbone and ligation samples were used for transformation of *E. coli* OmniMAX T1 cells for plasmid amplification. Generated constructs were subsequently purified and verified by Sanger sequencing (plasmid maps in Appendix Fig. I.2).

A similar cloning approach was followed for *CACNB3*-containing constructs. The insert encoding the β_3-subunit was extracted from the template plasmid pReceiver-M98_*CACNB3*_Kpn1_mCherry_BamHI and prepared for subsequent ligation into the vector pCDNA3_mCherry over restriction sites EcoRI and SalI. Ligations were transformed in *E. coli* OmniMAX T1 cells for amplification and constructs were subsequently verified by Sanger sequencing (plasmid maps in Appendix Fig. I.3).

2.5.3 Transient Transfection of $Ca_V2.2$ in HEK293T Cells

HEK293T cells were cultured under standard conditions as previously described (see 2.1.1.1). For optimization of transient transfection protocols, HEK293T cells were seeded at a density of 8×10^4 cells/cm^2 on coverslips coated with poly-D-lysine and cultured to reach confluency of around 70%. Cells were transfected using lipofectamine 2000 reagent (Invitrogen) according to the manufacturer's protocol. In brief, different concentrations of lipofectamine (5 µL, 7.5 µL, 10 µL and 12.5 µL per 6-well) were diluted in OptiMEM (Gibco, Thermo Fisher Scientific) and 2.5 µg/well of DNA, encoding $Ca_V2.2$-subunits, in OptiMEM was added at different ratios between α_{1B} : β_3 : $\alpha_2\delta_1$ (1:1:1, 2:1:1, 3:1:1, 1:2:1, 2:2:1, 3:2:1). The transfection sample was added to the culture medium after incubation for 5 min and cells were incubated for 48 h at 37°C, 5% CO_2 and saturated humidity before checking for expression.

2.5.3.1 Immunofluorescent Staining of $Ca_V2.2$ in HEK293T Cells

To analyze expression levels of $Ca_V2.2$ in transiently transfected HEK293T cells, coverslips with transfected cells were fixed 48 h post-transfection by washing with PBS and incubating the cells with 3.7% (v/v) formaldehyde (Sigma-Aldrich) in PBS for 30 min at 4°C. For immunofluorescence staining, cells were washed in TBS-T and permeabilized in a solution consisting of 0.3% (v/v) Triton-X-100 (AppliChem), 1% (w/v) BSA, 1% (v/v) DMSO in PBS for 1 h at RT. Primary anti-$Ca_V2.2$ antibody (Sigma-Aldrich) was diluted at a ratio of 1:200 in PBS supplemented with 0.3% (v/v) Triton-X-100 and 1% (v/v) DMSO and the staining was carried out overnight at RT. Next, cells were washed three times using PBS supplemented with 0.1% (v/v) Tween-20 (PBS-T) and incubated again with a secondary Goat anti-Rabbit IgG H&L (Alexa Fluor 488) antibody (1:500; Abcam) supplemented with 0.5 ng/mL 4′,6-diamidino-2-phenylindole (DAPI; Merck KGaA, Darmstadt, Germany) in PBS-T for 45 min at RT in the dark. After additional washing three times with PBS-T and a final washing step using ddH_2O, stained coverslips with cells were mounted onto glass slides using Dako Fluorescence Mounting Medium (Agilent Technologies).

2.5.3.2 Cell Membrane Labeling

To study the subcellular localization of $Ca_V2.2$ in transiently transfected cells, CellMask plasma membrane stain (Thermo Fisher Scientific) was used to label the cellular plasma membrane as recommended by the manufacturer. In brief, cells grown on coverslips were washed once with pre-warmed PBS and subsequently incubated for 5 min at 37°C with a 1 × concentration of CellMask in PBS. The suspension was exchanged for fresh PBS and cells were used for live cell imaging or fixed and stained as previously described (see 2.5.3.1).

2.5.3.3 Confocal Imaging and Image Analysis

Images of immunolabeled cells were taken using a laser scanning LSM 710 confocal microscope (LSM; Carl Zeiss, Oberkochen, Germany) in combination with a Plan-Apochromat 63×/1.4 Oil DIC M27 objective lens using Immersol 518F Immersion Oil (Carl Zeiss). For image acquisition the ZEISS ZEN 2008 Microscope Software (Carl Zeiss) was used. During imaging, laser powers, channel gain and other acquisition settings were kept constant to allow subsequent quantitative comparison. After acquisition, images were analyzed using ZEN analysis software (Carl Zeiss) and ImageJ software (Schneider, Rasband et al. 2012) using different plugins.

2.5.3.4 Relative Quantification of $Ca_V2.2$ Expression Levels in transiently transfected HEK293T Cells

For comparative analysis of $Ca_V2.2$ expression levels in transiently transfected cells, protein levels were analyzed by western blotting. 48 h post-transfection, cells were washed twice with ice-cold PBS and were incubated for 5 min on ice in an appropriate volume of pre-chilled cell lysis buffer, containing 20 mM HEPES, 2 mM magnesium chloride ($MgCl_2$; Carl Roth), 5 mM KCl, pH 7.5, freshly supplemented with 1 × cOmplete EDTA-free protease inhibitor cocktail. Cells were then detached from the surface using mechanical force, applied with a cell scraper, and nuclei and cell debris were removed using centrifugation for 10 min at 1,000 × g and 4°C. Centrifuging for 1 h at 100,000 × g and 4°C separated the crude cytosolic fraction as supernatant from the membrane fraction in the pellet. The latter was solubilized in a small volume of cell lysis buffer. SDS-PAGE and western blotting were performed as previously described (see 2.3.1 and 2.3.2) and membranes were stained against $Ca_V2.2$ using immunostaining for subsequent analysis.

2.5.4 Co-Localization of $Ca_V2.2$ with RD2

To analyze *in vitro* association of RD2 with $Ca_V2.2$ channels in a mammalian expression system, HEK293T cells were transiently transfected as previously described (see 2.5.3) to express fluorescently labeled $Ca_V2.2$ channels. In brief, HEK293T cells, grown on coated glass coverslips, were transfected using lipofectamine 2000 reagent at a concentration of 2.5 µL per 24-well and 0.5 µg/well DNA encoding $Ca_V2.2$ α_1-subunit, C-terminally fused to EGFP, as well as β_3- and $\alpha_2\delta_1$-subunits at equimolar concentrations following manufacturer's recommendations. Cells were incubated for 48 h until visual confirmation of $Ca_V2.2$-EGFP expression. RD2 (CBL Patras, Patras, Greek), fluorescently tagged with Atto 647

(ATTO-TEC GmbH, Siegen, Germany), or Atto 647 alone were added to transfected HEK293T cells, that transiently express $Ca_V2.2$ channels, to a final concentration of 6 µM and incubated for up to 1 h at 37°C, 5% CO_2 and saturated humidity. The medium was aspirated and cells were washed once with pre-warmed PBS. Fixation was performed at 4°C for 30 min in 3.5% (w/v) formaldehyde in PBS and nuclear staining was achieved by incubating with 0.5 ng/mL DAPI in 0.3% (v/v) Triton-X-100, 1% (w/v) BSA and 1% (v/v) DMSO in PBS for 15 min at RT in the dark. Subsequently, coverslips were mounted onto glass slides and image acquisition was performed at an LSM microscope (Carl Zeiss) as previously described (see 2.5.3.3).

2.6 Purification of Native $Ca_V2.2$

Subsequent binding studies of potential $Ca_V2.2$-inhibiting compounds and optimization strategies require the purification of $Ca_V2.2$ α_1-subunits from mammalian expression systems in the native secondary conformation. Stably transfected $Ca_V2.2$-expressing CHO cells were used as expression system for the optimization of $Ca_V2.2$ purification, as they show high expression levels of $Ca_V2.2$ and functional channel integration within the plasma membrane. Because $Ca_V2.2$ is expressed as a native variant without additional affinity tags for purification, the protein has to be purified with regard to its biochemical and biophysical properties using different purification approaches. The aim of this chapter was the optimization of the protocol for purification of natively folded $Ca_V2.2$ channels for the use in following experiments.

2.6.1 Lysis and Solubilization

The first step in purification of proteins from mammalian expression systems is the performance of a sufficient and suitable cell lysis method in order to extract protein from the intact mammalian cell. In addition, as the pore-forming α_1-subunit of $Ca_V2.2$ channels contains membrane spanning, hydrophobic regions, it is crucial to identify a suitable method and buffer for solubilization. A series of tests was performed to identify optimal combinations for lysis of CHO cells and subsequent solubilization of $Ca_V2.2$ to gain the highest possible protein yield.

Approximately 3×10^6 cells of a stable $Ca_V2.2$-expressing CHO cell line were used for each lysis and solubilization combinatorial approach. Trypsin-EDTA was used to harvest the cells and cells were collected by centrifugation for 5 min at 200 × g and 4°C. After washing once with PBS, cells were lysed by either osmotic shock, sonication or by incubation in a detergent-containing buffer.

For cell lysis by **osmotic shock**, cells were resuspended in cell lysis buffer comprising 25 mM HEPES pH 7.4 and 150 mM NaCl, freshly supplemented with 1 × cOmplete EDTA-free proteinase inhibitor and 1 mM phenyl-methyl-sulfonyl-fluoride (PMSF; Carl Roth). Glucose (Sigma-Aldrich) was added to a final concentration of 0.5 M to induce cell lysis through osmotic swelling. Samples were incubated for 30 min on ice and cell lysates were centrifuged for 10 min at 3,600 × g to remove cell nuclei and cell debris. Lysis of cells via **sonication** was performed after resuspending the cell pellet in cell lysis buffer by using

a sonication protocol consisting of 3 × 15 s intervals at 80% amplitude, followed by 2 × 10 s intervals at 100% amplitude with 60 s breaks on ice in between. Nuclei and cell debris were removed by centrifuging for 10 min at 3,600 × g. For **detergent-based cell lysis**, cells were resuspended in pre-cooled cell lysis buffer, additionally supplemented with 1% (w/v) glyco-diosgenin (GDN; Anatrace Inc., Maumee, Ohio, USA), 0.2% (w/v) n-Dodecyl-β-D-maltopyranoside (DDM; Anatrace) and 0.04% (w/v) cholesteryl-hemisuccinate Tris salt (CHS; Anatrace). Samples were incubated on ice for 30 min while resuspending the sample using a 12 G needle (B. Braun, Melsungen, Germany) every 10 min.

Dependent on the test conditions, proteins were either solubilized as whole cell lysate fractions or previously separated into crude membrane and cytosol fractions. To create crude membrane fractions, cell lysates were centrifuged using an ultracentrifuge at 150,000 × g for 45 min and 4°C. The pellet, containing insoluble membrane fractions of cell lysates, was resuspended in 1 Vol cell lysis buffer supplemented with respective detergents to a final concentration of 1% (w/v) GDN, 0.2% (w/v) DDM and 0.04% (w/v) CHS. Whole cell lysates in 1 Vol cell lysis buffer were similarly supplemented with respective detergents. Solubilization of proteins in lysis buffer, supplemented with respective detergents, was allowed for either 2 h or overnight at 4°C. As a last step, insoluble proteins were separated by centrifugation for 1 h at 100,000 × g and 4°C and the protein content after lysis with different methods and solubilization was assessed by SDS-PAGE and western blotting with subsequent immunostaining.

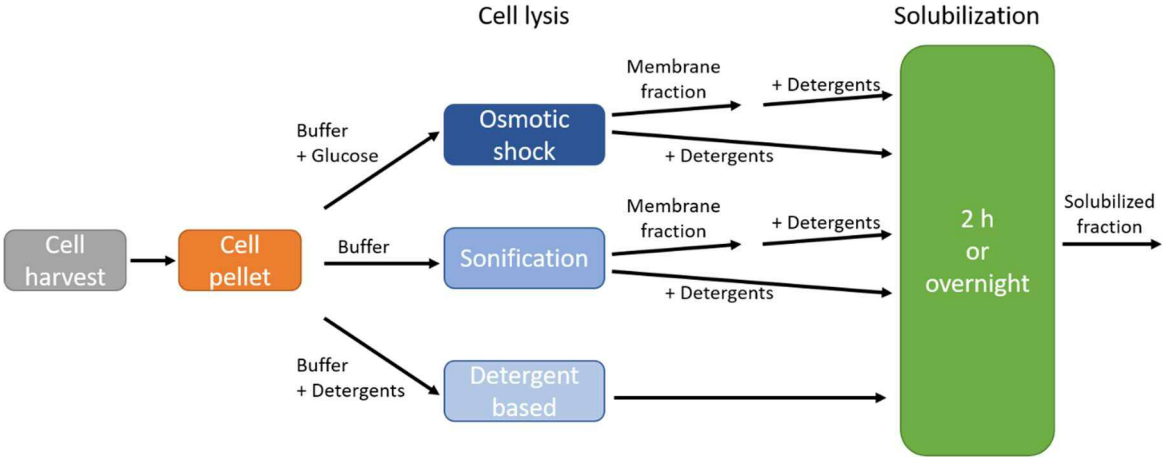

Figure 2.3: Schematic representation of the lysis and solubilization screening for Cav2.2 purification
Cells were harvested and resuspended in different buffers suitable for subsequent cell lysis by osmotic shock, sonication or detergent-based lysis. Cell lysates were either separated into crude cytosol and membrane fraction, latter supplemented with detergents, or directly supplemented with detergents. Solubilization of proteins was allowed for 2 h or overnight before separating and analyzing the fraction of solubilized protein with regard to the total protein and the Cav2.2-specific protein content.

2.6.2 Individual Purification Approaches

Following purification approaches were performed on cell lysates generated through previously optimized methods. In brief, stably transfected CHO-cells, expressing $Ca_V2.2$ channels, were seeded in T175-flasks and cultivated at 37°C, 5% CO_2 and saturated humidity in an incubator as described in 2.1.1.1. After reaching confluency, cells were washed once with pre-warmed PBS and subsequently harvested using Trypsin-EDTA, incubating at 37°C for 1 min. Detached cells were pelleted by centrifugation for 5 min at 200 × g, washed with PBS and were pelleted again. Cell pellets were resuspended in ice-cold cell lysis buffer and cells were lysed by sonication for 3 × 15 s at 100% amplitude with 30 s breaks on ice in between. After supplementation with detergents, cell lysates were incubated for 2 h at 4°C and insoluble material was removed by centrifugation for 1 h at 100,000 × g and 4°C. The supernatant was either applied to the respective column as is, or, where indicated, additionally pre-treated. Furthermore, for some purification strategies the supernatant was concentrated with an Amicon Ultra-0.5 mL Centrifugal Filter Unit (Merck), using a cut-off of 100 kDa, by centrifugation for 5 min at 14,000 × g to reach approximately ten-fold concentration. Samples were kept at 4°C until further purification.

2.6.2.1 Size Exclusion Chromatography

Size exclusion chromatography (SEC) is a chromatographic purification technique that separates molecules and macromolecular complexes according to their overall size (Irvine 2001). The principle relies on the porous texture of the column matrix, in which smaller proteins can enter more efficiently, which results in a longer retention time on the column. In contrast, large proteins and macromolecular complexes cannot enter the matrix and will elute earlier. This will subsequently lead to a size-dependent separation of complex protein samples after elution (Fig. 2.4). For purification of the sample by SEC, fast protein liquid chromatography (FPLC), as well as high-performance liquid chromatography (HPLC) systems were used to subsequently compare the purification efficiency.

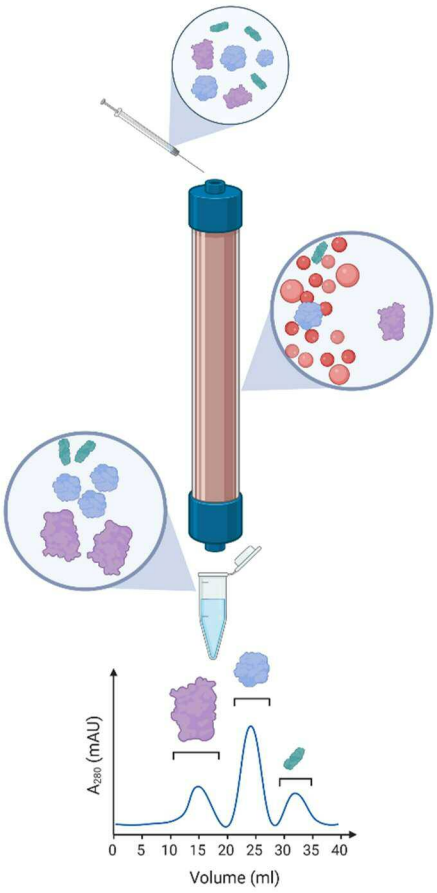

Figure 2.4: Schematic representation of the principle of size exclusion chromatography Based on the specific composition and structure of the column material, purification by SEC will separate a complex sample of proteins and macromolecular complexes with regard to their overall size. Proteins that exhibit a smaller size are able to enter the porous matrix more efficiently and retain longer on the column, whereas large proteins elute earlier. Figure created with BioRender.com

SEC over HPLC was conducted using an Analytical HPLC System (1260 Infinity II LC System; Agilent Technologies) in combination with a Bio SEC-3, 300 Å column (Agilent Technologies) equilibrated in SEC running buffer (25 mM HEPES, 150 mM NaCl, 2 mM $CaCl_2$ (Sigma-Aldrich) and 0.01% (w/v) GDN, pH 7.4). The run was performed at a constant flow rate of 1 mL/min after 50 µL of concentrated solubilized protein sample was injected via an autosampler module. Signals were acquired at wavelengths of 214 nm and 280 nm and elution fractions were collected every 0.5 min (500 µL) and subsequently analyzed via SDS-PAGE and immunostaining of western blots. To test whether prior concentration of the sample may have an influence on protein stability or the final $Ca_V2.2$ concentration, a side-by-side comparison was performed injecting 100 µL each of unconcentrated and four-fold concentrated sample.

A similar approach was performed on an ÄKTA pure FPLC chromatography system (Cytiva) using a suitable column. For the expected protein size of 250 kDa for the α_1-subunit of the $Ca_V2.2$ channel, a Superdex 200 Increase 10/300 GL column (Cytiva) was chosen. The column was previously equilibrated in SEC running buffer and a constant flow rate of 0.75 mL/min was maintained during the run. 500 µL of solubilized protein was injected and signals was acquired at wavelengths of 214 nm and 280 nm. Elution fractions of 0.5 min (375 µL) were collected.

Analysis of the overall protein composition and specific separation of $Ca_V2.2$ were performed via SDS-PAGE and subsequent western blot analysis using a $Ca_V2.2$-specific antibody.

2.6.2.2 Ion Exchange Chromatography

The overall net charge of proteins and the dependence of their charge on the surrounding pH as indicated by their respective isoelectric point (pI) is an important characteristic of proteins and can therefore be used as a separation strategy. Ion exchange chromatography (IEX) makes use of this protein-characteristic biochemical property by separating proteins according to their net charge under specific conditions (Cummins, Rochfort et al. 2017). Based on the charge of the functional groups of the column resin, it can be differentiated between cation and anion exchange chromatography.

In cation exchange chromatography (CIEX), highly negatively charged groups like sulfonates are used to capture positively charged proteins on the column material, whereas column material for anion exchange chromatography (AIEX) captures negatively charged proteins through its positively charged functional groups. Elution is usually performed by increasing the ionic strength of the buffer over a salt gradient, which competes against and subsequently exchanges bound analyte proteins. Furthermore, proteins can be eluted by running a pH gradient which leads to a change in the overall net charge of the protein with regard to their respective pI. Using this method, proteins can be separated with regard to their protein-specific pI (Fig. 2.5).

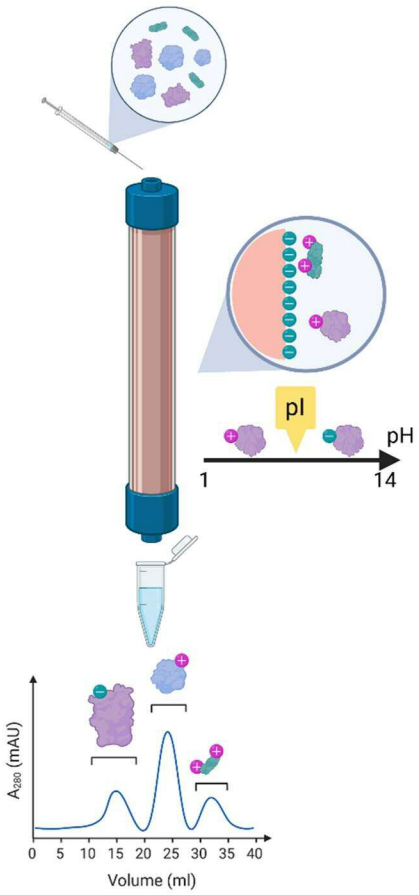

Figure 2.5: Schematic representation of the principle of ion exchange chromatography Based on their biochemical properties, proteins will bind to the charged column material (positively charged for AIEX, negatively charged for CIEX) with different affinity. Elution can be performed through changing the pH, which changes the overall net charge of bound protein and subsequently their binding affinity, or by increasing the ionic strength of the buffer. By this, proteins are separated with regard to their charge and protein-specific pI. Figure created with BioRender.com

$Ca_V2.2$ is a protein with a high charge density with an expected pI of about 8.8 as calculated with the ProtParam tool in the ExPASy server (Wilkins, Gasteiger et al. 1999) and was therefore chosen for purification by IEX. Purification of $Ca_V2.2$ via **CIEX** was performed on an Analytical HPLC System using a Bio SCX NP5 CIEX column (Agilent Technologies). The column was equilibrated in CIEX buffer A, comprising 25 mM HEPES, 150 mM NaCl, 2 mM $CaCl_2$ and 0.01% (w/v) GDN at pH 7.4. Cell lysates, solubilized as previously described (see 2.6.1), were used as input and 50 µL of ten-fold concentrated sample was loaded at a flow rate of 1 mL/min for 5 min. Elution was performed using CIEX buffer B, composed of 25 mM glycine, 150 mM NaCl, 2 mM $CaCl_2$ and 0.01% (w/v) GDN at pH 10 by introducing a linear gradient ranging from 0% to 100% B within 30 min, which was finalized by washing the column for 5 min in CIEX buffer B. The shift in pH throughout the gradient was previously determined by measuring the pH of different ratios of buffer A:B to estimate the elution point of $Ca_V2.2$ (Tab. 2.3).

Table 2.3: pH changes during CIEX elution at different concentrations of CIEX buffer B

% Buffer B	pH
0%	7.53
10%	7.68
20%	7.84
30%	8.11
40%	8.51
50%	9.28
60%	9.78
70%	10.05
80%	10.23
90%	10.37
100%	10.52

Chromatograms were acquired at 214 nm, 260 nm and 280 nm and elution fractions were collected as 0.5 min (500 µL) samples. The overall protein composition and specific separation of $Ca_V2.2$ was subsequently analyzed via SDS-PAGE and western blot analysis using a $Ca_V2.2$-specific antibody.

In addition, for purification of $Ca_V2.2$ using **AIEX**, a Cytiva Resource Q 1 mL column (Cytiva) on an ÄKTA pure FPLC system was chosen and protein elution was performed using a buffer gradient of increasing ionic strength. The column was pre-equilibrated in AIEX buffer A, comprising 25 mM HEPES, 150 mM NaCl, 2 mM $CaCl_2$ and 0.01% (w/v) GDN at pH 7.4. For purification, 1 mL of $Ca_V2.2$-containing solubilized sample was loaded in AIEX buffer A at a constant flow rate of 1 mL/min. The column was washed for 5 column volumes (CV) in AIEX buffer A and elution was performed by applying a linear gradient from 0% to 50% AIEX buffer B, composed of 25 mM HEPES, 1.5 M NaCl, 2 mM $CaCl_2$ and 0.01% (w/v) GDN at pH 7.4 over the course of 20 CV, finalizing the gradient with 100% AIEX buffer B wash for 5 CV. Eluted proteins were collected as 1 min (1 mL) fractions and analyzed in SDS-PAGE and western blot staining with regard to their overall protein composition and specific $Ca_V2.2$ content.

Furthermore, different bead-based IEX column materials were tested for $Ca_V2.2$ purification in batch-mode. 50 µL or 100 µL of bead solution (AIEX: 50 µL Q-sepharose beads (Pharmacia Biotech, Pfizer, New York, New York, USA), 100 µL DEAE-sepharose beads (Pharmacia Biotech), 100 µL Capto-Q beads (GE Healthcare, Chicago, Illinois, USA); CIEX: 100 µL Capto-S beads (GE Healthcare)) was equilibrated in IEX buffer A, consisting of 25 mM HEPES, 150 mM NaCl, 2 mM $CaCl_2$ and 0.01% (w/v) GDN at pH 7.4. Separation of the beads was achieved by spinning down and removing the supernatant. To each type of IEX-beads, 500 µL of $Ca_V2.2$-containing sample was added and incubated for 30 min at 4°C on a rotation wheel. The supernatant was collected as unbound fraction and beads were washed in 500 µL washing buffer by incubating for 30 min at 4°C on a rotation wheel. Elution of the protein was performed by addition of IEX buffer B, consisting of 25 mM HEPES, 1.5 M NaCl, 2 mM $CaCl_2$ and 0.01% (w/v) GDN at pH 7.4 at increasing ratios, diluted in washing buffer to a final volume of 500 µL and incubation was performed for 5 min to 30 min at 4°C on a rotation wheel. Samples were analyzed using SDS-PAGE and immunostaining of western blots.

2.6.2.3 Hydrophobic Interaction Chromatography

Proteins can also be purified with regard to their hydrophobicity by performing hydrophobic interaction chromatography (HIC) (McCue 2009). For this, samples are supplemented with ammonium sulfate ($(NH_4)_2SO_4$) prior to application of the sample to the chromatography column, in order to remove the hydrate shell from proteins to subsequently expose their hydrophobic patches. As a next step, a hydrophobic matrix is used to which proteins can bind to over their hydrophobic patches. Elution of the proteins is achieved by decreasing the concentration of $(NH_4)_2SO_4$ in the running buffer which leads to reformation of the hydrate shell, masking of the hydrophobic patches and subsequent elution from the hydrophobic matrix (Fig. 2.6).

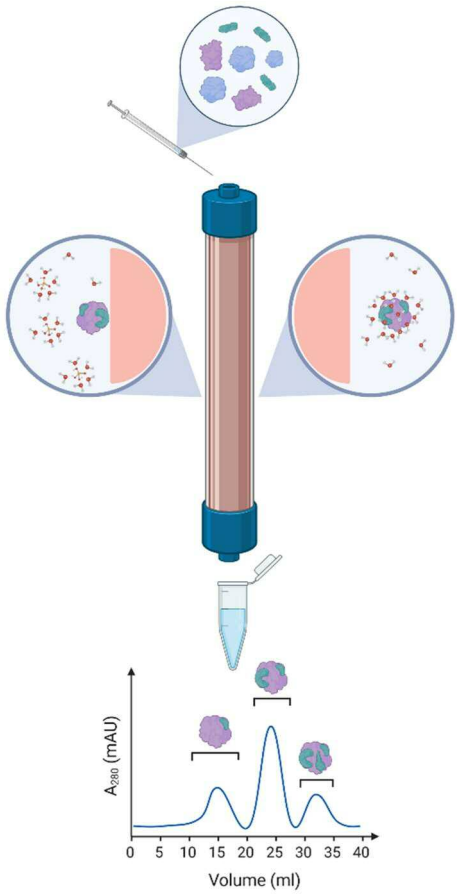

Figure 2.6: Schematic representation of the principle of hydrophobic interaction chromatography Ammonium sulfate is used to remove protein-surrounding hydrate shells, which subsequently demasks the hydrophobic patches on the protein, enabling the binding of the protein to a hydrophobic matrix. Elution is achieved by gradually decreasing the concentration of ammonium sulfate. By this, proteins are separated with regard to their hydrophobicity. Figure created with BioRender.com

$Ca_V2.2$ is a membrane spanning protein and therefore contains a significant number of hydrophobic regions distributed across its surface. For this reason, HIC was chosen as a purification approach. Cell lysates of $Ca_V2.2$-expressing CHO cells were prepared and proteins were solubilized as previously described (see 2.6.1). 1.5 M of $(NH_4)_2SO_4$ (Carl Roth) was added to the sample and after centrifugation for 1 min at 20,000 × g the supernatant was used as input for HIC. In addition, precipitated proteins, present in the pelleted fraction, were resolubilized in buffer without $(NH_4)_2SO_4$ and analyzed with regard to $Ca_V2.2$ content by SDS-PAGE and western blotting.

For purification of the $(NH_4)_2SO_4$-soluble protein fraction, an ÄKTA pure chromatography system, equipped with a Resource Eth 1 mL HIC column (VWR), was used. Equilibration of the column was performed in HIC buffer A, composed of 25 mM HEPES, 150 mM NaCl, 2 mM $CaCl_2$ and 0.01% (w/v) GDN at pH 7.4. 500 µL of the sample was applied over 1 min at a constant flow rate of 1 mL/min, followed by 5 min of column wash with HIC buffer A. For elution, a linear gradient of 0% to 100% HIC buffer B, consisting of 25 mM HEPES,

150 mM NaCl, 2 mM $CaCl_2$ and 0.01% (w/v) GDN, 1.5 M $(NH_4)_2SO_4$, pH 7.4, was applied over 15 min, finalizing with 3 min at 100% HIC buffer B, followed by 5 min column wash using HIC buffer A. Elution profiles were acquired at 280 nm and elution fractions were collected as fractions of 1 min (1 mL) and analyzed with regard to the overall protein composition via SDS-PAGE. Specific elution of $Ca_V2.2$ was subsequently analyzed by western blot analysis using a $Ca_V2.2$-specific antibody.

2.6.2.4 Immobilized Metal Affinity Chromatography

Purification of proteins via immobilized metal affinity chromatography (IMAC) is widely known and used for purification of recombinant proteins that were fused to a short peptide affinity tag, such as a His6-tag. The interaction relies on transition metal ions like zinc (Zn^{2+}), copper (Cu^{2+}), cadmium (Cd^{2+}), mercury (Hg^{2+}), cobalt (Co^{2+}), nickel (Ni^{2+}) and iron (Fe^{2+}), which are chelated to a chromatographic medium like nitrilotriacetic acid (NTA). Not only recombinant affinity tags, but also naturally occurring surface-exposed amino acid residues histidine, cysteine and tryptophan equally exhibit high affinity to the IMAC matrix via formation of complexes with chelated metal ions. In addition, IMAC can be used in variations by loading the column material with Ca^{2+} ions, which allows for separation of Ca^{2+}-binding proteins, as well as loading with Fe^{2+} ions, to separate proteins with regard to their phosphorylation state (Fig. 2.7) (Charlton and Zachariou 2008).

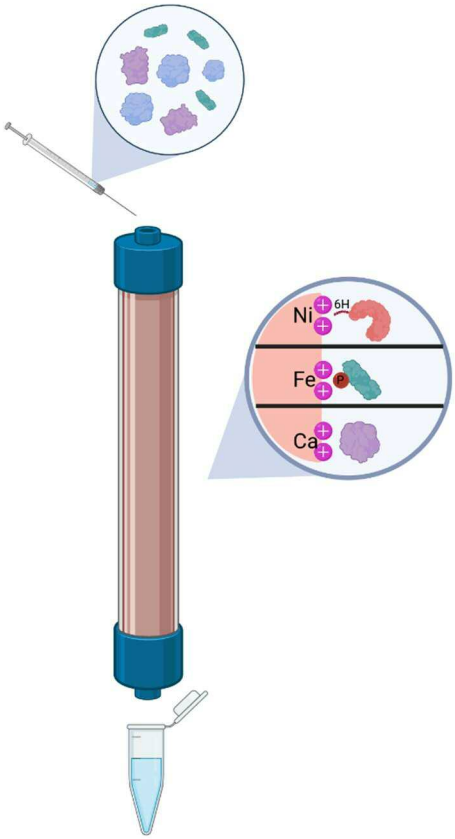

Figure 2.7: Schematic representation of the principle of immobilized metal affinity chromatography Metal ions are immobilized via chelation to a matrix. Formation of complexes with amino acids histidine, cysteine or tryptophan with chelated metal ions allows for purification of proteins, for example by the use of specific affinity tags. Using Fe^{2+} as chelated ions, proteins can additionally be separated with regard to their phosphorylation state. Immobilized chelated Ca^{2+} ions allow for separation of Ca^{2+}-binding proteins. Figure created with BioRender.com

Several characteristics of the $Ca_V2.2$ α_1-subunit suggested IMAC as interesting technique for selective separation of $Ca_V2.2$ from other proteins. No affinity tag was present on the $Ca_V2.2$ channel stably expressed in CHO cells, but an intrinsically, natural occurring penta-histidine stretch is found located in the C-terminal loop region of the $Ca_V2.2$ α_1-subunit, which, through its solvent-exposed location, may be available and effective for purification via IMAC using a Ni^{2+}-NTA-column. Furthermore, it was previously reported that $Ca_V2.2$ contains several phosphorylation sites, especially located in intra- and extracellular loop regions. Therefore, a second IMAC-based purification approach was tested, using Fe^{2+}-loaded NTA columns. As $Ca_V2.2$ is specifically transporting Ca^{2+} across the membrane, it also contains a Ca^{2+}-binding selectivity filter, which is known to associate with Ca^{2+} ions. For this reason, an additional approach was tested, using Ca^{2+}-NTA as column material for the purification of $Ca_V2.2$.

For purification of $Ca_V2.2$ with regard to its intrinsic penta-histidine tag, 1 Vol (100 µL) of Ni^{2+}-NTA agarose beads (Cube Biotech, Monheim, Germany) was equilibrated in IMAC buffer, consisting of 25 mM HEPES, 150 mM NaCl, 2 mM $CaCl_2$ and 0.01% (w/v) GDN at pH 7.4 by washing twice with 4 Vol. Following equilibration, 4 Vol of solubilized $Ca_V2.2$-containing samples was added to the equilibrated beads and incubated for 10 min at 4°C on a tumbling mixer. Beads were separated by centrifuging for 2 min at 2,500 × g and were washed twice with 4 Vol IMAC buffer and twice with IMAC buffer, supplemented with 10 mM imidazole, to remove unspecifically bound proteins. Elution was performed by the addition of 4 Vol IMAC buffer, supplemented with increasing concentration of imidazole, comprising consecutive elution steps using 50 mM, 100 mM, 250 mM imidazole and finally eluting twice with 500 mM imidazole in IMAC buffer.

For purification of $Ca_V2.2$ with regard to its phosphorylation state, 500 µL of 50% Ni^{2+}-NTA bead slurry was washed twice with 1 mL of 0.5 M EDTA to remove chelated Ni^{2+} ions. The matrix was reloaded by incubation with 100 mM iron(II) sulfate ($FeSO_4$; Sigma-Aldrich). To prevent oxidation of Fe^{2+} to Fe^{3+}, all subsequent steps were performed using buffers supplemented with 1 mM NaCl as reducing agent. Approximately 500 µL $Ca_V2.2$-containing sample was added to the column and incubated for 30 min at 4°C on a tumbling mixer. Beads were separated by centrifugation for 2 min at 2,500 × g to remove unbound proteins. After washing twice with running buffer, supplemented with 10 mM sodium-dihydrogen-phosphate (NaH_2PO_4; AppliChem), elution was performed by adding running buffer, supplemented with consecutively increasing concentrations of NaH_2PO_4 (50 mM, 100 mM and 200 mM).

For purification of $Ca_V2.2$ with regard to its Ca^{2+}-binding property, Ni^{2+}-NTA agarose beads were stripped as previously described in this chapter and reloaded with 1 M $CaCl_2$. After equilibration of the beads with running buffer, samples were loaded onto the beads. Elution was performed in the same way as elution of proteins bound by Ni^{2+}-NTA, using increasing concentrations of imidazole.

The overall protein composition and purification efficiency of $Ca_V2.2$ was subsequently analyzed via SDS-PAGE and western blot analysis using a $Ca_V2.2$-specific antibody.

2.6.2.5 Immunoprecipitation

A different technique for purification of specific proteins is immunoprecipitation (IP), which makes use of specific antibodies, directed against a unique epitope of a protein (Kaboord and Perr 2008). A commercially available $Ca_V2.2$-specific antibody was used for purification and different antibody-binding beads were tested for immobilization of the complex during purification. In addition, different elution techniques, using either the antibody-specific antigen for competitive elution of the protein or lowering the pH to chemically disrupt the binding, were used for subsequent dissolution of the complex and further purification (Fig. 2.8).

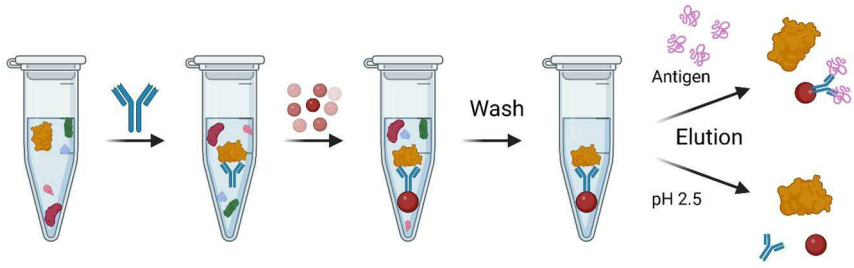

Figure 2.8: Schematic representation of the principle of immunoprecipitation Protein-specific antibodies are added to a complex protein sample, binding to the protein of interest. Protein A/G beads are added that bind the antibody/protein complex, which enables unbound proteins to be selectively washed away. Elution of the complex is either performed by lowering the pH to disrupt the binding, or by competitive elution using the antibody-specific antigen in molar excess. Figure created with BioRender.com

For IP-based purification of proteins, solubilized complex protein samples were prepared from $Ca_V2.2$-expressing CHO cells as described previously (2.6.1). Approximately 1% (v/v) of *CACNA1B* Rabbit Polyclonal Antibody (OriGene) was added to 1 Vol of solubilized protein sample and incubated for 2 h at 4°C on a tumbling mixer to allow for antibody-protein complex formation. 10% (v/v) of bead slurry of agarose Protein A/G beads (GE Healthcare) was equilibrated before in 1 Vol of IP washing buffer, comprising 25 mM HEPES, 150 mM NaCl, 2 mM $CaCl_2$ and 0.01% (w/v) GDN at pH 7.4, and beads were subsequently added to the samples to incubate for additional 1 h at 4°C on a tumbling mixer. After incubation, the sample was washed three times with 1 Vol of washing buffer by centrifuging for 2 min at 2,500 × g and discarding the supernatant after each washing step. Elution was performed at low pH by resuspending the beads in 0.2 Vol of IP elution buffer (200 mM glycine, pH 2.5) and constantly pipetting up and down for 1 min at RT. Beads were sedimented by centrifugation and the supernatant was collected and neutralized by adding 10% (v/v) of IP neutralization buffer (1 M Tris, pH 10.4). The elution was repeated once to increase elution efficiency. For analysis of the remaining bound protein, beads were resuspended in 0.2 Vol of 2 × Laemmli buffer and were boiled for 5 min at 95°C. All

samples were analyzed with regard to the $Ca_V2.2$-specific content by SDS-PAGE and immunostaining of western blots.

As the secondary structure of proteins can be de-stabilized at low pH, an additional protocol for elution of $Ca_V2.2$ from its specific antibody was established. For this, the specific antigen of the antibody, which corresponds to a stretch of amino acid residues of $Ca_V2.2$ in the intracellular loop, spanning between domains II and III, was designed as a peptide ((C)-PRRHHRHRDRDKTSASTPAGG) and ordered from Caslo (Caslo ApS, Kongens Lyngby, Denmark) for the use in competitive elution of $Ca_V2.2$ from the antibody. Antibody-protein complexes were incubated as previously described in this chapter and 10% (v/v) of bead slurry of either magnetic Protein A/G beads (Proteintech Group Inc., Rosemont, Illinois, Germany) or agarose Protein A/G beads was equilibrated in 1 Vol of IP washing buffer before adding it to the sample. After incubation, the sample was washed three times with IP washing buffer either by separating the beads over a magnetic stand for magnetic beads, or by centrifuging for 2 min at 2,500 × g for samples incubated with agarose beads, while removing the supernatant each time. Elution was performed by adding the antigen-peptide in molar excess (10 mM in 0.2 Vol of IP washing buffer) and incubating for 1 h at 4°C on a tumbling mixer. Beads were separated and the supernatant was collected as elution fraction. All samples were analyzed regarding their $Ca_V2.2$-specific content by SDS-PAGE and subsequent immunostaining of western blots.

2.6.2.6 Hydroxyapatite Chromatography

Another strategy tested for purification of $Ca_V2.2$ was mixed mode chromatography over hydroxyapatite (HAC) (Cawley 2023). The combination of ions on the surface of hydroxyapatite exhibits unique and selective purification properties. Ca^{2+} ions (C-sites), present on the material, provide sites for metal affinity purification. Chelation through Ca^{2+} predominantly occurs on acidic amino acids or C-termini of proteins, or by interactions with phosphate groups. In addition, presence of phosphate groups (P-sites) on the surface of hydroxyapatite column material provide ion exchange chromatography properties, forming cationic exchange interactions with positively charged groups of basic amino acids or N-termini of proteins (Fig. 2.9). Elution of proteins bound by hydroxyapatite is achieved by applying increasing concentrations of phosphate groups in the respective elution buffer.

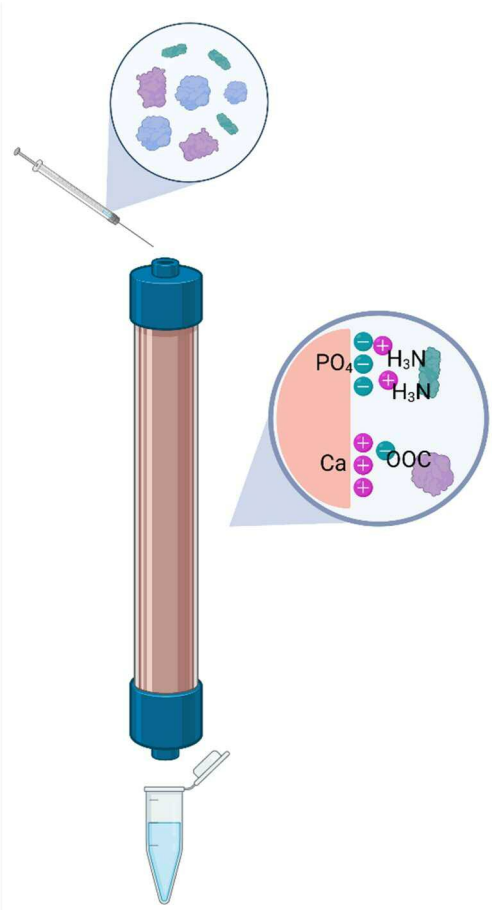

Figure 2.9: Schematic representation of the principle of mixed mode chromatography using hydroxyapatite Ions, present on the surface of hydroxyapatite, will specifically bind to proteins for subsequent purification. Ca^{2+} sites provide metal affinity properties, by chelating negatively charged functional groups of acidic amino acids, phosphate groups, as well as C-termini of proteins, whereas phosphate groups of hydroxyapatite function as cation exchange chromatography, by binding to basic amino acids or the N-terminus of proteins. Elution is performed by increasing the concentration of phosphate groups in the buffer. Figure created with BioRender.com

The hydroxyapatite column material was synthesized briefly following a protocol from Hunte, Von Jagow et al. (2003). To summarize, 40 mL of 1 M NaCl was heated to 70°C. Over the course of 3 h, 180 mL of 0.5 M $CaCl_2$ and 0.5 M Na_2HPO_4 were added continuously to the sample and incubated at 70°C to 80°C while stirring. Next, the same volume of both solutions was added at once and incubated for 1 h at 70°C to 80°C, which results in the formation of brushite ($CaCl_2 + Na_2HPO_4 \rightarrow Ca[PO_3(OH)] \times 2\ H_2O$). The formed brushite crystals were separated through filtration and washed with 500 mL ddH_2O and stored overnight at RT. On the following day, 500 mL ddH_2O and 45 mL of 4.4 M sodium hydroxide (NaOH; AppliChem) were added to the brushite crystals and the solution was heated over the course of 45 min to 1 h to 90°C to subsequently incubate for 1 h at 95°C while stirring. Hydroxyapatite was precipitated from solution through cooling while stirring the solution was stopped after reaching 85°C ($Ca[PO_3(OH)] \times 2\ H_2O \rightarrow Ca_5[OH(PO_4)_3]$).

The supernatant was decanted and crystals were washed once with 500 mL ddH_2O. To remove remaining brushite, 500 mL ddH_2O and 10 mL NaH_2PO_4 were added to the crystals twice with subsequently heating of the solution to 80°C while stirring. The supernatant was decanted from the hot solution and the procedure was repeated using 10 mL of 0.5 M NaPi, pH 6.8 instead of NaH_2PO_4. The generated hydroxyapatite was stored as 50% (v/v) suspension in 0.5 M NaPi, pH 6.8 at 4°C and was used for subsequent chromatography approaches.

For purification of $Ca_V2.2$ over hydroxyapatite chromatography, crude membrane fractions of stable $Ca_V2.2$-expressing CHO cells were prepared and solubilized as previously described (see 2.6.1) and used for batch purification over hydroxyapatite. 1 mL of 50% (v/v) hydroxyapatite column material was equilibrated in HAC washing buffer, consisting of 25 mM HEPES, 150 mM NaCl, 2 mM $CaCl_2$ and 0.01% (w/v) GDN at pH 7.4, supplemented with 100 mM trisodium phosphate (Na_3PO_4; Sigma-Aldrich), by washing twice with 2 CV of buffer and separating the column material by centrifugation for 1 min at 500 × g. The $Ca_V2.2$-containing sample was supplemented with 100 mM Na_3PO_4 to allow for binding of the proteins to hydroxyapatite and subsequently added to the column material and incubated for 1 h at 4°C on a rotation wheel. After removing the supernatant, the column material was washed twice with 2 CV HAC washing buffer, supplemented with 100 mM Na_3PO_4. Elution was performed by incubating the sample for 1 h at 4°C on a rotation wheel in 0.5 CV HAC washing buffer, supplemented with 250 mM Na_3PO_4. The supernatant was separated and a second elution was performed incubating in 400 mM Na_3PO_4 in 0.5 CV HAC washing buffer overnight.

To assess the remaining bound proteins after elution with 400 mM Na_3PO_4, hydroxyapatite was dissolved through acidification. For this, increasing concentrations of hydrogen chloride (HCl) were added to the column material until clearing of the solution was observed. Addition of 0.4 CV of 16% (v/v) HCl (Carl Roth) was effective and the sample was neutralized by addition of 1 CV of 1 M Tris, pH 9.2.

The overall protein composition of the flow-through, wash and elution fractions, as well as the content of $Ca_V2.2$ in the different fractions was subsequently analyzed via SDS-PAGE and western blot analysis using a $Ca_V2.2$-specific antibody.

2.6.2.7 Centrifugation-Based Separation

In addition to purification via size exclusion chromatography, proteins can also be separated with regard to their size and molecular weight and their respective density through different centrifugation-based separation techniques. **Differential centrifugation** is the simplest form of particle separation by centrifugation and relies on differences in the sedimentation speed between particles with varying size and density. In general, larger particles with higher density have a faster sedimentation rate and will move faster through a medium when applying a certain centrifugal force for a given time. By varying the centrifugation speed and time, separation of proteins is achieved by pelleting of proteins with regard to their sedimentation rate (Fig. 2.10). This process is called differential pelleting.

A more specific centrifugation-based separation technique is **density gradient centrifugation** (DGC) (Ifft 1976). By using media gradients, comprising solutions with different densities, this centrifugation-based method is able to separate particles on basis of their specific densities. Particles will sediment upon centrifugation until their density is equal to the surrounding medium in the gradient which causes them to stop moving (Fig. 2.10). Different gradient materials are available and have to be selected with respect to the sample material aimed to be separated. The respective gradients are cast by over-layering the gradient solutions of increasing density, the lighter the higher, and samples are added as final layer on top of the gradient to allow movement of all particles through the gradient.

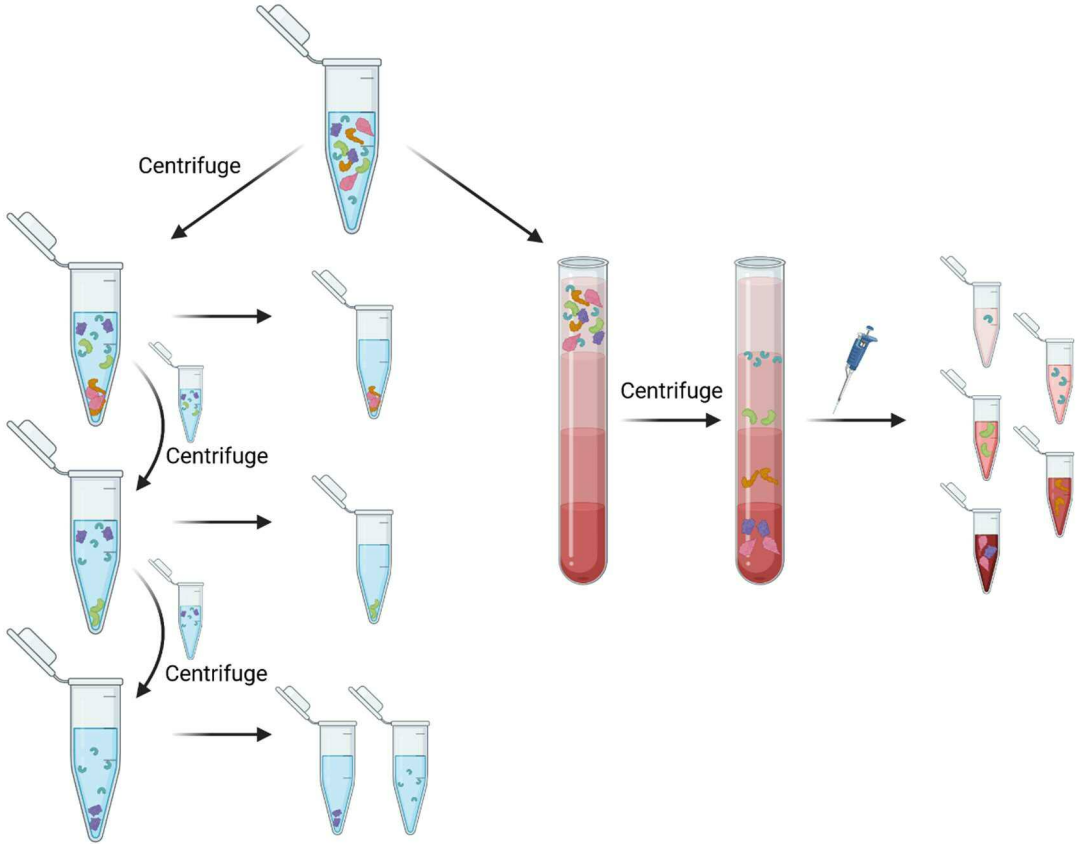

Figure 2.10: Schematic representation of protein purification via centrifugation-based techniques Separation of particles from complex samples can be achieved by differential centrifugation (left), which separates proteins with regard to their sedimentation speed by combining centrifugation steps of varying time and speed, which result in separation of particles by differential pelleting. Another technique is separation through density gradient centrifugation (right), in which proteins are separated with regard to their density. Using a density gradient, cast from materials exhibiting different densities, particles will move along the centrifugation force until they reach a point of equilibrium where their density corresponds to the density of the surrounding media. By this, proteins can be separated according to their specific density. Figure created with BioRender.com

Pre-purification of complex protein samples of crude membrane fractions was tested by performing **differential centrifugation** at varying centrifugation speed and time. Cell lysis was performed by sonication as described before, with the deviation that samples were lysed in cell lysis buffer without detergents. Afterwards, samples were centrifuged at 1,000 × g and 4°C for 10 min to remove cell debris and nuclei. The pellet was resuspended in 100 µL cell lysis buffer, for subsequent analysis via SDS-PAGE. Further centrifugation of the supernatant at 20,000 × g was performed for 30 min at 4°C to separate soluble and insoluble particles. The supernatant was used for analysis and pellets were washed twice with 100 µL lysis buffer before centrifuging again at 20,000 × g for 30 min at 4°C. The supernatant was removed and the pellet was solubilized by addition of 1% (w/v) GDN, 0.2% (w/v) DDM and 0.04% (w/v) CHS and incubation for 2 h at 4°C on a rotation wheel. Samples were subsequently analyzed with regard to their total protein composition and their $Ca_V2.2$-specific content via SDS-PAGE and immunostaining of western blots.

For purification of $Ca_V2.2$ from complex protein samples by **density gradient centrifugation**, gradients based on different media were tested for the respective separation efficiency. All gradients were cast in 1 × 34 mm polypropylene ultracentrifugation tubes (Beckman Coulter) to a final volume of 1.92 mL. The stock solutions were prepared in GDN buffer (25 mM HEPES, 150 mM NaCl, 2 mM $CaCl_2$ and 0.01% (w/v) GDN at pH 7.4) supplemented with the respective concentration of iodixanol (Sigma-Aldrich), glycerol or sucrose (AppliChem) and gradients were cast by pipetting the respective volume of each gradient fraction (Tab. 2.4) starting with the highest concentration. The different gradient components were pipetted using cut pipette tips and placed exactly on top of the previous layer without disturbing the lower layer. Solubilized $Ca_V2.2$ samples were prepared as previously described (see 2.6.1) and 80 µL sample was added on top of the gradient as a final layer, increasing the total volume to 2 mL. Centrifugation was performed for 3 h at 259,000 × g and 4°C with maximum acceleration and break, using an Optima MAX-TL ultracentrifuge equipped with the TLS-55 rotor (Beckman Coulter). After centrifugation, sample fractions were separated by removing 140 µL fractions at a time from the upper layer until all liquid was separated.

The separation of total protein was assessed throughout the different fractions using SDS-PAGE. Furthermore, all fractions were analyzed with regard to their $Ca_V2.2$-specific content via western blot analysis using a $Ca_V2.2$-specific antibody.

Table 2.4: Gradient composition used for density gradient centrifugation for separation of $Ca_V2.2$

Gradient							
Iodixanol: 5-50%		Iodixanol: 10-40%		Glycerol: 10-30%		Sucrose: 5-20%	
Gradient [%]	Volume [µL]	Gradient [%]	Volume [µL]	Gradient [%]	Volume [µL]	Gradient [%]	Volume [µL]
50	260	40	480	30	640	20	480
40	260	30	480	20	640	15	480
30	260	20	480	10	640	10	480
20	780	10	480	-	-	5	480
10	260	-	-	-	-	-	-
5	100	-	-	-	-	-	-

2.6.3 Multistep Purification Approaches

Combination of different purification approaches provides the opportunity to separate proteins with regard to multiple biophysical and biochemical characteristics. By this, a more specific separation of proteins from complex samples can be achieved. Different individual purification approaches can be combined as desired, but in order to achieve protein samples of high purity and high yield, a suitable strategy has to be developed. Furthermore, it is important to consider sample start and end conditions for each individual purification method in order to comply with prerequisites for subsequent purification steps. Here, different individual purification techniques were combined and tested for effectiveness and efficiency in purification of $Ca_V2.2$ from complex protein samples. Most promising individual purification strategies (see 3.3.2) were combined and combinations with the highest separation efficiency are presented in this work.

As previously described (see 2.6.1), a first separation step is the removing of all insoluble material after cell lysis and solubilization by ultracentrifugation. This technique was used as initial purification step for all subsequently described multistep purification approaches.

2.6.3.1 Differential Centrifugation and Density Gradient Centrifugation

Purification of $Ca_V2.2$ from complex cell lysates was tested through combining previously tested centrifugation-based techniques for differential centrifugation and density gradient centrifugation with slight optimization of respective protocols (see 2.6.2.7). In brief, samples were collected from $Ca_V2.2$-expressing cells after cell lysis by sonication in 25 mM HEPES pH 7.4, 150 mM NaCl, freshly supplemented with 1 × cOmplete EDTA-free proteinase inhibitor, and centrifuged for 10 min at 1,000 × g and 4°C. The supernatant was further centrifuged for 30 min at 200,000 × g and 4°C and the pellet was solubilized by addition of 1% (w/v) GDN, 0.2% (w/v) DDM and 0.04% (w/v) CHS for 2 h at 4°C on a rotation wheel. 400 µL of the sample was added to a 10% to 40% (v/v) iodixanol gradient, cast from 400 µL of each 10%, 20%, 30% and 40% iodixanol, and centrifugation was performed at 259,000 × g for 3 h at 4°C using an Optima MAX-TL equipped with a swinging TLS-55 rotor. Afterwards, samples were collected as 140 µL fractions from top to bottom of the gradient and were analyzed by SDS-PAGE and western blot staining.

2.6.3.2 Anion Exchange Chromatography and Size Exclusion Chromatography

Solubilized samples were prepared as previously described (see 2.6.1) and 500 µL of the sample was subjected to AIEX using a Cytiva Resource Q 1 mL column on an ÄKTA pure FPLC system as previously described with slight variations (see 2.6.2.2). In brief, samples were loaded to the equilibrated column using AIEX buffer A at a constant flow rate of 1 mL/min. Column wash was performed for 5 CV in AIEX buffer A, followed by elution using a linear gradient from 0% to 100% AIEX buffer B over 20 CV, finalizing the gradient with 100% AIEX buffer B for 5 CV. 1 mL fractions were collected and analyzed in SDS-PAGE and western blot staining with regard to their overall protein composition and $Ca_V2.2$ content.

AIEX fractions showing highest $Ca_V2.2$-specific signals were pooled and concentrated to a final volume of approximately 75 µL using Amicon Ultra-0.5 Centrifugal Filter Units. The resulting sample was applied to a Bio SEC-3 300 Å column, equilibrated in SEC buffer, on an HPLC system at a flow rate of 1 mL/min as previously described (see 2.6.2.1). Elution fractions were collected every 0.5 min (0.5 mL) and analyzed using SDS-PAGE analysis and immunostaining of western blots with regard to overall protein composition and $Ca_V2.2$ content, respectively.

2.6.3.3 Size Exclusion Chromatography and Hydroxyapatite Chromatography

For a multistep purification approach, combining protein separation via SEC with separation through hydroxyapatite chromatography, $Ca_V2.2$-containing samples were prepared and solubilized as previously described (see 2.6.1) and subsequently concentrated approximately five-fold to a final volume of 100 µL. After equilibration of a Bio SEC-3 300 Å column in SEC buffer, samples were loaded onto the column at a flow rate of 1 mL/min as previously described (see 2.6.2.1). Elution samples were collected as fractions of 0.5 min (0.5 mL) and analyzed subsequently in SDS-PAGE and western blot staining.

SEC elution fractions with highest $Ca_V2.2$-specific signald were supplemented with Na_3PO_4 to a final concentration of 100 mM and applied to 500 µL pre-equilibrated hydroxyapatite column material in a gravity flow column. The column was washed twice with 500 µL SEC buffer, supplemented with 100 mM Na_3PO_4, and samples were eluted with 500 µL elution buffer (25 mM HEPES, 150 mM NaCl, 2 mM $CaCl_2$, 0.01% (w/v) GDN, 400 mM Na_3PO_4, pH 7.4). Respective fractions were analyzed with regard to overall protein composition by SDS-PAGE and the specific separation of $Ca_V2.2$ by immunostaining of western blots.

2.7 Binding Studies of $Ca_V2.2$ with RD2

2.7.1 Determination of Binding Kinetics using Surface Plasmon Resonance Spectroscopy

To determine the binding kinetics, including the equilibrium dissociation constant (K_D), of the interaction between the D-enantiomeric peptide RD2 and $Ca_V2.2$, surface plasmon resonance (SPR) spectroscopy was employed for characterization. Experiments were either performed on a Biacore T200 instrument (GE HealthCare) or a Biacore 8K device (GE HealthCare). RD2 and its tandem repeat D-peptide RD2RD2, as well as a control using the known $Ca_V2.2$ inhibitor ω-CgTx GVIA, were used as ligands. Immobilization of the ligands was performed onto series S Carboxymethyl-dextran CM-5 sensor chips (Cytiva), using amine-coupling of the ligand via amine-reactive crosslinker groups. Activation of sensors was achieved by running 50 mM N-hydroxysuccinimide (NHS; XanTec, Düsseldorf, Germany) and 16.1 mM N-ethyl-N'-(dimethylaminopropyl)carbodiimide (EDC; XanTec) for 7 min at a flow rate of 30 µL/min. RD2 or its tandem repeat D-peptide RD2DR2 (CBL Patras) and ω-CgTx GVIA (Bachem Holding, Bubendorf, Switzerland) were prepared at a final concentration of 50 µg/mL in 10 mM sodium acetate (Merck), pH 6. Samples were injected each over one of the activated flow cells at a time and immobilization was performed until a final signal of 1000 resonance units (RU) was reached. Following immobilization, all flow cells were inactivated by injecting 1 M ethanolamine, pH 8.5 (XanTec) for 7 min.

For analysis of the binding kinetics of the immobilized ligands interacting with $Ca_V2.2$, pre-purified samples of $Ca_V2.2$ were used as analyte in single-cycle experiments. As no protocol for specific purification of $Ca_V2.2$ from complex cell lysates was available, samples were only partially purified using SEC, as previously described (see 2.6.2.1). Fractions containing the highest concentration of $Ca_V2.2$ were collected and protein concentrations were determined by measuring the absorbance of the sample at 280 nm using an UV/Vis-spectrophotometer (Shimadzu, Kyoto, Japan). The sample was diluted to a final concentration of 100 nM in running buffer (25 mM HEPES, 150 mM NaCl, 2 mM $CaCl_2$ and 0.01% (w/v) GDN, pH 7.4) and a 1:2 dilution series was created to run single-cycle analysis. Samples were injected for 180 s at a flow rate of 10 µL/min over all flow cells, starting from the lowest concentration and successively increasing the concentration of the analyte. In addition, a final dissociation step of 900 s in running buffer was included.

Sensorgrams of the ligand-loaded flow cells were referenced by subtracting the respective reference flow cell signal. Data evaluation of the binding experiment was performed by fitting the respective sensorgrams using global 1:1 stoichiometric kinetic fitting, implemented in the Biacore T200 Evaluation Software 3.2 (GE HealthCare). As these experiments were part of initial exploratory studies for the verification of RD2 binding to partially purified $Ca_V2.2$, experiments were performed in duplicates only.

2.7.2 Determination of Binding Kinetics using Microscale Thermophoresis

In order to determine the K_D of the interaction of $Ca_V2.2$ and the D-enantiomeric peptide RD2, microscale thermophoresis (MST) measurements were performed. For this, the D-peptide RD2 was labeled covalently with the thiol-reactive Atto 633 label (maleimides) (ATTO-TEC) according to the manufacturers protocol. In brief, RD2 was constructed to contain an additional C-terminal cysteine group with an amidated C-terminus. The D-peptide was dissolved in PBS buffer at pH 7.4 at 1 mg/mL. Next, the conjugation was performed by adding the dye-maleimide in a 1.3-fold molar excess and incubating for 2 h at RT and slight agitation. Purification of the labeled D-peptide was achieved by performing Reversed Phase Liquid Chromatography using an Agilent 1200 system (Agilent Technologies) equipped with a Zorbax SB-300 C-18 column (4.6 × 250 mm, 5 µm; Agilent Technologies). Respective samples were loaded using a mobile phases that comprised buffers A: ddH_2O + 0.1% (v/v) trifluoroacetic acid (TFA; Sigma-Aldrich) and B: Acetonitrile (Carl Roth) + 0.1% (v/v) TFA, applying a linear gradient ranging from 15% buffer B to 45% buffer B in 20 min at a flow rate of 1 mL/min. Atto 633-labeled RD2 was eluted, collected and lyophilized (Alpha 2-4 LSCbasic; Martin Christ Gefriertrocknungsanlagen GmbH, Osterode am Harz, Germany).

The protein $Ca_V2.2$ was partially purified from stably transfected CHO cells using a combination of SEC and HAC. In contrast to previously described methods (see 2.6.3.3), the order of the chromatography steps was modified to produce a final sample in a buffer suitable for subsequent experiments. In brief, after HAC, the $Ca_V2.2$-containing fraction was collected and concentrated using Amicon Ultra-0.5 Centrifugal Filter Unit (Merck) with a 100 kDa cut-off and the sample was further purified by size exclusion chromatography (Agilent Technologies Bio SEC-3, 300 Å, 7.8 × 300 mm, 3 µm) after pre-equilibration of the column with $Ca_V2.2$ buffer. Peak fractions were pooled and the concentration was determined measuring the absorbance at 280 nm on an UV/Vis-spectrophotometer.

Labeled RD2-cys-NH2-Atto 633 or only CF-633 (control) were dissolved in $Ca_V2.2$ buffer (25 mM HEPES, 150 mM NaCl, 2 mM $CaCl_2$ and 0.01% (w/v) GDN, pH 7.4) to a final stock concentration of 20 nM. The partially purified protein $Ca_V2.2$ was diluted separately to the respective concentration using the same buffer. $Ca_V2.2$ was then titrated in 1:2 serial dilution steps to the ligand samples to create 16 samples ranging from 50 nM to 1.5 pM, while keeping RD2-cys-NH2-Atto 633 or CF-633 at a constant concentration of 10 nM.

MST measurements were conducted on a Nano Temper Monolith NT.115 instrument (NanoTemper Technologies GmbH, Munich, Germany) using Monolith NT.115 Premium Capillaries (NanoTemper), using the red LED at 70% power and MST power of 40%. The temperature was maintained at a constant 25°C throughout the experiment. To obtain the dissociation constant K_D, data evaluation was performed using the "Thermophoresis with T-Jump evaluation" in the NanoTemper MO. Affinity Analysis software (v2.1.2333) with a respective cold region ranging from -1 s to 0 s and a hot region from 27.42 s to 28.42 s. Changes in normalized fluorescence (F_{Norm}), dependent on the concentration of the titrant $Ca_V2.2$, were fitted to the K_D model, incorporated in the analysis software. Finally, the dissociation constant K_D was calculated as mean of three independent experiments.

2.8 *In Vivo* Wide-Field Ca^{2+} Imaging

As RD2 was previously observed to inhibit $Ca_V2.2$ *in vitro*, the *in vivo* effect of the lead compound RD2 on Ca^{2+} fluxes in the brain of awake mice was analyzed by performing wide-field Ca^{2+} imaging. Wide-field Ca^{2+} imaging provides a high spatiotemporal resolution and enables visualization of neuronal activity based on neurotransmitter or Ca^{2+} fluxes over large areas of the cortex simultaneously. Using transgenic mouse lines that stably express the fluorescent Ca^{2+} indicator GCaMP6f provides signals with a high signal-to-noise ratio originating from the bright GCaMP fluorescence. By this, changes in neuronal activity in response to various stimuli can be visualized in the cortex of the awake mouse.

2.8.1 Ethics

All respective procedures and experiments were approved by the Animal Care and Ethics Committee within the Florey Institute of Neuroscience and Mental Health under #19-021-FINMH and were performed under standard procedures and guidelines provided.

2.8.2 Mouse Strain

For *in vivo* Ca^{2+} imaging approaches, Ai148 x Cux2-Cre ERT2 B6 mice were used for all experiments. These mice were generated from a mouse strain genetically encoding the Ca^{2+} indicator GCaMP6f (Ai148 (TIT2L-GC6f-ICL-tTA2)), cross-bread with a Cre-driver line (Cux2-CreERT2) on a B6 background. These double-transgenic mice show robust transgene expression of the Ca^{2+} indicator in cortical L2/3 pyramidal excitatory neurons in response to low-dose tamoxifen induction. Mice were housed in standard cages with littermates and migrated to single housing after surgeries. Cages were kept in a 12 h light and dark cycle and food and water was provided *ad libitum* at all times. All experiments were performed during the light cycle.

2.8.3 Tamoxifen Induction

To induce stable expression of the genetically encoded Ca^{2+} indicator GCaMP6f, tamoxifen was administered to the mice via oral gavage at an age of three to five months. Tamoxifen (Sigma-Aldrich) was previously dissolved in 100% ethanol (ChemSupply Australia, Gilman, Australia) at 208 mg/mL and further diluted in corn oil (Sigma-Aldrich) to a final concentration of 20 mg/mL. Under slight anesthesia, a 20 G feeding tube (Walker Scientific, Joondalup, Australia) was gently inserted in the mouth to deliver 5 µl per g bodyweight.

2.8.4 Skull-Intact Surgical Preparation

Surgical preparation of the cortical skull window for imaging of Ca^{2+} fluxes was performed in adult mice at approximately two to five months of age. Surgeries were performed following standard protocols with slight modifications (Ren and Komiyama 2021). Briefly, mice were anesthetized using isoflurane (3% (induction) or 1.5% (maintenance) in O_2), and an *intraperitoneal* (*i.p.*) injection of 2 mg/kg meloxicam (ilium, Troy Animal Healthcare, Glendenning, Australia) was further applied for pain relief. All following surgical steps were performed under aseptic conditions. Starting from a small incision, the scalp was carefully removed from the area of interest to expose the dorsal area of the skull. Next, the periosteum was separated and any remaining tissue was further removed using 3% (w/v) NaOH (ChemSupply). After being fully dried, a UV curable glue (Tetric Evo Flow; Henry Schein Medical GmbH, Melville, New York, USA) was applied to the skull in thin layers, while individually curing each layer in between. For head-fixation during the imaging process, an

additional head-frame was attached to the skull, rostral to the imaging window, using dental cement (Super-Bond Quick Monomer and Catalyst V; SUN MEDICAL CO. LTD, Moriyama, Shiga, Japan). After successful completion of the surgery, the exposed skull window was covered with a silicone cap, formed from Body Double silicone rubber (Smooth-On Inc., Macungie, Pennsylvania, USA) until further experiments were performed.

2.8.5 Wide-Field Ca^{2+} Imaging in Response to Sensory Stimuli

Cortical neuronal Ca^{2+} fluxes were analyzed in the awake mice before and after application of respective compounds. Animals were head-fixed to the device in order to stabilize the imaging window and images were acquired following the respective protocols.

Images were acquired using an ORCA-Flash 4.0 CMOS camera (Hamamatsu Photonics, Shizuoka, Japan) connected to a National Instruments Data Acquisition Systems board (NI DAQ; NI, Austin, Texas, USA) to link data acquisition and respective trial steps.

Pre-drug Ca^{2+} fluxes were imaged for overall 20 min, covering 21 to 26 trials distributed over the time frame. One trial consisted of an initial delay period of 2 s, followed by a baseline imaging period of 3 s and a subsequent sensory stimulus using a 200 Hz signal to the right forepaw at 5 s for 0.3 s. Image acquisition was started at the baseline period and, for each trial, 500 images were acquired over 10 s at a resolution of 1024 × 1024 pixels by alternating blue (470 nm) and green (565 nm) excitation light derived from two LED sources (LEDD1B; Thorlabs, Newton, New Jersey, USA), projected on the brain surface while capturing the emission light.

The compound RD2, diluted in sterile 0.9% (w/v) saline solution (Pfizer) to a final concentration of 1 mg/mL, or the respective volume of 0.9% (w/v) saline solution for vehicle-treated mice, was injected *i.p.* at a final concentration of 10 mg/kg. Mice were returned to cages and experiments were started at 30 min post-injection based on previously determined pharmacokinetic properties of the compound (Leithold, Jiang et al. 2016). Ca^{2+} fluxes post-RD2 or post-vehicle injection were analyzed in 56 to 72 trials over a time course of 1 h as previously described in this chapter.

2.8.6 Image Processing and Data Analysis

All images were pre-processed using ImageJ and custom-written routines in Python, containing different steps of signal correction and normalization. To summarize, image stacks of acquired blue and green images were initially deinterlaced and motion-corrected to account for motion drifts in vertical and horizontal direction due to animal movement. This was performed by comparing each frame to a reference image, using whole-frame cross-correlation, which was initially carried out based on all green images and in the following applied to all blue images. Next, averaging of all baseline images per trial was performed for all blue as well as green images. For this, baseline signals were averaged over several frames prior to the sensory stimulus for each trial to then determine the rolling median of all baselines for one tested condition (F_0). The fluorescent intensity of all time points was further normalized to the overall baseline and displayed as the relative change in fluorescent intensity ($\Delta F/F_0 = (F–F_0)/F_0$). Subsequently, all images of the green channel were reference-subtracted from the blue channel images to account for hemodynamic changes and background noise and pre-processing was finalized by applying global signal regression (GSR) correction, which uses linear regression to subtract the average intensity over the whole-brain signal from each individual pixel to account for physiological noise.

Images were then analyzed for the average evoked intensity over the course of all trials by calculating the mean intensity per pixel over all trials. These images were subsequently overlaid with a grid, allowing to match the acquired data with certain cortical brain regions, based on the mouse brain atlas from the Allen Institute (Wang, Ding et al. 2020) (Fig. 2.11). Regions of interest (ROI) were defined based on the identified brain regions and the signal intensity per region was plotted against the trial time course. Change in fluorescence was assessed for respective brain regions of interest, and the neuronal activation patterns in response to the sensory stimulus were compared before and after treatment for each individual animal.

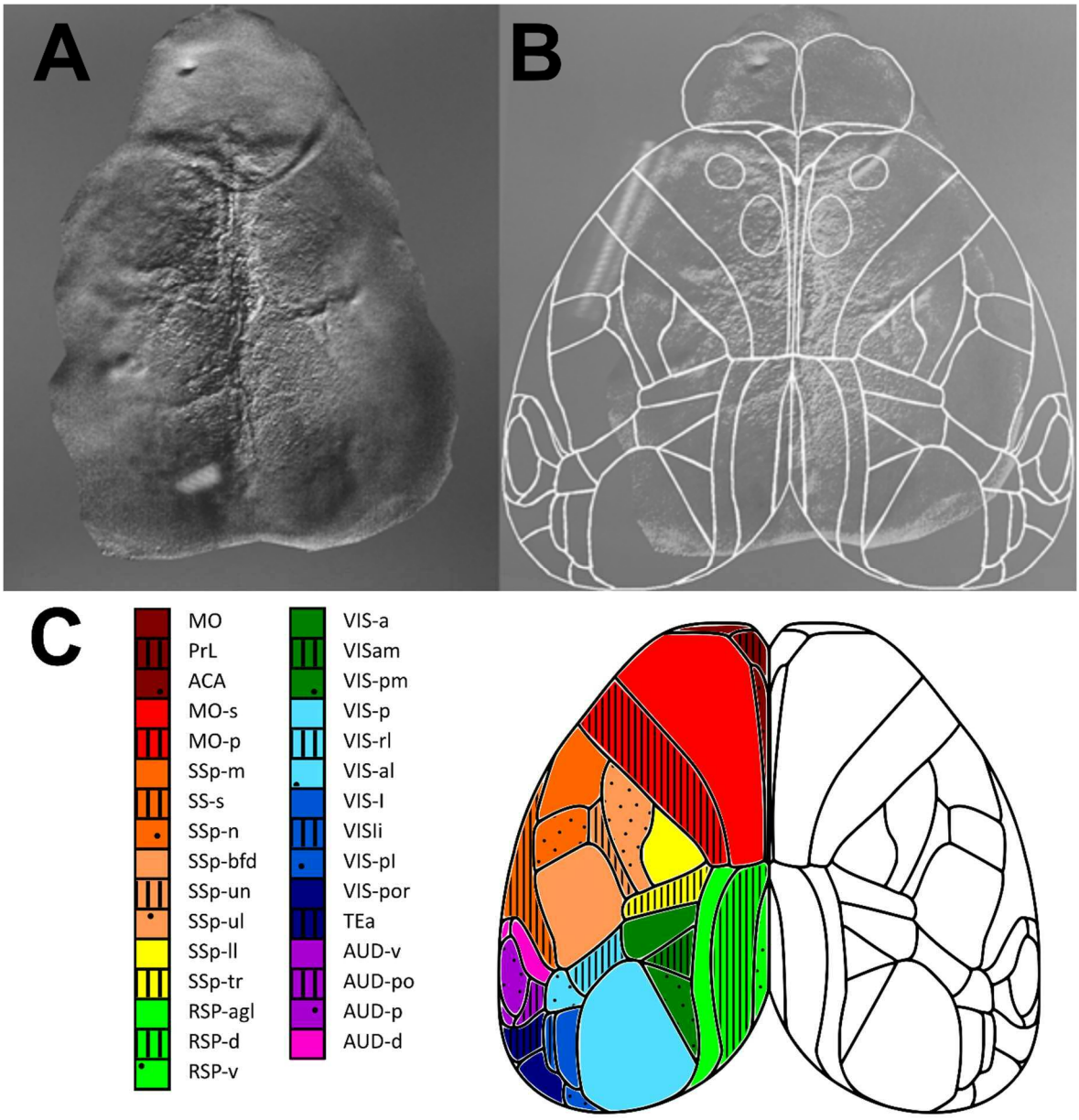

Figure 2.11: Wide-field Ca^{2+} imaging of cortex-wide neuronal activity Pre-processed images, displaying the evoked average fluorescent intensity ($\Delta F/F_0$) for each respective time point (**A**) were overlaid with a grid identifying different brain regions based on the mouse brain atlas from the Allen Institute (**B**, **C**). *MO* – medial orbital; *PrL* – prelimbic cortex; *ACA* – anterior cingulate area; *MO-s* – motor area - secondary; *MO-p* – motor area - primary; *SSp-m* – primary somatosensory area - mouth; *SS-s* – somatosensory area - supplemental; *Ssp-n* – primary somatosensory area - nose; *Ssp-bfd* – primary somatosensory area - barrel field; *Ssp-un* – primary somatosensory area - unassigned; *Ssp-ul* – primary somatosensory area - upper limb; *Ssp-ll* – primary somatosensory area - lower limb; *Ssp-tr* – primary somatosensory area - trunk; *RSP-agl* – retrosplenial area - lateral agranular; *RSP-d* – retrosplenial area - dorsal; *RSP-v* – retrosplenial area - ventral; *VIS-a* – visual area - anterior; *VIS-am* – visual area - anteromedial; *VIS-pm* – visual area - posteromedial; *VIS-p* – visual area - primary; *VIS-rl* – visual area - rostrolateral; *VIS-al* – visual area - anterolateral; *VIS-l* – visual area - lateral; *VIS-li* – visual area - laterointermediate; *VIS-pl* – visual area - posterolateral; *VIS-por* – visual area - postrhinal; *TEa* – temporal association area; *AUD-v* – auditory area - ventral; *AUD-po* – auditory area - posterior; *AUD-p* – auditory area - primary; *AUD-d* – auditory area - dorsal.

2.9 Phage Display for the Selection of New $Ca_V2.2$-Binding Peptides

For the identification for new putative $Ca_V2.2$-binding peptides, a phage display with three selection rounds was performed using partially purified $Ca_V2.2$ protein.

2.9.1 Toxicity of GDN on Phages

To exclude any putative toxic effects of detergents, present in the sample buffer, a pre-experiment investigated phage survival in buffer with or without GDN. For this, 1.66×10^{13} phages of the respective phage library (TriCo-16 phage display peptide library, lot number: CBLX090318; Creative Biolabs, Shirley, New York, USA) were incubated for 30 min in 100 µL $Ca_V2.2$ buffer (25 mM HEPES, 150 mM NaCl, 2 mM $CaCl_2$, pH 7.4) with or without the addition of 0.01% (w/v) GDN. After incubation of the sample, the respective output titer was determined by diluting 1 µL of the phage solution in LB-Medium to subsequently create a dilution series of six 1:10 dilutions (10^{-3} to 10^{-8}) in 100 µL LB_{tet} (20 µg/mL tetracycline in LB). After addition of equal volumes of a *E. coli* K12 ER2738 culture (OD_{600} = 0.6), 190 µL of the solution was plated with 800 µL top-agar (LB-Agar with 210 mM isopropyl β-D-thiogalactopyranoside (IPTG; UBPBio, Dallas, Texas, USA) and 98 mM 5-bromo-4-chloro-3-indolyl-beta-D-galacto-pyranoside (X-Gal; Carl Roth)) on titer-plates (35 × 10 mm; Sarstedt, Nümbrecht, Germany) and incubated at 37°C overnight. The number of colonies was determined on the next day and used for determination of the output titer.

2.9.2 Phage Display

For the phage display selection on, the target protein $Ca_V2.2$ was immobilized on amino-coupling plates (Nunc Immobilizer Amino 96-well plate, polystyrene; Thermo Fisher Scientific). All following steps were performed at RT on a shaking incubator. Plates were reactivated to ensure sufficient binding levels by incubating with 50 mM NHS and 16.1 mM EDC for 10 min. $Ca_V2.2$ protein, partially purified using a combination of SEC and HAC (described in 2.6.3.3), was diluted to a final concentration of 100 nM in $Ca_V2.2$ buffer (25 mM HEPES, 150 mM NaCl, 2 mM $CaCl_2$ and 0.01% (w/v) GDN, pH 7.4). For each target selection (TS) well, 100 µL of the $Ca_V2.2$ protein solution, equivalent to 10 pmol of $Ca_V2.2$ per well, was added. Empty selection (ES) wells were filled with the same volume of $Ca_V2.2$ buffer, not containing any $Ca_V2.2$ protein, and plates were incubated for 30 min. After immobilization, the plates were quenched with 200 µL of 1 M ethanolamine, pH 8.5

for 10 min, followed by blocking for 30 min with 200 µL of 1% (w/v) BSA in $Ca_V2.2$ buffer. After three washing steps with $Ca_V2.2$ buffer supplemented with 0.2% (w/v) BSA (washing buffer), phages from a phage library (TriCo-16 phage display peptide library, lot number: CBLX090318; Creative Biolabs) with an initial input titer of 2.66×10^{12} phages/mL were diluted 1:100 in 100 µL $Ca_V2.2$ buffer and subsequently added to each well and incubated for 20 min, followed by five washing steps using washing buffer to remove unbound phages. Elution of the phages was first performed following the original protocol for phage display selection via pH-dependent elution by adding 100 µL elution buffer (0.2 M glycine-HCl, pH 2.2) and incubating for 10 min before transferring the elution solution to a fresh reagent tube and adding 25 µL of neutralization buffer (1 M Tris-HCl, pH 9.1). In addition, a competitive elution approach, using 125 µL of $Ca_V2.2$ buffer supplemented with 1 µM ω-CgTx GVIA was performed by incubating for 10 min in order to select $Ca_V2.2$-binding peptides that exhibit a similar binding mode as the known $Ca_V2.2$ inhibitor ω-CgTx GVIA.

Determination of the number of eluted phages was performed by diluting 1 µL of the eluted phage solution in 100 µL LB-Medium. This was used to create a dilution series of six 1:10 dilutions in 100 µL LB_{tet} which was further supplemented with 100 µL of an *E. coli* K12 ER2738 culture at $OD_{600} = 0.6$. 190 µL of each solution was plated with 800 µL top-agar on titer-plates (35 × 10 mm) and incubated at 37°C overnight. The number of grown positive colonies was assessed on the next day to determine the output titer of each selection round.

Eluted phages were amplified by inoculating 20 mL culture of *E. coli* K12 ER2738 ($OD_{600} = 0.1$) in LB_{tet} with 120 µL of phage solution and incubating for 4 h at 37°C and 120 rpm in a bacterial shaking incubator. After amplification of the phages, cells were centrifuged for 20 min at 2,700 × g at 4°C and phages were precipitated from the supernatant by addition of 7 mL of polyethylene glycol (PEG)-NaCl (20% (w/v) PEG-8000 (Sigma-Aldrich), 2.5 M NaCl) and incubation overnight at 4°C on ice. On the next day, precipitated phages were centrifuged for 1 h at 2,700 × g and 4°C and the pellet was resuspended in 1 mL $Ca_V2.2$ buffer. After an additional centrifugation step at 11,000 × g for 5 min at 4°C, 200 µL PEG-NaCl was added to the separated supernatant and phages were precipitated on ice for 1 h. Solutions were centrifuged for 45 min at 2,700 × g and 4°C before resuspending the pellet in 100 µL $Ca_V2.2$ buffer.

The absorption of the phage solution was measured at 269 nm and 320 nm in an UV/Vis-spectrophotometer for determination of the input titer:

$$\frac{phages}{ml} = \frac{(A_{269\,nm} - A_{320\,nm}) * 6 * 10^{16}}{number\ of\ bases/phage}$$

Phages were stored at 4°C until starting the next selection round. The selection procedure was repeated twice for control selection following the same protocol to ensure quality and specificity of the selection. Phages derived from TS1 were further incubated in a second round of target selection using immobilized $Ca_V2.2$ or were applied to direct control (DC) wells, which did not contain any target protein. Phages obtained in ES1 were applied to a second round of empty selection. The third selection round was performed in an analogue way, using eluted phages from TS2 in TS3 and DC3, and phages from ES2 in ES3.

2.9.3 Enrichment ELISA

The successful selection of specific $Ca_V2.2$-binding peptides in the phage display was validated by performing an enrichment ELISA. For this, Nunc amino-coupling 96 microtiter-plates (Thermo Fisher Scientific) were reactivated by incubating with 50 mM NHS and 16.1 mM EDC for 10 min at RT. Immobilization of the target protein $Ca_V2.2$ was performed as previously described for 30 min at a total amount of 100 pmol per well, followed by quenching, blocking and three washing steps (see 2.9.2). Immobilized $Ca_V2.2$ was incubated for 1 h at RT with 100 µL of phages from the library or with phages eluted in either one of the three target selection rounds eluted via pH reduction or competitive elution, which were previously diluted in $Ca_V2.2$ buffer to a final concentration of 2.5×10^{11} phages/mL, or as control with $Ca_V2.2$ buffer alone. Following three wash steps, all wells were incubated with 100 µL anti-M-13 pVIII HRP-coupled antibody (Sino Biological, Peking, China), diluted to a final concentration of 0.35 ng/µL in washing buffer and incubated for 1 h at RT. All wells were washed six times and subsequently incubated with 100 µl of 3,3′,5,5′-tetramethylbenzidine (TMB) solution, previously prepared by dissolving 1 mg TMB (Sigma-Aldrich) in 1 mL of DMSO, which was further diluted in 9 mL of 50 mM phosphate citrate buffer, pH 5 (Sigma-Aldrich) to a final TMB concentration of 0.1 mg/mL. The reaction was stopped after approximately 2 min by addition of equal volumes of 2 M sulfuric acid (AppliChem) and the color reaction was quantified by measuring the absorbance of the solution at 450 nm using a microplate reader.

2.9.4 Next Generation Sequencing and Sequence Analysis

For sequence analysis of selected and enriched phages from the phage display, single stranded DNA (ssDNA) was extracted from phages from the library, all target and empty selections, as well as from the direct controls. For this, 10 µL of the phage input solution was diluted in 590 µL TBS, followed by phage precipitation by addition of 200 µL PEG-NaCl solution and incubation for 20 min at RT. Afterwards, samples were centrifuged for 10 min at 20,800 × g and 4 °C and the supernatant was discarded. Pellets were resuspended in 200 µL of a 10:1 mixture of 3 M sodium acetate (Merck) pH 5.2 and TE buffer (10 mM Tris, 1 mM EDTA, pH 8.0). Samples were supplemented with 500 µL of 99% ethanol (Carl Roth) and incubated for 15 min at RT to extract DNA. Following additional centrifugation for 10 min at 20,800 × g and 4 °C, pellets were washed once carefully with 250 µL of 70% (v/v) ethanol, followed by another centrifugation step for 10 min at 20,800 × g and 4 °C. All DNA-pellets were dried by incubation for 7 min at 30°C to allow for solvent evaporation, before resuspending in 40 µL of 10 mM Tris, pH 8.0. The concentration and quality of the extracted DNA samples were determined by measuring the absorption at 260 nm at 280 nm using a nanophotometer.

Specific amplification of the DNA was performed via PCR using the KAPA HiFi HotStart ReadyMix PCR Kit (Kapa Biosystems, Wilmington, USA). For each sample, 25 ng of template DNA was added to 12.5 µL KAPA HiFi HotStart ReadyMix (Kapa Biosystems), supplemented with 5 µM of specific forward and reverse primer (forward: 5′-TCGTCGGCAGCGTCAGATGTGTATAAGAGACAGCGCAATTCCTTTAGTGGTACC-3′; reverse: 5′-GTCTCGTGGGCTCGGAGATGTGTATAAGAGACAGCCCTCATAGTTAGCGTAACG-3′) filled to a total volume of 25 µL using ddH_2O. The amplification reaction via PCR was run using an initial denaturation step for 3 min at 95°C, followed by 25 cycles, each comprising 30 s denaturation at 95°C, 30 s annealing at 55°C and elongation at 72°C for 30 s, finalized by an ultimate elongation step for 5 min at 72°C before storing samples at 4°C. Respective concentrations were determined using absorbance measurements at 260 nm and the quality was further checked by performing gel electrophoresis on a 1% (w/v) agarose gel (see 2.2.5).

Sequences were obtained using next-generation sequencing (NGS), performed at the Genomics & Transcriptomics Labor at the Heinrich-Heine-Universität Düsseldorf, Germany. Sequencing results were analyzed using the Python-based Target Sequencing Analysis Tool (TSAT). This evaluation software was previously developed in-house for the

analysis and identification of DNA sequences enriched in the target selection. Using NGS-data as input in FASTA format, the program identified randomized peptide coding regions in the phage genome based on their respective framing regions and corresponding peptides were translated according to the identified DNA sequences. Normalization of the sequence frequency was performed with regard to enrichment of the specific sequence in each selection round compared with previous selections or the phage library. They were further compared to sequence-specific frequencies in respective empty selections and direct controls, to account for unspecific binding. Sequences that show successive enrichment of their respective sequence frequency over the course of all selection rounds, starting from the phage library, while exhibiting an equal or higher frequency in the target selection compared with direct control or empty selection, were ranked highest. More in detail, identified sequences were defined and ranked by their empty score (EmS = sequence frequency in TS3 / sequence frequency in ES3) or their specific enrichment score (EnS = sequence frequency in TS3 / sequence frequency in library) and saved in FASTA format for subsequent analysis.

Clustering analysis of the identified sequences was performed using Hammock (Krejci, Hupp et al. 2016). By this, it was aimed to identify potential common motifs in the enriched sequences contributing to the specific binding to the target protein $Ca_V2.2$. The analysis was performed using the standard parameters provided in the software.

2.10 Electrophysiological Recordings

To test the putative inhibitory potential of different newly identified peptides on $Ca_V2.2$-mediated currents, electrophysiological recordings were performed.

2.10.1 Cell Preparation

For electrophysiological recordings of $Ca_V2.2$ channels, stably transfected HEK293 cells, expressing human α_{1B-1} ($Ca_V2.2$: M94172.1) splice variant and in addition auxiliary subunits $\alpha_{2b}\delta_1$ (M76559.1) and β_{3a} (NM_000725), which were a kind gift from the laboratory of David J. Adams (University of Wollongong, Australia), were used. Cells were cultured under standard conditions in DMEM supplemented with 10% (v/v) FCS, 1% (v/v) penicillin/streptomycin and appropriate selection antibiotics (50 µg/mL geneticin, 10 µg/mL blasticidin and 40 µg/µL zeocin).

Electrophysiological recordings of $Ca_V1.2$-mediated currents were performed in HEK293 cells grown under standard conditions and co-transfected using lipofectamine 2000 to transiently express rabbit $Ca_V1.2$ channels (UniProtKB: P15381) as well as the $Ca_V\beta_{2e}$ (UniProtKB: Q8VGC3-4) auxiliary subunit.

For experiments, cells were seeded on uncoated glass coverslips and left to adhere for 24 h to subsequently analyze cells 24 h to 36 h post-transfection.

2.10.2 Whole-Cell Patch Clamp Recordings

Recordings were performed as whole-cell patch clamp experiments using an EPC-10 amplifier implemented in the PatchMaster software (HEKA Instruments Inc., Holliston, Massachusetts, USA). Prior to the recording, glass electrodes (borosilicate pipettes) were fabricated using a Sutter P-1000 puller (Harvard Apparatus, Holliston, Massachusetts, USA). Pulled pipettes were further fire-polished using a MF-830 microforge (Narishige (International) Ltd., London, United Kingdom) and electrodes exhibiting a resistance range between 1.8 MΩ and 4.5 MΩ were chosen for whole-cell patch clamp experiments.

For experiments, coverslips were transferred to a bath containing external recording solution, comprising 140 mM triethylammonium methanesulfonate (TEA-$MeSO_3$; Sigma-Aldrich), 10 mM barium chloride ($BaCl_2$; Sigma-Aldrich), 10 mM HEPES, pH 7.3, adjusted with triethylammonium hydroxide (TEA-OH; Sigma-Aldrich). Barium (Ba^{2+}) was used as charge carrier, as it was previously demonstrated that it is able to prevent channel inactivation, which allows for longer recording duration. Glass electrodes were filled with internal solution, containing 135 mM caesium methanesulfonate ($CsMeSO_3$; Sigma-Aldrich), 10 mM egtazic acid (EGTA; Sigma-Aldrich), 5 mM caesium chloride ($CsCl_2$; Sigma-Aldrich), 14 mM phosphocreatine (Sigma-Aldrich), 1 mM $MgCl_2$, 4 mM magnesium adenosine triphosphate (MgATP; Sigma-Aldrich), 0.4 mM disodium guanosine triphosphate (Na_2GTP; Sigma-Aldrich) and 10 mM HEPES, pH 7.3, adjusted with caesium hydroxide (CsOH; Sigma-Aldrich). During recordings, cells were continuously perfused with external recording solution. Testing compounds were freshly dissolved in ddH_2O to a final concentration of 1 mM. For recording of inhibitory effects of the peptides, the external recording solution was supplemented with testing compounds to a final concentration of 6 µM for RD2 and RD2-derived D-peptides RD2A-E. In addition, control experiments were performed using 1 µM of the known $Ca_V2.2$-specific inhibitor ω-CgTx GVIA, or 10 µM of nifedipine (Sigma-Aldrich) for inhibition of $Ca_V1.2$-mediated currents. Whole-cell currents

were induced by applying a depolarizing test pulse at 10 mV and/or 15 mV, triggering maximum inward currents every 10 s from a holding potential of -90 mV.

Data analysis was performed using a combination of FitMaster (HEKA), Origin(Pro), Version 2022 (OriginLab Corporation, Northampton, Massachusetts, USA) and Microsoft Excel 2019 (Microsoft Corporation, Redmond, Washington, USA) software. Currents were leak-subtracted and adjusted for capacitive currents using a P/4 protocol. All data is presented as mean ± standard error of the mean (SEM).

2.11 Peptide Docking Modeling

To gain more insight into putative binding motifs of RD2 and RD2-derived D-peptides on $Ca_V2.2$ channels and to identify respective key interacting residues for subsequent optimization cycles, the interaction of the D-peptides with $Ca_V2.2$ channels was modeled using a peptide docking approach.

2.11.1 Peptide and Protein Structure Preparation

To generate structural models of D-enantiomeric peptides, respective peptide models, based on the primary sequence, were first build as linear L-enantiomeric chains exhibiting antiparallel β-sheet secondary structure using the peptide builder implicated in the PyMol software (Schrodinger 2015). To change the overall chirality of the peptides, all amino acids were inverted at each respective C_α-atom as origin atom for inversion, while keeping neighboring N- and C-atoms stationary so the residue was converted into their respective D-enantiomeric analogue. Amino acids with two stereogenic centers (threonine and isoleucine) were additionally inverted at the second chiral carbon as previously described for C_α-atoms to overall convert the stereochemistry to D-enantiomeric. Furthermore, for structural transformation of the N-terminal proline residue, the bond between C_D- and C_G-atoms was removed to allow for inversion of the C_α-atom as previously described. The φ-torsion angle was manually set to -65°, as expected for proline residues due to restrictions of the angle in the ring formation. After reforming the bond, structures were locally minimized using UCSF Chimera 1.17.1 software, (Pettersen, Goddard et al. 2004), allowing only for structural changes in atoms C_D, C_B and C_G. To finalize, overall structures of the peptides were energy-minimized in the AMBER force field using the Chimera software.

As RD2 was able to replace the known $Ca_V2.2$ channel inhibitor ω-CgTx in previously performed competitive elution assays, a similar binding and pore-blocking mode was assumed for RD2 binding for exhibiting its observed inhibitory effect on $Ca_V2.2$ channels. Therefore, the ω-CgTx binding groove on the $Ca_V2.2$ channel was selected as input model for peptide docking predictions. The cryo-EM based structural model of the ω-CgTx MVIIA analogue ziconotide in complex with $Ca_V2.2$ (PDB: 7MIX) was used as input for the preparation of protein structures used for peptide docking modeling. All attached ligands and water molecules were removed. Using the PyMol software, all $Ca_V2.2$ residues in proximity of 5 Å around the ligated ziconotide were selected and exported as a new structural model. This model was further manually completed to resemble coherent structural elements forming the ω-CgTx binding groove.

To further incorporate the carboxylated N-terminus of the D-peptides into the docking approach, which was not supported in the respective web-based docking server for D-enantiomeric amino acids, a mirror-image peptide docking analysis was performed additionally. To identify key residues in the putative binding models of L-enantiomeric peptides, the $Ca_V2.2$ ω-CgTx binding groove input structure was modified to reflect D-enantiomeric stereochemical configuration. This was achieved by inverting the structural model with regard to the stereochemical configuration by flipping the structure within the Cartesian coordinate system along the *x*-axis (Fig. 2.12).

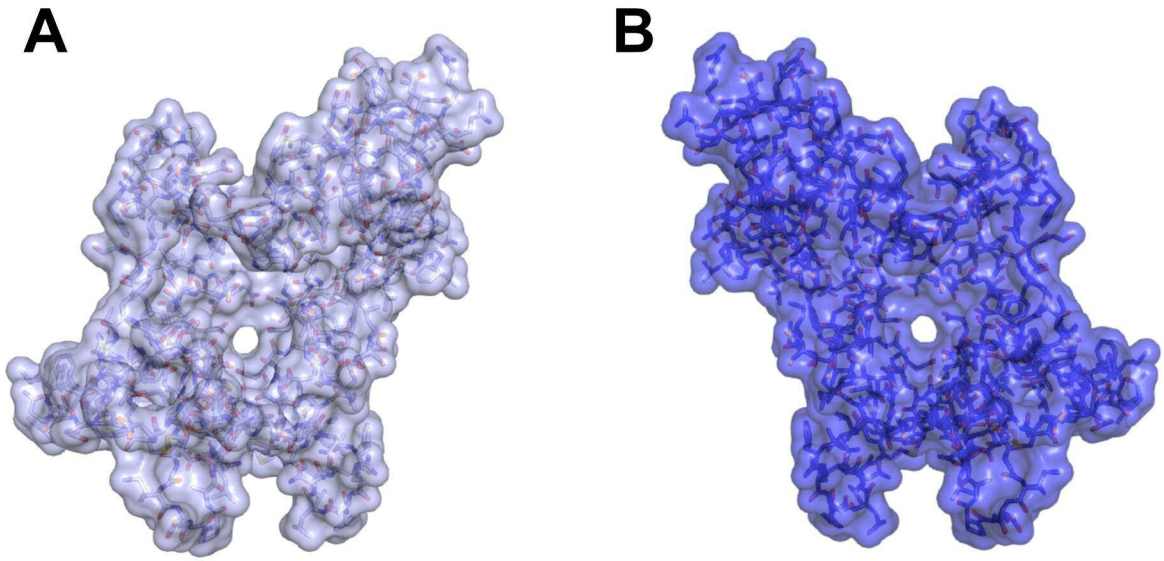

Figure 2.12: Inversion of the stereochemical configuration of the $Ca_V2.2$-ω-CgTx binding groove model
A The binding groove of ω-CgTx on $Ca_V2.2$ channels was identified and a model was created based on published structural data (PDB: 7MIX) and structures were prepared using PyMol. **B** Flipping of the structure along the *x*-axis was performed to invert the stereochemical configuration to resemble a D-enantiomeric structural model of the $Ca_V2.2$ ω-CgTx binding groove for mirror-image peptide docking.

2.11.2 Peptide Docking Modeling and Docking Assessment

To analyze the putative peptide docking modes of RD2 and lead-derived D-peptides on $Ca_V2.2$ channels, it is of high interest to understand on a structural level how RD2 is able to compete with the strong and specific binding of ω-CgTx. Using the cryo-EM-based structural model of the ω-CgTx MVIIA analogue ziconotide in complex with $Ca_V2.2$ (PDB entry 7MIX), the $Ca_V2.2$/ω-CgTx contact surface was analyzed and structures prepared as input for peptides docking modeling as previously described (see 2.11.2).

Docking models of RD2 or the D-peptide RD2C in complex with the previously identified structural model of the $Ca_V2.2$ ω-CgTx binding groove were created using the web-based docking software HPEPDOCK 2.0 (http://huanglab.phys.hust.edu.cn/hpepdock/; (Huang and Zou 2008; Zhou, Jin et al. 2018; Tao, Zhang et al. 2020). The minimal structural model of the ziconotide binding groove of $Ca_V2.2$ was provided as static receptor input and the D-enantiomeric structures of RD2 and RD2C were used as peptide input, respectively. For mirror-image peptide docking, the peptide sequences of RD2 and RD2C were used as flexible docking input and the inverted, D-enantiomeric structure of the $Ca_V2.2$ ω-CgTx binding groove in PDB format was selected as receptor input. Docking experiments were performed using the global docking algorithm provided in the docking software, selecting default parameters. Best 100 models of the peptide-channel complex were initially selected based on the lowest binding free energy score, provided by the HPEPDOCK server. Models of the complex were then visualized using PyMol software and analyzed with regard to the respective exhibited binding mode, while further comparing the binding mode to the $Ca_V2.2$-ziconotide complex.

Respective formed contacts in all models of the peptide-channel complexes, comprising polar contacts, especially salt bridges and hydrogen bonds, as well as hydrophobic interactions, were identified using the PyMol and ChimeraX software (Meng, Goddard et al. 2023) and verified and analyzed using LigPlot+ v2.2 (Wallace, Laskowski et al. 1995). Furthermore, contacted surface ratios in each model were determined using the online software PDBePISA (Krissinel and Henrick 2007). Common patterns and key residues, crucial for complex formation, were finally identified based on the frequency of the involvement of respective residues amongst the top 100 complex models.

3 Results

3.1 $Ca_V2.2$ Channel Levels are Increased in a Mouse Model of AD

To determine if age-dependent Ca^{2+} dysregulation in AD is possibly related to aberrant membrane density of $Ca_V2.2$ channels in the brain, relative protein levels of $Ca_V2.2$ were analyzed in a mouse model of AD at different disease states and further compared with age-matched WT littermates. Different brain regions were assessed, comprising tissue from cortex and cerebellum. After separation of brain homogenates into crude cytosolic and membrane fractions, $Ca_V2.2$ was only quantifiable in the membrane fraction (data not shown). Analysis of relative protein levels of $Ca_V2.2$, normalized to total protein content, revealed a non-significant upregulation of $Ca_V2.2$ in the cortex of mice compared with WT mice during early disease progression states at 15 and 21 months of age (1.18-fold, 1.21-fold) (Fig. 3.1). During later disease stages, a significant approximately 2-fold upregulation of normalized $Ca_V2.2$ protein levels is observed compared to protein levels in younger animals. Furthermore, a significant 2.12-fold increase in the $Ca_V2.2$ protein levels in the cortex of $APP_{swe}/PSEN1^{\Delta E9}$ mice compared with age-matched WT animals was found. In contrast, only a slight non-significant trend towards increased $Ca_V2.2$ protein levels was observed in the cerebellum of $APP_{swe}/PSEN1^{\Delta E9}$ mice compared with WT animals. Remarkably, this trend did not change with regard to disease progression. Taken together, this data suggests an upregulation in membrane-associated $Ca_V2.2$ levels, which is positively correlated with disease progression in the cortex, but not the cerebellum of a mouse model of AD.

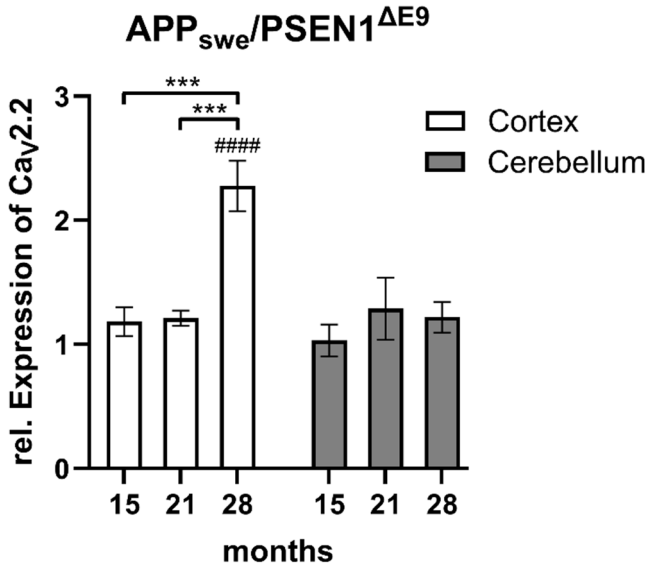

Figure 3.1: $Ca_V2.2$ protein levels in the brain of $APP_{swe}/PSEN1^{\Delta E9}$ mice Semi-quantitative western blotting analysis of $Ca_V2.2$ protein content in crude membrane fractions from cortex and cerebellum of 15, 21 and 28 months old $APP_{swe}/PSEN1^{\Delta E9}$ mice, analyzed with specific α-$Ca_V2.2$ antibodies. Histograms show the respective densitometry analysis of $Ca_V2.2$ protein bands, normalized to total protein levels presented as relative expression in the AD mouse model normalized to WT control. Data presented as mean ± SEM from at least n = 6 animals, analyzed per age group and genotype. Statistical analysis was performed using one-way ANOVA followed by Tukey's post-hoc test with * $p < 0.05$, ** $p < 0.01$, *** $p < 0.001$ vs. indicated age and $^{\#}$ $p < 0.05$, $^{\#\#}$ $p < 0.01$, $^{\#\#\#}$ $p < 0.001$, $^{\#\#\#\#}$ $p < 0.0001$ vs. WT.

3.1.1 Increased $Ca_V2.2$ Levels in an AD Mouse Model Are Sex-Dependent

Although both female and male AD model $APP_{swe}/PSEN1^{\Delta E9}$ mice show behavioral implications, the disease-associated phenotype, especially with regard to cognitive deficits, was previously reported to be associated with sex (Hulshof, Frajmund et al. 2022). For this reason, the data was further analyzed, taking the animals' sex into account. Interestingly, a significant age-dependent upregulation of $Ca_V2.2$ protein levels was only observed in the cortex of male AD mice (Fig. 3.2, A). At early disease stages, no significant difference in $Ca_V2.2$ levels could be observed between male AD and WT mice, although a non-significant trend towards upregulation (1.25-fold) could be seen at an age of 21 months. Old-aged male AD mice show extensive and significant upregulation compared with younger animals and age-matched WT mice of about 2.33-fold. In contrast, female AD mice only show a slight upregulation of $Ca_V2.2$ protein levels, which is mostly stable during disease progression. At an age of 28 months, female AD mice show a slight, non-significant upregulation of $Ca_V2.2$ levels compared with younger animals or age-matched WT mice. In contrast, $Ca_V2.2$ protein levels in the cerebellum were observed to be unaffected by disease and respective disease progression (Fig. 3.2, B). No significant trend in differentially regulated $Ca_V2.2$ levels could be seen in the cerebellum of female or male $APP_{swe}/PSEN1^{\Delta E9}$ versus WT mice at any age.

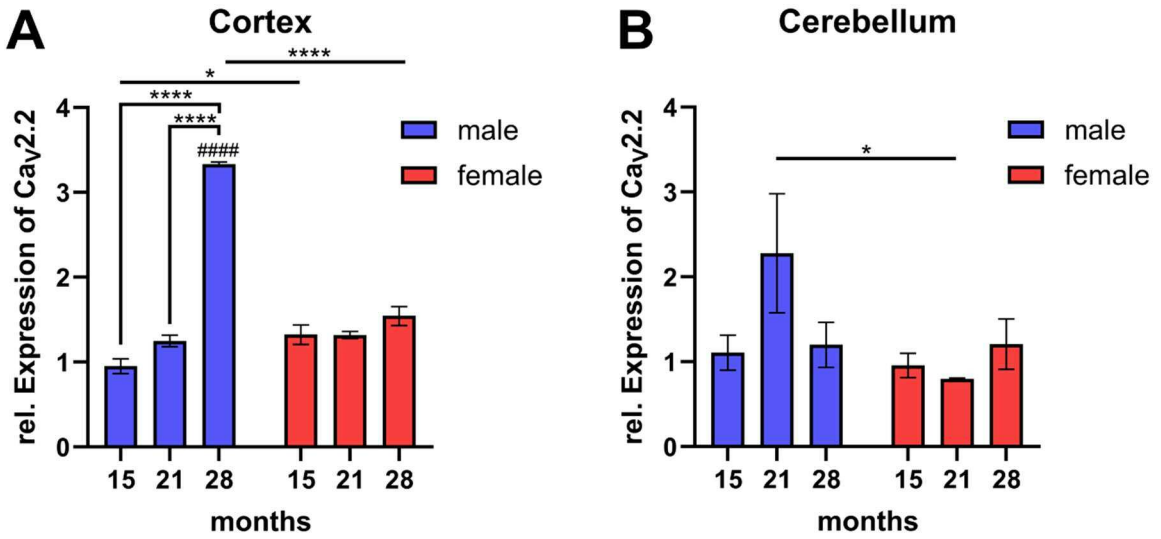

Figure 3.2: $Ca_V2.2$ protein levels in different brain regions of male and female $APP_{swe}/PSEN1^{\Delta E9}$ mice
Semi-quantitative western blotting analysis of $Ca_V2.2$ protein levels in crude membrane fractions of cortices (**A**) and cerebellum (**B**) of 15-, 21- and 28-months aged male and female $APP_{swe}/PSEN1^{\Delta E9}$ mice and age-matched WT littermates were performed using specific α-$Ca_V2.2$ antibodies. Histograms show the respective densitometry analysis of $Ca_V2.2$ protein bands, normalized to total protein levels presented as relative expression to WT mice and compared with regard to sex. Data presented as mean ± SEM. Samples from at least n = 3 animals have been analyzed per age group, sex and genotype. Statistical analysis was performed using two-way ANOVA followed by Bonferroni's post-hoc test with * $p < 0.05$, ** $p < 0.01$, *** $p < 0.001$ and **** $p < 0.0001$ vs. indicated age or sex and one-way ANOVA followed by Tukey's post-hoc test with $^{\#}$ $p < 0.05$, $^{\#\#}$ $p < 0.01$, $^{\#\#\#}$ $p < 0.001$, $^{\#\#\#\#}$ $p < 0.0001$ vs. WT.

3.2 Transient Transfection and Expression of $Ca_V2.2$

3.2.1 Optimization of Transient Transfection of $Ca_V2.2$

For expression of $Ca_V2.2$ channels in a mammalian expression system, HEK293T cells were transiently transfected with plasmids encoding α_1-, β_3- and $\alpha_2\delta_1$-subunits of $Ca_V2.2$ channels. The best transfection strategy was identified based on transfection efficiency, expression levels and subcellular distribution of $Ca_V2.2$ with regard to specific membrane or cytosolic localization. For the transfection, lipofection was chosen, previously determined as the method gaining highest transfection efficiency, and the transfection protocol was further optimized with regard to the concentration of the transfection reagent as well as the ratio between the different co-transfected plasmids encoding the α_1-subunit and auxiliary subunits of $Ca_V2.2$ channels. Cells were observed to be healthy after transient transfection and immunofluorescent staining revealed successful expression of $Ca_V2.2$ with an evident primary localization in the plasma membrane of cells. The transfection efficiency was observed to be modestly low (approximately 20% to 30% of cells), but differed greatly with regard to transfection conditions (Fig. 3.3).

In general, a higher concentration of transfection reagent was observed to result in higher transfection and $Ca_V2.2$ expression levels and greater channel density in the plasma membrane (Fig. 3.3, A). As immunofluorescent staining of $Ca_V2.2$ in transiently transfected cells may result in differences in fluorescent intensity between each condition due to unspecific binding or cell-autofluorescence, rendering a semi-quantitative comparison ineffective, the expression levels of $Ca_V2.2$ were further confirmed in an analysis via western blots of cell lysate of respectively transfected cells, separated in crude cytosolic and membrane fractions (Fig. 3.3, B). $Ca_V2.2$ was only present in the crude membrane fraction, whereas no signal could be found in the cytosolic fraction of total cell lysates. A semi-quantitative comparison revealed increased $Ca_V2.2$ expression levels in cells transfected with higher concentrations of transfection reagent.

Furthermore, a strong effect of the ratio between the plasmids encoding for different subunits in the transfection sample was observed. In the literature, a ratio of 3:2:2 (α_{1B} : β_3 : $\alpha_2\delta_1$) was previously reported to gain sufficient and optimal transfection and expression efficiency (Cassidy, Ferron et al. 2014; Dahimene, Page et al. 2024). However, results presented in this study show a positive correlation of higher expression levels of $Ca_V2.2$ with increasing concentrations of auxiliary subunits. The transfection efficiency and $Ca_V2.2$ cellular expression was higher in cells transfected at a ratio of 1:1:1 (α_{1B} : β_3 : $\alpha_2\delta_1$), compared with cells transfected at other ratios (Fig. 3.3, A). This was further confirmed in western blot analysis, where the overall $Ca_V2.2$ protein level was dependent on the plasmid ratio, reaching a maximum at a ratio of 1:1:1 using high concentrations of transfection reagent (Fig 3.3 B). In addition, a similar effect was observed at ratios with higher levels of plasmid encoding for the β_3-subunit. Overall, expression levels were positively correlated with a higher ratio of plasmids encoding auxiliary subunits to the plasmid encoding the α_1-subunit of $Ca_V2.2$ channels. Although western blot analysis revealed similar overall protein levels compared to transfection with lower concentration of plasmid encoding β_3-subunit, a higher transfection efficiency and higher $Ca_V2.2$ channel density in the membrane was observed in cells transfected with a ratio of 1:1:1 and 1:2:1 (Fig. 3.3).

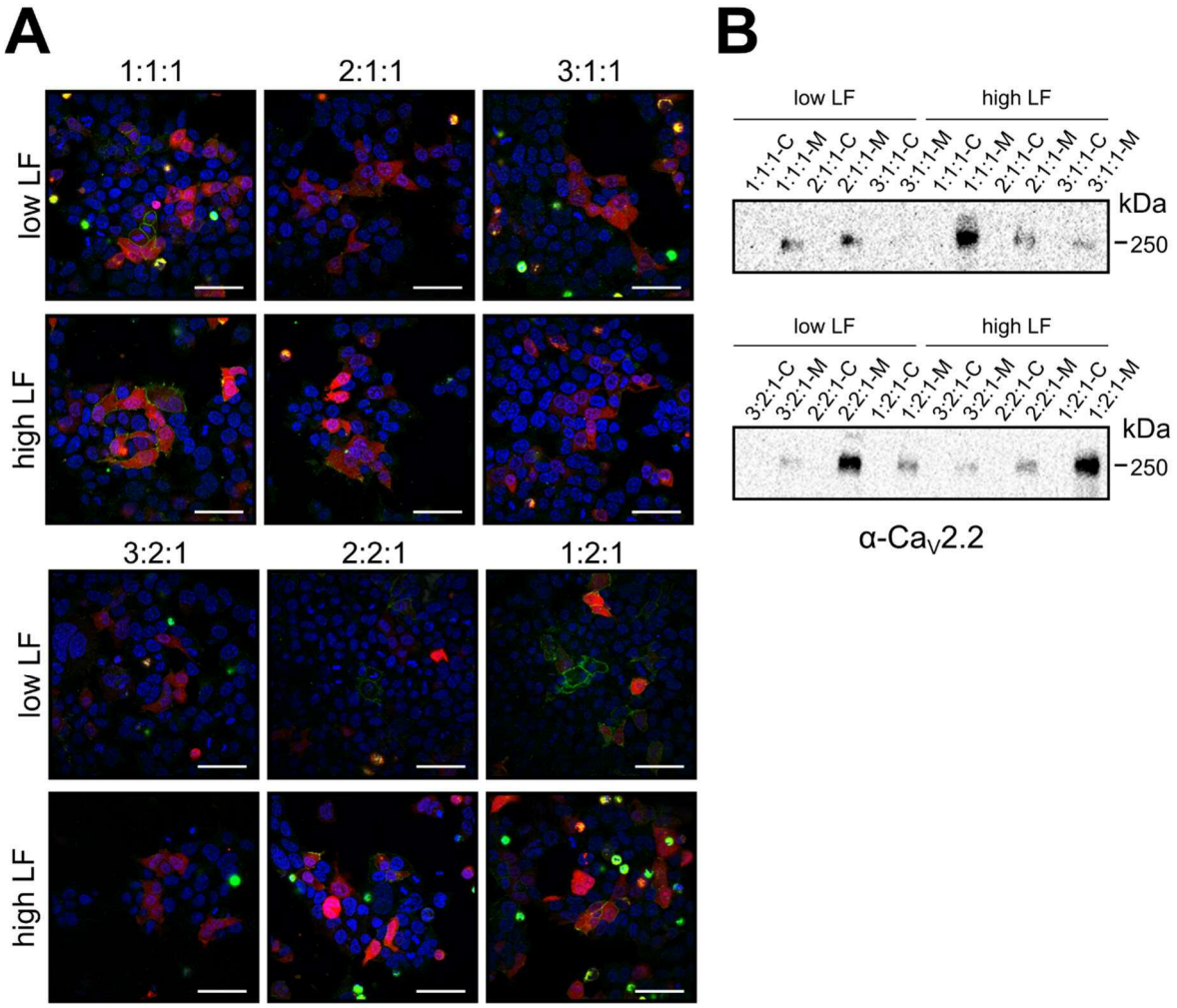

Figure 3.3: Expression of $Ca_V2.2$ in transiently transfected HEK293T cells HEK293T cells were transfected with lipofectamine (LF) at low or high concentrations. Plasmids encoding α_{1B}-, β_3- and $\alpha_2\delta_1$-subunits were used for transfection at different ratios (α_{1B} : β_3 : $\alpha_2\delta_1$). **A** Representative confocal images of immunofluorescent labeling of $Ca_V2.2$ (green) after transfection of cells with different ratios of subunit-encoding plasmids and different concentrations of LF. β_3-subunits are labeled with mCherry (red) and cell nuclei are stained with DAPI (blue). Scale bar represents 50 µm. **B** Western blots of cell lysate from respectively transiently transfected HEK293T cells, separated into crude cytosolic (C) and membrane (M) fractions. Membranes were stained against $Ca_V2.2$ using specific antibodies.

3.2.2 Transient Expression of Fluorescently Labeled $Ca_V2.2$

For *in vitro* live imaging approaches, as well as for electrophysiological experiments, it was of high interest to generate cells expressing fluorescently labeled $Ca_V2.2$ channels. Transient transfections of a plasmid encoding for the $Ca_V2.2$ α_1-subunit, C-terminally fused to a fluorescent EGFP-tag, alongside auxiliary subunits, were performed according to previously optimized transfection strategies. A positive control using only EGFP-expressing plasmids for transfection, as well as a negative control with untransfected cells was included to verify results.

The transfection efficiency and $Ca_V2.2$ expression level in transiently transfected HEK293T cells were observed to be analogous to experiments with cells transfected with a plasmid encoding the α_{1B}-subunit without any tags (see 3.2.1). The subcellular localization of EGFP-tagged $Ca_V2.2$ channels was predominantly observed in outer regions of the cell, most probably incorporated into the cell plasma membrane (Fig. 3.4, A). Nevertheless, it was noted that a fraction of the expressed $Ca_V2.2$ channels exhibited localization within the cytosol, where they were observed to be arranged in distinct foci. In contrast to this, cells solely expressing the EGFP tag display a more homogenous signal throughout the cytosol, lacking any notable localization of the signal in the plasma membrane or foci organization within the cytoplasm (Fig. 3.4, B). No autofluorescence of the cell was detected, verified in the negative control, staining only for cell nuclei using DAPI (Fig. 3.4, C).

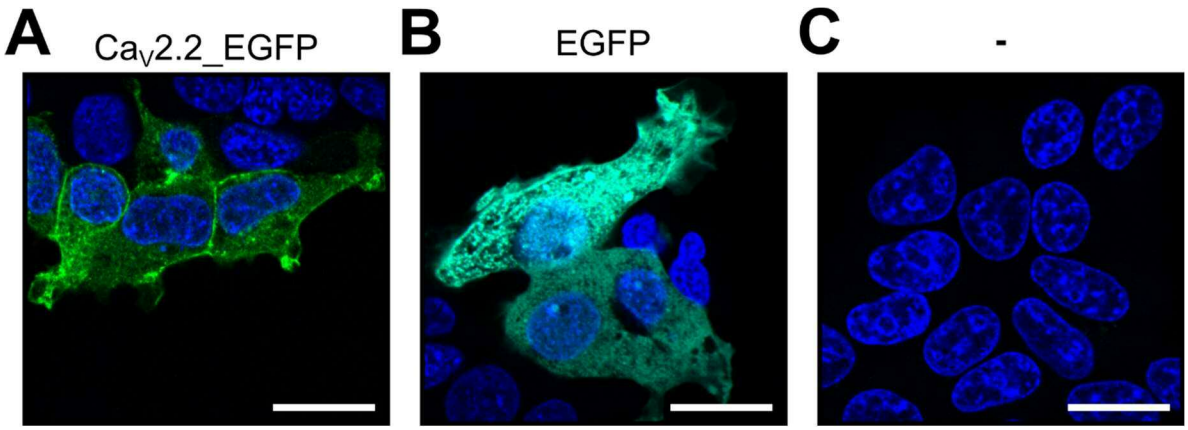

Figure 3.4: Expression of fluorescently labeled $Ca_V2.2$ in transiently transfected HEK293T cells
A HEK293T cells transiently transfected with $Ca_V2.2$ α_1-subunits, expressed as a fusion protein with a C-terminal EGFP-tag (green), co-transfected with auxiliary subunits. Cell nuclei stained with DAPI post-fixation (blue). Positive controls (**B**), showing HEK293T expressing EGFP alone and negative controls (**C**) without transfection were included. Scale bar represents 20 µm.

3.2.3 Subcellular Localization of Transiently Expressed $Ca_V2.2$

Transient transfection of HEK293T with native $Ca_V2.2$ as well as fluorescently labeled $Ca_V2.2$ resulted in expression of $Ca_V2.2$ channels with a subcellular distribution that may resemble a plasma membrane ring (see Fig. 3.3, A, and Fig. 3.4, A). To ensure that transiently expressed $Ca_V2.2$ channels are in fact localized and incorporated as integral membrane proteins in the plasma membrane of HEK293T cells, the fluorescent lipophilic dye CellMask was used for plasma membrane labeling to analyze the subcellular localization of $Ca_V2.2$ channels. Staining of cells with membrane-labeling dye resulted in a signal showing a cell-surrounding ring, which resembles the plasma membrane (Fig. 3.5, A). A similar localization was observed for EGPF-tagged $Ca_V2.2$ channels. Only markedly low

levels of $Ca_V2.2$-EGFP signal were found in the cytoplasm. Nevertheless, only a small fraction of the signals was found to co-localize with labeled membrane regions with a respective Pearson's correlation coefficient (PCC) of r = 0.77 and an overlap of the signal of around 40%. Although the lack of co-localization of the signals, a correlation in distribution was found. Analyzing the signal intensity of membrane labeling and $Ca_V2.2$-EGFP, while following a certain path at a region of interest (Fig. 3.5, B), revealed a similar pattern of subcellular localization. In general, the subcellular localization of $Ca_V2.2$ channels correlated with the structure of the plasma membrane, further showing a stronger localization toward the cytoplasm. However, there was only minimal signal observed in the cytoplasm itself (Fig. 3.5, C).

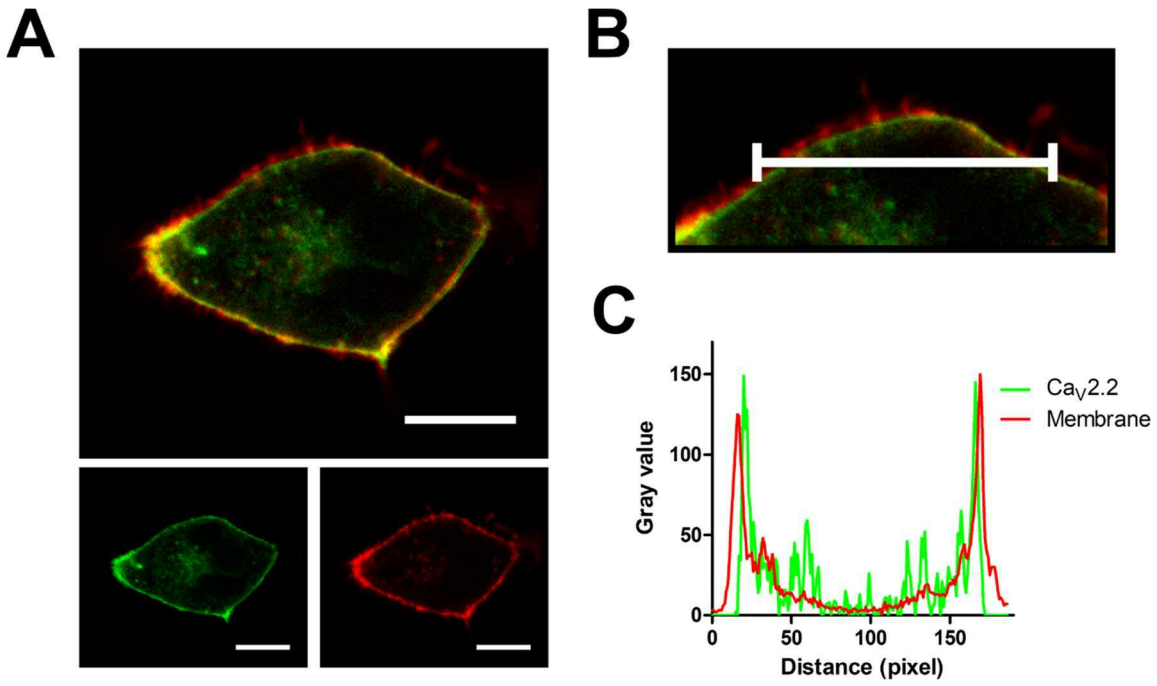

Figure 3.5: Subcellular localization of $Ca_V2.2$ in transiently transfected HEK293 cells A Transiently expressed $Ca_V2.2$-EGFP (green) was found localized in a subcellular distribution similar to staining of the plasma membrane (red), although only small fractions of the signals were observed to co-localize (yellow). Scale bar represents 10 µm. **B** A ROI was chosen to follow the expression pattern of $Ca_V2.2$ along a path following membrane - cytosol - membrane. **C** Analysis of the signal intensity along the ROI-path revealed correlation in signal distribution and $Ca_V2.2$ signals were predominantly found localized in close proximity to the membrane, with a slight shift towards a cytoplasmic localization.

3.2.4 Co-Localization of RD2 with $Ca_V2.2$ in Transiently Transfected Cells

Previous data suggests a direct binding of the compound RD2 to $Ca_V2.2$ channels, as it was effective in competing against ω-CgTx in a competitive binding assay (Kutzsche, Guzman et al. 2023). Furthermore, a direct inhibitory effect of RD2 on $Ca_V2.2$-dependent Ca^{2+} currents was observed in electrophysiological experiments. As transient expression of $Ca_V2.2$-EGFP constructs, co-transfected with auxiliary subunits β_3 and $\alpha_2\delta_1$, was observed to result in integration of functional $Ca_V2.2$ channels in the membrane, it was of interest to analyze if the compound RD2 is able to bind $Ca_V2.2$ channels under *in vitro* conditions in transiently transfected HEK293T cells.

In vitro association of fluorescently labeled RD2 was allowed for 1 h in HEK293T cells, transiently expressing $Ca_V2.2$-EGFP. After fixation, nuclei were stained using DAPI and images were acquired using confocal laser scanning microscopy. As previously reported, only approximately 20% to 30% of the HEK293T cells were successfully transfected and showed expression of $Ca_V2.2$ with respective integration of the channel in the plasma membrane. RD2 was observed to be localized within all cells, regardless of their transfection state. The predominant distribution of RD2 was observed to be localized in the cytoplasm of the cell (Fig. 3.6, A). No significant co-localization of RD2 with $Ca_V2.2$ was found. However, in cells with high $Ca_V2.2$ channel plasma membrane density, a comparable distribution was evident for RD2 (Fig. 3.6, B), contrasting with the absence of this pattern for cells labeled with the fluorescent label alone (data not shown). These cells, compared with untransfected cells, show increased localization of RD2 in regions of the plasma membrane and a smaller level of localization in the cytosol (Fig. 3.6, C). Despite the absence of significant results that could verify co-localization of RD2 with transiently expressed $Ca_V2.2$ channels in a mammalian cell model, a trend for consistent distribution of both components along the cross-section path of the cell suggests a potential association of RD2 and $Ca_V2.2$ in this *in vitro* model.

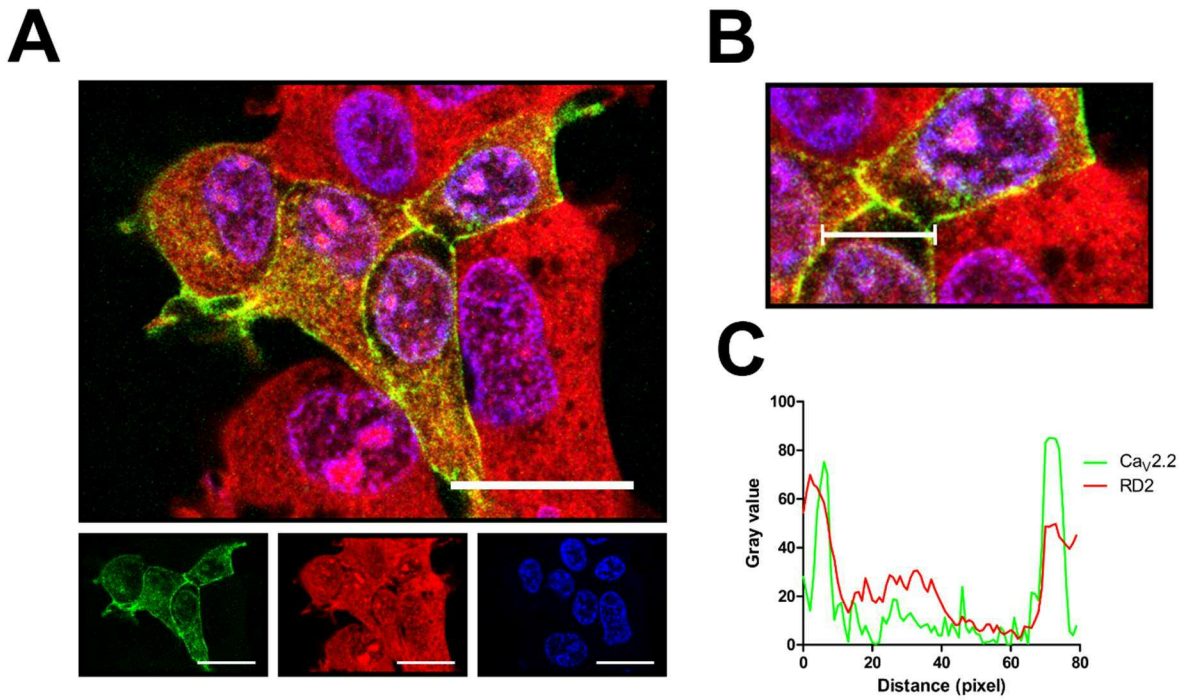

Figure 3.6: Co-localization analysis of RD2 with Cav2.2 in transiently transfected HEK293T cells A Cells expressing Cav2.2-EGFP (green) were incubated with fluorescently labeled RD2 (red) pre-fixation to analyze potential co-localization. Cell nuclei were additionally labeled with DAPI (blue). Scale bar represents 20 µm. **B** A ROI was chosen following the localization pattern of Cav2.2 and RD2 along a path spanning membrane - cytosol - membrane regions. **C** Analysis of the signal intensity along the ROI-path revealed a tendency towards correlation in signal distribution.

3.3 Purification of Cav2.2 Channels

We could previously show that transiently as well as stably transfected mammalian cells express Cav2.2 channels with a predominant localization in the plasma membrane. In additional electrophysiological experiment, these channels were further observed to be functional, assuming a native three-dimensional structure. For subsequent binding analysis of Cav2.2-inhibiting compounds as well as subsequent lead compound optimization it is crucial to establish a suitable method for purification of Cav2.2 channels from mammalian expression systems while retaining the native three-dimensional structure. Working with purified proteins instead of crude protein extract will diminish unspecific binding mediated by other components present. So far, no method was established for purification of Cav2.2 channels based on their biophysical and biochemical properties, giving the necessity for the establishment of a suitable protocol.

3.3.1 Optimization of Cell Lysis and Protein Solubilization

As a first step, the optimal method for cell lysis and subsequent protein solubilization in detergent-containing buffer was assessed by conducting a series of experimental tests and subsequently analyzing the final level of solubilized $Ca_V2.2$ protein content in each sample. Cells were either lysed by osmotic shock, via sonication or by membrane disruption through incubating cells on ice in a detergent-containing buffer. Generated cell lysates were either used as whole cell lysates or membrane fractions were separated as insoluble fractions from aqueous buffers via ultracentrifugation. Solubilization was performed in the respective buffer system containing a combination of suitable detergents. Furthermore, solubilization was optimized with regard to incubation time.

For comparison of the efficiency of different lysis and solubilization methods, western blot analysis was performed, using an anti-$Ca_V2.2$ antibody to visualize solubilized $Ca_V2.2$ protein levels (Fig. 3.7).

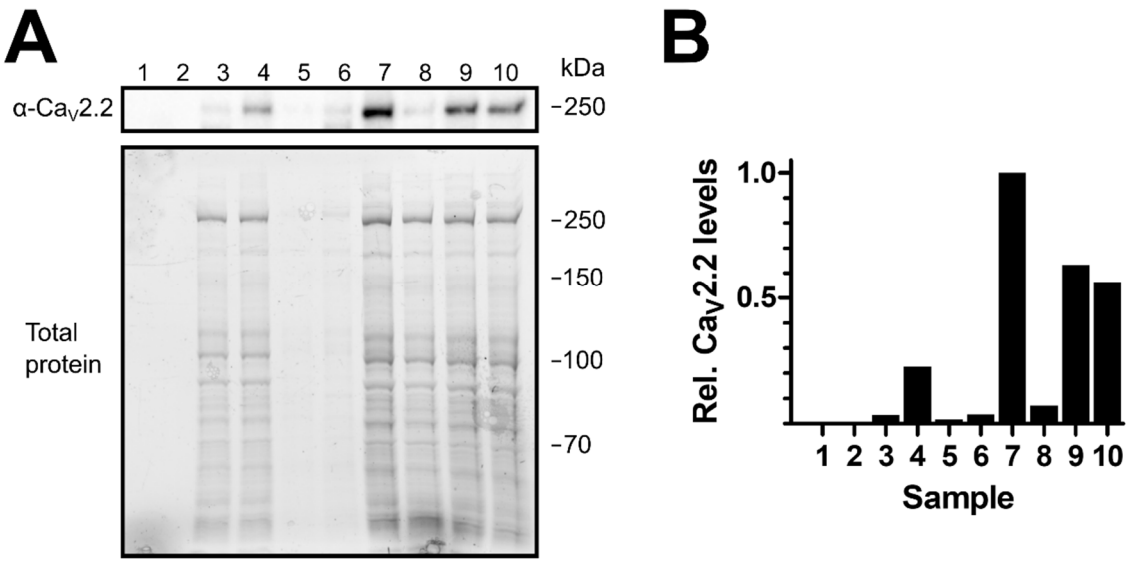

Figure 3.7: $Ca_V2.2$ protein levels during cell lysis and solubilization optimization A Total protein levels as analyzed via SDS-PAGE (lower panel) and immunostaining-based visualization of $Ca_V2.2$ (upper panel) of samples, generated with different cell lysis and solubilization protocols. Samples 1-4 were lysed by osmotic shock, 5-8 by sonication and samples 9 and 10 were lysed by a detergent-based approach. Samples were either solubilized as whole cell lysates (3, 4, 7, 8, 9, 10) or as previously separated membrane fractions (1, 2, 5, 6) and subsequently either solubilized for 2 h (1, 3, 5, 7, 9) or overnight (2, 4, 6, 8, 10). **B** Relative quantification of total $Ca_V2.2$ protein levels after solubilization, normalized to sample 7.

$Ca_V2.2$-specific content was detected in most of the samples after solubilization, but a substantial difference in the amount of solubilized protein could be observed with regard to the underlying cell lysis and solubilization method. In general, solubilization of whole cell lysates showed higher final $Ca_V2.2$ solubilization levels, compared with solubilization of initially separated membrane fractions only. Separation of crude membrane fractions from crude cytosolic fractions was achieved by ultracentrifugation, followed by resuspension of pellets in detergent-containing buffer in order to achieve solubilization. By this, the overall protein concentration was drastically reduced as evidenced by visualization of total proteins after SDS-PAGE. Furthermore, this was accompanied by a similar reduction in final protein levels of solubilized $Ca_V2.2$. In fact, no $Ca_V2.2$-specific signal was observed after solubilization of separated crude membrane fractions in cell samples lysed by osmotic shock (Fig. 3.7, A, samples 1 and 2) and only low levels could be seen for crude membrane fractions of sonication-generated cell lysates (Fig. 3.7, A, samples 5 and 6). In contrast to this, solubilized $Ca_V2.2$ protein was detected in all samples when different cell lysis methods were used, specifically when solubilization was carried out on whole cell lysates. However, cell lysis by osmotic shock resulted in lower $Ca_V2.2$ protein levels after solubilization compared with other lysis methods. Only around 23% of the maximal signal of $Ca_V2.2$ protein levels was found after solubilization of osmotic shock-derived whole cell lysates with detergents overnight (Fig. 3.7, sample 4). For this lysis and solubilization approach, solubilization time increased the solubilization levels of $Ca_V2.2$. In contrast to this, 2 h of solubilization of whole cell lysates, generated by sonication, was observed to be most effective in $Ca_V2.2$ solubilization, as the highest $Ca_V2.2$-specific signal could be reported (Fig. 3.7, sample 7). Interestingly, a contrary effect for solubilization time was observed, reducing the relative protein level of solubilized $Ca_V2.2$ by about 90% when incubating overnight (Fig. 3.7, sample 8). A combination of detergent-based cell lysis with whole cell lysate solubilization was additionally observed to be efficient for $Ca_V2.2$ protein extraction and solubilization. In comparison to the protocol determined to be most efficient, this method led to a reduction of approximately 40% in final $Ca_V2.2$ protein levels, while showing lower sensitivity to solubilization time (Fig. 3.7, sample 8 and 9).

Overall, despite the effectiveness of several methods in cell lysis and subsequent $Ca_V2.2$ solubilization, comparative relative quantification demonstrated highest total protein levels and specific $Ca_V2.2$ solubilization following cell lysis through sonication and solubilization of whole-cell lysates in detergent-supplemented buffer for 2 h.

3.3.2 Purification of $Ca_V2.2$ Using Individual Purification Approaches

Purification of $Ca_V2.2$ was assessed with regard to separation based on different biochemical and biophysical properties. For this, different purification approaches were tested for efficiency and effectiveness in separating $Ca_V2.2$ from complex samples.

3.3.2.1 Purification of $Ca_V2.2$ via Size Exclusion Chromatography

Crude membrane fractions of cell lysates, containing solubilized $Ca_V2.2$ protein, were purified with regard to the overall size of proteins and macromolecular complexes via SEC using an HPLC as well as an FPLC system. Fractions were collected and analyzed with regard to their total protein content and specific $Ca_V2.2$ content.

Chromatograms of elution profiles of SEC on an HPLC system acquired at 214 nm or 280 nm showed a similar course and protein retention times varied greatly across the run, showing elution of proteins between 5 min and 15 min after injection (Fig. 3.8, A). Using a protein standard of known molecular weight, a retention time of 7 min was determined for proteins of molecular weight in the range of 250 kDa, whereas proteins with an overall size of over 300 kDa were observed to elute already after 5 min. For this reason, fractionation of the elution was started after a retention time of 4 min and continued for the following 6 min. With regard to the total protein content, a clear separation, dependent on the protein size, was found distributed over consecutive fractions. Earlier fractions contained proteins of higher molecular weight, whereas smaller proteins showed an increased retention time. Although a separation effect was observed, elution fractions continued to contain a diversity of proteins as detected in SDS-PAGE analysis (Fig. 3.8, B). Analysis of the $Ca_V2.2$-specific retention time and distribution across different elution fractions revealed a peak of $Ca_V2.2$-specific content in fraction 3 with a respective retention time of 5 min to 5.5 min. In addition, the neighboring fraction 4 also contained a significant amount of $Ca_V2.2$ protein. Furthermore, in fractions 2 to 7 minor levels of $Ca_V2.2$ were detectable. Consistent with prior findings, the $Ca_V2.2$ antibody did not only stain protein components with an associated molecular weight of 250 kDa, but further resulted in signals corresponding to proteins of lower molecular weight. Notably, SEC effectively resolved distinct anti-$Ca_V2.2$ antibody-responsive proteins, with only the 250 kDa signal present in fraction 3 (Appendix Fig. I.4). Furthermore, an analysis was conducted, assessing the stability of $Ca_V2.2$ during a preceded concentration process of the cell lysate sample to further determine whether this step could increase the $Ca_V2.2$ protein yield in the respective fractions after SEC. Equal final volumes of the same protein sample from crude membrane fractions of cell

lysates were either applied as is or previously concentrated four-fold in Amicon Ultra-0.5 Centrifugal Filter Units (Merck) using a cut-off of 100 kDa for separation of smaller proteins. Similar elution profiles were observed for both samples between retention times of 5 min and 10 min, but only unconcentrated samples show an additional peak of elution at approximately 12 min retention time (Fig. 3.8, C). Furthermore, an overall higher signal was observed for concentrated compared with unconcentrated samples. A comparable total protein distribution was found in the respective elution fractions with similar tendency to increased overall protein concentration for concentrated samples (Fig. 3.8, D). Furthermore, $Ca_V2.2$-specific signals were found in a similar distribution across the fractions showing a peak in signal in fraction 3 as well as lower $Ca_V2.2$ protein content in fractions 2 to 6. Relative quantitative analysis of the $Ca_V2.2$-specific signal revealed an increase in intensity by a factor of approximately 5.5-fold in fractions 3 of concentrated samples compared with the respective elution fraction from SEC of unconcentrated cell lysates.

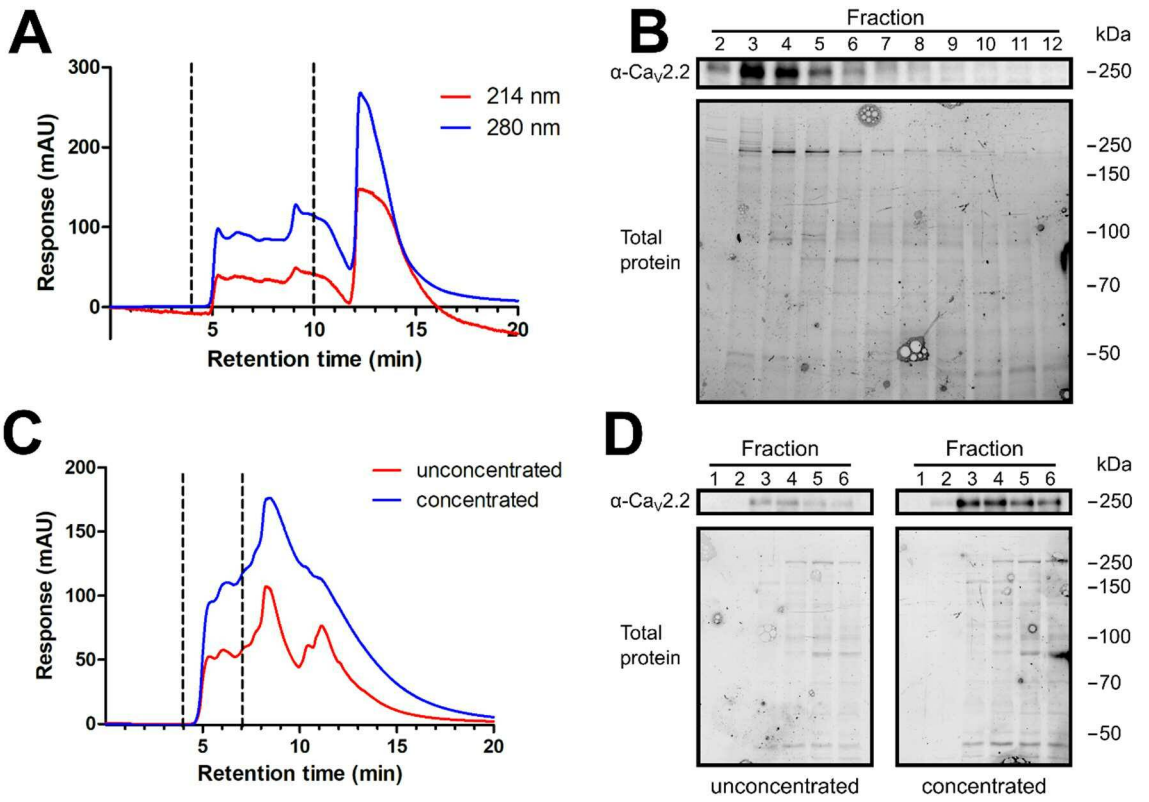

Figure 3.8: Purification of $Ca_V2.2$ via size exclusion chromatography on an HPLC system **A** Chromatogram of the elution profile of proteins acquired at 214 nm and 280 nm with respective 0.5 min fractionation between 4 min and 10 min (dashed line). **B** Elution fractions were analyzed via SDS-PAGE for total protein content (lower panel) and immunostaining of western blots shows $Ca_V2.2$-specific distribution across the elution fractions (upper panel). **C** Chromatogram of the elution profile of proteins from total cell lysate and concentrated cell lysate, as acquired at 280 nm. **D** Respective elution fractions of 0.5 min were analyzed via SDS-PAGE for unconcentrated (left) and concentrated (right) samples for total protein content (lower panel) and immunostaining of western blots showing $Ca_V2.2$-specific distribution (upper panel).

In addition, purification of $Ca_V2.2$ was performed by SEC on an FPLC system to potentially improve the separation efficiency by using a column with larger column volume. Elution fractions were collected and analyzed with regard to their total protein content, visualized in SDS-PAGE, and specific $Ca_V2.2$ content by immunostaining of western blots (Fig. 3.9).

Chromatograms were acquired at 214 nm and 280 nm and a variety of elution peaks was observed between 16 min and 52 min after sample injection. Respective fractions of 0.5 min were collected and analyzed. A diversity of proteins was found in the sample, whereby the distribution of proteins across the fractions was overall changing in relation to protein size. A distinct size-dependent separation was found across early to later elution fractions. Later fractions, after 20 mL elution volume, did not contain significant levels of protein within the analyzed size range of 50 kDa to 250 kDa. By conducting $Ca_V2.2$-specific immunostaining on western blots, $Ca_V2.2$ was detected at an elution volume ranging from 9 mL to 12 mL, with a peak concentration in fraction 21 after 10.5 mL elution volume. Nevertheless, the separation of various proteins responsive to anti-$Ca_V2.2$ antibodies was not achieved using this method (Appendix Fig. I.5). In fraction 21, where the $Ca_V2.2$-specific signal at 250 kDa was present, a variety of other signals was detected at lower corresponding molecular weight.

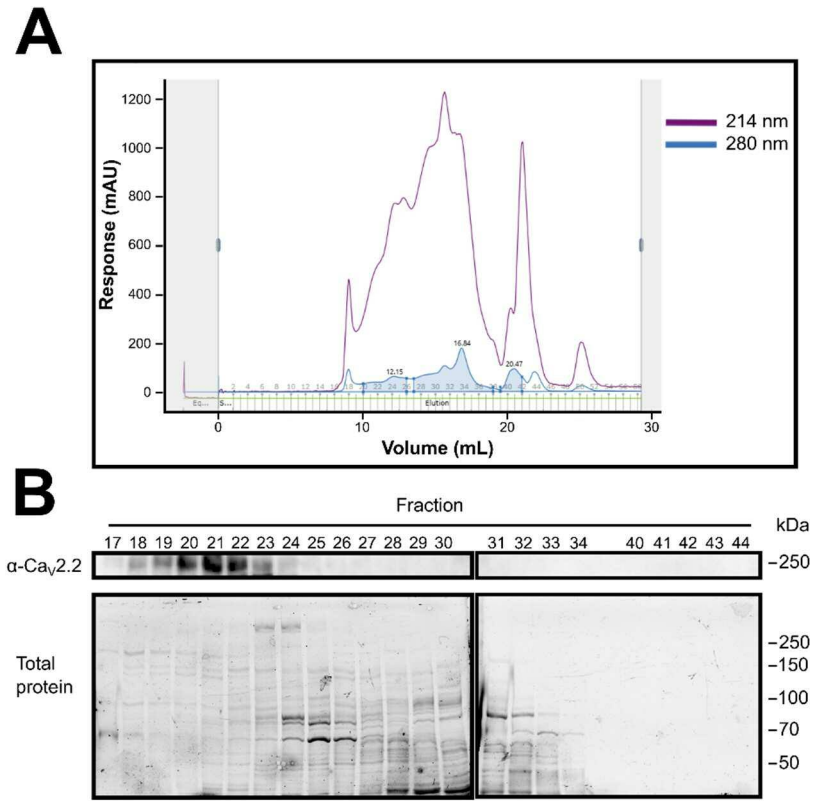

Figure 3.9: Purification of $Ca_V2.2$ via size exclusion chromatography on an FPLC system **A** Chromatogram of the elution profile of proteins acquired at 214 nm and 280 nm, with respective 0.5 min fractionation (indicated by grey lines). **B** Elution fractions were analyzed via SDS-PAGE for total protein content (lower panel) and immunostaining of western blots shows $Ca_V2.2$-specific distribution (upper panel).

3.3.2.2 Purification of $Ca_V2.2$ via Ion Exchange Chromatography

The goal was to purify $Ca_V2.2$ from a complex protein mixture based on its net charge and pI using IEX. As the pH of the running buffer was lower than the expected pI of $Ca_V2.2$, a CIEX column was selected for the purification process. Elution from the column was performed by gradually increasing the pH of the buffer to more alkaline values. Chromatograms, acquired at 260 nm and 280 nm, revealed that the majority of proteins was present in the flow-through, as indicted by the initial peak in the chromatogram (Fig. 3.10, A). Only minor signal peaks were detected in the early fractions during the elution process. Analysis of the overall protein composition of flow-through fraction 2 revealed a similar protein composition to that of the input fraction. Nevertheless, $Ca_V2.2$-specific analysis revealed only low levels of $Ca_V2.2$ in fraction 2, compared to protein levels in the input fraction. No other fractions at the beginning of the elution process showed any $Ca_V2.2$-specific signals. Furthermore, in elution fractions spanning the pH range that correlates with the expected pI of $Ca_V2.2$, no signals for total protein or $Ca_V2.2$-specific signals could be detected. In addition, other proteins of lower molecular weight, observed to be reactive to the $Ca_V2.2$ antibody, were only present in early elution fractions 2 to 6 but no efficient separation from $Ca_V2.2$ was evident (Appendix Fig. I.6).

As no initial binding of $Ca_V2.2$ was observed after application to a CIEX column in a buffer at pH 7.4, an additional purification approach using AIEX was tested. Purification of $Ca_V2.2$ through AIEX with elution using a salt gradient produced a different outcome compared with CIEX. The chromatogram revealed two main peak areas of total protein signal, one in early fractions, resembling the unbound protein in the flow-through (fractions 4-7), and one area with several peaks in early fractions (27-35) of elution (Fig. 3.10, C). In fact, analysis of the protein composition in the respective fractions revealed a complex mixture of proteins present in each fraction. The overall composition was considerably different between the flow-through and the elution fractions, and slightly differed between consecutive fractions (Fig. 3.10, D). A $Ca_V2.2$-specific signal at a height corresponding to approximately 250 kDa was found in high intensity in the input fraction. After purification, only marginal quantities of $Ca_V2.2$ were found in the flow-through fraction, with the highest intensity in fraction 6. The remaining $Ca_V2.2$ content was observed to be eluted early on in the gradient, showing highest signal intensities in fractions 29 and 30. The overall protein composition of this fractions showed a variety of other proteins present in the sample, whereby the complexity and total concentration is markedly reduced compared with the input fraction (Fig. 3.10, D).

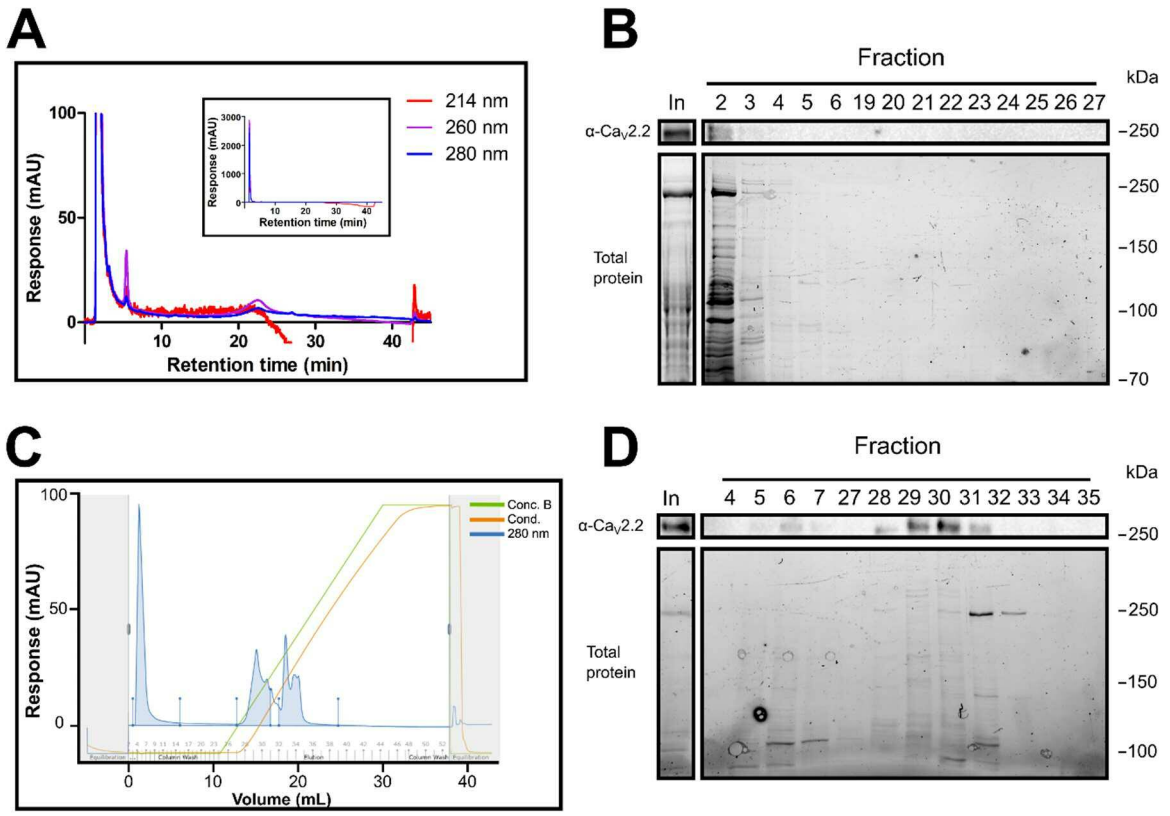

Figure 3.10: Purification of CaV2.2 via ion exchange chromatography A Chromatogram of the elution profile of proteins in CIEX via change in pH as acquired at 214 nm, 260 nm and 280 nm, as overall view (insert) and zoomed-in version. **B** Input (In), as well as flow-through (2-6) and interesting elution fractions (19-27) of 0.5 min were analyzed via SDS-PAGE for total protein content (lower panel) and immunostaining of western blots shows CaV2.2-specific distribution across the elution fractions (upper panel). **C** Chromatogram of the profile of proteins eluted from AIEX column by increasing the ionic strength of the buffer (green) as acquired at 280 nm (blue). **D** Input (In), as well as flow-through (4-7) and elution fractions of 1 min (27-35) were analyzed via SDS-PAGE for total protein content (lower panel) and immunostaining of western blots shows CaV2.2-specific distribution across the elution fractions (upper panel).

In addition to column-based IEX, purification of CaV2.2 was further tested in batch-mode using different IEX matrix beads. The beads comprised different matrix material with weak and strong anion or cation exchange capability. Analysis of the input fractions showed overall complex protein samples with high concentration of CaV2.2 as evidenced by immunostaining with anti-CaV2.2 antibodies resulting in a signal at a corresponding height of 250 kDa. The use of sepharose-beads with quaternary ammonium as strong anion exchange surface (Q-sepharose) achieved minor separation of proteins through elution as evidenced by total protein staining (Fig. 3.11, A). While most of the proteins in the input sample did not bind to the column and were eluted in the unbound fraction, several distinctive bands were eluted at varying low concentration of buffer B as the ionic strength increased. The overall protein composition differed between the elution fractions across the gradient. Nevertheless, no CaV2.2-specific signal was found in any elution fraction, as all of the CaV2.2 protein content was observed to be present in the unbound fraction.

AIEX-purification over quaternary ammonium groups was further tested using Capto-Q beads, differing in the underlying resin. Similarly, most of the proteins in the input sample did not bind to the column material and were found in the unbound fraction (Fig. 3.11, B). Proteins that showed binding were eluted at different concentrations of buffer B. Interestingly, although the majority of $Ca_V2.2$-specific signals was observed in the unbound fraction, wash and elution fractions also contained low amounts of $Ca_V2.2$ with the peak concentration in the fraction eluted with 40% of buffer B. In order to enhance the selectivity of the purification approach, a weak anion exchanger, using diethylaminoethyl as ion exchange group immobilized on sepharose beads (DEAE-sepharose), was additionally tested. The separation of proteins yielded similar results compared to AIEX using strong anion exchangers with the majority of proteins present in the unbound fraction and a smaller quantity detected in elution fractions. Although a high concentration of $Ca_V2.2$ was present in the input sample, only faint $Ca_V2.2$-specific bands were detected after purification. Compared with protein separation using a strong anion exchanger, $Ca_V2.2$ was not found in the unbound fraction. Low levels of $Ca_V2.2$-specific signals could be detected after elution with 5% buffer B. Nevertheless, despite increasing the ionic strength no additional elution of the protein was observed. Furthermore, analysis of proteins that remained bound to the beads after elution with 100% buffer B was performed by boiling the beads in 2 × Laemmli buffer for 5 min at 95°C. No $Ca_V2.2$-specific signals or total protein signals were found in the final elution sample (data not shown).

Furthermore, batch purification via CIEX was performed using the strong cation exchanger group methyl sulfonate (Capto-S beads). At buffer pH 7.4, most of the proteins in the sample did not bind to the column material and were found in the unbound fraction. Although $Ca_V2.2$ was initially present in high abundance in the input sample no binding was observed and a $Ca_V2.2$-specific signal was only detected in the unbound and wash fractions. Interestingly, compared with strong anion exchangers, the concentration of $Ca_V2.2$ after CIEX purification was higher in the wash fraction compared with the unbound fraction. This may indicate very weak binding affinity to strong cation exchangers under the conditions employed in this study.

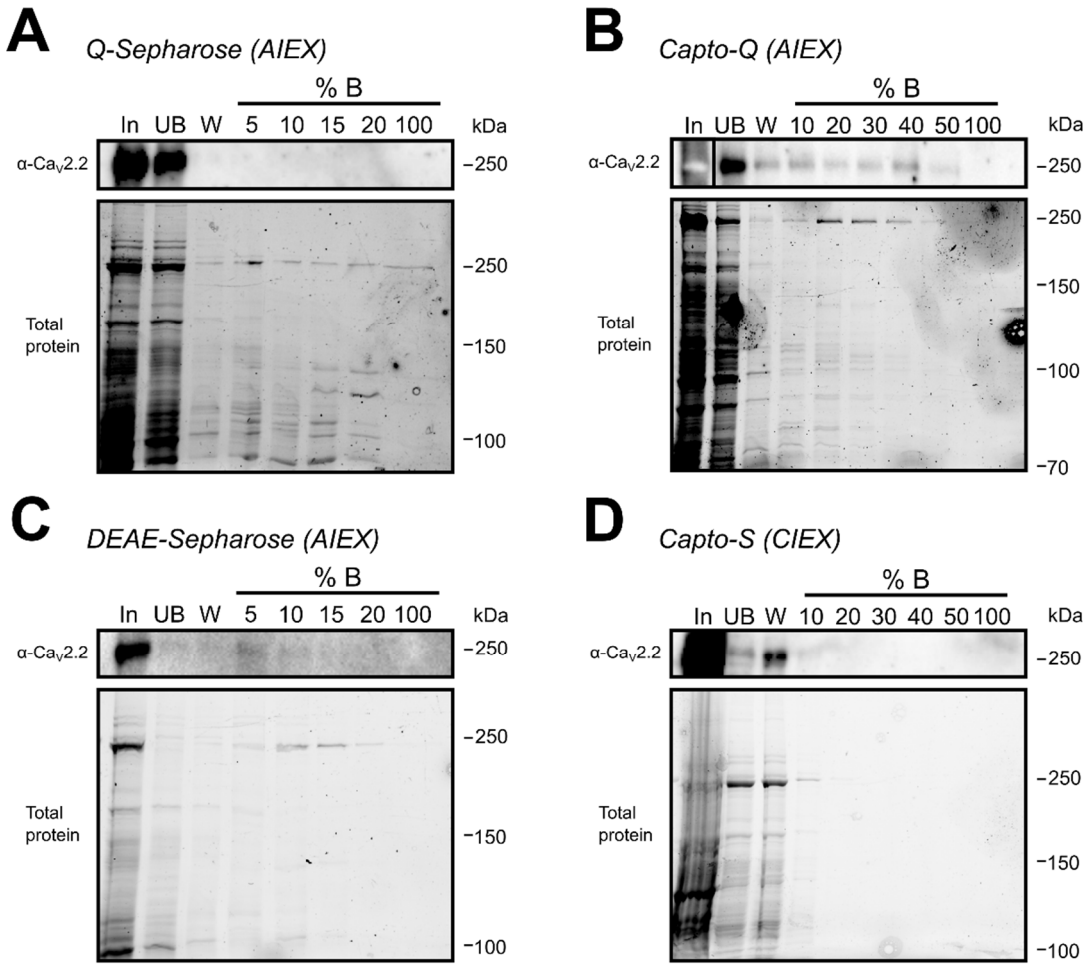

Figure 3.11: Purification of Cav2.2 via batch ion exchange chromatography Cav2.2 was separated from complex protein samples via IEX using anion (**A**, **B**, **C**) or cation (**D**) exchanger-loaded beads. Elution was performed by increasing the ionic strength in the buffer (% buffer B). Samples from input (In), unbound (UB), wash (W) and elution fractions were analyzed with regard to the overall protein composition in SDS-PAGE (lower panel) and Cav2.2-specific content through immunostaining of western blots (upper panel).

3.3.2.3 Purification of $Ca_V2.2$ via Hydrophobic Interaction Chromatography

Another approach for $Ca_V2.2$ purification was separation of the protein sample with regard to the specific hydrophobicity of proteins using HIC. Pre-treatment of the sample with ammonium sulfate led to partial precipitation of the proteins present in the sample (Fig. 3.12, A). Analysis of the supernatant and resolubilization of precipitated proteins revealed a large amount of proteins that were precipitated by ammonium sulfate without any visible difference in overall composition of the protein sample or significant separation. In the input sample, a strong $Ca_V2.2$-specific signal was observed at a corresponding height of 250 kDa, but further protein components of lower molecular weight were observed to be also responsive to the $Ca_V2.2$-specfic antibody. Comparison between ammonium sulfate-soluble and -insoluble fractions revealed that the majority of $Ca_V2.2$ is present in the supernatant, laying the foundation for subsequent purification of $Ca_V2.2$ by HIC.

Following loading of the samples and respective washing steps, elution of the bound protein was initiated by decreasing the concentration of ammonium sulfate in the buffer. The chromatogram depicting the protein elution profile was acquired at 280 nm (Fig. 3.12, B). An initial peak was observed during column wash, with subsequent gradual decrease in signal intensity. After induction of elution, an additional slight increase in signal could be detected, decreasing over the course of the elution process. Towards the end of the chromatography run, no noteworthy signal was detected.

Analysis of the protein composition revealed partial separation of proteins across the different fractions (Fig. 3.12, C). In general, the flow-through (fraction 2) showed a different protein composition compared with fractions collected from column wash (fraction 4-9). Inducing protein elution resulted in a further alteration in the protein profile of fractions 10 to 26, demonstrating a consistent composition during elution, with a gradual decrease in overall protein content. With regard to $Ca_V2.2$-specific content in the different fractions, the largest protein quantity was observed in the flow-through fraction 2. Interestingly, low amounts of $Ca_V2.2$ were found in elution fractions 12 and 13. In contrast, other proteins of lower molecular weight observed to be reactive to $Ca_V2.2$ antibody were only present in early wash fractions (fraction 4-6) (Appendix Fig. I.7).

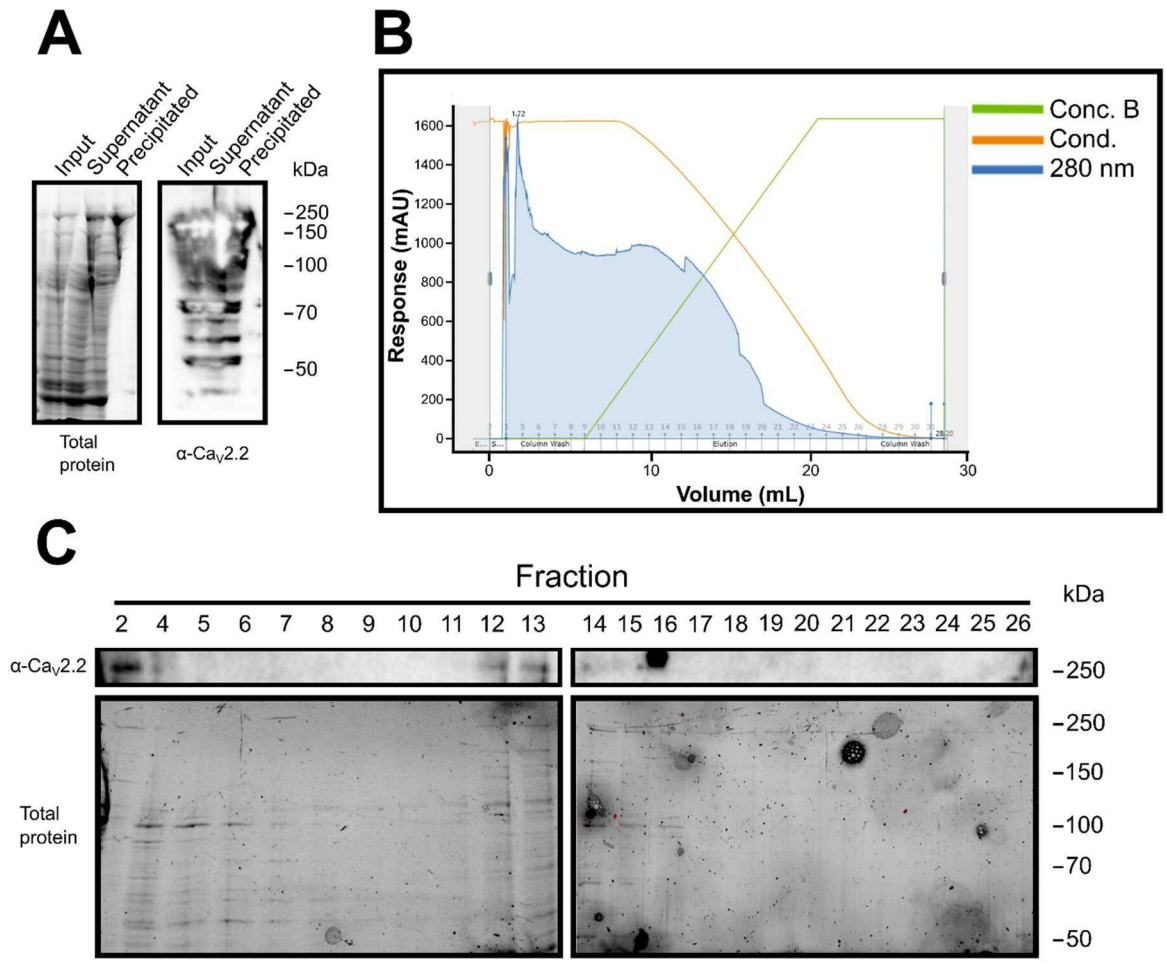

Figure 3.12: Purification of $Ca_V2.2$ via hydrophobic interaction chromatography A Input of solubilized proteins from cell lysate before and after ammonium sulfate precipitation, separated in soluble supernatant and resolubilized precipitated fraction. **B** Chromatogram of the elution profile of proteins as acquired at 280 nm (blue), with respectively indicated concentration of buffer B (green) and conductivity (orange). **C** Flow-through (2), wash (4-9), as well as elution fractions (10-26) of 1 min were analyzed via SDS-PAGE for total protein content (lower panel) and immunostaining of western blots shows $Ca_V2.2$-specific distribution across all fractions (upper panel).

3.3.2.4 Purification of $Ca_V2.2$ via Immunoprecipitation

Immunoprecipitation is a way of affinity-purifying a certain antigen or protein over a specific antibody immobilized onto a matrix. For the purification of $Ca_V2.2$ from a complex mixture of different proteins, a commercially available $Ca_V2.2$-antibody was utilized and the purification was optimized for efficient complex formation and separation, as well as with regard to the respective elution method.

Crude solubilized membrane fractions from cell lysates were incubated with the respective anti-$Ca_V2.2$ antibody allowing formation of a complex, consisting of the protein of interest, bound over the antibody-specific antigen to the antibody, which is the further immobilized on protein A/G beads through association over its F_c-region. Analysis of the input sample revealed the presence of a variety of different proteins in the sample, comprising $Ca_V2.2$ amongst others, as evidenced by immunodetection (Fig. 3.13, A). An intense $Ca_V2.2$-specific signal was observed at a height corresponding to approximately 250 kDa. In addition, several other signals at lower corresponding molecular weight regions were seen after staining with $Ca_V2.2$-specific antibody, including prominent bands at approximately 130 kDa, 100 kDa, 70 kDa and under 50 kDa. Unbound flow-through protein fraction appeared to contain the same protein composition compared to the input sample. In addition, similar $Ca_V2.2$-specific antibody responsive signals were found in the flow-through sample. No significant changes could be observed with regard to composition or ratio. One of the classic approaches for elution of proteins after IP is lowering the pH to an acidic value, where the binding of the protein-antigen complex is disrupted. After elution, a prominent signal at around 80 kDa was detected, which was not observed in input or flow-through samples. The same band, only with reduced signal intensity is present after the second elution. In addition, a very faint band was observed at a height corresponding to approximately 130 kDa. Final boiling of the sample in 2 × Laemmli buffer revealed two faint bands at approximately 50 kDa and 60 kDa.

In order to stabilize the tertiary protein structure during the process of purification by IP an additional different elution approach was chosen. For this, the antibody-specific antigen is utilized as peptide in molar access for the competitive elution of $Ca_V2.2$ from anti-$Ca_V2.2$ antibodies. Two different matrices were tested for protein-antibody complex immobilization to potentially reduce unspecific matrix-binding effects. Analysis of the protein composition of the input sample showed high complexity of the sample, as a variety of proteins of different sizes is present (Fig. 3.13, B). $Ca_V2.2$-specific signals were detected in the input sample at a height corresponding to approximately 250 kDa as well as in high intensity at

lower molecular weights, especially around 80 kDa. Unbound proteins from flow-through and wash fractions contained proteins of similar overall composition only in diluted concentration. $Ca_V2.2$-specific immunostaining revealed a diffuse band at around 80 kDa in the flow-through and wash fraction, independent of the used beads. In the elution fraction, an additional faint band at around 250 kDa was observed, as well as a signal at a height corresponding to 130 kDa (Fig. 3.13, B). Nevertheless, analysis of the total protein composition of the elution fraction revealed remaining high complexity of the sample.

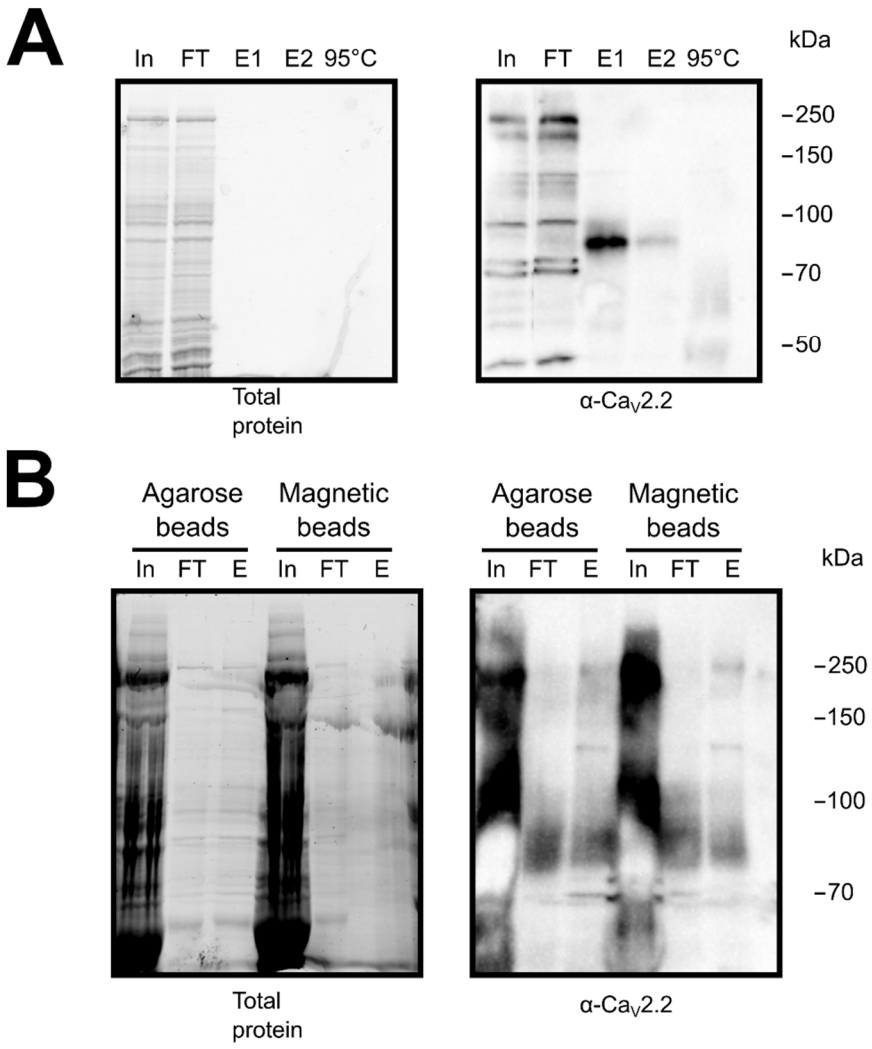

Figure 3.13: Purification of $Ca_V2.2$ via immunoprecipitation $Ca_V2.2$ was purified from complex crude membrane fractions of $Ca_V2.2$-expressing mammalian cells via immunoprecipitation using a $Ca_V2.2$-specific antibody immobilized to a matrix. Elution was performed either by lowering the pH (**A**) or through competitive elution using the antibody-specific antigen as peptide in molar access (**B**). Samples were analyzed by SDS-PAGE with regard to their total protein composition (left panel) or their $Ca_V2.2$-specific signals by immunodetection of western blots (right panel).

3.3.2.5 Purification of $Ca_V2.2$ via Immobilized Metal Affinity Chromatography

Purification and enrichment of $Ca_V2.2$ from crude membrane fractions was aimed for performing IMAC using an NTA-based matrix with different complexed metal ions in order to purify proteins with regard to their phosphorylation state (Fe^{2+}), their Ca^{2+}-binding capability (Ca^{2+}) or the presence of intrinsic surface-located histidine patches (Ni^{2+}). Crude membrane fractions or partially pre-purified samples that contained $Ca_V2.2$ were used as input sample for IMAC and the respective flow-through, wash and elution fractions were analyzed with regard to the overall protein composition and $Ca_V2.2$-specific content to assess purification efficiency as well as specificity.

Separation of pre-purified samples of $Ca_V2.2$ via IMAC using an Fe^{2+}-NTA column revealed a complex overall protein composition as input, with only low concentrations of $Ca_V2.2$ present (Fig. 3.14, A). The majority of proteins were not found to interact with the matrix and were detected in the flow-through fraction. However, no $Ca_V2.2$-specific band could be found in this fraction. Elution was performed at increasing concentrations of NaH_2PO_4. In all elution fractions, no visible bands were observed in total protein visualization. In contrast, a faint band in elution fraction 2, eluted with 100 mM NaH_2PO_4, showed a $Ca_V2.2$-specific signal. Nevertheless, the overall concentration of $Ca_V2.2$ appeared to be very low, as indicated by the faint signal intensity.

IMAC, using Ca^{2+}-NTA as matrix, was employed for the purification of $Ca_V2.2$ with regard to its Ca^{2+}-binding capability. Analysis of the input sample revealed a complex protein composition, containing a variety of proteins. Additionally, a strong $Ca_V2.2$-specific signal at a corresponding molecular weight of 250 kDa was detected (Fig. 3.14, B). A similar sample composition was observed in the flow-through fraction, containing the majority of the total protein content, alongside a significant portion of the $Ca_V2.2$-specific signal, which remains unbound to the matrix. Following wash and elution fractions showed a similar pattern with gradually decreasing concentrations of overall as well as $Ca_V2.2$-specific protein content.

A pre-purified sample containing enriched levels of $Ca_V2.2$ was used for evaluation of an IMAC-based purification approach, targeting a naturally occurring surface-exposed penta-histidine stretch, located in the C-terminal loop of $Ca_V2.2$. The overall protein composition of the pre-purified input sample was observed to be rather complex, with a variety of protein bands at different corresponding molecular weights detectable in the sample (Fig. 3.14, C).

A strong $Ca_V2.2$-specific signal was observed at a height corresponding to a molecular weight of 250 kDa. Purification of the sample over Ni^{2+}-NTA involved elution with incremental concentrations of imidazole. Most of the proteins present in the input sample were additionally detected in the flow-through fraction, indicating absent binding to the matrix for these proteins. Furthermore, a faint band, resembling a $Ca_V2.2$-specific signal, could be detected in the flow-through fraction at a corresponding height of 250 kDa. No other wash or elution fractions contained measurable $Ca_V2.2$ content of 250 kDa, further confirmed by total protein visualization. Interestingly, a strong $Ca_V2.2$-specific signal was found at a height corresponding to a lower molecular weight, approximately corresponding to 200 kDa. The detected signal was present in the flow-through and wash fractions, and was also identified in the elution fractions, exhibiting a diminishing signal intensity with each subsequent elution step.

Overall, due to the low protein concentration during the purification process, gels were exposed for extended duration, emphasizing artifacts as foam or inhomogeneity of TCE in the gel (Fig. 3.14, A, C).

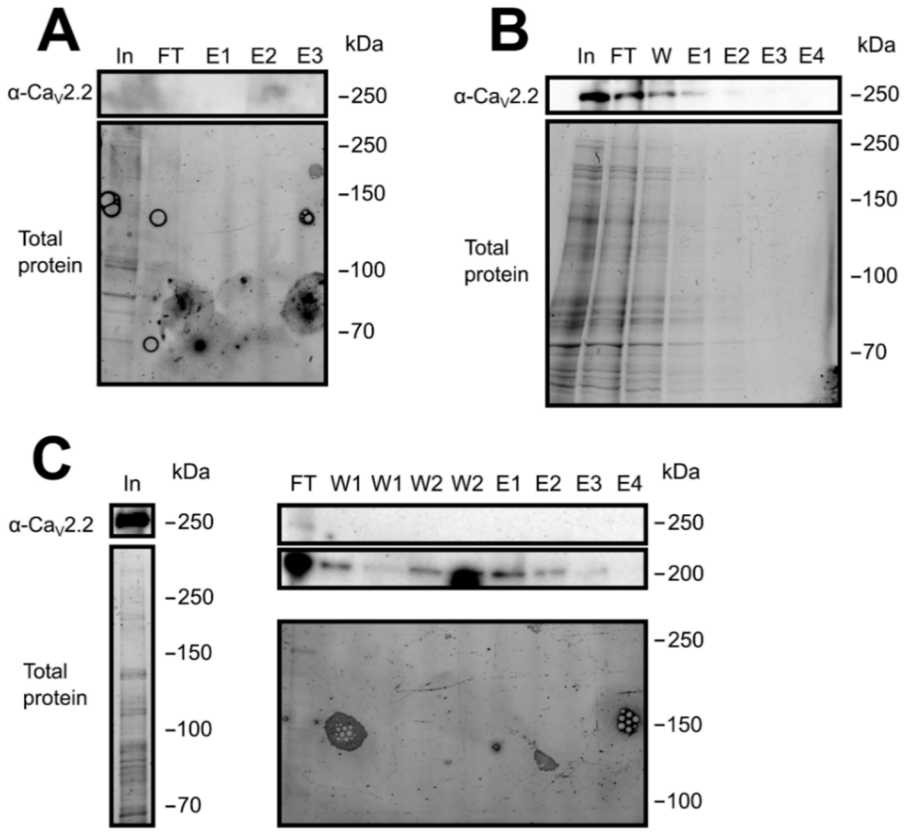

Figure 3.14: Purification of $Ca_V2.2$ via immobilized metal affinity chromatography $Ca_V2.2$ was purified from complex crude membrane fractions of $Ca_V2.2$-expressing mammalian cells via IMAC. Different chelated ions were used on the NTA matrix for capture of the proteins, comprising Fe^{2+} (**A**), Ca^{2+} (**B**) and Ni^{2+} (**C**). Input (In), flow-through (FT), wash (W) and elution (E) samples were analyzed by SDS-PAGE with regard to their total protein composition (left panel), or $Ca_V2.2$-specific signals in western blots (right panel).

3.3.2.6 Purification of $Ca_V2.2$ via Hydroxyapatite Chromatography

Mixed-mode chromatography through hydroxyapatite was further used for the purification of $Ca_V2.2$ from complex samples. Input samples were analyzed with regard to their protein composition and a complex mixture of different proteins was present and visualized in SDS-PAGE staining of the input fraction (Fig. 3.15, A). Furthermore, strong $Ca_V2.2$-specific signals were detected in the input sample as bands of varying size, including a band at a height corresponding to 250 kDa. Additional prominent bands were detected at a height corresponding to 100 kDa and 70 kDa, respectively (Fig. 3.15, B). Purification by hydroxyapatite chromatography resulted in partial separation of the total protein content, as an enriched band at a corresponding height of 250 kDa was observed in the flow-through and first wash fraction. Several other protein bands were visible at lower abundance, predominantly seen at a corresponding molecular weight below 100 kDa. Analysis of immunostaining with a $Ca_V2.2$-specific antibody revealed the presence of a signal corresponding to molecular weights of 100 kDa and 50 kDa, along with an additional faint double band at 70 kDa present in the flow-through fraction. The latter was prominently present in both elution fractions. Dot blot analysis showed the highest overall $Ca_V2.2$-specific signal in both elution fractions in addition to a less intense signal in the flow-through and the first wash fraction. Interestingly, although a $Ca_V2.2$-specific band at a corresponding height of 250 kDa was present in the input sample, no corresponding signal was found in any fraction after purification. For this reason, the protein content of the remaining bound fraction was assessed by dissolving the hydroxyapatite column. Further examination of the protein content that remained bound to hydroxyapatite after elution with 400 mM Na_3PO_4 indicated the presence of proteins at very low levels (Fig. 3.15, C). $Ca_V2.2$-specific analysis identified that amongst the remaining bound proteins $Ca_V2.2$-specific signals are detectable in form of a double band at height corresponding to 70 kDa, which was also observed during the elution process. No signal at a corresponding height of 250 kDa was detected.

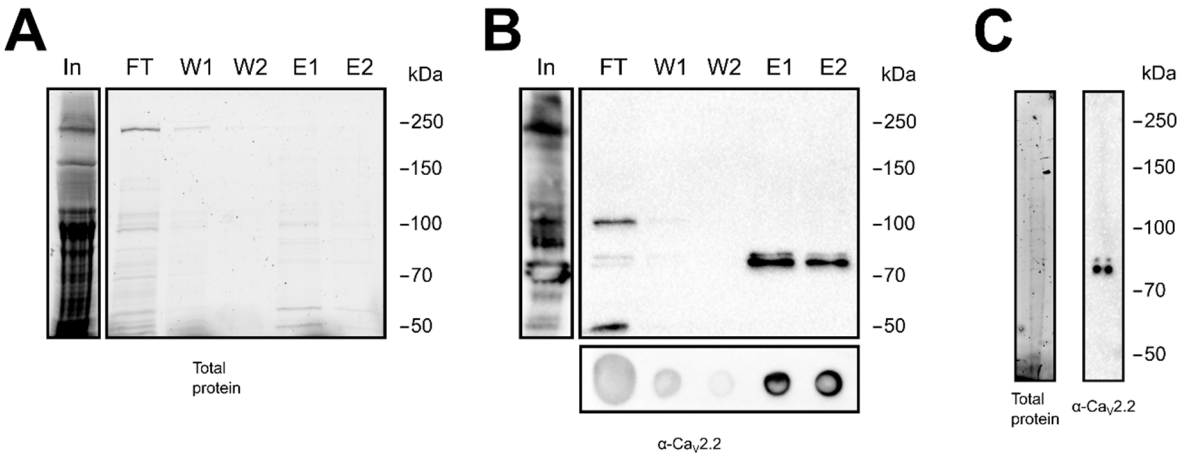

Figure 3.15: Purification of Ca$_V$2.2 via hydroxyapatite chromatography Ca$_V$2.2 was purified from solubilized crude membrane fractions of cell lysates through mixed mode chromatography using hydroxyapatite. Samples were analyzed by SDS-PAGE (**A**) with regard to the total protein composition in input (In), flow-through (FT), wash (W) and elution (E) fractions. **B** Ca$_V$2.2-specific signals were assessed in immunostaining of western (upper panel) or dot blots (lower panel). **C** Remaining bound protein was analyzed after dissolving the hydroxyapatite column material with regard to total protein content (left panel) and Ca$_V$2.2-specific signals (right panel).

3.3.2.7 Purification of Ca$_V$2.2 via Centrifugation-Based Separation

Purification of proteins by centrifugation-based approaches relies on separation of the different particles in a sample with regard to their respective density, sedimentation speed as well as corresponding equilibrium position in a surrounding gradient medium.

Differential centrifugation was performed iteratively at different velocities in order to improve the separation of Ca$_V$2.2 from other proteins in the sample. Following centrifugation at the lowest speed of 1,000 × g, a variety of proteins was present in high overall concentration in the pellet fraction (Fig. 3.16). Remarkably, only a faint Ca$_V$2.2-specific protein band at a corresponding size of approximately 250 kDa was found in the 1,000 × g pellet. Further centrifugation at 20,000 × g was performed to effectively separate soluble proteins from insoluble proteins and particles. The supernatant after centrifugation comprised a complex and heterogenous mixture of proteins at relatively high concentrations. Washing of the respective pellet resulted in separation of the proteins of identical composition but at lower concentration. Following centrifugation at 20,000 × g, only trace quantities of Ca$_V$2.2 were detected in the supernatant. Although the solubilized proteins in the pellet obtained by centrifugation at 20,000 × g displayed a heterogenous protein profile in terms of molecular weight, a strong Ca$_V$2.2-specific signal was detected in the pellet fraction at a molecular weight of approximately 250 kDa, demonstrating the efficiency of centrifugation at 20,000 × g to partially separate Ca$_V$2.2 from complex samples (Fig. 3.16).

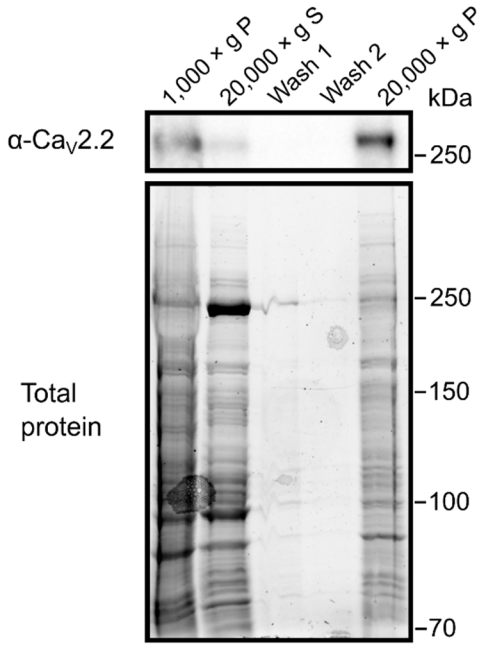

Figure 3.16: Separation of $Ca_V2.2$ via differential centrifugation Centrifugation of $Ca_V2.2$-containing cell lysate samples was performed at 1,000 × g as well as 20,000 × g to separate proteins with regard to their size, molecular weight, density and resulting sedimentation speed. Fractions of resulting solubilized pellets (P) and supernatant (S), as well as wash fractions were analyzed with regard to their overall protein composition by SDS-PAGE (lower panel), and their $Ca_V2.2$-specific content by immunostaining (upper panel).

In addition, purification of $Ca_V2.2$ from complex samples was carried out through density gradient centrifugation employing different gradient media. Analysis of the input sample of all examined gradients revealed a complex mixture of different proteins present in the sample, as evidenced by protein bands at distinct corresponding molecular weights (Fig. 3.17, A). Furthermore, a $Ca_V2.2$-specific signal was detected in western blots at a height of a corresponding molecular weight of 250 kDa.

Total protein fractionation was consistently observed across all density gradients after centrifugation, regardless of the medium employed. A similar overall separation pattern was observed across various gradient media, where proteins of lower molecular weight were detected in earlier fractions, while proteins of higher molecular weight were located in later fractions as a result of their differential migration behavior in the gradient. The distinct protein composition of each fraction was dependent on the density range of each gradient. Broader ranges in iodixanol gradients resulted in reduced separation and more similar overall protein composition among the samples (Fig. 3.17, A). Conversely, narrower gradients of the same medium exhibited increased separation efficiency with greater variation in protein composition among consecutive fractions (Fig. 3.17, B). The use of other gradient media, such as sucrose or glycerol, showed only slight variation in the protein separation ability and very similar distribution of protein of differing size across the gradient (Fig. 3.17, C and D).

As this separation method aimed to semi-purify and enrich $Ca_V2.2$ from complex protein mixtures, the content of $Ca_V2.2$ across the gradient fractions was assessed. Using a broad density-range iodixanol gradient resulted in a primary localization of $Ca_V2.2$ in fractions with lower density, particularly peaking in fraction 10, while also displaying noticeable amounts in adjacent fractions 7 to 12, indicating a widespread distribution along the gradient (Fig. 3.17, A). Narrowing down the range of iodixanol concentration used in the gradient to 10% to 40% led to an enhanced separation of $Ca_V2.2$ from complex samples. The highest concentration of $Ca_V2.2$ was detected in fractions 7 and 8, with only faint signals in adjacent fractions 9 and 10. This was accompanied by a reduction in visual complexity in the sample, as indicated by the analysis of the total protein content (Fig. 3.17, B). Using a 10% to 30% gradient of glycerol, $Ca_V2.2$-specific signals were found in fractions 8 to 14, with a peak in signal intensity in fraction 10 and adjacent fractions 9, 11 and 12 (Fig. 3.17, C). Although the same $Ca_V2.2$-containing input sample was used for purification with all gradients, separation using a 5% to 20% sucrose gradient did not show a $Ca_V2.2$-specific signal in any of the fractions analyzed, although a similar overall protein separation was achieved (Fig. 3.17, D).

As seen before, staining with anti-$Ca_V2.2$ antibodies further revealed several other protein bands at different corresponding molecular weights. A distinctive protein double band, responsive to anti-$Ca_V2.2$ antibodies, was detected at a corresponding molecular weight of approximately 70 kDa. Density gradient centrifugation using various media effectively separated this component from another anti-$Ca_V2.2$ antibody-responsive protein band at a corresponding molecular weight of approximately 250 kDa, as the lower molecular weight particle was consistently detected in earlier fractions of the gradient.

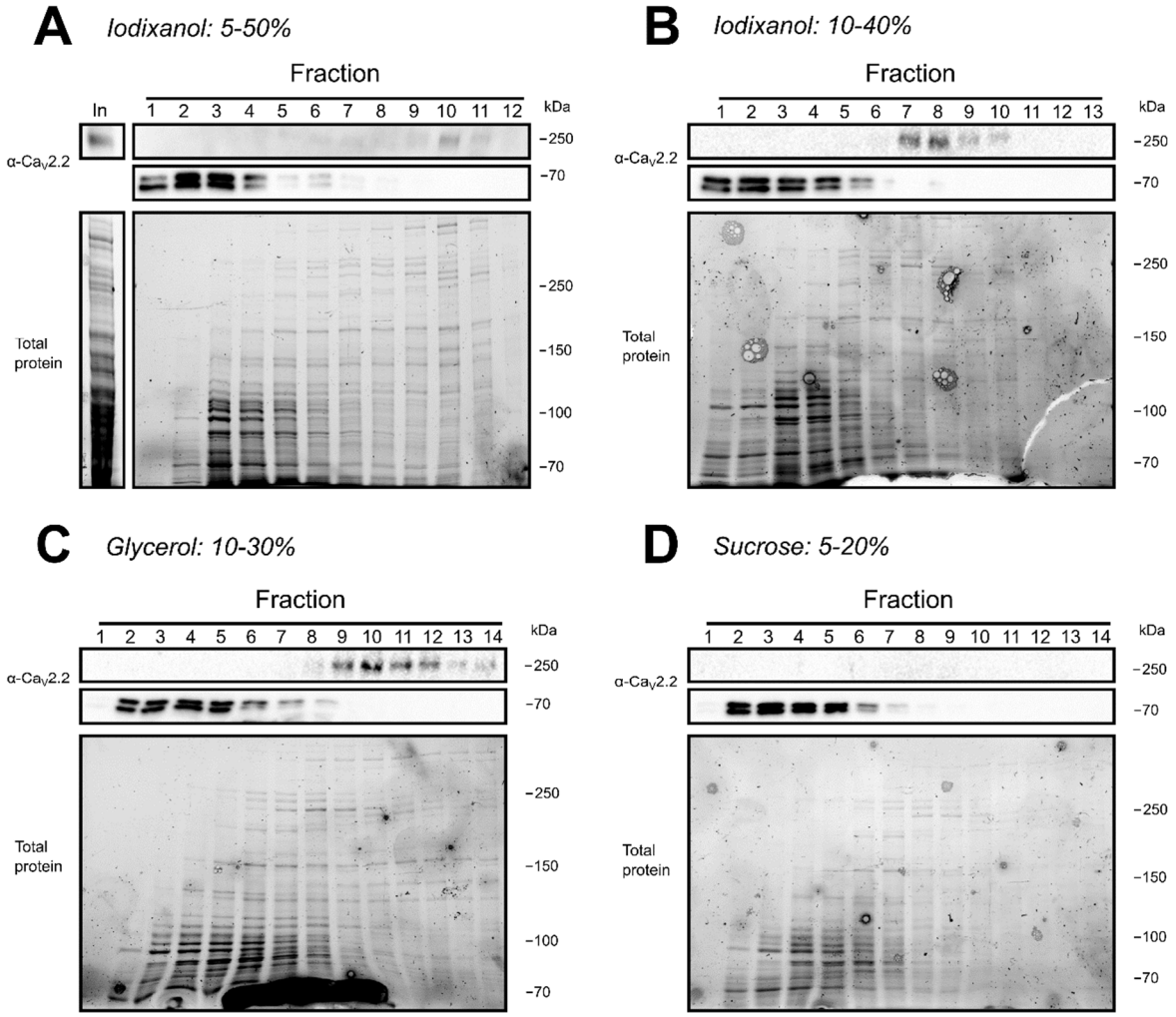

Figure 3.17: Purification of $Ca_V2.2$ via density gradient centrifugation Solubilized $Ca_V2.2$ was separated from other proteins of crude membrane fractions of cell lysates with regard to the protein-specific density by centrifugation in different gradients. Iodixanol gradients were used with concentrations of 5% to 50% (**A**) and 10% to 40% (**B**) iodixanol, respectively. Furthermore, proteins were separated using a gradient of 10% to 30% glycerol (**C**) and 5% to 20% sucrose (**D**). The overall protein composition of different fractions was assessed using SDS-PAGE analysis (lower panel), whereas $Ca_V2.2$-specific signals were obtained through immunostaining of western blots (upper panel).

3.3.3 Purification of $Ca_V2.2$ via Multistep Purification Approaches

3.3.3.1 Anion Exchange Chromatography and Size Exclusion Chromatography

Ion exchange chromatography and size exclusion chromatography separate proteins with regard to distinct biophysical and biochemical properties. Furthermore, it was previously observed, that AIEX, as well as SEC were successful in partially separating $Ca_V2.2$ from complex protein samples. These features make them ideal candidates for combination in a multistep purification approach.

In line with other purification approaches using AIEX, the chromatogram for the purification of crude $Ca_V2.2$-containing membrane fractions revealed two main peaks of protein-specific signals detected at 280 nm. A first peak was observed in early fractions, resembling the unbound protein contained in the flow-through (fractions 4-7). Modification of the elution conditions resulted in a more focused peak area during the elution process within fractions 27-35 (Fig. 3.18, A), indicating an increased protein concentration compared with previous attempts (Fig. 3.10, A). $Ca_V2.2$-specific signals at a height corresponding to approximately 250 kDa were found in high intensity in the input fraction and during elution. The highest $Ca_V2.2$-specific signal intensity was observed in fractions 29 and 30. Although the complexity and total concentration of proteins were found to be reduced compared with the input sample, the overall protein composition in the final fractions remained rather complex. For this reason, samples from fraction 29 and 30 were pooled and subjected to an additional purification step using SEC. After concentration of the sample, a variety of proteins was found in the sample as seen in the chromatogram as well as by visualization of the total protein content (Fig. 3.18, B). Separation of the sample through SEC reduced the complexity by separating the overall protein composition across the different fractions with regard to protein size. However, samples remained to contain a diverse range of proteins in each fraction. $Ca_V2.2$-specific signals were found in fractions 4 and 5 with a peak in intensity in fraction 4 corresponding to an elution after 6 min. Nevertheless, a marked reduction of the $Ca_V2.2$-specific signal was seen after purification over SEC, which was not proportional to the dilution of the applied sample throughout the chromatography process.

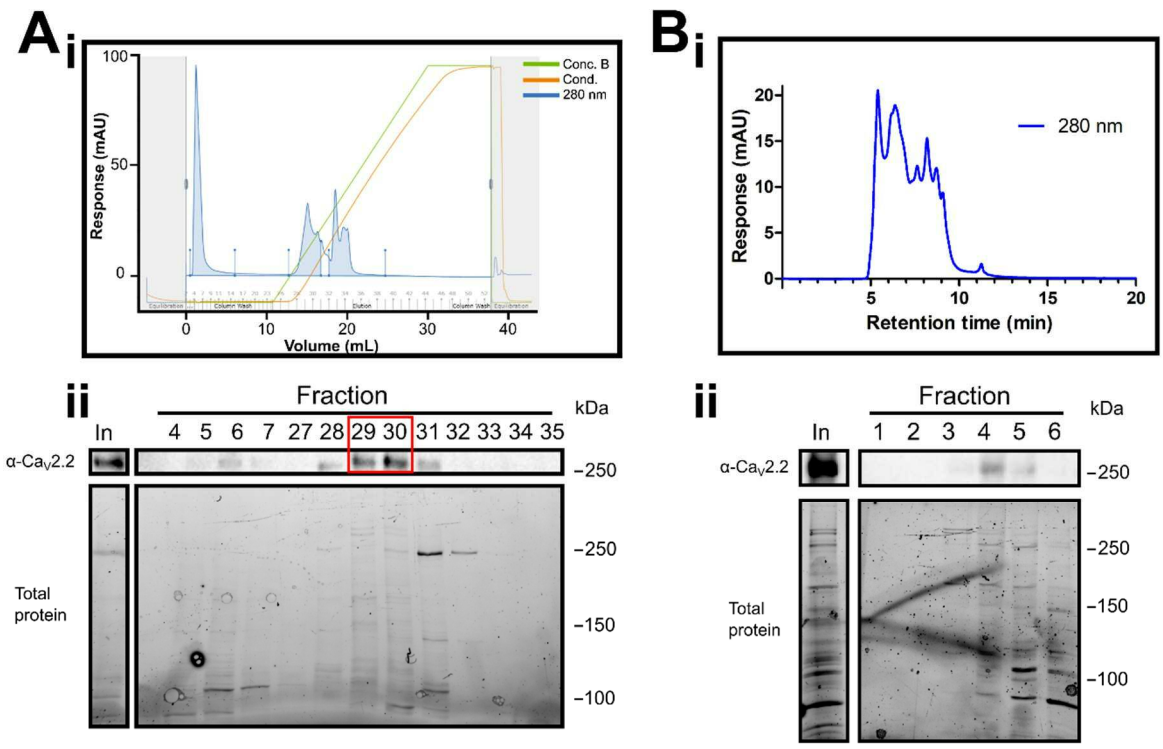

Figure 3.18: Purification of CaV2.2 via a combination of anion exchange chromatography and size exclusion chromatography A Complex CaV2.2-containing samples were initially purified through AIEX. Elution was performed through an increase in ionic strength (green) and chromatograms (**Ai**) were acquired at 280 nm (blue). Elution fractions were collected every 1 mL and were analyzed by SDS-PAGE analysis (**Aii**) with regard to total protein composition (lower panel) and via immunostaining of western blots for CaV2.2-specific content (upper panel). **B** Chromatogram of the elution profile of proteins from concentrated AIEX fractions 29/30 purified over SEC is shown acquired at 280 nm (**Bi**). Respective elution fractions of 0.5 min starting from 4 min were analyzed via SDS-PAGE (**Bii**) for total protein content (lower panel) and immunostaining of western blots to determine the CaV2.2-specific fractionation (upper panel).

3.3.3.2 Size Exclusion Chromatography and Hydroxyapatite Chromatography

Hydroxyapatite chromatography is a specific technique for protein purification, serving as both cation as well as anion exchanger. Beyond that, it can also separate proteins with regard to their phosphorylation state and Ca^{2+}-binding capacity. As purification with other size-dependent separation methods already resulted in partial separation of CaV2.2, but a variety of proteins remained as impurities, hydroxyapatite chromatography was chosen as additional technique for a multistep purification approach. For this, samples were partially purified prior through size exclusion chromatography and further subjected to purification using hydroxyapatite chromatography.

Analysis of the input sample revealed the presence of a complex mixture of proteins spanning different molecular weights (Fig. 3.19). Separation through SEC markedly reduced the overall sample complexity by separating proteins based on their overall size. One of the proteins present in the sample is a dominant protein band at a height corresponding to a molecular weight of approximately 250 kDa, which is present in fractions 4, 5 and 6. A respective $Ca_V2.2$-specific signal at 250kDa was on the contrary seen in fractions 3, 4 and 5, with a peak in intensity in fraction 4. Because of this, fractions 4 and 5 were pooled and further purified using hydroxyapatite chromatography. Purification through hydroxyapatite chromatography further reduced the overall sample complexity, as evidenced by total protein visualization. Following application of the sample to a column, a single dominant protein band at a height of a corresponding molecular weight of 250 kDa was visualized using total protein staining following SDS-PAGE. This protein component was primarily present in the initial wash fraction. Analysis of the $Ca_V2.2$-specific content showed only a faint band at a corresponding height of 250 kDa in the wash fraction, which did not correlate with the sample concentration difference observed in SDS-PAGE analysis.

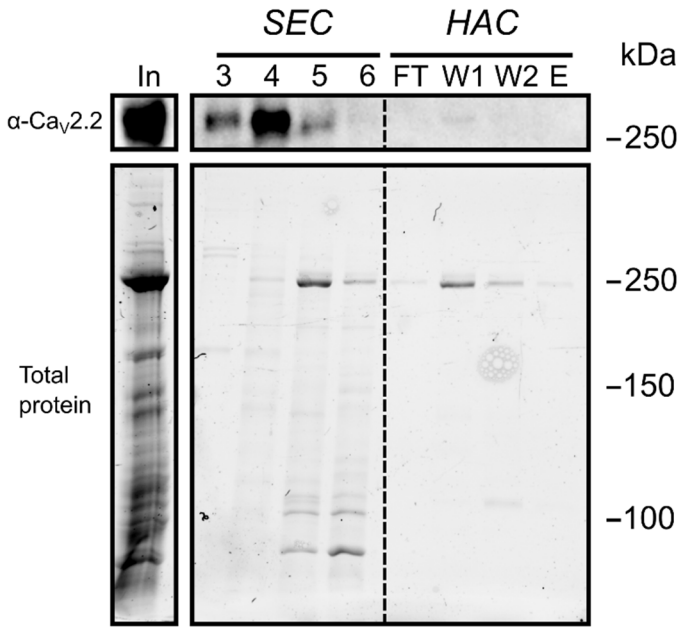

Figure 3.19: Purification of $Ca_V2.2$ via a combination of size exclusion chromatography and hydroxyapatite chromatography Complex $Ca_V2.2$-containing samples (In) were first separated with regard to their size through SEC. Fraction 4, showing the highest $Ca_V2.2$-specific signal, was further applied to a hydroxyapatite column for purification (HAC). Elution was performed with high concentration of Na_3PO_4. Flow-through (FT), wash (W) and elution (E) fractions were analyzed by SDS-PAGE regarding their overall protein composition (lower panel) and for $Ca_V2.2$-specific content in western blots (upper panel).

3.3.3.3 Differential Centrifugation and Density Gradient Centrifugation

Both centrifugation-based purification methods demonstrated adequate separation efficiency without compromising the overall yield of $Ca_V2.2$. However, the isolated fractions remained to contain a variety of other proteins, prompting an evaluation of a combined approach to enhance separation efficacy (Fig. 3.20, A).

To compare the effect of pre-purification of samples via differential centrifugation, equal amounts of $Ca_V2.2$-containing unpurified samples were applied on 10% to 40% iodixanol gradients to subsequently perform density gradient centrifugation. Separation of total protein was observed over the course of the gradient with regard to the respective molecular weight of the proteins as evidenced by an overall varying protein composition among consecutive fractions (Fig. 3.20, B). The most intense $Ca_V2.2$-specific signal at a height corresponding to a molecular weight of 250 kDa was detected in fraction 11, whereas fraction 12 showed a lower abundance of the same protein while a variety of proteins remained present in the sample.

For pre-purification of the sample, two additional differential centrifugation steps were included prior to density gradient centrifugation. In line with previous observations, centrifugation in aqueous buffer at low centrifugation speed (1,000 × g) separated a minor portion of proteins without removing a significant quantity of $Ca_V2.2$ from the sample. In contrast, centrifugation at higher speed (20,000 × g) resulted in pelleting of a variety of insoluble proteins, whereas most of the soluble proteins were found in the supernatant after centrifugation (Fig. 3.20, C_i). The majority of proteins was separated by removing the supernatant, while the main fraction of $Ca_V2.2$ could be restored from the pellet through subsequent solubilization. Nevertheless, the sample remained to contain a variety of proteins as evidenced through analysis of the total protein composition.

The pre-purified sample, solubilized from the pellet after centrifugation at 20,000 × g, was subjected to density gradient centrifugation on a discontinuous 10% to 40% iodixanol gradient. In general, proteins of lower molecular weight appeared to be present in earlier fractions, whereas larger proteins were found in lower fractions, with a peak in protein concentration in fraction 11 (Fig. 3.20, C_{ii}). Compared with density gradient centrifugation conducted without pre-purification via differential centrifugation, the overall separation of proteins was observed to be similar, with a positive correlation between higher protein size and earlier gradient fraction. Nevertheless, the fraction-specific protein composition showed minor variances, demonstrating an increased relative concentration of certain proteins in the

corresponding fractions. Pre-purification further did not influence separation of $Ca_V2.2$, as the same distribution of $Ca_V2.2$-specific signals with a peak in fraction 11 was observed after both density gradient centrifugation approaches.

Although, quantification and direct comparison of the specific concentration of $Ca_V2.2$ in respect to overall protein concentration is not possible, an enrichment of $Ca_V2.2$ in the sample is indicated by results of differential centrifugation (Fig. 3.20, C_i).

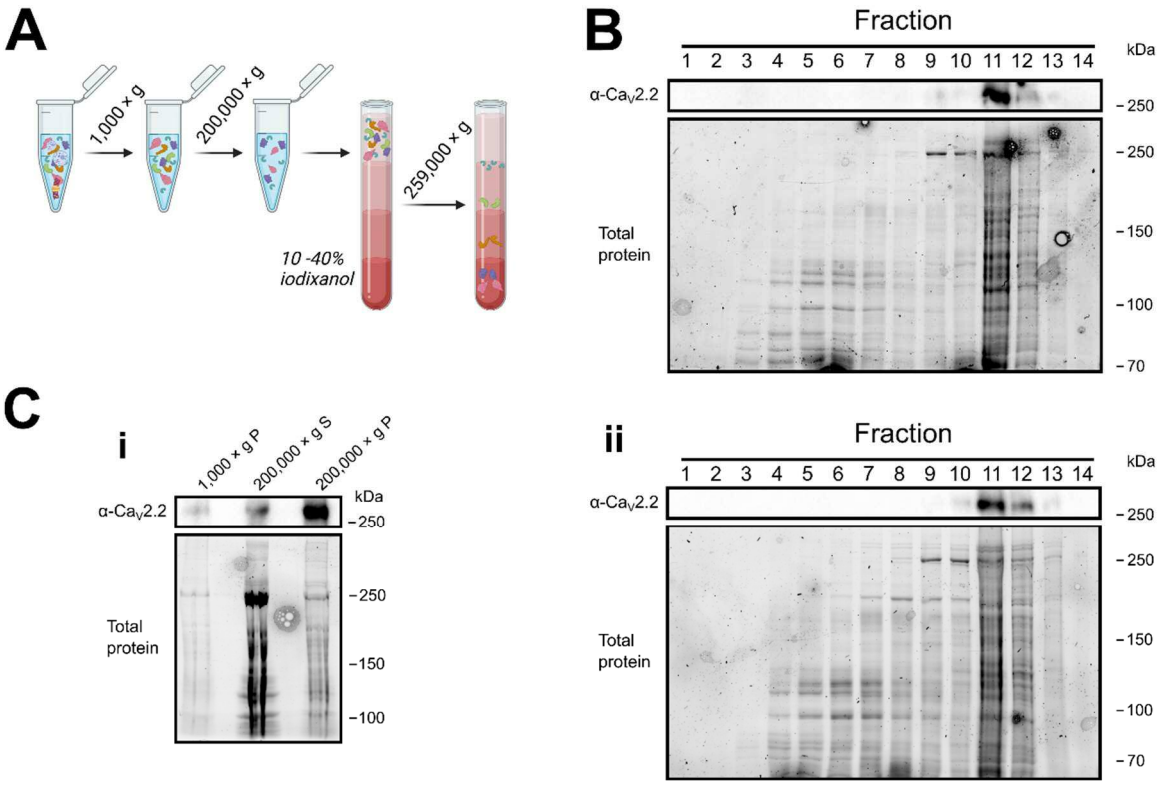

Figure 3.20: Purification of $Ca_V2.2$ via a combination of differential centrifugation and density gradient centrifugation A Schematic overview of the purification process: Complex $Ca_V2.2$-containing samples were either directly applied to the gradient after solubilization without previous purification steps as reference (**B**) or pre-purified through differential centrifugation (**C_i**) and then subjected to separation by density gradient centrifugation on a 10% to 40% iodixanol gradient (**C_{ii}**). SDS-PAGE analysis revealed total protein composition (lower panel) and $Ca_V2.2$-specific content was visualized by immunostaining of western blots (upper panel).

3.4 Binding Studies of $Ca_V2.2$ and RD2

Previous data already suggested a specific association of the D-enantiomeric peptide RD2 with $Ca_V2.2$ channels (Kutzsche, Guzman et al. 2023). In *in vitro* pharmacological screening tests performing a radioligand competition assays with ω-CgTx, the affinity of the binding of RD2 to $Ca_V2.2$ was determined within the range of 120 nM. To further verify and characterize the interaction in direct binding assays and additionally analyze the binding kinetics of the interaction, SPR- and MST-based experiments were performed.

3.4.1 Kinetics of RD2 Binding to Partially Purified $Ca_V2.2$ Measured by Surface Plasmon Resonance Spectroscopy

Binding experiments of partially purified $Ca_V2.2$ to immobilized RD2 and its tandem repeat version RD2RD2 were analyzed with regard to affinity and binding kinetics. The known $Ca_V2.2$-specific inhibitor ω-CgTx GVIA was included in the experiments as positive control for verification of the $Ca_V2.2$-specific content in the sample. Experiments were performed as single-cycle kinetic experiments. $Ca_V2.2$ did show a strong binding to all immobilized peptides in both experiments, using a Biacore T200 instrument or a Biacore 8K device (Fig. 3.21). The overall binding response was observed to increase in a dose-responsive way. As ω-CgTx is known to bind $Ca_V2.2$ at a single distinct binding site and a similar binding mode was hypothesized for RD2, data was globally fitted using a 1:1 kinetic fitting model, assuming a 1:1 stoichiometric binding. Global 1:1 fitting showed dissociation constants K_D in the pM range for the binding of $Ca_V2.2$ to immobilized peptides.

The K_D value for the interaction of $Ca_V2.2$ and RD2 was determined to be 226 pM, using a Biacore T200 instrument. Repetition of the binding analysis using the Biacore 8K device revealed a slightly lower K_D value of 121 pM (Fig. 3.21, A_{iv}, B_{iv}). In line with this, analysis revealed a similar rate constant of dissociation (k_d) for both experiments of 2.4×10^{-4} s^{-1} and 3.5×10^{-4} s^{-1}. In addition, a respective association rate constant (k_a) of the binding of RD2 to $Ca_V2.2$ was determined in the range of 2.9×10^6 $M^{-1}s^{-1}$ to 1.1×10^6 $M^{-1}s^{-1}$ in both experiments.

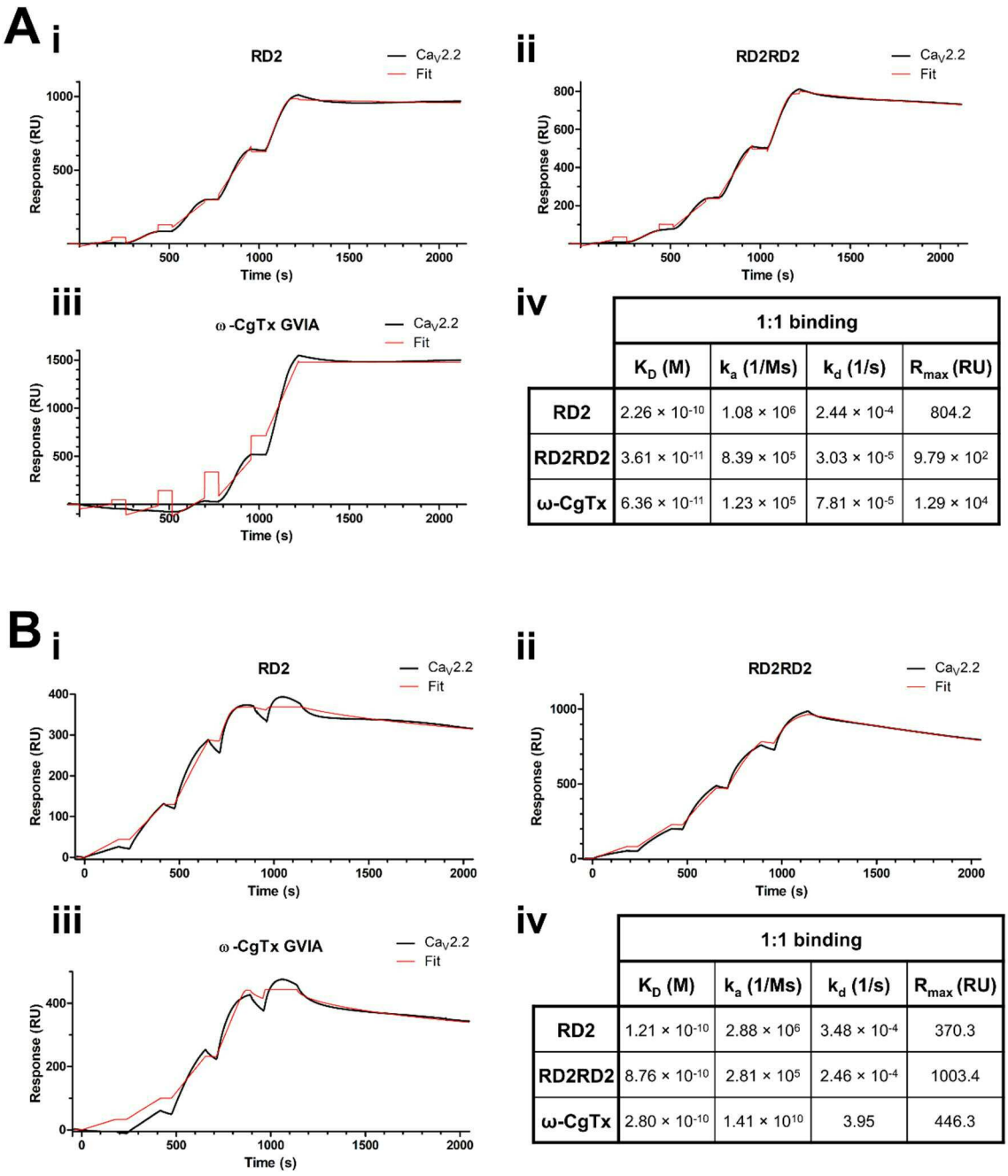

A iv	1:1 binding			
	K_D (M)	k_a (1/Ms)	k_d (1/s)	R_{max} (RU)
RD2	2.26×10^{-10}	1.08×10^{6}	2.44×10^{-4}	804.2
RD2RD2	3.61×10^{-11}	8.39×10^{5}	3.03×10^{-5}	9.79×10^{2}
ω-CgTx	6.36×10^{-11}	1.23×10^{5}	7.81×10^{-5}	1.29×10^{4}

B iv	1:1 binding			
	K_D (M)	k_a (1/Ms)	k_d (1/s)	R_{max} (RU)
RD2	1.21×10^{-10}	2.88×10^{6}	3.48×10^{-4}	370.3
RD2RD2	8.76×10^{-10}	2.81×10^{5}	2.46×10^{-4}	1003.4
ω-CgTx	2.80×10^{-10}	1.41×10^{10}	3.95	446.3

Figure 3.21: SPR measurements of the binding of partially purified $Ca_V2.2$ to immobilized RD2, RD2RD2 and ω-CgTx Partially purified $Ca_V2.2$ was analyzed for its binding to different immobilized peptides at concentrations ranging from 6.25 nM to 100 nM using SPR spectroscopy on a T200 device (**A**) or an 8K device (**B**). Sensorgrams display the binding response (black line) and the respective kinetic 1:1 binding fit (red line) of the binding to RD2 (i), RD2RD2 (ii) or ω-CgTx GVIA (iii), respectively. Tables show kinetic rates and dissociation constants as determined by a global 1:1 kinetic fitting of data from binding experiments (iv).

Measurements of the binding kinetics of $Ca_V2.2$ interacting with the tandem repeat D-peptide RD2RD2 obtained rather different K_D values for both SPR-based approaches, ranging from 36 pM to 876 pM. The observed discrepancies can be attributed to a ten-fold increase in the respective k_d value from 3×10^{-5} s^{-1} to 2.5×10^{-4} s^{-1}. In contrast, the k_a value was rather constant between the two experiments, showing only a slight decrease of the k_a value from 8.4×10^5 $M^{-1}s^{-1}$ in the experiment conducted on a Biacore T200 system, compared with 2.8×10^5 $M^{-1}s^{-1}$, which was obtained when analyzing the binding on a Biacore 8K device.

The binding response of $Ca_V2.2$ to its known inhibitor ω-CgTx GVIA was further assessed as positive control for verification of $Ca_V2.2$-specific content. Although $Ca_V2.2$-samples were observed to bind to ω-CgTx GVIA-loaded sensor chips, a global 1:1 fit model could only be applied with limitations. The obtained dissociation constant K_D ranged from to 63.6 pM to 280 pM, but results have to be handled with care due to the high residuals and standard deviation observed in the kinetic fit.

SPR-based analysis of the binding kinetics of partially purified $Ca_V2.2$ binding to the immobilized D-enantiomeric peptide RD2 or its tandem repeat D-peptide RD2RD2 showed overall clear binding response. However, while using this method, consistent and quantifiable results were not achieved for all interactions, suggesting the potential for further exploration of these interactions using other experimental approaches.

3.4.2 Kinetics of RD2 Binding to Partially Purified $Ca_V2.2$ Measured by Microscale Thermophoresis

It was further aimed to investigate the K_D value for the interaction of the fluorescently labeled D-peptide RD2 with partially purified $Ca_V2.2$ protein in MST experiments in order to analyze the binding kinetics without obtaining putative immobilization effects. The analysis provided well-defined thermographic curves, showing a dose-responsive change in motion of fluorescently labeled D-peptide RD2 along a local temperature gradient starting at 0 s (Fig. 3.22, A). In the following, thermophoresis increased with regard to the applied temperature gradient and dependent on the concentration of $Ca_V2.2$, as evidenced by changes in relative fluorescence over time and compared between different runs. F_{cold}-regions were defined as -1 s to 0 s, before application of the temperature gradient, while F_{hot}-regions were defined within the time interval of 27.42 s to 28.42 s.

A dose-response curve was generated by plotting the concentration of $Ca_V2.2$ against F_{Norm}, a parameter defined as the ration of F_{hot} to F_{cold}, which further showed dose-responsiveness of the binding event. In this setup, the binding curve yielded a K_D value of 3.99 nM ± 1.33 nM for the binding of RD2 to partially purified $Ca_V2.2$ protein.

Experiments were repeated using only the fluorescent label CF-633. Analysis of the thermophoresis events after incubation with varying concentrations of $Ca_V2.2$ showed no dose-responsiveness, indicating that the thermophoretic movement of the fluorescent label is not affected by the presence of $Ca_V2.2$. The data demonstrated that CF-633 alone did not exhibit notable affinity towards the $Ca_V2.2$ protein sample (Fig. 3.22, B).

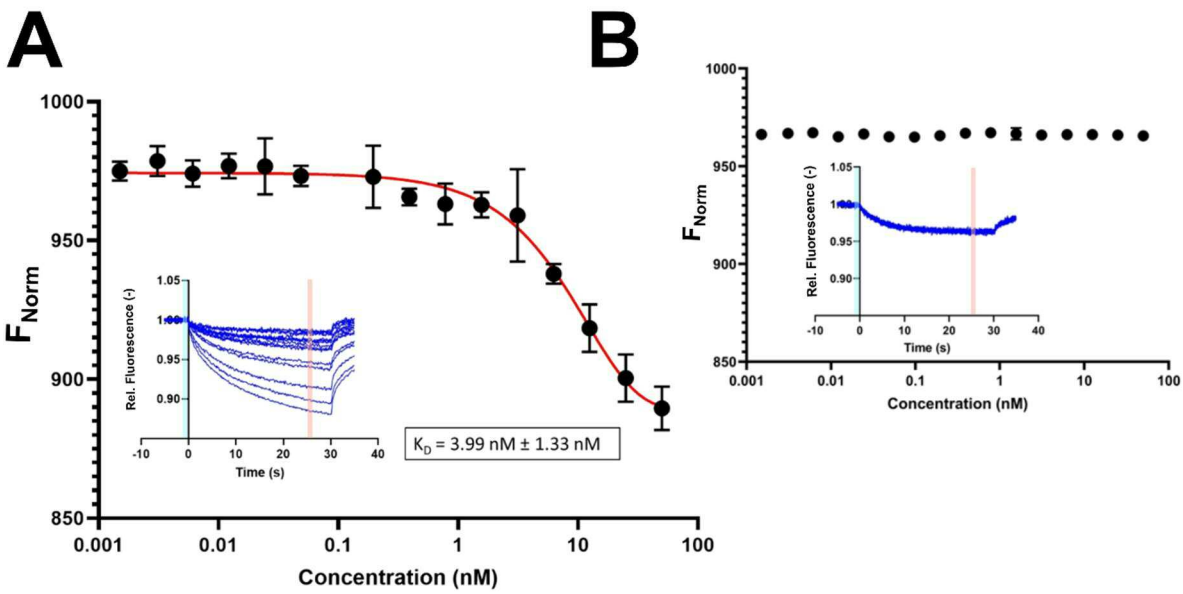

Figure 3.22: Microscale thermophoresis (MST) analysis for the determination of the dissociation constant (K_D) of the $Ca_V2.2$ and RD2 interaction Measurements for the interaction of 10 nM fluorescently labeled RD2 (**A**), or 10 nM CF-633 (**B**) with 50 nM to 1.5 pM partially purified $Ca_V2.2$ were performed at a constant temperature of 25°C, 70% LED and 40% MST power. Representative time traces of relative fluorescent signals from one measurement are shown in blue. F_{Norm} was calculated based on the time traces with regard to the cold region (-1 s to 0 s, cyan) and the hot region (27.42 s to 28.42 s, pink) and fitting was performed according to the K_D model implemented in the NanoTemper MO.Affinity Analysis software (v2.1.2333). Samples were prepared in triplicate and data is presented as representative time traces from one experiment and mean ± SEM.

3.5 *In Vivo* Ca^{2+} Imaging of Neuronal Activity in Response to a Sensory Stimulus Before and After RD2 Application

As RD2 was previously observed to reduce Ca^{2+} fluxes mediated through $Ca_V2.2$ channels in an *in vitro* assay in cells expressing $Ca_V2.2$ channels (Kutzsche, Guzman et al. 2023), it was further of interest to assess the effect of RD2 on neuronal cells in the living brain in *in vivo* experiments. Therefore, neuronal activity was analyzed via imaging of Ca^{2+} fluxes in the dorsal cortex of awake mice in response to a sensory stimulus before and after *i.p.* application of RD2.

In line with other studies using wide-field Ca^{2+} imaging to assess neuronal activity in response to a sensory stimulus, respective sensory stimulation of the right forepaw subsequently resulted in an evoked Ca^{2+} response in the contralateral left upper limb area of the primary somatosensory cortex (L-SSp-ul; Fig. 3.23). Moreover, it could be observed that a single sensory stimulus subsequently resulted in two distinct evoked responses, an early and a second later component. The early evoked response reached a maximal intensity approximately 300 ms after stimulus onset with a rapid decline in neuronal activity in this region after the stimulus, whereas a second evoked response reached its maximum later at approximately 700 ms to 800 ms after stimulus onset.

Trials with vehicle-treated animals (Ai390) did reveal a similar overall evoked activation in response to a sensory stimulus before and after *i.p.* application of 0.9% saline solution, evidenced by a comparable overall change in fluorescence pre- and post-saline (Fig. 3.23, B) with two distinct peaks at 300 ms and 700 ms after stimulus delivery onset (Fig. 3.23, C_i). In contrast to that, animals treated with RD2 (Ai382 and Ai407C) displayed an overall decrease in the amplitude of their stimulus-evoked response post-RD2 application as analyzed based on the area under the curve (AUC) compared with pre-drug trials (Fig. 3.23, B), while the time-to-peak remained constant at 300 ms after stimulus onset (Fig. 3.23, C_{ii}, C_{iiI}). Additionally, a markedly decrease of the second late stimulus-evoked response was noted following the administration of RD2. This pattern was consistently observed in all RD2-treated animals.

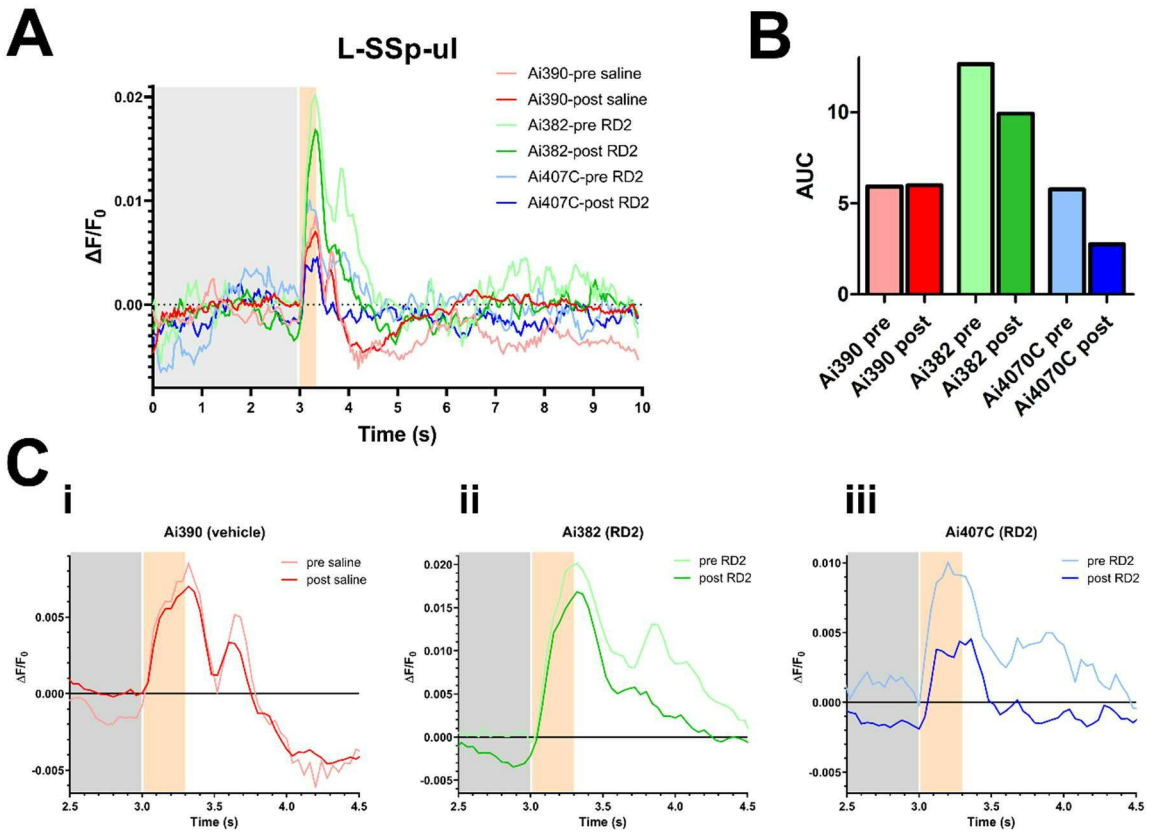

Figure 3.23: Neuronal activity in the cortex of awake mice in response to a sensory stimulus before and after RD2 application A Ca^{2+} fluxes in the cortex of awake mice were analyzed via wide-field Ca^{2+} imaging. Mice were *i.p.* injected either with the compound RD2 (Ai382, Ai407C) or the respective vehicle (Ai390) and Ca^{2+} fluxes were imaged pre- and post-injection before (grey), during (orange) and after a sensory stimulus to the right forepaw over a time period of 10 s. Neuronal activity in the left forelimb area of the primary somatosensory cortex (L-SSp-ul) is presented as the mean change in fluorescence over $n \geq 21$ (pre) and $n \geq 56$ (post) trials, normalized to baseline activity as $\Delta F/F_0$. **B** Normalized calcium traces from L-SSp-ul neurons were quantified using area under the curve (AUC). **C** Overview of the tested animals before, during and after stimulus delivery.

Further analysis was performed to assess the effects of RD2 on brain regions that additionally displayed sensory stimulus-evoked activation. In addition to the area of the primary somatosensory cortex that displays activation in response to sensory stimulation of the upper limb, the left lower limb area (L-SSp-ll) also showed a stimulus-evoked activation following a similar pattern comprising two distinct peaks, one at 300 ms and a second peak between 700 ms and 900 ms after stimulus delivery onset. RD2 administration resulted in alterations in the stimulus-evoked response, which were characterized by a decrease in peak intensity, particularly observed in the second peak, displaying a consistent pattern with previous findings in the L-SSp-ul area (Fig. 3.24, A).

Conversely, the ipsilateral primary somatosensory cortex showed no stimulus-evoked response in the upper limb area, providing evidence for a specific stimulus-evoked activation of the respective brain region in the contralateral hemisphere rather than spontaneous brain activity (Fig. 3.24, B).

Interestingly, several brain regions showed putative downstream activation following the sensory stimulus-evoked activation of the primary somatosensory cortex. The secondary motor cortex of the contralateral hemisphere (L-MO-s) as well as the anterior cingulate cortex area (L-ACA) showed evoked activation approximately 500 ms to 700 ms after onset of the stimulus. In both regions of the brain, the response amplitude displaying activation was reduced after application of RD2, but not solely using the vehicle solution (Fig. 3.24, C, D).

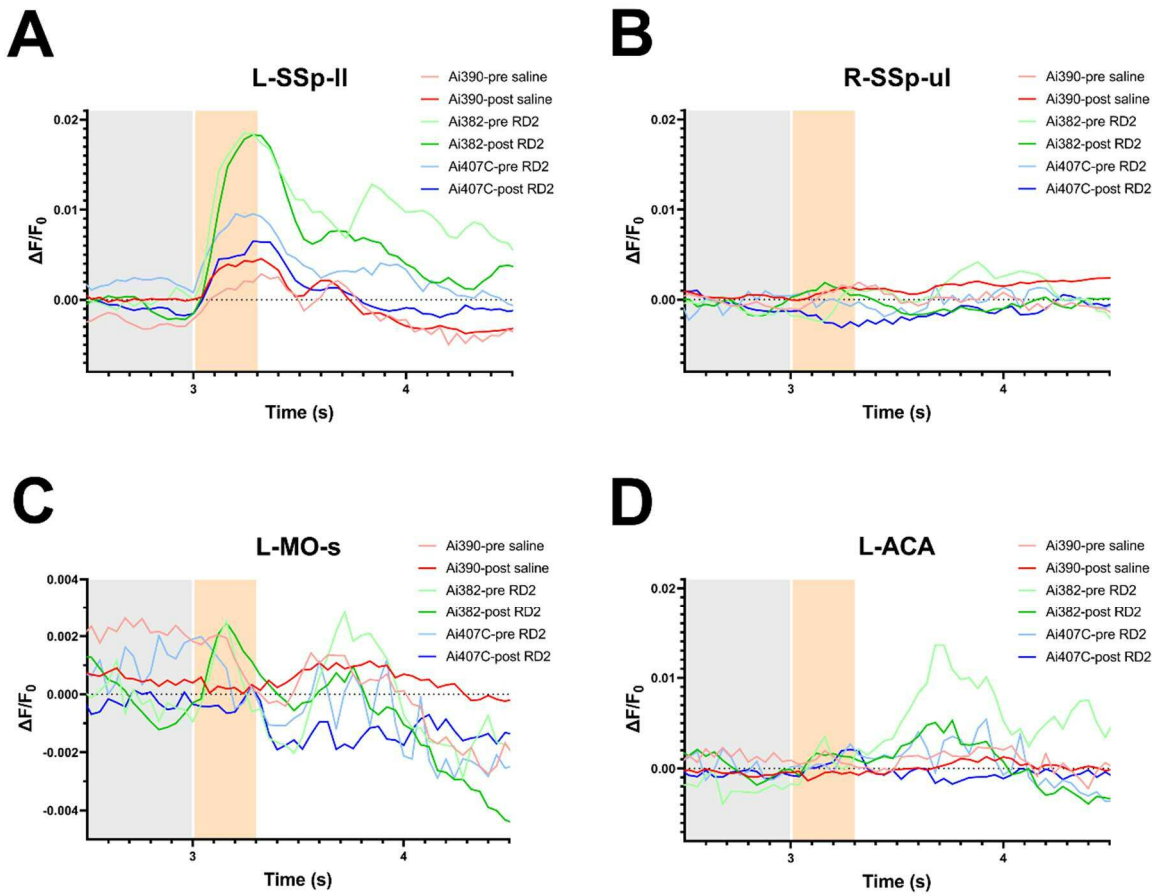

Figure 3.24: Sensory stimulus-evoked neuronal activity in different cortical areas before and after RD2 application Ca^{2+} fluxes in the cortex of awake mice in response to a sensory stimulus before and after *i.p.* administration of the compound RD2 or vehicle (saline) were analyzed via wide-field Ca^{2+} imaging. Neuronal activity in response to a sensory stimulus (orange) was assessed in the contralateral lower limb area of the primary somatosensory cortex (**A**) and in the ipsilateral upper limb area of the primary somatosensory cortex (**B**), as well as in the contralateral secondary motor cortex (**C**) and the anterior cingulate cortex (**D**). Data is presented as the mean change in fluorescence over n ≥ 21 (pre) and n ≥ 56 (post) trials, normalized to baseline activity (grey) as $\Delta F/F_0$.

Furthermore, the spatiotemporal dynamics of the cortico-cortical processing in response to the sensory stimulus were investigated in more detail. In general, it could be observed that stimulation of the right forepaw activated the secondary motor cortex 100 ms, and the primary somatosensory cortex in the upper limb area approximately 300 ms after stimulus onset, followed by an additional activation of the secondary motor cortex at 700 ms and a second late evoked activation of the upper limb area of the primary somatosensory cortex 900 ms after stimulus onset (Fig. 3.25, A, C). Following application of RD2, the amplitude of the second peak of activation in the secondary motor cortex, as well as in the primary somatosensory cortex was observed to be reduced, whereas the time-to-peak interval remained unchanged (Fig. 3.25, A)

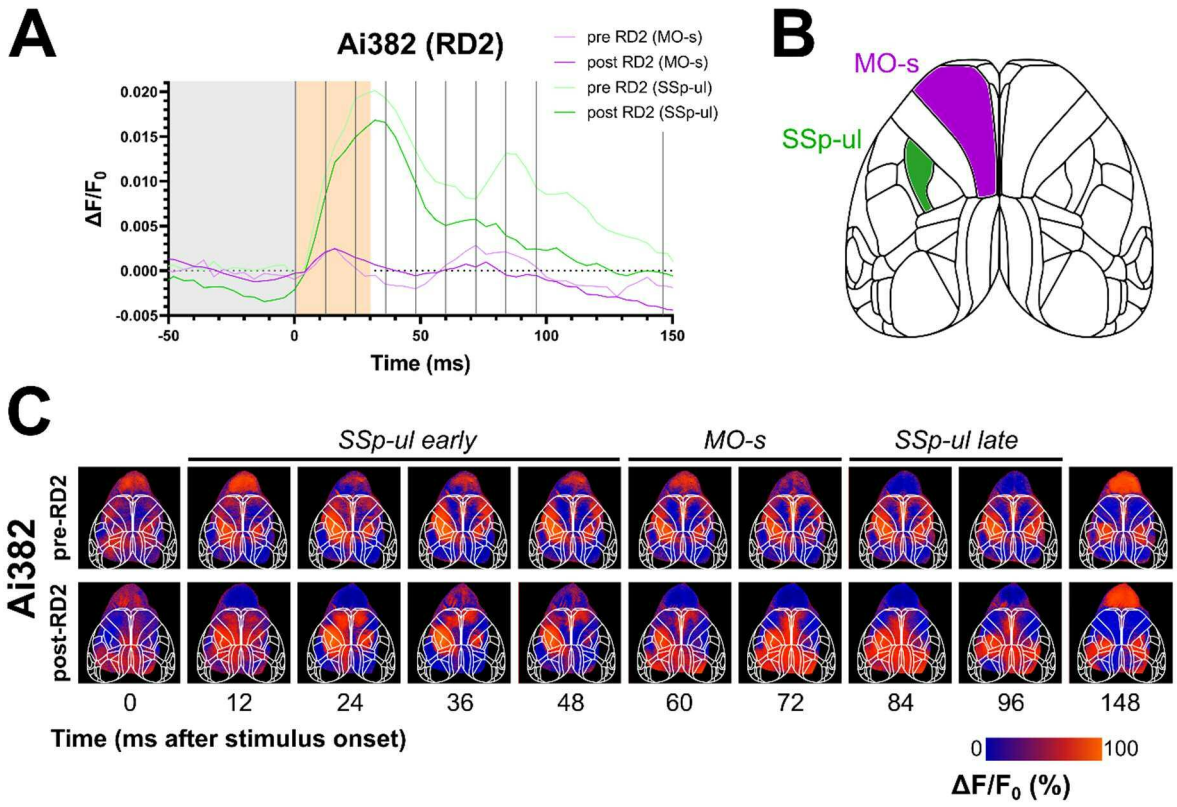

Figure 3.25: Spatiotemporal changes of sensory stimulus-evoked neuronal activity Neuronal activity in the secondary motor cortex (MO-s) and the upper limb area of the somatosensory cortex on the contralateral side (SSp-ul) to a sensory stimulus (orange) was measured using Ca^{2+} wide-field imaging. **A** Ca^{2+} fluxes are presented as the mean change in fluorescence over n ≥ 21 (pre) and n ≥ 56 (post) trials of one exemplary mouse, normalized to baseline activity (grey) as $\Delta F/F_0$. **B** Respective analyzed cortical regions, identified based on the mouse brain atlas from the Allen Institute. **C** Average evoked responses to a sensory forepaw stimulation before (pre) and after (post) application of RD2 for one exemplary mouse presented as heat map of $\Delta F/F_0$ over the dorsal cortex.

Other brain regions did not show a significant difference in the sensory stimulus-evoked activation between subjects treated with saline as vehicle or RD2-treated animals, when comparing the pattern of Ca^{2+} response before and after injection (data not shown).

3.6 Identification of New Putative $Ca_V2.2$-Binding and -Inhibiting Peptides via Phage Display Selection

To identify new putative $Ca_V2.2$-binding and -inhibiting peptides, a phage display screen was performed on partially purified $Ca_V2.2$, with a TriCo-16 phage display peptide library as the source of peptides. This library contains randomized sequences encoding a 16-mer peptide library with a capacity of 2.6×10^{10} unique peptides. The selection was performed following two different strategies. In the first strategy, bound phages were eluted via a drop in pH. Three successive selection rounds were performed to enrich phages that show required high binding affinity to the target protein. For more specific selection of phages displaying peptides that exhibit a similar binding mode as known $Ca_V2.2$ channel inhibitors, a second strategy using competitive elution was performed with ω-CgTx GVIA. Although an increased output titer was observed after the first round of target selection using pH-based elution when compared with empty selection, the following rounds of selection markedly reduced the overall number of phages in all selections (Fig. 3.26, A). No increase in number of phages was observed in target selection of round 2 and 3 compared to the respective direct control or empty selection. A similar trend of reduced overall number of phages in selection rounds 2 and 3 was observed following competitive elution (Fig. 3.26, B). Interestingly, in contrast to the other selection approach, an increase in the phage output titer was observed in the target selection compared with empty selection and direct control after three rounds of selection. To further analyze the $Ca_V2.2$-specific affinity of selected phages, an enrichment ELISA was performed. Examination of the initial affinity of the phage library prior to selection revealed a low binding affinity, indicating a modest enrichment of $Ca_V2.2$-binding phages already present in the library for both selection strategies (Fig. 3.26, C and D). During phage display selection, a noticeable enrichment of phages that exhibit specific binding to immobilized $Ca_V2.2$-containing protein samples was observed, as evidenced by the gradual increase in $Ca_V2.2$-specific association signals in the enrichment ELISA.

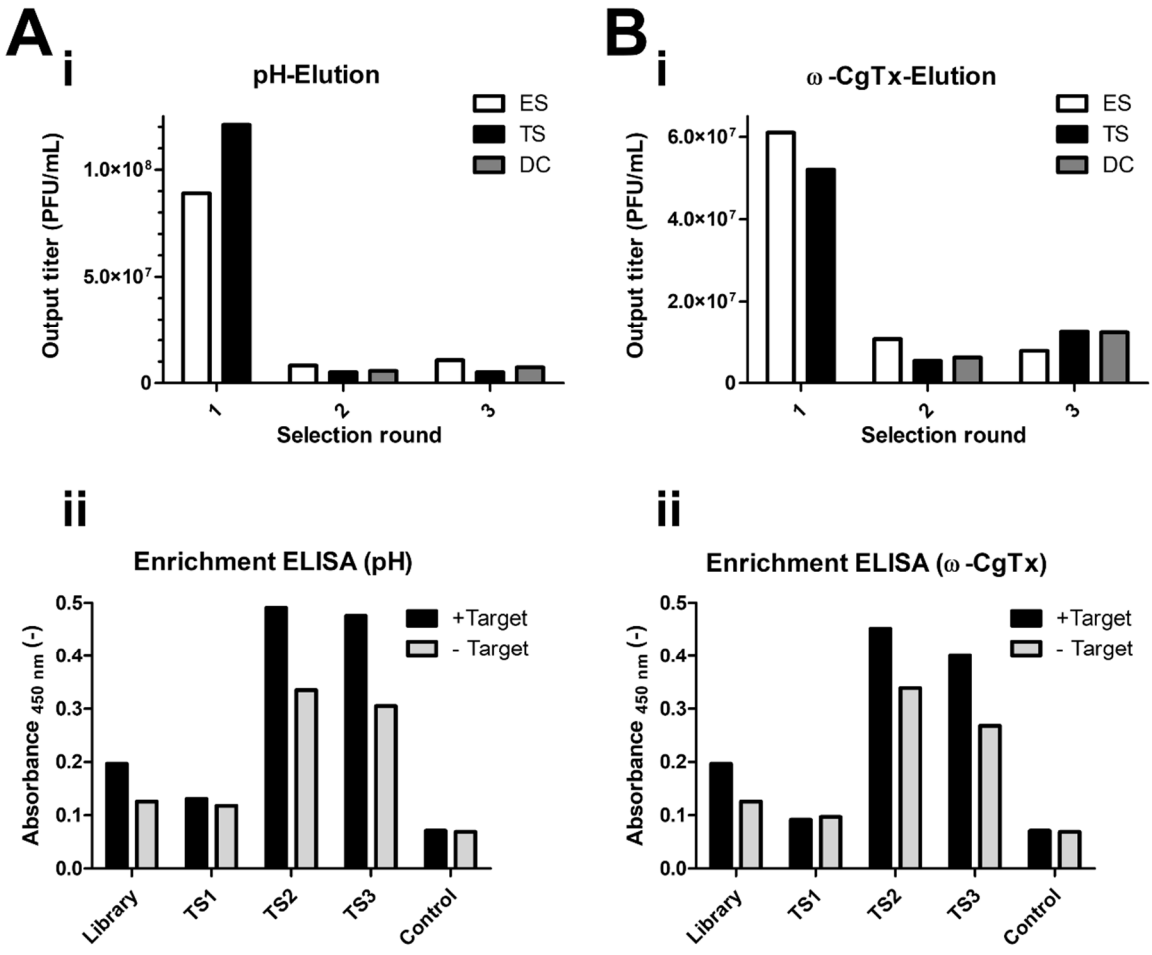

Figure 3.26: Phage display selection on $Ca_V2.2$ Two strategies for peptide selection via phage display screening were performed on immobilized partially purified $Ca_V2.2$ protein, either by eluting bound phages via pH-elution (**A**) or via competitive elution using the known $Ca_V2.2$ inhibitor ω-CgTx GVIA (**B**). **A_i**, **B_i** Output titers were determined for target selection (TS), empty selection (ES) and direct control (DC) of each phage selection round and are presented as the number of plaque-forming units per volume (PFU/mL). **A_{ii}**, **B_{ii}** For verification of the target-specificity of the selected peptide-displaying phages, relative binding affinities of selected phages towards $Ca_V2.2$-coated (+ Target), or empty surfaces (- Target) were determined in an enrichment ELISA.

All sequences of putative $Ca_V2.2$-binding peptides were obtained by NGS and subsequently analyzed with regard to target specificity and enrichment via TSAT analysis. Sequencing of the peptides that were selected based on the strategy using pH elution revealed a total number of 205,176 sequences. The selection strategy, using competitive elution, resulted in 185,792 identified sequences. Analysis of enriched specific $Ca_V2.2$-binding peptides via TSAT filtered sequences to a final number of 37,576 peptides for pH-based elution, whereas elution with ω-CgTx GVIA resulted in 31,417 sequences of putative $Ca_V2.2$-binding peptides.

Ranking of the sequences was performed according to the respective empty and enrichment scores. In the pH-based selection, the highest-scoring identified peptide with regard to empty score showed a 340-fold increased abundancy in the target selection compared with empty selection, but exhibited only slight 17-fold enrichment compared with its frequency in the phage library. Further peptides were identified, displaying approximately 100-fold to 200-fold increased frequency in the target selection compared with the empty selection. These peptides further exhibited enrichment scores up to 440. Highest-scoring peptide sequences were selected for binding analysis with $Ca_V2.2$ (Tab. 3.1).

In the second selection strategy, using ω-CgTx GVIA for competitive elution of phages that potentially display peptides which show a similar binding motif to known channel inhibitors, the peptide with the highest enrichment and highest target specific enrichment displayed and empty and enrichment score of 240. Several more sequences with high empty or enrichment scores were selected as putative $Ca_V2.2$-specific binding peptides (Tab. 3.1).

Table 3.1: Ranking of peptides selected in $Ca_V2.2$-phage display with pH elution or competitive elution using ω-CgTx GVIA Peptides were ranked based on their respective Empty Score (EmS) and Enrichment Score (EnS).

Selection strategy I: pH				Selection strategy II: ω-CgTx GVIA			
Name	**Sequence**	**EmS**	**EnS**	**Name**	**Sequence**	**EmS**	**EnS**
EW7	YFPYDWWYTHPGGAND	342	16.8	EW1	SWEYSHQPSRHAGVVP	240.2	240.3
EW8	KHTNEAYPQWHTRHNV	221.3	391	EW2	HVHKSYWSWPRHLQEH	180.1	25.8
EW9	TKSPFPNLPEGPITRY	207.2	11.4	EW3	WPHEEHLQHMHSNTTW	160.8	20.1
EW10	WTNQNQQAPMKKHAWR	205.2	362.6	EW4	QQQHHYTWGWSGGKVP	131.7	263.6
EW11	HKASADREQAHPHLYR	203.2	359	EW5	SFTQVFASKPYMHQMK	125.9	126
EW12	HPHKERSWAPHYWAAH	124.7	440.8	EW6	SFTQTAYNHVEYGHNW	124	248.1
				EW13	YQWHPPEQAALKNHIP	110.4	221
				EW14	QAYHYPTDHIQRKVMH	6	891.6

Cluster analysis using Hammock did not reveal any significant common binding motif and was therefore not used for identification of putative $Ca_V2.2$-binding peptides.

3.7 Lead Optimization of RD2 with regard to $Ca_V2.2$ Inhibition

In addition to screening strategies on purified $Ca_V2.2$ protein to identify new putative binding motifs for the inhibition of $Ca_V2.2$ channels, the study aimed to optimize the lead compound RD2, previously observed to bind and specifically inhibit $Ca_V2.2$-mediated currents. The primary objective of this investigation was to enhance the efficacy and specificity of RD2 in terms of its binding and inhibition of $Ca_V2.2$ channels without compromising its advantageous characteristics such as oral bioavailability, BBB permeability and its excellent safety profile. Initially, lead optimization was performed by rational design, exchanging key amino acid residues to modify the respective $Ca_V2.2$-specific binding and inhibition capacity. Identified novel D-peptides were subsequently characterized with regard to toxicity and inhibition kinetics.

3.7.1 Rational Design for Lead Optimization of RD2

Rational design was used to optimize the lead compound RD2 with regard to increased $Ca_V2.2$ binding affinity and channel inhibition capacity. Through substitution of putative key residues with amino acids containing conserved groups that display similar or different biophysical properties, this study aimed to identify central motifs in the peptide sequence, subsequently facilitating the targeted optimization of the $Ca_V2.2$-inhibition potential of these peptides.

The RD2-based designed D-peptides RD2A-E each featured three sequence mutations, including the substitution of two amino acids to residues with semi-conserved properties (T2S, L3V) as well as the replacement of a histidine residue to phenylalanine to introduce analogous characteristics (H4F). The N-terminal proline residue as well as the penta-arginine stretch at the C-terminus remained unchanged. D-peptides RD2B-E featured further variance through substitution of a fourth amino acid, replacing either T5, H6 or N7 with a conserved or semi-conserved residue (Fig. 3.27).

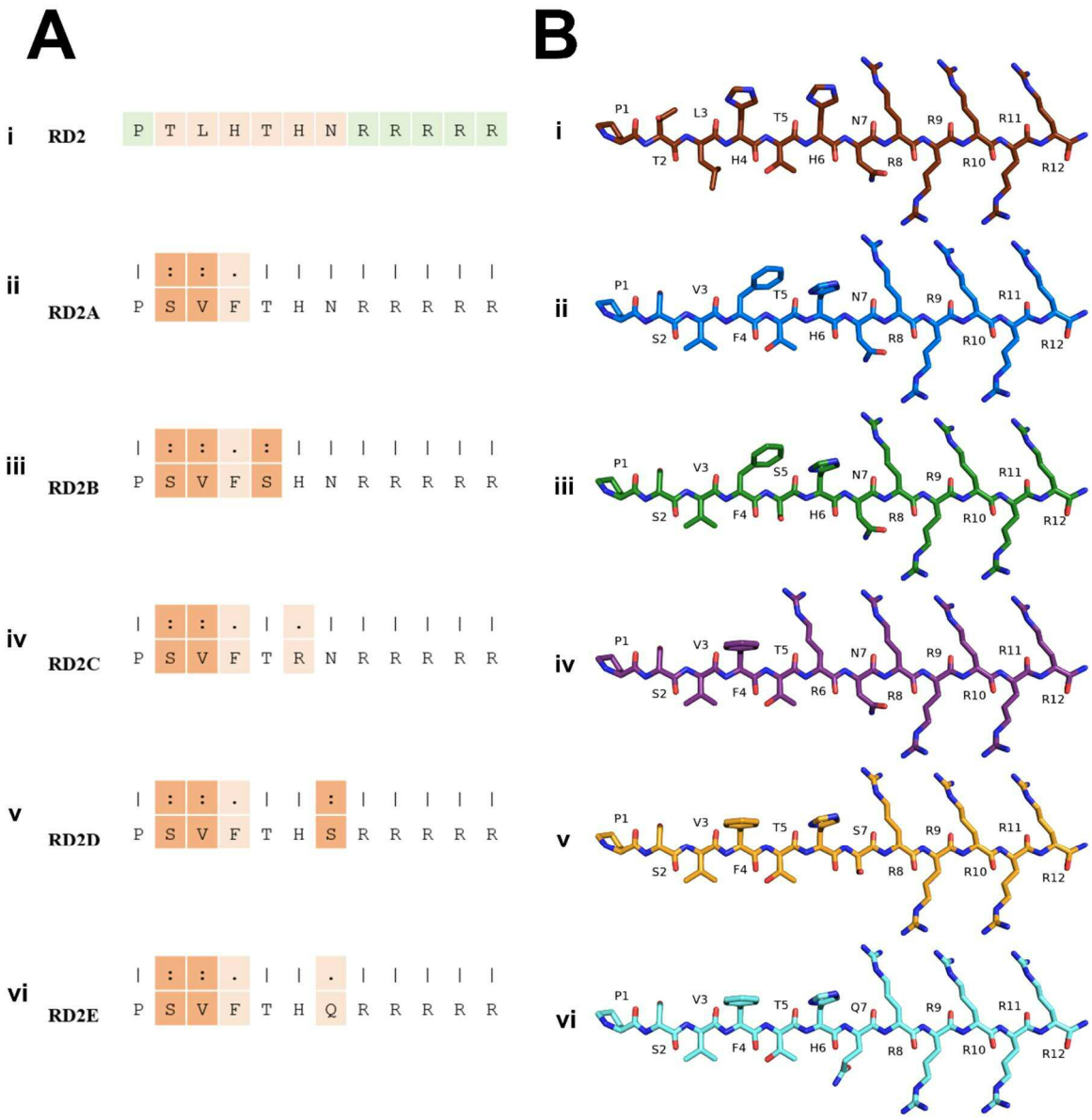

Figure 3.27: Amino acid sequences of RD2 and RD2-derived D-peptides A Pairwise sequence alignment of RD2 and RD2-derived D-peptides (**i** RD2, **ii** RD2A, **iii** RD2B, **iv** RD2C, **v** RD2D, **vi** RD2E) with highlighted sequence differences (orange). Sequence similarities are indicated by | (line) and amino acid exchanges to conserved groups exhibiting strongly similar properties are marked by **.** (point), whereas semi-conserved substitutions are indicated by **:** (colon). **B** Schematic structure of RD2 and RD2-derived D-peptides were prepared in PyMol with labeled residues and colored by heteroatom (N: blue, O: red).

3.7.1.1 $Ca_V2.2$ Inhibition by RD2-Derivatives

In an electrophysiological screening approach, the RD2-derived D-peptides RD2A-E were tested regarding their potential to inhibit $Ca_V2.2$-mediated currents. Measured currents were almost completely abolished after perfusion with the known $Ca_V2.2$ inhibitor ω-CgTx GVIA, showing an inhibition of currents of over 90%. This result facilitated a precise attribution of the analyzed currents to $Ca_V2.2$ channels. Of all RD2-derived D-peptides, only RD2C showed fast and significant channel inhibition of approximately 40%, whereas other candidates only led to a reduction of $Ca_V2.2$-mediated currents of under 15% (Fig. 3.28, A). Moreover, all RD2-derived D-peptides displayed a substantial recovery rate of currents after $Ca_V2.2$ inhibition, with each D-peptide exhibiting over 85% relief shortly after wash-out of the compound. Conversely, ω-CgTx GVIA was observed to block $Ca_V2.2$ channels irreversibly, showing close no recovery of $Ca_V2.2$-mediated currents after wash-out (Fig. 3.28, B).

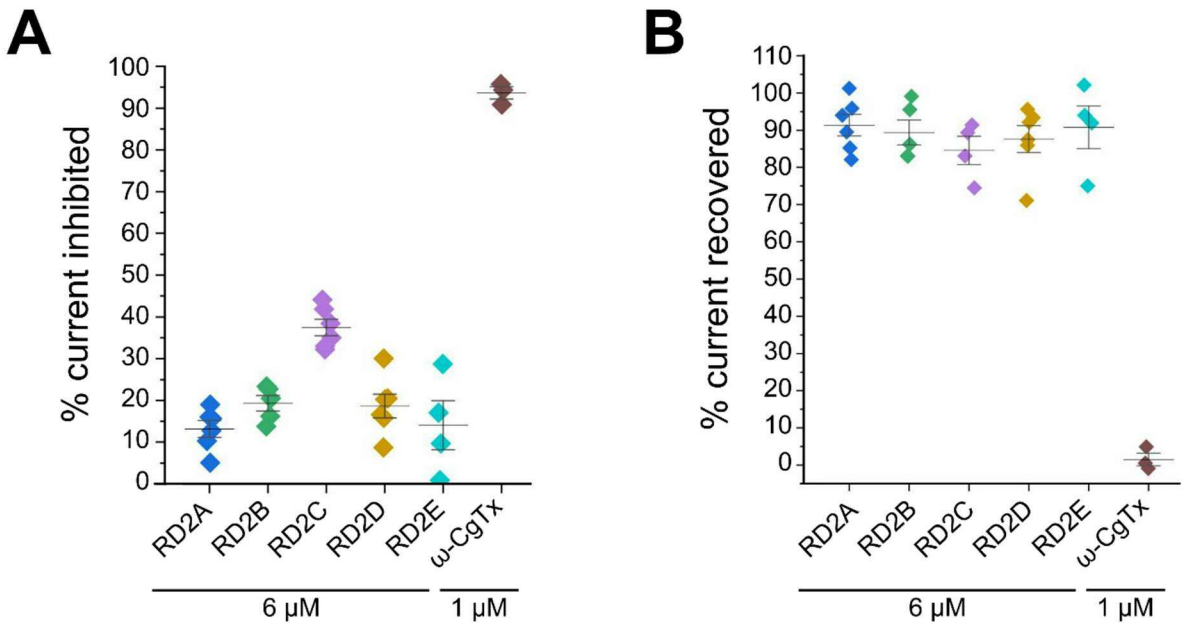

Figure 3.28: Inhibition of $Ca_V2.2$ channels by RD2-derived D-peptides **A** Inhibitory property of RD2-derived D-peptides RD2A-E (n = 6) and ω-CgTx GVIA (n = 3) on $Ca_V2.2$-mediated ionic currents. **B** Recovery potential of $Ca_V2.2$-mediated currents after blocking through RD2A-E (n ≥ 4) or ω-CgTx (n = 3). Data presented as individual measurements and mean ± SEM.

3.7.1.2 Comparison of RD2-Derived Compound RD2C with Known $Ca_V2.2$ Inhibitors

Previous results identified the RD2-derived D-peptide RD2C as most promising candidate for the specific inhibition of $Ca_V2.2$-mediated currents. To assess the functional effects of RD2-derivatization to RD2C on $Ca_V2.2$-specific inhibition, $Ca_V2.2$-mediated currents were analyzed in electrophysiological experiments before, during and after application of the compounds. In addition, compounds RD2 and RD2C were compared with the known specific channel inhibitor ω-CgTx GVIA as positive control.

Application of all tested compounds, but not perfusion with the external solution alone, resulted in a significant decrease of $Ca_V2.2$ mediated currents (Fig. 3.29, A). The known inhibitor ω-CgTx GVIA almost completely attenuated $Ca_V2.2$-mediated currents at a concentration of 1 µM, reducing peak currents by approximately 93.7% ± 1.5% (Fig. 3.29, B). Blocking of $Ca_V2.2$ channels by ω-CgTx GVIA was further observed to be irreversible, as only 1.5% ± 1.7% of $Ca_V2.2$-mediated currents were observed to recover after wash-out of the compound (Fig. 3.29, C).

In contrast to this, application of 6 µM of the lead compound RD2 was able to reduce $Ca_V2.2$-mediated currents by 15.3% ± 1.8%. At equivalent concentrations, the RD2-derivative RD2C exhibited rapid attenuation of $Ca_V2.2$-mediated currents by 37.4% ± 2.1%, indicating a significant enhancement of blocking activity relative to RD2-mediated inhibition (Fig. 3.29, B, $p = 0.00002$). Removing of compounds by washing-out with external solution was analyzed to determine the recovery rate of currents after channel inhibition. An overall rapid and high relief from RD2 and RD2C-mediated inhibition of $Ca_V2.2$ channels was found. Shortly after wash-out of the compounds, $Ca_V2.2$-mediated currents returned back to 87.1%± 2.2% after blocking by RD2, and 84.6%± 3.7% of the current recovered after RD2C-dependent inhibition (Fig. 3.29, C), indicating a reversible inhibition of $Ca_V2.2$ channels by both substances.

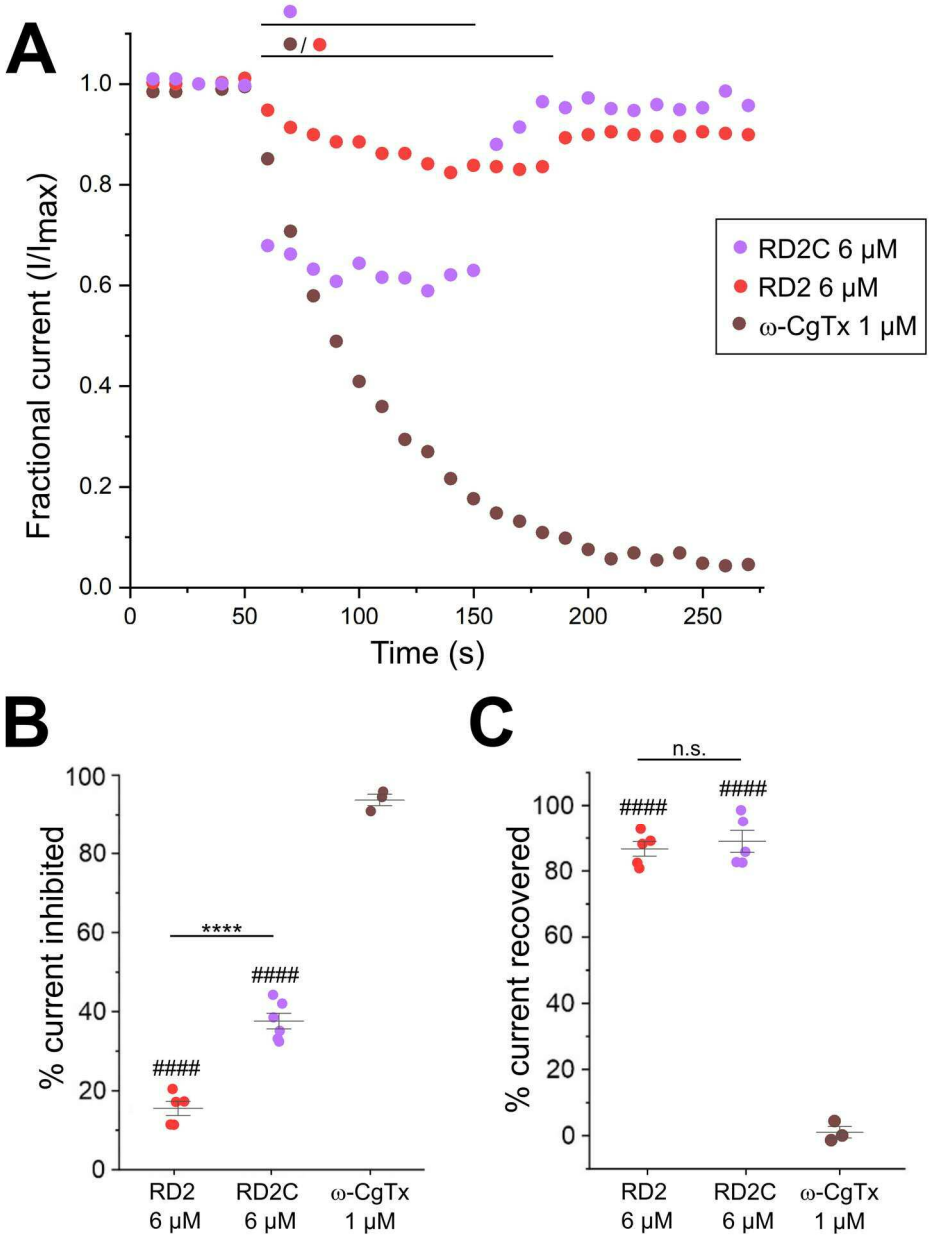

Figure 3.29: Inhibition of $Ca_V2.2$ channels by RD2-derived D-peptide RD2C compared with known inhibitors A Inhibition curve of $Ca_V2.2$-mediated currents after RD2, RD2C or ω-CgTx GVIA application, displayed as fractional current (I/I_{max}) over time. Perfusion of the testing substance was performed over a time frame indicated by the black lines. **B** Inhibition properties of RD2 (n = 5), RD2C (n = 6) and ω-CgTx GVIA (n = 3) on $Ca_V2.2$-mediated ionic currents. **C** Recovery potential of $Ca_V2.2$-mediated currents after blocking through RD2 (n = 5), RD2C (n = 5) or ω-CgTx (n = 3). Data presented as mean ± SEM. Statistical analysis was performed using one-way ANOVA followed by Tukey's post-hoc test with n.s. (non-significant), or * $p < 0.05$, ** $p < 0.01$, *** $p < 0.001$ and **** $p < 0.0001$ vs. indicated group and $^{\#}p < 0.05$, $^{\#\#}p < 0.01$, $^{\#\#\#}p < 0.001$, $^{\#\#\#\#}p < 0.0001$ vs. ω-CgTx.

3.7.1.3 RD2C-Mediated Inhibitory Effects on $Ca_V1.2$ Channels

As the different VGCC subtypes display high sequence and structural homology, it was of special interest to analyze the subtype specificity of the inhibitory capacity of RD2C more in detail, in particular with regard to putative inhibitory effects of RD2C on L-type channels. L-type $Ca_V1.2$ channels are known to be susceptible to inhibition by nifedipine, resulting in a rapid and significant reduction of $Ca_V1.2$-mediated currents by 87% (Fig. 3.30, A, B). In contrast, application of RD2C did not exert any substantial effects on $Ca_V1.2$-mediated currents, with only a minimal inhibition of $Ca_V1.2$-mediated currents of under 10% (8.6%). After wash-out of the compounds RD2C as well as nifedipine, a rapid recovery of $Ca_V1.2$-mediated currents (88.8% and 87.3%) was observed (Fig. 3.30, A, C).

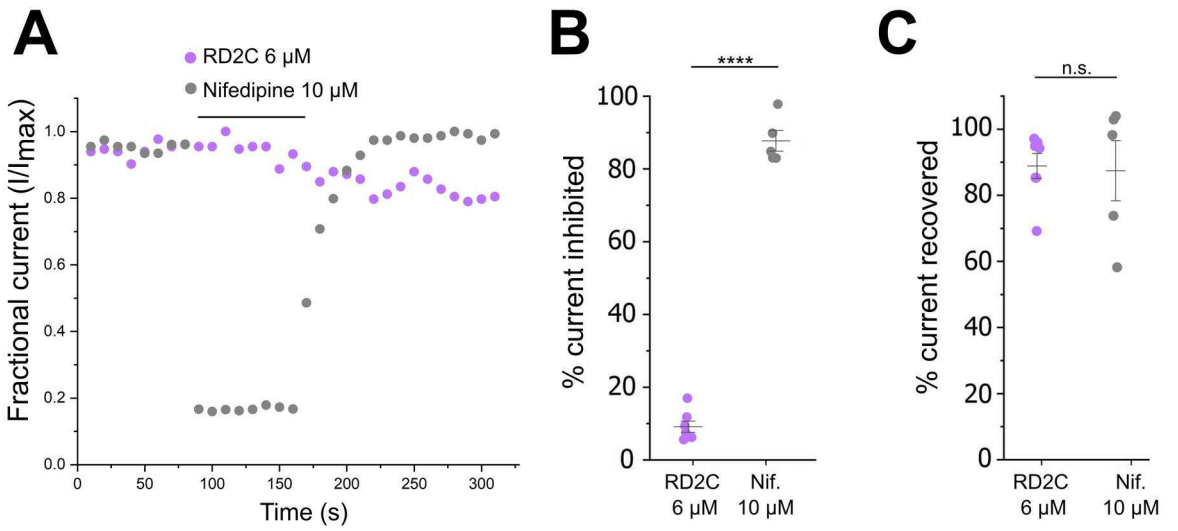

Figure 3.30: Effect of RD2-derived D-peptide RD2C on $Ca_V1.2$ channels A Inhibition curve of $Ca_V1.2$ by RD2C or nifedipine displayed as fractional current (I/I_{max}) over time. Perfusion of the testing substance was performed over a time frame indicated by the black line. **B** Inhibition properties of RD2C (n = 6) and nifedipine (n = 5) on $Ca_V1.2$-mediated ionic currents displayed as percentage of remaining currents in the presence of the compound. **C** Recovery potential of $Ca_V1.2$-mediated currents after blocking through RD2C or nifedipine. Data presented as scatter dot plot and mean ± SEM. Statistical analysis was performed using one-way ANOVA followed by Tukey's post-hoc test with n.s. (non-significant) or * $p < 0.05$, ** $p < 0.01$, *** $p < 0.001$ and **** $p < 0.0001$ vs. indicated group.

3.7.1.4 Toxicity of RD2-Derivative RD2C In Vitro

Analysis of the cellular toxicity of the D-enantiomeric peptide RD2 and its derived D-peptide RD2C was assessed performing MTT assays on neuroblastoma SH-SY5Y cells. Measurements were conducted in quadruplicate and the mean values were compared relative to the cell viability in medium. Cells incubated in 0.1% Triton-X 100 showed close to no viability after incubation, whereas incubation of the cells with vehicle solution (ddH_2O) resulted in similar viability levels compared to cells incubated in medium. Neither RD2 nor its derivative RD2C did exhibit negative effects on cellular survival *in vitro* (Fig. 3.31). Interestingly, it was observed that low concentrations of RD2, and more notably RD2C, were associated with an increase in cell viability compared with negative controls. This effect was negatively correlated with the respective D-peptide concentration.

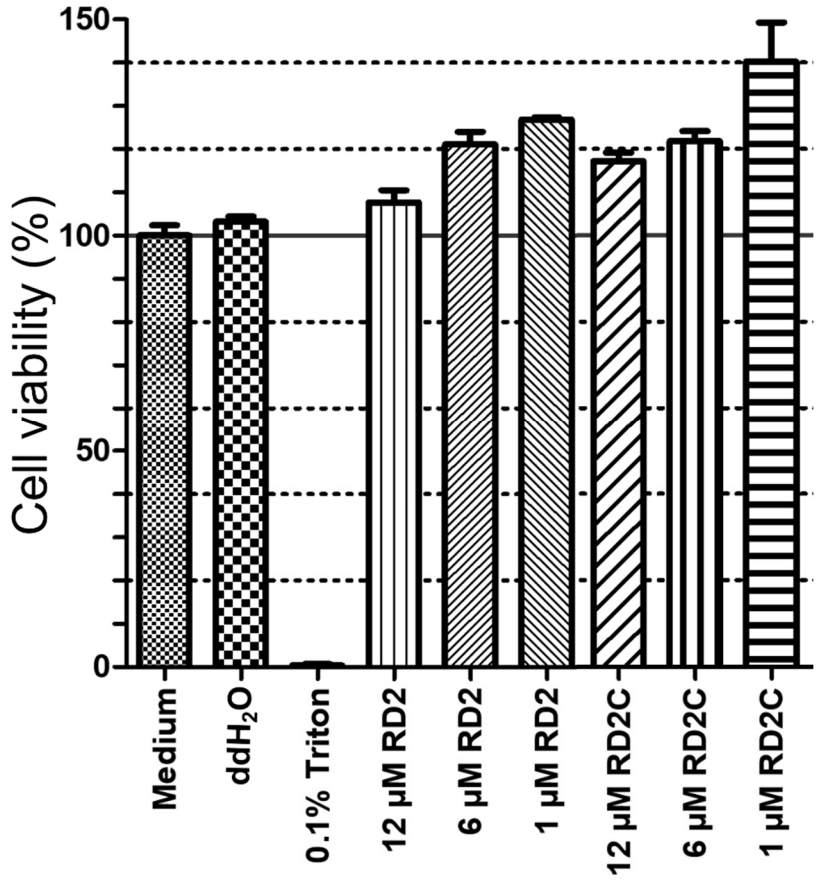

Figure 3.31: Cell viability assay of RD2 and RD2C in SH-SY5Y cells *In vitro* toxicity of RD2 and its derivative RD2C was assessed via MTT assay by determining cell viability of SH-SY5Y cells after application of different concentrations (1 µM, 6 µM and 12 µM) of D-peptides (RD2 and RD2C). Positive controls, using 0.1% Triton X-100, as well as negative controls with medium and ddH_2O as solvent were additionally analyzed. Data presented as mean (n = 4) ± SEM normalized to the medium control (= 100%, black line).

3.8 Peptide Docking Modeling

In addition to *in vitro* proof of concept of the inhibitory capacity of D-peptides on $Ca_V2.2$-mediated currents, putative binding modes and respective motifs of RD2 and the most promising lead-optimized D-peptide RD2C were analyzed more in detail using an *in silico* approach employing peptide docking modeling.

3.8.1 Putative Binding Modes of RD2 on $Ca_V2.2$

To identify putative binding modes of the D-peptide RD2 on $Ca_V2.2$ channels, peptide/receptor docking simulations were performed based on the previously defined structural model of the ziconotide binding groove on $Ca_V2.2$ channels. Using the docking software HPEPDOCK 2.0 (Huang and Zou 2008; Zhou, Jin et al. 2018; Tao, Zhang et al. 2020) the minimal structural model of the ziconotide binding groove of $Ca_V2.2$ was provided as static receptor input and the D-enantiomeric structure of RD2 was further used as peptide input. During the docking process of the D-peptide onto the $Ca_V2.2$ structure, the respective minimization algorithm resulted in the reconstruction of the peptide structure into proteinogenic L-enantiomeric conformation. This led to the characterization of the binding mode of an L-peptide onto an L-protein. As insights into the contribution of the stereochemical confirmation of the peptide in association with the channel was of specific interest, a mirror-image docking approach was used as an alternative. For this, the D-enantiomeric structural version of the $Ca_V2.2$ binding groove was created to subsequently dock the L-enantiomeric RD2 peptide, using the same approach as previously described. The 100 highest-scoring docking models were analyzed with regard to their putative binding mode, focusing on the specific pattern of residues involved in the interaction on both the channel and peptide sides. In general, three distinct overall binding modes could be identified for RD2 in docking models on the $Ca_V2.2$ ziconotide binding groove. Peptides were observed to either bind inside the binding groove and close to the Ca^{2+}-permeable pore (BG; Fig. 3.32), were associated with residues from below (intracellularly) the Ca^{2+}-permeable pore (below binding groove) or were found associated with putative allosteric binding sites at membrane-associated outer regions of the channel (allosteric binding).

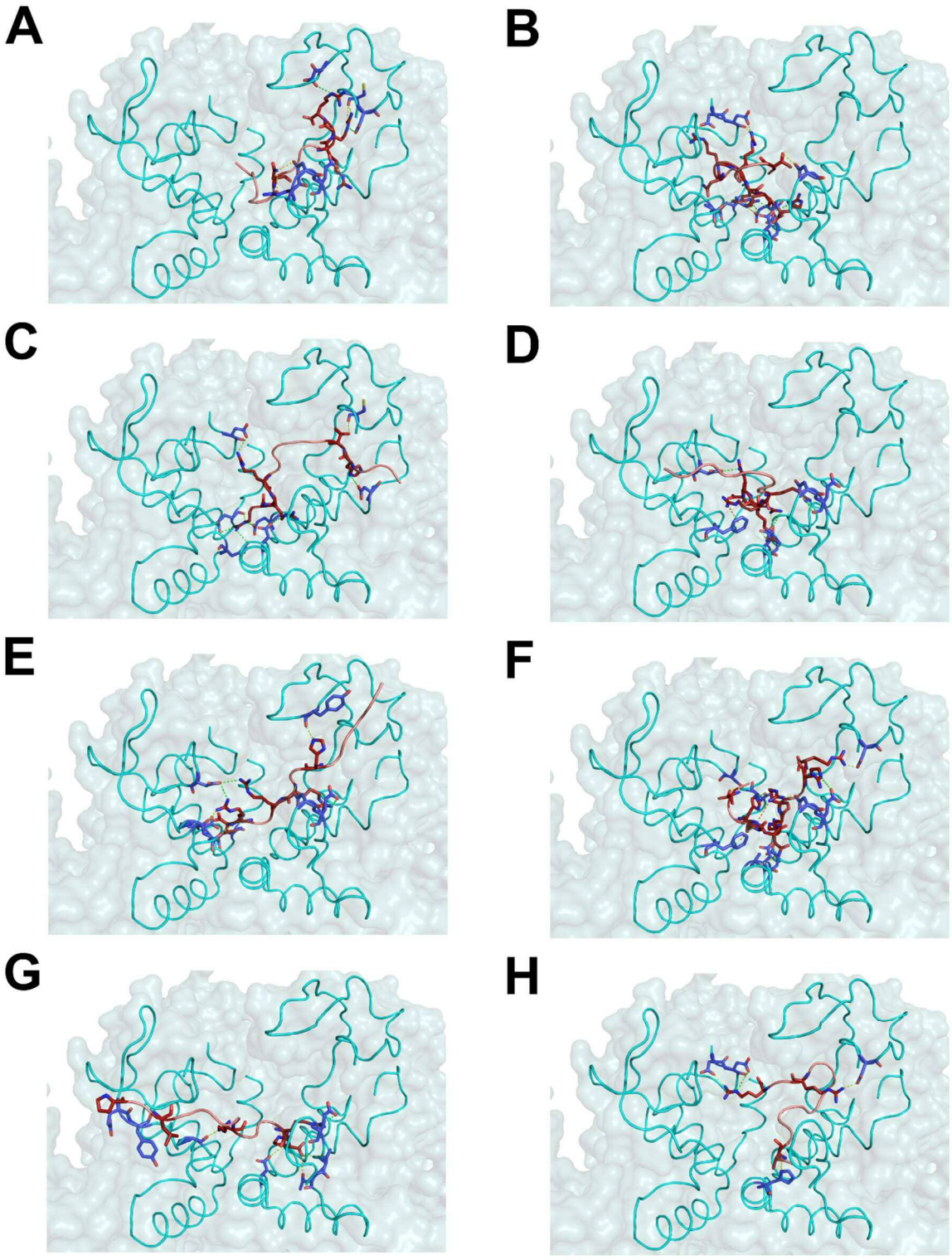

Figure 3.32: Peptide docking models showing putative binding modes of RD2 on $Ca_V2.2$ in the ω-CgTx binding groove Docking models, amongst 20 highest-scoring models, displaying an association of RD2 with $Ca_V2.2$ inside the binding groove. RD2 (salmon) binds $Ca_V2.2$ (cyan) at the pore-forming domain in different binding modes (**A-H**) revealing a putative pore-blocking mechanism. The interaction is mediated by hydrogen bonds (yellow dashed lines), salt bridges (green dashed lines) and π interactions (orange dashed lines) between different amino acid residues of RD2 (red) and $Ca_V2.2$ (blue) and further stabilized by other non-bonded contacts. All structure figures were prepared in PyMol.

To further investigate the binding mode of RD2 on $Ca_V2.2$ channels as observed in the 100 best-scoring docking models, a detailed analysis was conducted on the peptide residues engaged in the interaction with the channel and the corresponding formed contacts (Fig. 3.33). Hydrogen bonds (HB), salt bridges (SB) as well as other non-bonded contacts (NBC) were observed to contribute to the binding of RD2 residues with $Ca_V2.2$ regions, exhibiting variability in their involvement across different binding modes. Overall, a clear tendency of the C-terminal arginine-rich portion of RD2 (R8-R12) to engage in hydrogen bonds as well as salt-bridging interactions was consistently observed across all docking models. Charged and polar residues of RD2 (T2, H4, T5, H6, N7) were further involved in stabilization of the interaction via formation of additional hydrogen bonds. Moreover, the histidine residues were found to partake in formation of salt bridges in the interaction. Non-bonded contacts, such as hydrophobic interactions or contacts facilitated via van der Waals forces, were detected among all RD2 residues, particularly highlighting C- and N-terminal portions along with histidine residues H4 and H6 and arginine residue R8. Comparison of the top 100 models with models that specifically show a peptide docking mode within the binding groove revealed a similar overall contribution of the RD2 residues in a comparable contact manner. However, a tendency towards an increased number of contacts per model was observed for peptides associated with the binding groove (Fig. 3.33).

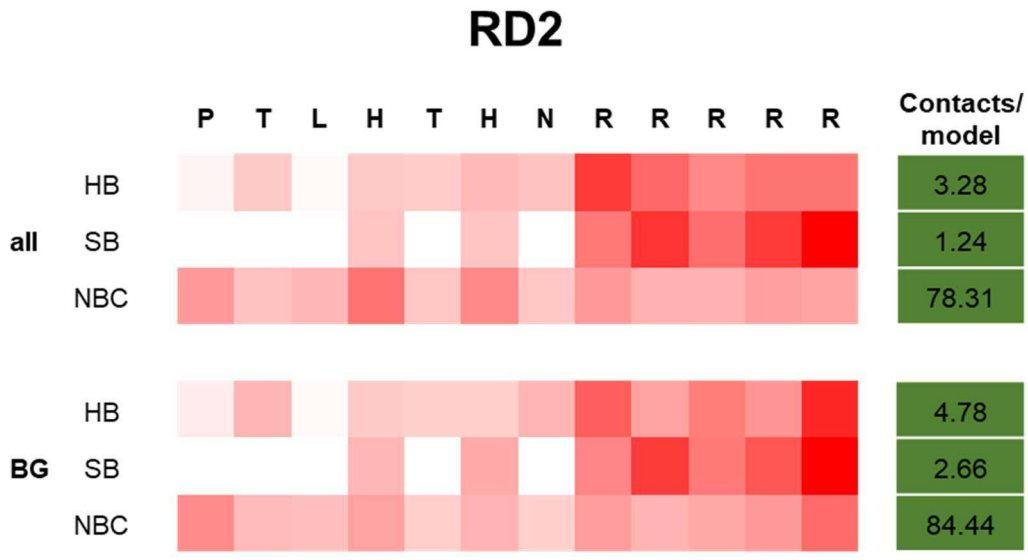

Figure 3.33: Contacts formed by RD2 residues in different docking models simulating the binding to $Ca_V2.2$ Putative binding modes of RD2 with $Ca_V2.2$ at the ω-CgTx binding groove were analyzed with regard to the residue-specific contribution and type of formed contact. Top 100 docking models (all), or docking models showing a binding groove-associated binding mode (BG) were analyzed with regard to their residue-specific contribution in formation of hydrogen bonds (HB), salt bridges (SB) or other non-bonded contacts (NBC). Contributions of the individual residues are expressed as the ratio of all specific associations of that residue type per model, whereby darker red indicates higher contribution of the residue in the respective contact type.

To assess the putative binding mode underlying the three identified classes of overall docking modes more in detail, the contribution of different types of contacts, formed between residues of RD2 and $Ca_V2.2$, was analyzed and compared between all three classes.

As previously observed, the C-terminal region of RD2, particularly arginine residues R8 and R12, were found to be strongly engaged in the formation of hydrogen bonds with residues of $Ca_V2.2$ in docking models showing peptide binding within the binding groove at a frequency of on average 4.8 hydrogen bonds formed per model (Fig. 3.34, HB). Conversely, although a similar engagement of the arginine-rich C-terminal region of RD2 was observed in hydrogen-bonded contacts in models showing association of the peptide below the Ca^{2+}-permeable pore of $Ca_V2.2$, a lower frequency of formed interactions with only 2.25 contacts per model was observed. In contrast to docking models showing RD2 situated within or underneath the binding groove, models in which RD2 was docked in a putative allosteric binding mode external to the groove exhibited a less distinct association of the C-terminal region of RD2 over hydrogen bonds. Although C-terminal arginine residues showed association with $Ca_V2.2$ over hydrogen bonds, the overall contribution was reduced compared with docking models showing RD2 binding in the binding groove. Furthermore, a reduced number of hydrogen bonds was formed on average per model. A similar pattern could be seen when assessing the putative association of RD2 with $Ca_V2.2$ residues over the formation of salt bridges (Fig. 3.34, SB). In peptide docking models showing RD2 associated within the binding groove domain of $Ca_V2.2$, salt bridges were formed between C-terminal arginine residues, predominantly R9 and R12, as well as to a lower extent over histidine residues H4 and H6. On average, 2.66 putative salt bridges were observed to be formed per model. In contrast, in peptide docking models where RD2 was engaged with $Ca_V2.2$ below the Ca^{2+}-permeable pore or at a putative allosteric binding site, a significantly reduced association over formation of salt bridges was observed. Peptide docking models categorized in the “below binding groove” class displayed on average 0.63 contacts per model, and models exhibiting allosteric binding form approximately 0.57 salt bridging contacts per model. Both classes of overall peptide docking modes demonstrated the formation of salt bridges facilitated by C-terminal arginine residues, although reduced overall association was observed. In contrast, no or only minimal involvement of histidine residues H4 and H6 was observed in these docking models. Other, non-bonded contacts were found to be formed between $Ca_V2.2$ and most residues of RD2, which was consistent in all analyzed peptide docking models (Fig. 3.34, NBC). Interestingly, in models, where the peptide was associated with $Ca_V2.2$ inside the binding groove, N- and C-terminal residues P1 and R12 were

observed to strongly engage in non-bonded contacts, whereas in models that show association of RD2 below or outside the Ca^{2+}-permeable pore a stronger involvement of histidine residues H4 and H6 could be observed. In addition, peptide docking models categorized into the class "binding groove binders" exhibited a slightly increased overall number of contacts per model compared with other putative binding modes.

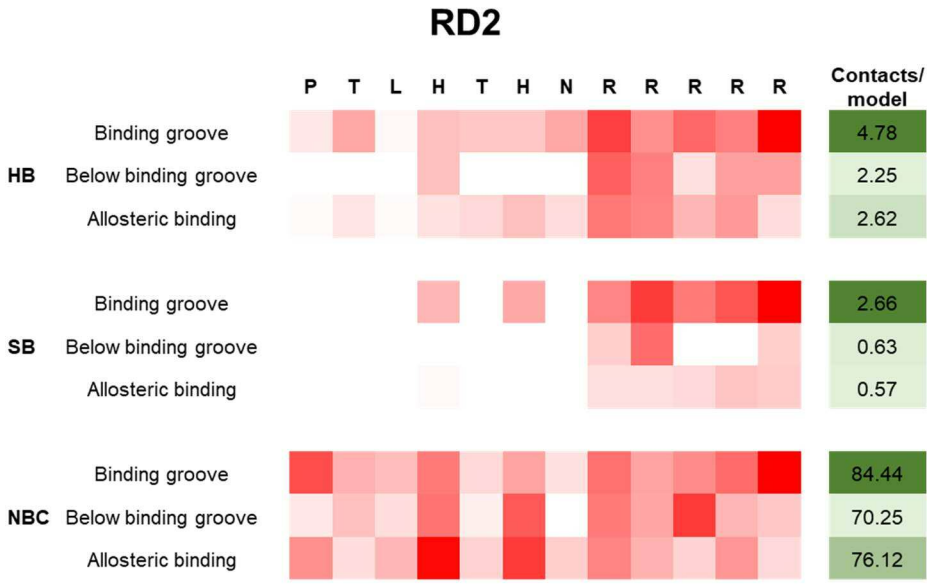

Figure 3.34: Contacts involved in the binding of RD2 to $Ca_V2.2$ dependent on the putative binding region
Putative binding modes of RD2 with $Ca_V2.2$ inside or outside the ω-CgTx binding groove were analyzed with regard to the contribution of respective residues and the type of contact. Top 100 highest-scoring models, showing either a binding groove-dependent binding mode, a putative allosteric binding or binding below the binding groove were analyzed with regard to the contribution of each residue in formation of hydrogen bonds (HB), salt bridges (SB) or other non-bonded contacts (NBC). Contribution of the individual residues are indicated as ratio of all associations of one type, whereby darker red indicates higher contribution of the residue in the respective contact type.

Furthermore, to identify any key residues in the binding of RD2 to $Ca_V2.2$ channels, the 100 best-scoring generated peptide docking models were analyze with regard to contribution of all $Ca_V2.2$ residues in the interaction with RD2. Residues that are frequently involved in the formation of strong associations like salt bridges or hydrogen bonds were identified to predominantly consist negatively charged glutamic acid residues (D265, D318, D639, D664 and D1629), as well as aspartic acid residues (E640, E1314 and E1659), often found in clusters within the structure of $Ca_V2.2$. Furthermore, aromatic residues tyrosine and phenylalanine were engaged in interactions with RD2 (F292, Y1310 and Y1344). In the analysis of the three-dimensional structure of the interaction between RD2 and the $Ca_V2.2$ model, it was observed that $Ca_V2.2$ residues, showing intense bonded contact over ionic or hydrogen bonds with RD2 residues, are typically situated within deeply buried regions or linked to inner sections of the Ca^{2+}-permeable pore domain of $Ca_V2.2$ (Fig. 3.35).

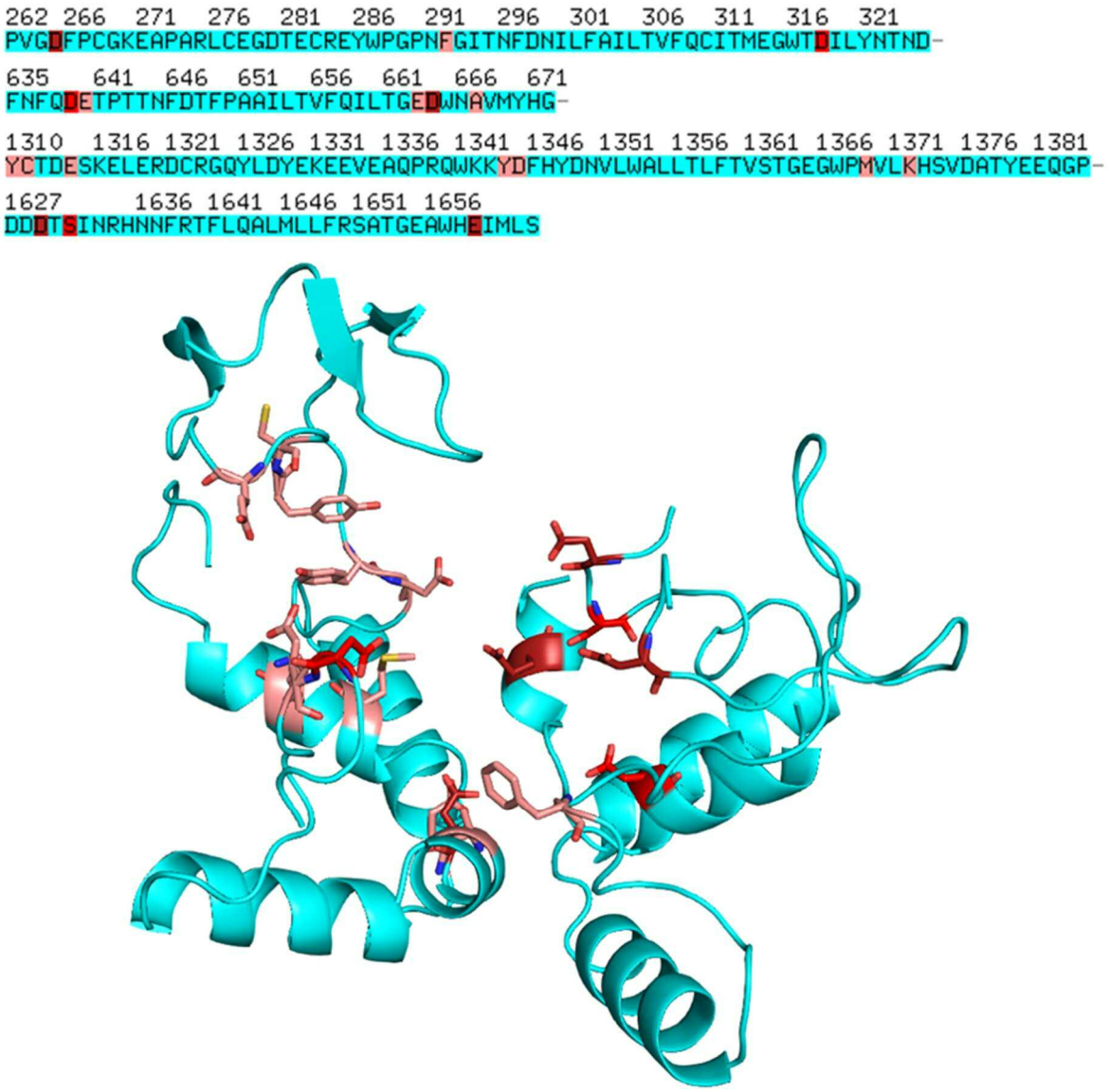

Figure 3.35: Cav2.2 residues involved in the binding to RD2 Top 100 highest-scoring docking models of RD2 in complex with $Ca_V2.2$ (cyan) were analyzed with regard to contribution of $Ca_V2.2$ residues in the interaction and the respective structure figure was prepared in PyMol. Frequently involved amino acids are presented as sticks (red), whereby darker red indicates higher contribution of the residue in the respective contacts with RD2.

3.8.2 Putative Binding Modes of RD2-Derived D-Peptides on $Ca_V2.2$

The RD2-derived D-peptide RD2C was observed to exhibit beneficial $Ca_V2.2$-inhibiting properties when compared with the lead compound RD2. Therefore, it was of further interest to analyze and compare the putative binding mode on $Ca_V2.2$ between both related D-peptides. Analysis of the highest-scoring docking models showed a similar association of RD2C with $Ca_V2.2$ in three categories as stated before; binding pocket-, below binding pocket- and allosteric-binders. Interestingly, compared with the highest-scoring binding models of RD2 associated with the structure of $Ca_V2.2$ (Fig. 3.36), RD2C was observed to bind with higher probability inside of the $Ca_V2.2$ electronegative cavity surrounding the Ca^{2+}-permeable pore. On average, binding models were observed to feature slightly favored docking scores. Furthermore, when comparing the spatial component of the binding, RD2C was observed to bind the groove in more deep-seated areas, close to the Ca^{2+}-permeable pore (Fig. 3.36, A, D, E, F).

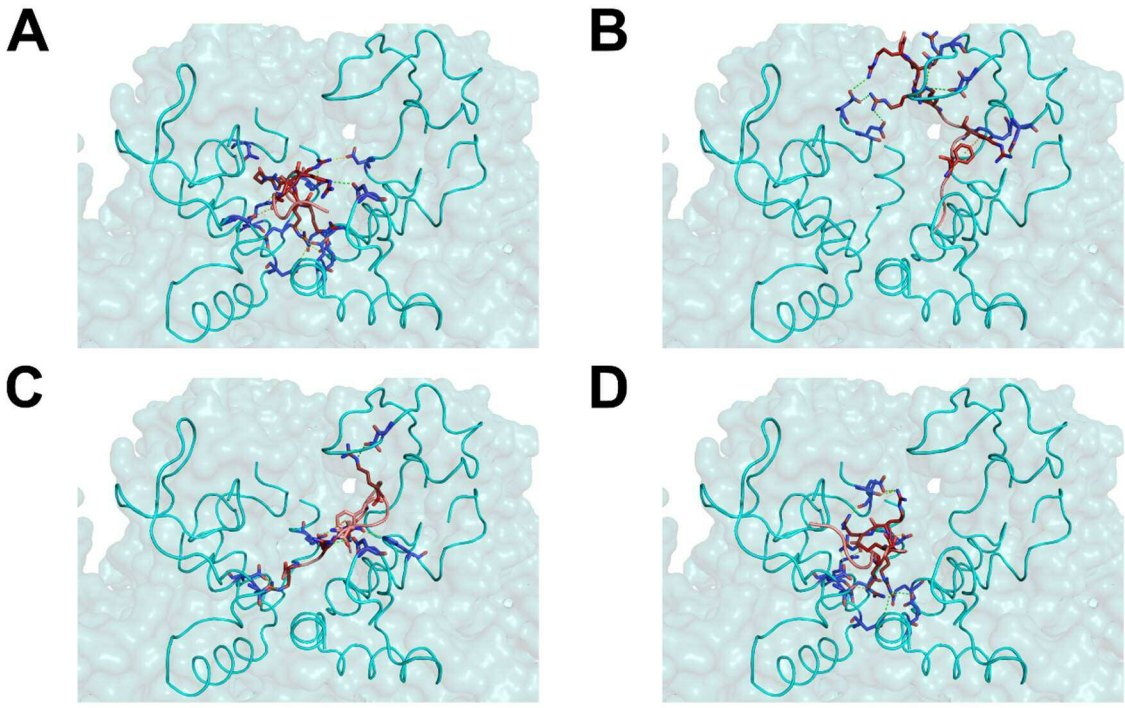

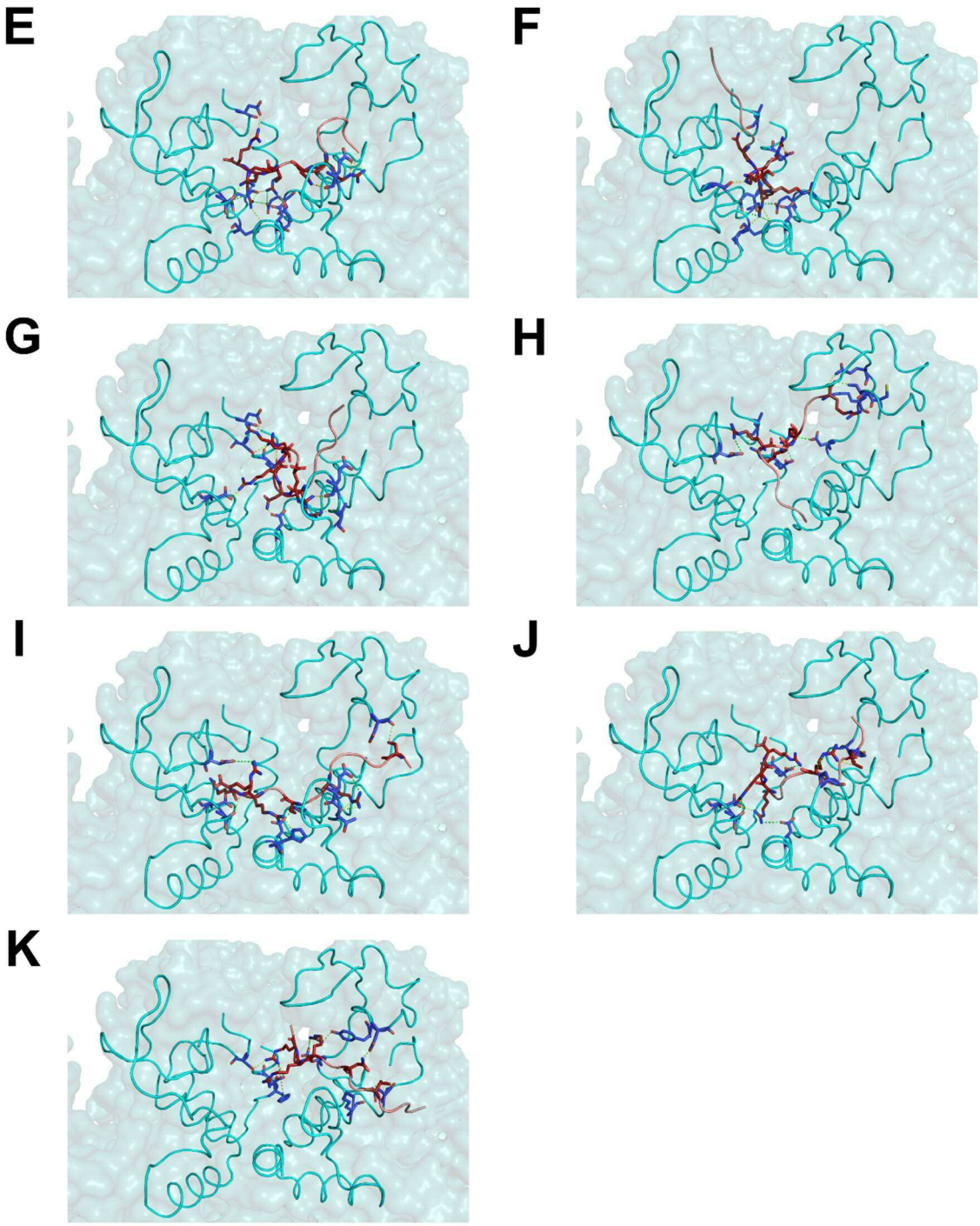

Figure 3.36: Peptide docking models showing putative binding modes of RD2C on $Ca_V2.2$ in the ω-CgTx binding groove Docking models found amongst the 20 highest-scoring docking models that show association of RD2C with $Ca_V2.2$ inside the electronegative cavity. RD2C (salmon) potentially binds $Ca_V2.2$ (cyan) at the pore-forming portion, revealing a putative pore-blocking mechanism. **A-K** show the highest-ranking binding models with the most favorable respective docking scores. The interaction is mediated by hydrogen bonds (yellow dashed lines), salt bridges (green dashed lines) and π interactions (orange dashed lines) between different amino acid residues from RD2C (red) and $Ca_V2.2$ (blue) and further stabilized by other non-bonded contacts. All structure figures were prepared in PyMol.

Similar to RD2, association of RD2C with $Ca_V2.2$ in all docking models as well as in all binding groove-associated models was observed to be coordinated over bonded contacts, predominantly mediated by the C-terminal arginine-rich region of RD2C (Fig. 3.37). Hydrogen bonds were observed to mainly form by arginine residues R6 and R8-R12, with a special focus on the C-terminal residue R12. Furthermore, salt bridges that were observed to be formed between RD2C and $Ca_V2.2$ were coordinated over arginine residues of RD2C, predominantly residues R6 and R11. Notably, the association of RD2C with $Ca_V2.2$ via bonded contacts exhibited variation from the binding modes of RD2, primarily attributed to a distinct engagement of the additional arginine residue R6, contributing to the enhancement in the binding probability of RD2C with $Ca_V2.2$ in docking modeling approaches. In addition, RD2C was associated with $Ca_V2.2$ over non-bonded contacts with high variability between the docking models. However, N- and C-termini (P1 and R12) as well as residues F4 and R6 show a slightly increased tendency to form non-bonded contacts as previously observed for RD2. Compared with putative binding modes of RD2 on $Ca_V2.2$, the highest-ranking docking models of the interaction of RD2C with $Ca_V2.2$ a displayed higher total number of contacts formed in the association, especially with regard to the formed hydrogen bonds per model.

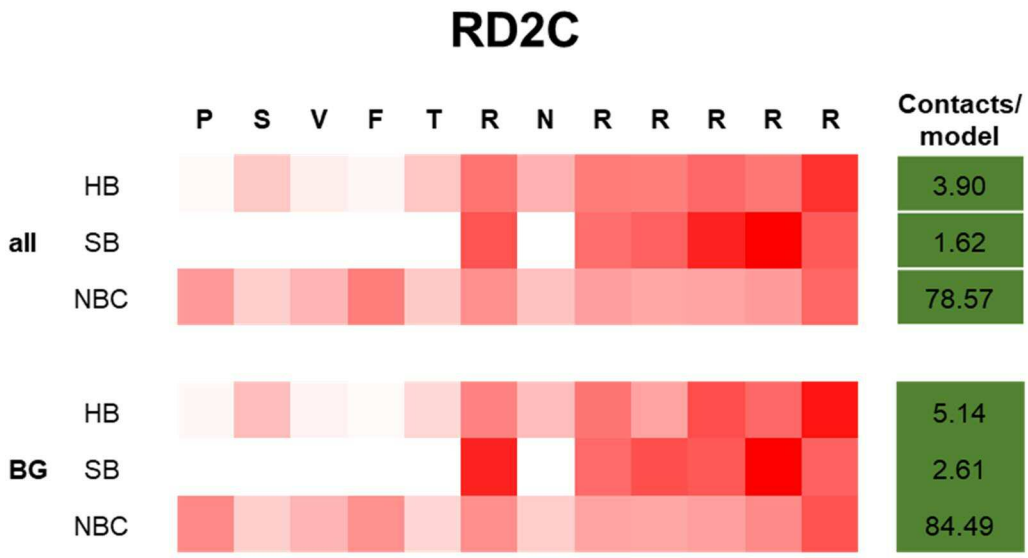

Figure 3.37: Contacts formed by RD2C residues in different docking models simulating the binding to $Ca_V2.2$ Putative binding modes of RD2C on $Ca_V2.2$ were analyzed with regard to the residue-specific contribution and type of formed contact. Top 100 docking models (all) or docking models showing a binding groove-associated binding mode (BG) were analyzed with regard to their residue-specific contribution in formation of hydrogen bonds (HB), salt bridges (SB) or other non-bonded contacts (NBC). Contribution of individual residues is indicated as ratio of all contact of one type, whereby darker red indicates enhanced contribution of the residue in the respective contact type.

The three different identified overall binding modes of RD2C to $Ca_V2.2$ were analyzed with regard to the type of contact formed in order to identify the respective contribution of each RD2C residue. Hydrogen bonds were predominantly formed between $Ca_V2.2$ and C-terminal arginine residues R10, R11 and R12 for peptides binding within the groove that surrounds the Ca^{2+}-permeable pore (Fig. 3.38, HB). In a similar way, in peptide docking models demonstrating a sub-pore association with $Ca_V2.2$, C-terminal arginine residues, mainly R9, R10 and R12, were identified to engage in hydrogen bond interactions with $Ca_V2.2$. However, these interactions exhibit overall diminished contribution, evidenced by a reduced number of contacts per model compared with other binding modes. In contrast to that, models in which the peptide was observed to bind to a putative allosteric binding site only showed a slight focus of engagement of the C-terminal region of RD2C in hydrogen bonds. In addition, these models displayed an overall weaker association with $Ca_V2.2$, mediated by hydrogen bonds of on average 2.98 contacts per model. Compared with docking models of RD2 on $Ca_V2.2$ the overall number of hydrogen bonds per model was slightly increased in models docking RD2C to $Ca_V2.2$, regardless of the identified binding mode.

Similarly, putative interactions of RD2C with $Ca_V2.2$ residues, mediated by the formation of salt bridges, were observed to be mainly coordinated over arginine residues (Fig. 3.38, SB). In peptide docking models showing RD2C associated within the binding groove domain of $Ca_V2.2$, salt bridges were formed between C-terminal arginine residues, mainly R11, along with a distinct contribution of arginine residue R6, the latter is unique to RD2C as opposed to RD2. In peptide docking models comprising peptides bound below the pore, the number of formed salt bridges per model was observed to be reduced by almost 75% and only a slight tendency of formation of salt bridges was seen for arginine residues R6 and R10-R12. A similar trend could be seen for docking models showing putative allosteric binding of RD2C, where interaction with $Ca_V2.2$ via salt bridges was observed for all arginine residues, although an overall reduced frequency of this contact type was identified.

Furthermore, most residues of RD2C showed association with $Ca_V2.2$ over non-bonded contacts, which was consistent over all putative binding modes (Fig. 3.38, NBC). In line with results for RD2, in models showing binding groove association for RD2C, N- and C-terminal residues P1 and R12 were observed to strongly engage in non-bonded contacts, whereas in other models, a stronger involvement of histidine residues H4 and H6 were found. Furthermore, docking models showing peptide binding inside the Ca^{2+}-permeable pore pocket show slightly increased overall number of non-bonded contacts per model.

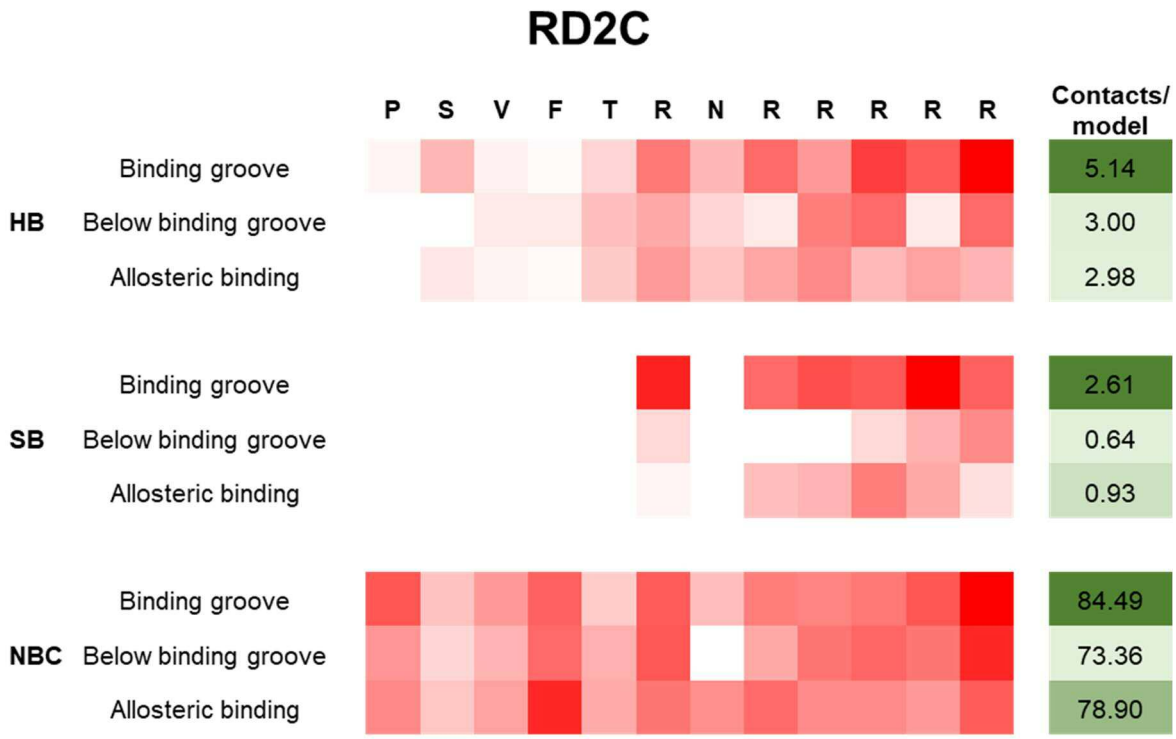

Figure 3.38: Contacts involved in the binding of RD2C to $Ca_V2.2$ dependent on the putative binding region Putative binding modes of RD2C on $Ca_V2.2$ inside or outside the ω-CgTx binding groove were analyzed with regard to contribution of the different residues and type of contact formed. The 100 highest-scoring docking models, either showing a binding groove-dependent binding mode, an allosteric binding or binding below the binding groove, were analyzed with regard to each residues' contribution in formation of hydrogen bonds (HB), salt bridges (SB) or other non-bonded contacts (NBC). Contributions of the individual residue are indicated as ratio of all contacts of one type, whereby darker red indicates stronger contribution of the residue in the respective contact type.

Identification of the key residues of $Ca_V2.2$ that are involved in the interaction with RD2C revealed that negatively charged glutamic acid residues (D265, D318, D639, D664 and D1629), as well as aspartic acid residues (E640, E1314 and E1659) were mainly involved in the formation of strong associations like salt bridges or hydrogen bonds, which was in line with findings for RD2 binding to $Ca_V2.2$. In addition, most of the key residues for binding of RD2C were identical with binding patterns observed for RD2, as most residues that are found to be engaged in bonded contact are structurally located in the inner part of the Ca^{2+}-permeable pore domain of $Ca_V2.2$, with a focus in an orientation close to the pore (Fig. 3.39).

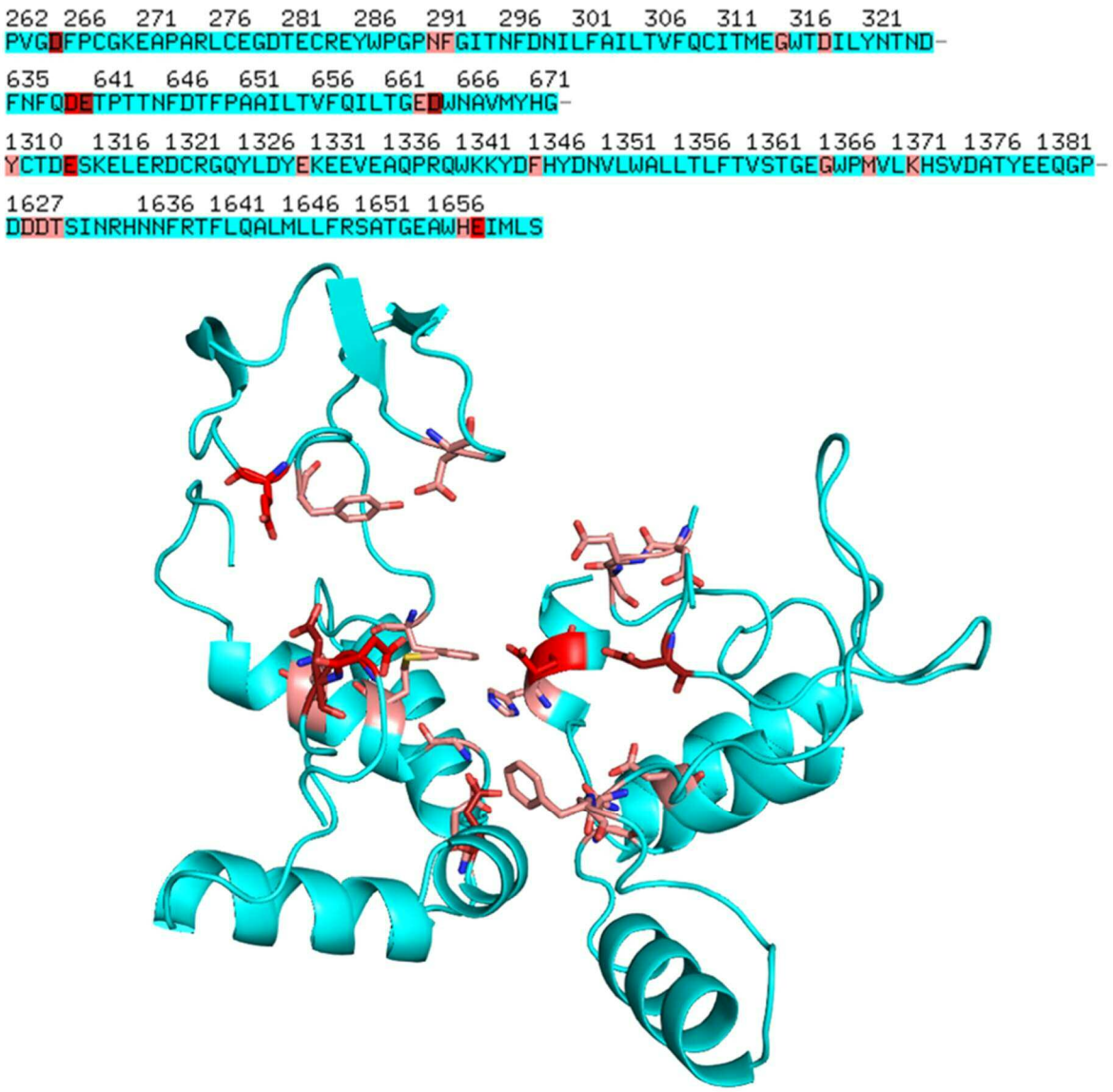

Figure 3.39: $Ca_V2.2$ residues involved in the binding to RD2C The 100 best-ranked docking models of RD2C in complex with $Ca_V2.2$ (cyan) were analyzed with regard to contribution of $Ca_V2.2$ residues in the interaction and the respective structure figure was prepared in PyMol. Frequently associated amino acids are presented as sticks (red), whereby darker red indicates higher contribution of the residue in the respective association with RD2C.

4 Discussion

Neurodegeneration is characterized by the progressive loss of neurons, which is the underlying mechanism of several neurodegenerative diseases affecting millions of people worldwide. To date, these diseases are considered incurable, given that neurodegeneration is irreversible and available treatment options only achieve deceleration of disease progression. Dyshomeostasis of Ca^{2+} is found as a pathological hallmark in a variety of neurodegenerative diseases. Therefore, targeting putative neurotoxicity-mediating Ca^{2+} channels provides an interesting therapeutic strategy for the treatment of neurodegeneration in the context of different diseases for a general neuroprotective approach.

The lead compound RD2, originally developed for targeting toxic Aβ oligomers and subsequently dissolve them into non-toxic monomers, was previously observed to exhibit a beneficial effect on cognitive performance in the context of AD in a study examining its effect in mice and beagles (Kutzsche, Schemmert et al. 2017; Kutzsche, Schemmert et al. 2023). Furthermore, evidence pointed towards an inflammation-reducing effect of the respective tandem repeat D-peptide RD2RD2 in a mouse model of ALS, which subsequently leads to improved behavioral and motor performance (Post, Kogel et al. 2021; Post, Schaffrath et al. 2021). As it is unlikely that the initial anti-Aβ-oligomer-directed treatment strategy of RD2 is the underlying reason for its inhibitory effect on neuroinflammation in ALS, an additional off-target effect was postulated for RD2. Interestingly, in a pharmacological screening test, the $Ca_V2.2$ channel was identified as a putative target of RD2. In line with this, we previously were able to show specific binding and inhibiting properties of RD2 on $Ca_V2.2$-mediated Ca^{2+} fluxes. Together, this suggests $Ca_V2.2$ channels as a putative missing link, partly responsible for Aβ-independent beneficial effects of RD2 in the context of neurodegenerative diseases. Therefore, it became of interest to analyze the role of $Ca_V2.2$ channels in the context of neurodegenerative diseases like AD more in detail to understand the underlying process and involvement of $Ca_V2.2$-mediated Ca^{2+} fluxes in neurodegeneration. In addition, analysis of binding kinetics as well as the *in silico* modeling of the putative binding mode of RD2 on $Ca_V2.2$ channels was undertaken to gain a more comprehensive understanding of the respective association that is responsible for channel inhibition. The information obtained were subsequently used to optimize RD2's binding with regard to its inhibitory capacity on $Ca_V2.2$ channels to finally develop therapeutic compounds for a $Ca_V2.2$-dependent general neuroprotective approach.

4.1 Upregulation of $Ca_V2.2$ in an Animal Model of Alzheimer's Disease

Ca^{2+} homeostasis and its perturbations are known to play a major role in the pathology of neurodegenerative diseases, such as AD. As VGCCs, particularly the $Ca_V2.2$ channel, contribute to the majority of Ca^{2+} influx in neurons at the pre-synapse after membrane depolarization, subtype-specific alterations in channel density or activity may be, at least in part, responsible for Ca^{2+} dyshomeostasis in disease context. Therefore, we aimed to analyze the $Ca_V2.2$ protein content in various brain regions of mice impacted by or without AD.

VGCCs in general are important components in neuronal signal transmission and are known to exhibit effector function in a diverse range of signaling pathways. By this, they couple membrane-depolarizing electrical stimuli to intracellular chemical signals. As only small deviations in the intracellular Ca^{2+} concentration are sufficient to trigger various downstream signaling cascades, a tight regulation of Ca^{2+} fluxes, partially mediated by VGCCs, is crucial for the physiological function of the cell. Dyshomeostasis of Ca^{2+} fluxes across the plasma membrane or between organelles and altered regulation of Ca^{2+}-dependent mechanisms are subsequently linked to several diseases, including a wide range of neurodegenerative diseases like PD, MS or AD (Mattson 2007; Bezprozvanny and Mattson 2008; Camandola and Mattson 2011; Zaichick, McGrath et al. 2017; Enders, Heider et al. 2020).

Analysis of the protein content in the brain of a mouse model of AD revealed an age- and disease progression-correlated upregulation of $Ca_V2.2$ in the cortex but not the cerebellum. Furthermore, a sex-dependence of the upregulation was observed, showing increased $Ca_V2.2$ protein levels in old-aged male mice, associated with full-blown AD disease pathology.

The cerebellum is commonly used as a control for quantification of the cortical protein content in the context of AD, as this brain region is spared from the majority of pathological changes associated with disease progression (Serrano-Pozo, Frosch et al. 2011). Alterations in the level of certain proteins in the cortex that are not detectable in the cerebellum can therefore be attributed more confidently to AD-specific processes rather than being caused by a general aging-related process or other unspecific effects. By this, the variability of the analysis can be reduced and the accuracy of quantification will subsequently be increased. In the here presented study, a disease-associated upregulation of $Ca_V2.2$ protein levels was detected in the cortex but not in the cerebellum of a mouse model of AD. These variations in $Ca_V2.2$ density can most probable be related to alterations up- or downstream of certain pathological changes associated with AD.

4.1.1 Putative downstream effects of $Ca_V2.2$ upregulation in AD

In neurons of the CNS, several VGCC subtypes are expressed and responsible for signal transmission. Through their predominant pre-synaptic localization, P/Q- and N-type VGCCs are mainly responsible for mediation of Ca^{2+} influx by triggering neurotransmitter release in response to membrane depolarization in a variety of subtypes of neurons (Takahashi and Momiyama 1993; Mintz, Sabatini et al. 1995; Wheeler, Randall et al. 1996; Ariel, Hoppa et al. 2012). Altered surface density or perturbations in the regulatory mechanisms that control $Ca_V2.2$ channel activation, inactivation or respective opening kinetics may subsequently lead to hyperexcitability in neuronal cells, which is caused by excessive cellular Ca^{2+} influx. The primary underlying mechanism driving this phenomenon is the reduction in the threshold potential for the generation of action potentials, subsequently leading to prolonged hyperexcitability of neurons, which was previously observed to eventually cause neuronal cell death through a process termed excitotoxicity (Choi 1988; Tymianski and Tator 1996; Sattler and Tymianski 2000; Arundine and Tymianski 2003; Bano and Nicotera 2007). By this, upregulation of $Ca_V2.2$ channels in disease context as observed in this study in a mouse model of AD could be, at least in part, responsible for neurodegeneration, mediated by excessive Ca^{2+} influx.

Nevertheless, it remains to be elucidated to which extent increased levels of Ca^{2+} channels, in particular N-type VGCCs, contribute to neuronal hyperexcitability and subsequent neurodegeneration, caused by excitotoxicity, in the context of various neurological and neurodegenerative diseases. It was previously demonstrated that the condition of neuropathic pain is associated with increased expression of $Ca_V2.2$ in the PNS (Cizkova, Marsala et al. 2002; Lu, Zhang et al. 2010). One study further suggested an underlying redistribution and altered channel trafficking of Ca_V1 and Ca_V2 channels due to modulation mediated by the auxiliary subunit $\alpha_2\delta_1$ in a model of neuropathy (Bauer, Nieto-Rostro et al. 2009). The upregulation of $Ca_V2.2$ in the soma of uninjured DRG neurons in the context of peripheral nerve injury-induced neuropathic pain was further reported to subsequently increase neuronal excitability (Yang, Xie et al. 2018). In a similar way, protein levels of $Ca_V2.2$, but not $Ca_V2.1$, were found to increase with disease progression in a mouse model of the neurodegenerative disease ALS, which was further accompanied by increased Ca^{2+} current density, putatively contributing to neuronal damage in this ALS mouse model (Pieri, Caioli et al. 2013; Chang and Martin 2016).

Although increased $Ca_V2.2$ protein levels in neurons were previously found to be associated with increased excitability in different diseases, upregulation of $Ca_V2.2$, as described in this study, may not necessarily result in neuronal hyperexcitability. Originally, it was hypothesized, that besides the quantity of Ca^{2+} influx the source of Ca^{2+} controls the subsequent toxicity (Tymianski, Charlton et al. 1993; Sattler, Charlton et al. 1998). For the longest time, VGCCs were thought not to carry lethal Ca^{2+} fluxes, which has led to these channels being overlooked in research. More recent work provided new hypotheses stating that Ca^{2+} fluxes may become toxic under certain circumstances like certain disease states or in subpopulations of neurons (Yagami, Kohma et al. 2012; Cataldi 2013). In line with this, neuronal vulnerability was observed to be associated with elevated intracellular Ca^{2+} levels in a subset of neurons with increased Ca_V expression and activity, which was subsequently followed by cell death (Stanika, Villanueva et al. 2012).

Previously, it was observed that $Ca_V2.2$ channels exhibit overlapping function with P/Q-type $Ca_V2.1$ channels in the pre-synapse of various neuronal cell types in the CNS, although $Ca_V2.2$ is thought to be the major contributor for synaptic vesicle release (Meir, Ginsburg et al. 1999; Wu, Westenbroek et al. 1999; Reid, Bekkers et al. 2003). Functional compensation of various VGCC subtypes was previously described in different contexts. For instance, previous studies could show that decreased $Ca_V2.1$ current density can be compensated almost entirely by Ca^{2+} influx through $Ca_V2.2$ channels (Qian and Noebels 2000; Murchison, Dove et al. 2002; Etheredge, Murchison et al. 2007). The upregulation of $Ca_V2.2$ channels may therefore be compensated for by a corresponding downregulation of $Ca_V2.1$ protein levels, indicating a potential negative correlation between both channels in a cellular compensation mechanism. Further studies are required to assess the overall protein content of various pre-synaptic VGCCs in the brain of the AD mouse model assessed in this study.

Furthermore, neurotransmitter release in response to Ca^{2+} influx through $Ca_V2.2$ channels relies on tight coupling, which is facilitated by close spatial proximity of the channel to the synaptic vesicle release machinery (Bucurenciu, Kulik et al. 2008; Muller, Haupt et al. 2010). Therefore, not only the overall cell surface channel density, but also the exact localization of the channel in the plasma membrane of neuronal cells of the CNS is of importance and channel modulation via subcellular relocalization may contribute to Ca^{2+}-dependent cell death. In fact, it was previously observed that, in the context of PD, $Ca_V2.2$ activity is altered through reorganization of plasma membrane microdomains, which subsequently leads to an increased release of neurotransmitters (Ronzitti, Bucci et al. 2014).

Further analysis is needed to determine putative alterations in the density and spatial distribution of $Ca_V2.2$ channels in the diseased brain with regard to the affected specific type of neuronal cell.

Besides causing hyperexcitability in neurons, increased $Ca_V2.2$ protein levels may alternatively, but not mutually exclusively, cause other neuronal damage by altering the intracellular Ca^{2+} concentration. Prolonged elevated intracellular Ca^{2+} levels will subsequently lead to perturbations in Ca^{2+}-dependent signaling pathways, resulting in metabolic changes that subsequently may contribute to neuronal cell death (Tymianski and Tator 1996; Brini, Cali et al. 2014).

The exact downstream effects of upregulated protein levels of $Ca_V2.2$, as observed in an AD mouse model, remain to be elucidated. However, the here presented results, in line with previous findings, point towards a putative regulatory function of $Ca_V2.2$ channels in Ca^{2+}-dependent neurodegeneration.

4.1.2 $Ca_V2.2$ upregulation is associated with AD pathological progression

Furthermore, the findings of this study raise the question of a causal relationship between upregulated $Ca_V2.2$ protein levels and AD disease progression, as a strong positive correlation was observed in the assessed mouse model of AD. It was previously reported that one of the key players in AD, the poly-peptide Aβ, was able to modulate activity as well as expression levels and surface density of different VGCC subtypes (Price, Held et al. 1998; MacManus, Ramsden et al. 2000; Kasparova, Lisa et al. 2001; He, Chen et al. 2002; Ramsden, Henderson et al. 2002; Rovira, Arbez et al. 2002; Freir, Costello et al. 2003; Bobich, Zheng et al. 2004; Chiou 2006; Anekonda, Quinn et al. 2011; Kim and Rhim 2011; Hermann, Mezler et al. 2013; Kaisis, Thei et al. 2022). The modulation of VGCCs by Aβ was observed to target all levels of protein regulation, from transcriptional to translational changes, as well as post-translational regulation of channel activity. The majority of Aβ species, considered to be toxic in disease context, was observed to induce elevated channel surface density and activity of VGCCs. This phenomenon was also notably observed for $Ca_V2.2$ channels (Price, Held et al. 1998; MacManus, Ramsden et al. 2000; Ramsden, Henderson et al. 2002; Chiou 2006), although opposite findings were reported as well (Ramsden, Henderson et al. 2002; Yagami, Ueda et al. 2004; Hermann, Mezler et al. 2013; Kaisis, Thei et al. 2022). The discrepancies in these studies are most probably attributable to the variation in Aβ species, aggregation state and the concentration employed in the

respective experiment. In general, channel modulation was dependent on the Aβ species and its respective aggregation state (monomer, oligomer, fibril), which may lead to different modulation of channels in dependence on disease state. In the here described study, protein levels of $Ca_V2.2$ were positively correlated with disease progression, especially in later stages, which indicates a putative mechanism of downstream regulation of $Ca_V2.2$ by toxic Aβ species present in the cortex and hippocampus in this AD mouse model already after six months of age, with intensive abundance after 12 months (Jankowsky, Fadale et al. 2004; Garcia-Alloza, Robbins et al. 2006). Our study provides a preliminary indication of the relationship of $Ca_V2.2$ channel protein levels with pathological progression and putatively with key players in AD, but additional testing is required to establish causality and rule out alternative explanations. Therefore, it may be of interest to analyze $Ca_V2.2$ protein levels at earlier time points, prior to disease onset, in order to gain more insight into the time course of $Ca_V2.2$ expression and channel density in the context of AD.

An alternative pathway leading to $Ca_V2.2$ modulation is mediation through inflammatory processes, associated with several neurological diseases. In a complete Freund's adjuvant (CFA) model of inflammatory pain, inflammation-induced upregulation of $Ca_V2.2$ was detected in the periphery, which subsequently increased $Ca_V2.2$-mediated Ca^{2+} currents, suggesting an underlying $Ca_V2.2$-dependent mechanism for pain hypersensitivity in this model (Pitake, Middleton et al. 2019). Furthermore, chronic inflammation in a rat model of persistent inflammation modulated $Ca_V2.2$ in subpopulations of cutaneous DRG neurons (Lu, Zhang et al. 2010). Although reduced current densities of N-, L- and P/Q-type channels were found in neurons that innervate the site of inflammation, increased $Ca_V2.2$ protein levels could be observed in the central nerve of L4 and L5 ganglia ipsilateral to the site of inflammation, showing a tissue-specific regulation in this context. Interestingly, the pro-inflammatory cytokine Il-1β did upregulate $Ca_V2.2$ expression in DRG neurons, subsequently leading to neuropathic pain, whereas the anti-inflammatory cytokine interleukin-10 (Il-10) was observed to exhibit a contrary effect (Yang, Xie et al. 2018). In line with this is the finding that $Ca_V2.2$ KO mice show reduced inflammation in a model of neuropathic pain (Saegusa, Kurihara et al. 2001). Inflammation is a major pathological hallmark found in most neurodegenerative diseases, including AD (Kinney, Bemiller et al. 2018). In $APP_{swe}/PSEN1^{\Delta E9}$ mice, astrogliosis develops in parallel with plaque pathology and reaches its peak in the cortex at an age of 15 months (Kamphuis, Mamber et al. 2012). Conversely, in this context, Il-1β is postulated to exhibit pro-inflammatory, but neuroprotective functions. Consequently, the observation that $Ca_V2.2$ expression and

$Ca_V2.2$-evoked Ca^{2+} currents were inhibited by Il-1β in the CNS may provide an interesting hypothesis regarding the tissue- and disease-specific regulation of $Ca_V2.2$ through a mechanism involving inflammation pathways (MacManus, Ramsden et al. 2000; Zhou, Ye et al. 2006). For these reasons, downstream upregulation of $Ca_V2.2$ channels provides a putative mechanism by which AD-associated neuroinflammation could finally lead to neuronal damage and neurodegeneration.

Summarizing, the here presented study revealed a positive correlation between cortical protein levels of $Ca_V2.2$ and both, aging and disease progression, in a transgenic mouse model of AD. Notably, the extent of this correlation shows gender-specific differences. The underlying causal mechanism, driving the upregulation of $Ca_V2.2$ protein levels, remains unclear with potential mediating factors comprising transcriptional regulation, channel internalization, redistribution or post-translational modifications that are modulated in disease context. Neuroinflammation or Aβ-plaque pathology may act as putative modulators in the context of neurodegenerative diseases, and further exploration could elucidate the underlying relationship for a deeper understanding of the specific disease mechanism. Furthermore, continued investigations will focus on unraveling the underlying pathological mechanism linking certain pathological hallmarks in AD to the dysregulated expression, channel density and activity of $Ca_V2.2$ channels. Clarifying the causal relationship between Ca^{2+} dyshomeostasis, mediated through $Ca_V2.2$ channels, and other hallmarks like plaque accumulation, neuroinflammation or neurodegeneration can advance our understanding of the disease and potentially unveil new therapeutic strategies. In general, as increased concentrations of intracellular Ca^{2+} levels are widely found amongst neurodegenerative diseases, inter alia AD, the finding of differences in $Ca_V2.2$ protein levels in a mouse model of AD provides an interesting hypothesis and putative strategy for neuroprotective treatment strategies targeting $Ca_V2.2$ channels for specific inhibition of toxic neuronal Ca^{2+} fluxes.

4.1.3 RD2-dependent inhibition of $Ca_V2.2$ as therapeutic strategy in AD

A wide range of evidence suggests a link of Ca^{2+} dysregulation in neurons with neurodegeneration, observed as pathological hallmark in AD, which resulted in the establishment of the Ca^{2+} hypothesis of neurodegeneration (Simon, Griffiths et al. 1984; Khachaturian 1989; Khachaturian 1994). Therefore, identification of toxic sources of Ca^{2+} influx provides an interesting therapeutic target for the treatment of neurodegenerative diseases like AD. As previously discussed (see 4.1.2), channel density or activity of VGCCs, particularly that of $Ca_V2.2$ channels, may increase in the context of AD, potentially in response to exposure to toxic Aβ species, which subsequently could account for their neurotoxic effects. Modulation of $Ca_V2.2$-mediated Ca^{2+} currents by Aβ may be one of the physiological functions of Aβ which is thought to be, amongst others, the regulation of synaptic function (Plant, Boyle et al. 2003; Bishop and Robinson 2004). In contrast to that, in the pathological context of AD, chronically elevated levels of Aβ and certain toxic species of Aβ in the brain may facilitate $Ca_V2.2$-mediated Ca^{2+} dyshomeostasis, as seen early on in disease progression. Subsequently, this is known to cause neurodegeneration through excitotoxicity. The specific inhibition of Ca^{2+} fluxes, mediated by $Ca_V2.2$ channels, was previously reported to rescue cognitive dysfunction in a mouse model of glutamate-induced excitotoxicity, which was mainly mediated by balancing the secretion of neurotransmitters in the hippocampal trisynaptic circuitry (Keimasi, Salehifard et al. 2023; Keimasi, Salehifard et al. 2023). Analogous excitotoxic mechanisms were also reported in the context of AD (Esposito, Belli et al. 2013). Using RD2, a similar effect may be achieved for a therapeutic strategy in AD with regard to upregulated excitotoxicity-mediating $Ca_V2.2$ currents. Nevertheless, AD is a complex multifactorial disease and it remains to be elucidated if inhibition of Ca^{2+} fluxes mediated by $Ca_V2.2$ channels will subsequently lead to the reduction of excitotoxicity-induced neurodegeneration and as a result alleviate cognitive decline in patients short-, as well as long-term.

Interestingly, previous work could additionally show that membrane depolarization-induced elevated intracellular Ca^{2+} concentrations were able to induce modifications of intracellular APP and tau in a similar fashion as observed in the context of AD (Pierrot, Santos et al. 2006). Persistently elevated intracellular Ca^{2+} levels were further observed to increase the production of Aβ species, which is subsequently followed by neuronal cell death (Querfurth and Selkoe 1994; Pierrot, Ghisdal et al. 2004; Green, Smith et al. 2007). Furthermore, secondary hallmark pathologies of AD, such as hyperphosphorylation of the protein tau and

subsequent aggregation and deposition into intracellular neurofibrillary tangles (NFT), were found to be dependent on extracellular fibrillar Aβ as well as on dysregulated Ca^{2+} homeostasis (Takashima, Noguchi et al. 1993; Pierrot, Santos et al. 2006). In return, these aggregated species of tau were observed to induce activation of VGCCs itself (Messing, Decker et al. 2013; Decker, Kruger et al. 2015; Esteras, Kundel et al. 2021). This suggests a role of both key players in AD, Aβ and tau, as affectors as well as effectors of Ca^{2+} dysregulation, at least in part mediated by $Ca_V2.2$ channels. Postulating this as a central dogma subsequently presents $Ca_V2.2$ as promising therapeutic target. Targeting $Ca_V2.2$ channels with RD2 or lead-optimized D-peptides in the context of AD may counteract Ca^{2+} dysregulation either by directly targeting $Ca_V2.2$ channels or by specifically interfering with Aβ-dependent modulation of Ca^{2+} fluxes through $Ca_V2.2$ channels. This could possibly resolve Ca^{2+}-dependent downstream effects, subsequently improving neuronal survival. Since Aβ is believed to exhibit a physiological role in the CNS, the targeted attenuation of its toxic effects through the elimination of certain toxic species or the inhibition of downstream key modulators such as $Ca_V2.2$ by application of the compound RD2 or derivatives is therefore expected to yield favorable therapeutic outcomes in a treatment strategy targeting AD.

Taken together, application of RD2 as therapeutic agent for the treatment of neurodegenerative diseases like AD may not only be able to reduce putative overactivation of $Ca_V2.2$ channels in order to finally reduce excitotoxicity-dependent cognitive decline, but may further inhibit disease progression by preventing production and accumulation of downstream pathological effectors like Aβ or tau.

While the primary objective of this study was the development of RD2 as a modulator of $Ca_V2.2$ in the context of treating AD, the universal role of $Ca_V2.2$ channels in crucial neuronal processes suggests that inhibition of $Ca_V2.2$ through RD2 or RD2-derived D-peptides may exhibit general neuroprotective features in the context of various neurodegenerative diseases.

4.2 Expression and Purification of $Ca_V2.2$ from Mammalian Cells

As previous results suggested the use of $Ca_V2.2$ inhibitors for the treatment of neurodegenerative diseases, the main aim of this study was the analysis of the inhibitory capacity of our lead compound RD2 and the subsequent development of improved D-peptides for a new putative therapeutic treatment strategy targeting $Ca_V2.2$ channels. The analysis and improvement of lead candidates which inhibit $Ca_V2.2$ channels indispensably require the expression of this protein in its functional, membrane-integrated form. The optimization strategy of the lead compound RD2, aimed for in this study, further included the necessity of a pure protein sample of $Ca_V2.2$, making the development of respective suitable expression and following purification strategies an important prerequisite for the subsequent optimization process.

$Ca_V2.2$ channels are large, complex integral membrane proteins that not only require appropriate expression, post-translational modification and folding but further need to be associated with several auxiliary subunits in order to exhibit functional expression in the plasma membrane of cells (Ruth, Rohrkasten et al. 1989; Dolphin 2012; Dolphin 2013; Dolphin 2016). Due to the low abundance in natural sources, most of the integral membrane proteins used in structural or functional studies require recombinant overexpression in cellular systems to reach high quantities of protein (Tate 2001). In the past, several overexpression studies failed to functionally express integral membrane proteins in commonly used prokaryotic expression systems in sufficient quantity and quality, giving the need for expression in mammalian systems as alternative (Tate 2001; Andrell and Tate 2013).

In this study, mammalian *in vitro* cell systems were employed in the facilitation of recombinant $Ca_V2.2$ protein expression using either transiently or stably transfected cell lines. The expression and functional incorporation of the channel into the cellular membrane were consistently detected across all experimental conditions using immunofluorescent methods. The most robust levels of $Ca_V2.2$ protein expression were observed in stably transfected cell lines, thereby revealing them as the most suitable expression system for the subsequent establishment of a protocol for protein purification.

Another important factor to consider during protein purification is appropriate solubilization and the preservation of protein stability during all steps of protein purification. It is well known that integral membrane proteins have a propensity to become unstable and aggregate

or degrade during the purification process, necessitating the development of suitable protocols tailored for the unique characteristics of every protein (Tate 2010; Bill, Henderson et al. 2011). In this study, we were able to optimize the cell lysis and solubilization protocol based on previously reported methods (Dong, Gao et al. 2021; Gao, Yao et al. 2021), stating a combination of cell lysis via sonication and subsequent short solubilization in a buffer containing the detergents DDM, CHS and GDN is the most effective way to transfer $Ca_V2.2$ from its natural membrane-integrated state into solution.

As $Ca_V2.2$ was expressed without any affinity tags, purification was only possible with regard to its biochemical and biophysical properties. So far, no work was published assessing the purification of untagged $Ca_V2.2$ protein to the required purity and quality. Therefore, a screen for a suitable purification protocol was performed. To begin with, a variety of different approaches was tested, each separating the protein over certain protein-specific characteristics. Summarizing, tested methods comprised: size exclusion chromatography and centrifugation-based approaches, separating the proteins with regard to their overall size; ion exchange chromatography, separating proteins with regard to their overall charge; hydrophobic interaction chromatography, separating proteins with regard to their hydrophobic characteristics; immobilized metal chromatography, separating proteins with regard to their content of certain amino acid residue patches, their phosphorylation state, or their Ca^{2+}-binding capacity; immunoprecipitation, separating proteins based on a specific epitope by using antibodies; as well as mixed-mode hydroxyapatite chromatography, combining characteristics of metal affinity and ion exchange chromatography. Multiple approaches failed to separate $Ca_V2.2$ protein from other components present in the cell lysate after solubilization, likely attributable to potential masking of interacting sites within the four-dimensional multi-subunit complex assembly, comprising the pore-forming and the auxiliary subunits, or the presence of detergents surrounding the protein. The optimal separation of $Ca_V2.2$ from complex cell lysate samples was achieved through size-dependent purification methods such as differential or density gradient centrifugation and separation via size exclusion chromatography. In addition, chromatography techniques that separate proteins with regard to their overall charge, including ion exchange chromatography and mixed-mode hydroxyapatite chromatography, also exhibited high efficacy in isolating $Ca_V2.2$ protein from complex samples. Although neither of the mentioned above strategies succeeded to purify $Ca_V2.2$ from complex samples in a quantity and quality as required for following experiments, partial separation was observed with several methods, providing a great potential for further refinement of the purification method.

To enhance the efficacy of $Ca_V2.2$ purification, suitable individual chromatography methods were next combined into a multistep purification approach. The incorporation of multiple separation characteristics aimed to potentially overall improve the purity and protein recovery of the sample after purification. In general, the first purification step in a multistep approach is considered the capture step, which is focused on separating, concentrating and transferring the protein into a suitable buffer. This can be already successfully performed during the solubilization step, as the protein is stabilized and separated from a bulk of proteins, insoluble in the respective buffer. Next follows an intermediate purification step that aims to separate the protein of interest from as many impurities as possible, often performed using size exclusion or ion exchange chromatography for untagged proteins. Lastly, a polishing step is incorporated in the protocol to remove any remaining contaminating proteins. In this step, chromatography methods like size exclusion, ion exchange or hydrophobic interaction chromatography could be considered, dependent on the characteristics of the impurities.

Multistep approaches following solubilization with most promising $Ca_V2.2$ purification outcomes were observed to comprise differential centrifugation in combination with density gradient centrifugation, anion exchange chromatography followed by size exclusion chromatography, as well as size exclusion chromatography with subsequent ion exchange chromatography. Although the combination of size exclusion chromatography and hydroxyapatite chromatography showed an overall high purification capacity with high protein recovery, observed using total protein staining approaches after SDS-PAGE, specific immunostaining against $Ca_V2.2$ in western blots revealed a low content of $Ca_V2.2$ in the fractions of interest. The discrepancy between both visualization methods may be explained by a protein impurity of the same size, that was not separated in the purification process. Due to the low specific $Ca_V2.2$ protein content, this purification approach can most probably be considered not suitable. Anion exchange chromatography in combination with size exclusion chromatography as polishing step yielded a $Ca_V2.2$-containing sample of high purity, but low recovery was observed with this approach. As a majority of the protein content was lost during the purification process, this method turned out to be less efficient than other multistep approaches. Changing the conditions during the respective chromatography step offers the potential to subsequently improve the recovery rate while preserving high purity levels. Further refinement of the protocol will be performed in order to fully exploit this promising approach.

Combining differential centrifugation with density gradient centrifugation gained promising results in terms of overall separation while exhibiting high recovery rates. Although the final purity of the $Ca_V2.2$ sample after purification over centrifugation-based techniques remains incomplete and only partial, these findings provide a strong foundation for further optimization. By exploring a wider range of conditions and techniques, such as varying the density gradients with regard to media and respective density range, or by combining several centrifugation steps, enhancement of the purification process may be achieved to obtain an even higher level of purity.

To summarize, we developed a suitable expression system for the production of functional membrane-incorporated $Ca_V2.2$ channels as basis for subsequent purification approaches. Furthermore, an improved strategy for cell lysis and solubilization to prepare and stabilize $Ca_V2.2$ outside of the membrane context in solution was established. For further separation of $Ca_V2.2$ from most impurities present in the complex cell lysate, a multistep purification approach, combining different separation techniques based on protein size and charge, was identified to be best suitable. Nevertheless, there is potential for enhancement in the purification strategy, as so far tested methods did not reach the optimal purity and recovery. The current method has shown significant improvement in $Ca_V2.2$ sample purity, although samples have to be referred to as partially purified. Overall, obtained results inspire confidence in the capacity to further refine and optimize $Ca_V2.2$-specific purification strategies to subsequently uncover a protocol for the generation of pure $Ca_V2.2$ protein samples.

4.3 Effects of RD2 and RD2-Derived D-Peptides on $Ca_V2.2$ Channels

4.3.1 RD2 and Derived D-Peptides Bind and Inhibit $Ca_V2.2$ *In Vitro*

In previous studies, using an *in vitro* receptor screening approach, the $Ca_V2.2$ channel was identified as putative target for the D-peptide RD2. In a first assay, using radioligand competition assays against ω-CgTx, the affinity of the binding association between RD2 and $Ca_V2.2$ was determined to fall within the range of 120 nM (Kutzsche, Guzman et al. 2023). This association was further characterized to exhibit a concentration-dependent and reversible nature, the latter as a function of membrane potential, overall altering the gating properties of the channel voltage- and state-dependently. In contrast to this, inhibition of $Ca_V2.2$ channels, using the first identified inhibitor ω-CgTx GVIA, resulted in an irreversible block of the channel, in line with previously described effects (Williams, Brust et al. 1992).

Here, SPR as well as MST experiments were conducted, using partially purified recombinant $Ca_V2.2$ protein, in order to investigate the affinity and corresponding kinetics of the binding interaction between RD2 and $Ca_V2.2$ channels more in detail. Determination of the dissociation constant for the interaction between RD2 and partially purified $Ca_V2.2$ via SPR revealed a robust and dose-dependent binding affinity, yielding a corresponding K_D value within the picomolar range (40 pM to 120 pM). The respective tandem repeat D-peptide RD2RD2 was observed to bind with slightly lower affinity. An ω-CgTx positive control was incorporated in the experimental design to validate the assay, revealing a corresponding K_D value between 60 pM and 280 pM for the interaction with $Ca_V2.2$ channels. While prior studies have reported a slightly higher affinity for this interaction, our results are generally in accordance with findings in the literature describing a K_D value in the low picomolar range for the binding of ω-CgTx to $Ca_V2.2$ channels (Wagner, Snowman et al. 1988; Yamaguchi, Saisu et al. 1988; Williams, Brust et al. 1992). Limitations of this study can be traced back to the usage of partially purified $Ca_V2.2$ as analyte, as experiments using SPR are most effective with homogenously purified protein samples. The discrepancy in obtained K_D values compared with those described in the literature may be at least in part attributable to impurities present in the sample. While the limitations of the study demand cautious consideration of the exact K_D values of the binding of RD2 or its tandem repeat D-peptide RD2RD2 to $Ca_V2.2$ channels, the robust demonstration of a strong association of the D-peptides with $Ca_V2.2$ provides further validation of results from previous binding studies.

In addition to label-free evaluation techniques, the association of $Ca_V2.2$ with RD2 was further analyzed in solution using MST, facilitating uninhibited binding that is not affected by potential matrix interference effects. We were able to demonstrate a pronounced, dose-dependent association between the components under investigation. Determination of the binding affinity exhibited a high degree of precision across multiple biological replicates within the same experimental trial. The calculated dissociation constant was observed to be within the low nanomolar range (4 nM), indicating a lower affinity compared with results obtained from SPR experiments. However, the same limitations apply for these experiments, as only partially purified $Ca_V2.2$ was used as analyte, rendering the obtained K_D overall inaccurate. Additional in-depth investigations are essential to further evaluate the binding affinity and kinetics more in detail by performing experiments using highly pure $Ca_V2.2$ protein. Nevertheless, both tested methods indicate a robust association of RD2 with $Ca_V2.2$ channels purified from mammalian cells, confirming its potential as promising compound for the inhibition of $Ca_V2.2$ channels in the context of neuropathic pain or neurodegenerative diseases.

Through a rational design approach, we aimed to identify novel RD2-derived D-peptides that potentially bind $Ca_V2.2$ channels, using mutagenesis of key amino acids to residues exhibiting analogous or disparate biophysical properties. The obtained peptide library was first tested with regard to cellular toxicity in order to exclude D-peptides that exhibited toxic effects when applied to mammalian cells. In line with the previously described favorable biosafety profile of RD2 (Kutzsche, Jurgens et al. 2020), neither RD2 nor any of the RD2-derived D-peptides did show any negative effects on cell viability. In contrast, RD2 as well as RD2C were observed to even increase the metabolic activity as assessed in the MTT-assay. This may be caused by various underlying mechanisms, related to stimulation of cell proliferation, increased metabolic activity, interference with signaling pathways or reduced apoptosis. The specific process is dependent on the nature of the D-peptide under investigation and its biological activity. Further studies would be needed to elucidate the exact pathways involved.

Next, the inhibitory properties of RD2-derived D-peptides on ion fluxes mediated by $Ca_V2.2$ channels were evaluated through electrophysiological patch clamp experiments. In line with previous obtained results, the known $Ca_V2.2$ inhibitor ω-CgTx GVIA reversed $Ca_V2.2$-mediated ion fluxes completely and irreversibly, whereas RD2 was able to partially inhibit $Ca_V2.2$ channels in a reversible manner (Wagner, Snowman et al. 1988; Kutzsche, Guzman et al. 2023). In a similar way, the RD2-derived D-peptide RD2C was able to reduce approximately 40% of $Ca_V2.2$-mediated currents in a fast manner, further displaying rapid current recovery after wash-out of the compound. Although the kinetics of inhibition of $Ca_V2.2$ channels are comparable to inhibition through RD2, RD2C as only rationally designed RD2-derived D-peptide showed improved inhibitory capacity, showing first successful optimization of the lead compound.

Subsequent investigations will evaluate the inhibitory mechanism of RD2C on $Ca_V2.2$ channels more in detail, considering potential influence of the inhibitory capacity by $Ca_V\alpha_{1B}$ splice variants, the overall protein complex assembly with regard to associated auxiliary subunits or the respective cellular system employed in the experiments. Additionally, more work will be needed to elucidate the state dependence of the inhibition of $Ca_V2.2$-mediated currents through RD2C.

The strong binding affinity of ω-CgTx for $Ca_V2.2$ channels in combination with the irreversible nature of its inhibitory effect and limited brain clearance, due to its low BBB penetration, subsequently leads to severe side effects and an increased risk of irreversible overdosing. So far, the only approved drug for the inhibition of $Ca_V2.2$ channels is ziconotide (Prialt), a synthetic peptide derived from the natural occurring peptide ω-CgTx MVIIA, which exhibits comparable specific and high-affinity association with $Ca_V2.2$ channels. As a result of its limited ability to cross the BBB, an intrathecal application route is required. Together with CNS-related adverse effects, ziconotide administration provides a non-optimal treatment option for the pharmacological inhibition of $Ca_V2.2$ channels in the context of diseases, including pain or neurodegenerative diseases (Sanford 2013). In contrast to that, RD2 shows favorable characteristics, exhibiting oral availability, high BBB permeability, favorable pharmacokinetic properties as well as an excellent safety profile (Leithold, Jiang et al. 2016; Schartmann, Schemmert et al. 2018). While yet to be experimentally validated, a similar characteristics profile can be assumed for RD2-derived D-peptides like RD2C, presenting this class of compounds as a promising therapeutic strategy for $Ca_V2.2$ inhibition. Additional experimental work will be implemented to further improve the lead compound with regard to channel inhibition kinetics and subtype

specificity. Furthermore, by implementing additional research efforts it is anticipated to validate the concept of $Ca_V2.2$ inhibition by RD2 or RD2-derived D-peptides in disease context as therapeutic treatment strategy. These studies subsequently hold the potential to pave the way for the development of innovative therapeutic strategies, utilizing the properties of RD2 and RD2-derived compounds for improved patient outcomes.

To summarize, we confirmed that the lead compound RD2 binds and inhibits $Ca_V2.2$ channels with high affinity in a reversible and dose-dependent matter. We further were able to generate a first RD2-derived D-peptide, namely RD2C, that exhibits favorable $Ca_V2.2$ inhibition characteristics, presenting a first improved lead compound-derived D-peptide.

To further advance the improved lead compound RD2C with regard to subsequent clinical application, the next steps would include the conduction of preclinical studies to evaluate its efficacy, safety, pharmacodynamics, and pharmacokinetics in wild-type as well as relevant animal models of neurodegenerative diseases like AD. If the outcome is promising, phased clinical trials (Phase I to assess the overall safety of the compound, Phase II for analysis of efficacy and respective dosage, and Phase III for large cohort studies) would be needed for the collection of data that is required for the regulatory approval from the respective authorities. Compared with other treatment strategies, such as monoclonal antibodies (mAbs), that target for example Aβ, the inhibition $Ca_V2.2$ channel offers an approach with a different mechanism of action, potentially regulating neuronal excitability and synaptic function in a direct way. Thus, this neuroprotective strategy may be able to complement therapies that focus on specific pathological proteins by providing a broader neuroprotective approach. Ultimately, a combination of therapies, including both mAbs and calcium channel blockers, could yield synergistic effects, which might overall enhance therapeutic treatment outcomes in AD.

4.3.2 *In Vivo* Effects of RD2 on Ca^{2+} Fluxes in the Cortex of the Rodent Brain

In addition to assessment of *in vitro* effects of RD2 on $Ca_V2.2$-mediated Ca^{2+} fluxes, wide-field Ca^{2+} imaging was used to assess the *in vivo* effect of the $Ca_V2.2$-inhibiting compound RD2 on neuronal activity in healthy, awake mice in response to a sensory stimulus. This method allows for high spatiotemporal resolution analysis of the stimulus-evoked responses in the cortex of murine brains. The here analyzed type of neuron, excitatory neurons of layer 2/3 of the neocortex, can be found in the more superficial region of the cortex. These cells play a key role in identification, integration and subsequent processing of various information through intracortical connections and further amplify stimulus-evoked responses via output to less superficial cortical layers, subsequently projecting to other thalamic or striatal brain structures (Belgard, Marques et al. 2011; Luo, Hasegawa et al. 2017; Quiquempoix, Fayad et al. 2018).

Here we used a sensory stimulus to the right forepaw to activate the respective cortical brain area in response. Sensory stimuli are first perceived via specialized mechanoreceptors in the skin of the murine paw (Olson, Dong et al. 2016; Neubarth, Emanuel et al. 2020). These signals are then transduced via spinal grey matter feedforward pathways onto the thalamus where they stop in the respective thalamic nuclei to further ascend via two parallel thalamo-cortical pathways, projecting to the primary somatosensory cortex (Willis and Westlund 2001; Viaene, Petrof et al. 2011; Julius and Nathans 2012; Watson 2012; Sherman 2016; Mo and Sherman 2019). Sensory stimulation of certain areas of the body will subsequently lead to a stimulus-evoked response and activation of the corresponding area of the primary somatosensory cortex in the contralateral brain hemisphere. In line with findings in literature, in this study, a sensory stimulus to the right forepaw was able to trigger stimulus-evoked activation in the brain area that was previously described as the corresponding “upper limb” area of the primary somatosensory cortex (SSP-ul) (Lim, Mohajerani et al. 2012; Mohajerani, Chan et al. 2013). As only the SSP-ul region of the contralateral brain hemisphere, but not the respective ipsilateral area, displayed stimulus-evoked activation, spontaneous activation could be excluded. The absence of activation on the ipsilateral side indicates the successful evocation of a specific stimulus-dependent response.

Evaluating the activation pattern of the sensory stimulus-evoked response in the primary sensory cortex more in detail, it was observed to consist of two distinct components, an early activation, approximately 300 ms after stimulus onset, as well as a late response, found 700 ms to 900 ms after stimulus onset, which is in line with findings previously described in

the literature (Sur and Sinha 2009; Sachidhanandam, Sreenivasan et al. 2013; Manita, Suzuki et al. 2015; Bermudez-Contreras, Schjetnan et al. 2023). The early component is commonly thought to resemble the identification of the sensory stimulus, which gets feedforwarded from thalamic structures and, putatively, directly through additional connections from the spinal cord and the brain stem to the respective corresponding somatosensory cortical area (Kiritani, Wickersham et al. 2012; Manita, Suzuki et al. 2015).

$Ca_V2.2$ channels are highly expressed in primary sensory dorsal root ganglia, mainly involved in nociception and pain transmission, but are further found in the pre-synapse of neurons in the CNS. Given this, inhibition of $Ca_V2.2$ may lead to alterations in signal transmission in response to a sensory stimulus in the periphery as well as in the brain. Using wide-field Ca^{2+} imaging on awake mice, the stimulus-evoked response was analyzed and compared before and after *i.p.* application of RD2 or the respective vehicle control. A reduction of the overall amplitude of the stimulus-evoked cortical response was observed in the contralateral SSp-ul area after compound application, which was not found in vehicle-treated mice. It was previously shown that the activated brain area, as well as the amplitude of the evoked response, is positively correlated with the strength of the stimulus (Afrashteh, Inayat et al. 2021). As the stimulus was kept constant for all experiments, the observed effect is likely due to reduced signal transmission which is potentially mediated by inhibition of $Ca_V2.2$-mediated Ca^{2+} fluxes by RD2. This observation demonstrates a functional validation of the compound RD2's inhibitory capability on $Ca_V2.2$ channels evidenced in an *in vivo* experimental setup, consistent with the findings from previous *in vitro* experiments.

More in detail, a moderately reduced amplitude of the early evoked response was observed, whereby the second late component of the activation in the SSp-ul region was decreased more pronounced. It is thought that the second, later stimulus-evoked activation of the primary somatosensory cortex originates from feedback inputs mediated by cortico-cortical, thalamo-cortical or over cortico-thalamic-striatal neurocircuits (Guillery and Sherman 2002; Sachidhanandam, Sreenivasan et al. 2013; Manita, Suzuki et al. 2015; Mandelbaum, Taranda et al. 2019). These feedback inputs from other brain regions are thought to be involved in perceptual processing of the initial identified sensory stimulus, particularly mediated by the motor cortex of the brain (Ferezou, Haiss et al. 2007; Matyas, Sreenivasan et al. 2010; Kwon, Yang et al. 2016; Yamashita and Petersen 2016; Romo and Rossi-Pool 2020). A crucial characteristic of the secondary motor cortex is its rich interconnectivity with various other brain areas. It shows a variety of afferent as well as efferent neuronal connections with cortical areas, including the sensory cortex, involved in sensory perception, the retrosplenial

cortex, responsible for cognitive functions like episodic memory or planning, and the association area of the brain, the parietal cortex, but also receives inputs from thalamic structures (Reep, Goodwin et al. 1990; Reep and Corwin 1999; Zingg, Hintiryan et al. 2014; Yamawaki, Radulovic et al. 2016). By this, it functions as an important cortico-cortical link between sensory inputs and choice-related activity through stimulus processing (Barthas and Kwan 2017). It exhibits specific connectivity with regions in the primary somatosensory cortex over excitatory glutamatergic projections, which are involved in top-down control of processing in this area (Ferezou, Haiss et al. 2007; Matyas, Sreenivasan et al. 2010; Mao, Kusefoglu et al. 2011; Crochet and Petersen 2015; Funayama, Minamisawa et al. 2015). This was further highlighted by the finding that experimentally inactivating the secondary motor cortex results in suppression of the late component of the stimulus-evoked response, subsequently negatively influencing sensory perception (Manita, Suzuki et al. 2015). In this study, a similar stimulus-evoked activation and processing pattern was observed, showing a primary early response in the SSP-ul region, followed by an evoked response in the secondary motor cortex which is subsequently followed by a second peak of activity in the primary sensory cortex. This putative processing circuit was observed to be partially disrupted by the application of RD2, leading to a diminished activation peak in the secondary motor cortex and a corresponding decrease in the activation for the late component of the response in the primary somatosensory cortex. These effects may, at least in part, be mediated by inhibition of $Ca_V2.2$ through RD2, indicating a role of these Ca^{2+} channels in processing of sensory information.

In line with this, previous data suggested that RD2 may exhibit a higher affinity for splice variants of the $Ca_V\alpha_{1B}$ domain of $Ca_V2.2$ channels that are expressed in the CNS over other splice variants found predominantly expressed in the PNS (Lin, Haus et al. 1997; Lin, Lin et al. 1999; Kutzsche, Guzman et al. 2023). This characteristic could explain the finding that late stimulus-evoked cortical responses, generated via cortico-cortical neurocircuits, are more profoundly inhibited following application of RD2 compared with early stimulus-evoked responses, directly ascending from the periphery. Further experimental work could explore deeper into the complex underlying processes, shedding light on the mechanism involved in RD2-dependent inhibition of $Ca_V2.2$ in the CNS. This research will be crucial in expanding our understanding of the role of $Ca_V2.2$ in signal perception, as well as effects of $Ca_V2.2$ channel inhibition.

The ability of RD2 to influence neuronal Ca^{2+} fluxes in the cortex of awake mice strengthens our hypothesis for its use as neuroprotective therapeutic in the context of neurodegenerative diseases. In a healthy brain state, the neural processing of sensory information through the SSP-ul – MO-s – SSP-ul circuit may play a significant role in the behavioral manifestation of sensory perception. This is supported by the observed decline in performance that follows inhibition of this circuit in an experimental detection task in mice (Sachidhanandam, Sreenivasan et al. 2013). However, physiological changes in the context of neurodegenerative diseases may lead to a disruption of these circuits. It was previously described that experimentally induced TBI in rats causes degeneration and reorganization of neural circuits in the primary somatosensory cortex (Lifshitz and Lisembee 2012). Furthermore, it was observed that somatosensory dysfunction, especially in processing of sensory information, is found as pathological hallmark in patients with AD (Wiesman, Mundorf et al. 2021; Casagrande, Wiesman et al. 2022). In addition, AD patients exhibit impairment in habituation to sensory stimulus-evoked potentials (Curra, Marinelli et al. 2021). These findings indicate changed processes in perception and processing of sensory information in disease context, which remain to be analyzed with regard to the underlying cause. However, hypothesizing that neurodegeneration in brain areas responsible for somatosensory perception and processing is mediated, at least in part, by Ca^{2+}-dependent excitotoxicity would provide an interesting new therapeutic target for the use of RD2 as an inhibitor of Ca^{2+} fluxes mediated through $Ca_V2.2$ channels.

Nevertheless, the here presented study only presented data from three healthy mice, overall limiting the scope of the findings. Further work has to be performed to repeat these experiments with greater sample size. In addition, the here discussed processes are of high complexity, which gives the necessity to further investigate the hypothesis adequately. Incorporation of behavioral studies allows for the integration of the observed effects of RD2 on neuronal activity within the framework of higher cognitive processes, such as learning, memory or general behavior. Furthermore, considering that only healthy, young mice were used in this experimental setup, it remains to be elucidated how the processes under discussion may be altered during aging or in the context of various diseases. In addition, putative modulatory effects of disease conditions on RD2's effect on neuronal stimulus-evoked activation and processing holds great promise to subsequently advance our overall understanding of these processes. Lastly, it will be of special interest to further test newly identified RD2-derived D-peptides with favorable $Ca_V2.2$ inhibition kinetics in a similar experimental setup, comparing peptide-dependent modulation of neuronal activity.

To summarize, in this study we were able to demonstrate an inhibitory effect of RD2 on neuronal activation of Ca^{2+} fluxes in the primary somatosensory cortex of neocortical layer 2/3 excitatory neurons in response to a sensory stimulus. This was particularly evidenced by an overall reduction of stimulus-evoked cortical activation and observed alterations of the activation pattern in associated brain areas that are involved in subsequent processing of information. These findings provide a first *in vivo* proof of concept of the inhibitory capacity of the compound RD2 on neuronal Ca^{2+} fluxes in the cortex, most probably mediated by inhibition of $Ca_V2.2$ channels. Additional work will aim to elucidate the precise mechanism, specificity of inhibition, long-term course of the observed effects, including reversibility as well as involvement of this effect in higher-order processes. Overall, this will not only provide novel general insights into the role of $Ca_V2.2$ channels in mediation of Ca^{2+} fluxes during sensory processing in the CNS, but may also form the basis of a rationale for the inhibition of $Ca_V2.2$ channels by RD2 or optimized RD2-derived compounds for a putative therapeutic treatment strategy in the context of various diseases, such neurodegenerative diseases like AD.

4.4 Insights into the Binding Mode of RD2 on $Ca_V2.2$ channels

4.4.1 RD2 May Bind $Ca_V2.2$ in the Binding Groove of ω-CgTx

Findings from *in vitro* as well as preliminary *in vivo* experiments pointed towards an inhibitory effect of RD2 and the RD2-derived D-peptide RD2C on $Ca_V2.2$-mediated Ca^{2+} fluxes. To gain a deeper understanding of the mode of action of these D-peptides, it is of special interest to gain more insights into the specific binding mode of the respective D-peptide when forming a complex with the channel. To date, no structural data of the complex of RD2 binding to $Ca_V2.2$ is available. Therefore, a modeling approach was used to further elucidate putative contacts and key residues, coordinating the association.

In previous studies, RD2 successfully competed against the binding of the known inhibitor ω-CgTx to $Ca_V2.2$ channels, which was analyzed in a radioligand competition assay (Kutzsche, Guzman et al. 2023). This finding indicated a similar binding mode of RD2 and RD2-derived D-peptides, analogue to that of ω-CgTx. Previous studies demonstrated a common mode of action for various VGCC-inhibiting peptides, as they were observed to exhibit a pore-blocking mechanism (Catterall, Perez-Reyes et al. 2005; Zamponi, Striessnig et al. 2015). In line with this, the commercially available derivative of ω-CgTx, ziconotide, was previously reported to associate with $Ca_V2.2$ channels in an electronegative cavity, formed within the α_1-subunit with close proximity to the Ca^{2+}-permeable pore (Gao, Yao et al. 2021). This binding was mainly mediated by interactions of ziconotide with helices P1 and P2 of the P-loop that connects transmembrane helices S5 and S6 of $Ca_V2.2$ domains II, III and IV.

Molecular docking of small molecule ligands to their target structure is a fundamental component of structure-based drug discovery, as it enables the prediction of the binding conformation of ligands to their target sites with precision (Meng, Zhang et al. 2011). In this study, the web-based server HPEPDOCK2.0 was used to model binding of the D-peptide RD2 and the RD2-derived D-peptide RD2C to a predicted binding site on $Ca_V2.2$ channels. HPEPDOCK uses a blind global peptide docking approach, producing and docking an ensemble of peptide conformations through a hierarchical algorithm (Zhou, Jin et al. 2018). By this, putative binding modes of the D-peptides on $Ca_V2.2$ channels can be identified and analyzed with regard to key amino acids residues.

Amongst the 100 highest-scoring peptide docking models, RD2 and RD2C were observed to bind $Ca_V2.2$ by exhibiting three distinct binding modes; inside the electronegative pocket surrounding the Ca^{2+}-permeable pore, below the pore and outside of the pocket. The association of RD2 or RD2C inside and below the pocket primarily involved electrostatic interactions, resulting in the formation of several hydrogen bonds and salt bridges. In contrast, binding to external regions of the pocket demonstrated a higher contribution of hydrophobic interactions driving the association of the D-peptide with the channel.

It is important to note that the structural model of $Ca_V2.2$, used in this study, only represented a certain region of the channel and, furthermore, did not comprise any membrane components. As a consequence, modeled binding of RD2 or RD2C to the outside of the $Ca_V2.2$ minimal structure, as well as below the Ca^{2+}-permeable pore, may be prevented under native structural conditions due to steric or physical interference. Furthermore, most of the peptide docking models showed association of the peptide within the hydrophobic pocket of the $Ca_V2.2$ channel. These models also tended to exhibit lower docking scores, suggesting putatively increased association stability. This finding, in combination with previous results, indicating a similar binding mode of RD2 and ω-CgTx, signifies an increased likelihood of a binding mode of RD2 and RD2C inside the electronegative cavity of $Ca_V2.2$ channels that surrounds the Ca^{2+}-permeable pore.

The common Ca^{2+}-binding motif on VGCC channels, likewise present in $Ca_V2.2$ channels, is the EEEE pattern, formed by glutamic acid residues E314, E663, E1365 and E1655, which is localized in the electronegative cavity above the Ca^{2+}-permeable pore (Yang, Ellinor et al. 1993). Analysis of peptide docking models of RD2 as well as RD2C revealed a predominant association of the peptides with negatively charged moieties of glutamic acid and aspartic acid residues of the $Ca_V2.2$ channel. As a putative consequence, association of these compounds with residues responsible for Ca^{2+} binding may induce modifications of the gating properties of the channel. Interestingly, analysis of the highest-scoring peptide docking models revealed no frequently occurring association of the peptides with $Ca_V2.2$ residues that form the EEEE motif. However, several docking models of RD2 and particularly models docking RD2C to $Ca_V2.2$ showed binding of the peptide in regions deeply buried in the pocket surrounding the Ca^{2+}-permeable pore, with some residues of the peptides found in close proximity to the entrance of the ion selectivity pore (Fig. 3.32, B, C; Fig. 3.36, A, D, E, F). In fact, a similar direct pore-blocking mechanism was previously described for μ-CgTx KIIIA on the voltage-gated sodium channel $Na_V1.2$ (Pan, Li et al. 2019). Therefore, RD2 and RD2C may be able to exhibit their inhibitory effect on

$Ca_V2.2$-mediated Ca^{2+} fluxes, at least in part, by directly sealing the ion selectivity pore by interacting with surrounding negatively charged amino acids. In contrast to this, ziconotide shows no direct association with any residue close to the Ca^{2+}-permeable pore. Therefore, inhibition of $Ca_V2.2$-dependent Ca^{2+} fluxes via ziconotide is not mediated by sealing of the selectivity filter (Gao, Yao et al. 2021). Together, this suggests a different overall mode of action for the here described D-peptides RD2 and RD2C, as opposed to the known $Ca_V2.2$ inhibitor ziconotide.

In contrast to other pore blocking VGCC inhibitory compounds, previous studies of the complex formed by ziconotide and $Ca_V2.2$ demonstrated association of the peptide with negatively charged residues in the electronegative cavity of $Ca_V2.2$ surrounding the Ca^{2+}-permeable pore outside of the EEEE motif over the formation of ionic bonds (Gao, Yao et al. 2021). Subsequently, this association can lead to charge neutralization, thus hindering the entrance of Ca^{2+} ions into the respective pocket to establish contact to the ion selectivity filter. Observed putative binding modes of RD2 and RD2C on $Ca_V2.2$ channels share a common pattern with the binding mode of ziconotide, as all peptides were found to strongly associate with $Ca_V2.2$ residues D664, D1629 and E1659. These results indicate putative charge neutralization in the electronegative cavity of $Ca_V2.2$, mediated by binding of the compound to negatively charged patches on $Ca_V2.2$, as an alternative mode of action for the inhibition of $Ca_V2.2$ channels through RD2 and RD2C.

As not all of the $Ca_V2.2$ residues in contact with RD2 and RD2C are conserved in other VGCC subtypes (like D1629 or D1659), the subtype specificity of RD2, as observed previously, may be attributable to the crucial interaction of the D-peptide residues with these $Ca_V2.2$-specific sites. However, additional work has to be undertaken to verify and further improve the subtype specificity of RD2 as well as for RD2C. For this, identification of common $Ca_V2.2$-specific contact residues in highest-ranking docking models was used to create a library of RD2-derived D-peptides, which will subsequently be analyzed more in detail in high-throughput screening assays to identify D-peptides with improved $Ca_V2.2$-specific binding capacity.

Overall, the observed binding modes of both compounds inside the $Ca_V2.2$ electronegative pocket displayed high flexibility with no distinct static pattern identified, indicating a dynamic and adaptable interaction with $Ca_V2.2$. Through this, RD2 and RD2C may exhibit their inhibitory effects on Ca^{2+} fluxes through multiple mechanisms, combining the prevention of Ca^{2+} entry into the pocket by compensating negative charges in the electronegative cavity, while further concurrently blocking the Ca^{2+}-permeable pore sterically by interacting with amino acid residues of the surrounding ion selectivity filter. The observed flexibility of the binding inside of the Ca^{2+}-permeable pore groove may subsequently also account for the reversible character of RD2- and RD2C-mediated inhibition of $Ca_V2.2$ currents that was observed in electrophysiological studies.

Summarizing, the obtained results show a complex putative mode of action for the inhibitory effect of RD2 and RD2C on $Ca_V2.2$-mediated currents with regard to their binding mode. Nevertheless, the data has to be handled and interpreted with care, as the here performed structural modeling has limitations. Only a simplified model of the $Ca_V2.2$ channel, already assuming a binding mode, was used as input. Including more variables, such as the complete structure, association with auxiliary subunits, or performing molecular dynamics simulations, may subsequently influence the modeling results. Future work will assess theoretical evaluation of putative binding modes in more complex structural modeling approaches, including additional parameters to closer resemble the native environment of the interaction. Ultimately, an experimental approach for structural analysis of RD2 or RD2-derived D-peptides associated with $Ca_V2.2$ channels is needed for verification of the modeling approach. Possible methods include solving the structure of $Ca_V2.2$ channels in complex with RD2 or RD2-derived D-peptides using cryo-EM or crystallography approaches. Nevertheless, the here presented work provides an interesting framework for the rational design of $Ca_V2.2$-inhibiting D-peptides.

4.4.2 RD2 and Derived D-Peptides May Act as Cationic Arginine-Rich Peptides

In the last years, several sources of evidence pointed towards a new class of substances for the treatment of neurodegenerative diseases, based on their observed neuroprotective properties. The class of cationic arginine-rich peptides (CARPs) describes peptides of short length (4 to 40 amino acids) with an overall positive net charge, mainly contributed to by a high arginine content (20% to 100%) combined with additional positive charges from histidine or lysine residues (Meloni, Mastaglia et al. 2020). CARPs are known to exhibit membrane traversing properties and BBB permeability, which was found to be reinforced by additional tryptophan, phenylalanine or tyrosine residues that contribute to the amphiphilicity of the peptide. Our lead compound RD2 has an overall arginine content of 42% and, with additional positive charges from two histidine residues and an amidated C-terminus, the overall peptide charge is highly positive (net charge of 6.18 at pH 7.0). The D-peptide further exhibits amphiphilic properties attributable to an overall hydrophobic N-terminal and a hydrophilic C-terminal region, which results in favorable BBB permeation kinetics (Schartmann, Schemmert et al. 2018). Given these characteristics, RD2 may also be classified as a CARP.

CARPs are long known to exhibit neuroprotective properties over a wide range of actions. In an initial investigation, assessing the effects of CARPs, short arginine-containing peptides were observed to target NMDA receptors, subsequently reducing excitotoxicity by blocking ionic currents (Ferrer-Montiel, Merino et al. 1998). An overall reduction in Ca^{2+} influx after application of CARPs was further observed in models of glutamate-induced excitotoxicity (Vaslin, Rummel et al. 2009; Meloni, Milani et al. 2015; MacDougall, Anderton et al. 2020). Furthermore, CARPs fused to specific neuroprotective cargo proteins reduced intracellular Ca^{2+} influx by reducing the cell surface density of Ca^{2+} channels and modifying the activity of plasma membrane receptors, predominantly by regulating the internalization of different ion channels (Rothbard, Kreider et al. 2002; Meloni, Milani et al. 2015; Meloni, Mastaglia et al. 2020). Although most of this evidence reported regulation of Ca^{2+} influx through modulation of NMDA receptor density or activity, $Ca_V2.2$ was similarly observed to be regulated by compounds from the class of CARPs. In DRG-neurons, application of the CARP fusion peptides TAT-L1 or TAT-ct-dis was observed to reduce the potassium-evoked Ca^{2+} influx mediated by $Ca_V2.2$ channels (Wilson, Schmutzler et al. 2012). Furthermore, CARP fusion peptides Myr-tat-CBD3, R9-CBD3-A6K and t-CNRP1 were observed to

reduce the $Ca_V2.2$ cell surface density in DRG neurons which subsequently led to reduced $Ca_V2.2$-mediated Ca^{2+} currents (Francois-Moutal, Wang et al. 2015; Xie, Chew et al. 2016; Moutal, Wang et al. 2017). Interestingly, it was previously hypothesized that these fusion peptide-induced neuroprotective effects were not only mediated by the putative neuroprotective cargo molecule, but may instead be caused by the fused cell-penetrating peptide itself, mainly mediated through peptide-induced receptor internalization (Meloni, Milani et al. 2015). This postulated mode of action provides a convincing rationale for the modulatory effect of RD2, acting as a CARP in the inhibition of $Ca_V2.2$ channels. If application of RD2 or RD2-derived D-peptides will subsequently lead to reduced channel density in the plasma membrane remains to be elucidated in further experiments.

Modeling of the binding of RD2 and RD2C in a complex with $Ca_V2.2$ revealed similar interaction profiles for L- as well as D-enantiomeric peptides without a detected stereo-selectivity of the binding. This indicates a stronger contribution of electrostatic interactions over structural association, as reported for other neuroprotective CARPs in previous studies (Ferrer-Montiel, Merino et al. 1998; Edwards, Anderton et al. 2017; Milani, Bakeberg et al. 2018). This is further reinforced by the finding that the interaction surface in the docking models of RD2 or RD2C and $Ca_V2.2$ is predominantly stabilized by the formation of hydrogen bonds and salt bridges predominantly between C-terminal arginine residues of the peptide and negatively charged residues of $Ca_V2.2$. This tendency was further strengthened in the proposed binding area in close proximity to the Ca^{2+}-permeable pore. Binding of those D-peptides to the channel may subsequently lead to channel antagonization through alteration of channel kinetics or ion transport properties (Meloni, Mastaglia et al. 2020).

Furthermore, it was previously demonstrated that particularly the guanidinium group of arginine residues possesses the capability to bind distinct sites on the channel surface, resulting in modulation of the channel activity and alterations in ion transport properties (Garcia, King et al. 1990; Weng, Gai et al. 2003; Kalia and Swartz 2011; Armstrong, Mason et al. 2016; Duran-Riveroll and Cembella 2017). RD2, with its CARP-analog characteristics, may be able to directly bind to certain guanidinium group binding sites at negatively charged residues near the entrance of the Ca^{2+}-permeable pore region of the channel, subsequently altering $Ca_V2.2$ channel kinetics. A similar effect was reported for voltage-gated potassium channels, where guanidinium groups were observed to interfere with a hydrophobic interface between subunits, which subsequently locks the channel in closed conformation (Wulff and Zhorov 2008; Kalia and Swartz 2011).

An alternative mode of action of CARPs could comprise the replacement of $Ca_V2.2$-specific arginine residues in crucial interactions that are involved in channel modulation. Arginine residues are associated with negatively charged moieties by the formation of strong bidentate hydrogen bonds that are further stabilized by salt bridges with negatively charged residues (Asp or Glu) or over cation-π interactions with aromatic sidechains (Phe, Tyr, or Trp) (Zacharias and Dougherty 2002). Under physiological conditions, certain arginine residues of $Ca_V2.2$ channels, and in particular their guanidinium groups, function as gating charge carrier and are associated in important arginine-phosphate interactions with phospholipids of the surrounding plasma membrane. By this, they form an important component of the voltage sensor that is mainly involved in regulation of channel opening in response to membrane depolarization (Schmidt, Jiang et al. 2006; Armstrong, Mason et al. 2016). Introducing additional guanidinium groups over arginine-rich peptides, which are able to associate with phosphate groups of membranes, may disrupt this channel-membrane association by sequestering phospholipid groups, finally leading to channel inhibition. In addition, binding of positively charged guanidinium moieties to negatively charged phosphate groups in the extracellular plasma membrane of neurons could cause a reduction in surface potential, known as charge screening, which subsequently would alter the channel activation kinetics in response to a membrane depolarization stimuli (Green and Andersen 1991).

With regard to bioavailability, the amphiphilic character of RD2 and RD2-derived D-peptides, in combination with the guanidinium-phosphate binding-dependent association of those D-peptides with the plasma membrane, further allows for the membrane penetration capability of those compounds (Rothbard, Kreider et al. 2002; Suzuki, Futaki et al. 2002; Wender, Galliher et al. 2008; Takeuchi and Futaki 2016). This facilitates improved BBB permeability and, by this, the compounds exhibit favorable pharmacokinetic properties for the treatment of neurodegenerative diseases affecting the central nervous system.

Although direct modulation of the Ca^{2+} influx through $Ca_V2.2$ by RD2 and RD2C has been shown previously and in this study, neuroprotective properties of the D-peptide may also be mediated through other modes of action. As RD2 shows membrane association and penetrating properties, additional association with different cellular organelles may be able to influence key pathways in neurodegeneration. Other CARPs were previously observed to target mitochondrial components to subsequently prevent mitochondrial dysfunction-induced cell death (Szeto 2006; MacDougall, Anderton et al. 2019). In addition, direct scavenging of reactive molecules by CARPs may also provide an alternative mode of action

by reducing oxidative stress and the resulting cellular damage (Giardino, Fard et al. 1998; Courderot-Masuyer, Dalloz et al. 1999). As inflammatory pathways are found as major hallmarks in a variety of neurodegenerative diseases, the finding that CARPs also exhibit anti-inflammatory properties through modulation of Nuclear factor kappa B (NF-κB) signaling pathways presents an interesting branch of evidence (Wang, Xu et al. 2011). This may also provide an additional putative mode of action for the tandem repeat D-peptide RD2RD2, that showed anti-inflammatory properties in a mouse model of ALS (Post, Kogel et al. 2021; Post, Schaffrath et al. 2021). Lastly, a growing body of evidence hints towards the protein stabilizing and disaggregating properties of CARPs (Baynes, Wang et al. 2005; Shukla and Trout 2010). Interestingly, most of the aggregating proteins found as pathological hallmarks in various neurodegenerative diseases exhibit an overall negative charge and thereby provide excellent targets for CARPs. RD2 was originally designed and developed to specifically bind Aβ and, in line with other CARPs, shows extensive protein stabilization and disaggregating properties (van Groen, Wiesehan et al. 2008; van Groen, Schemmert et al. 2017; Kass, Schemmert et al. 2022).

Nevertheless, the precise contribution of the C-terminal arginine-rich stretch of the D-peptides remains to be elucidated in more detail. It is critical to investigate whether this highly positively charged region of the peptide plays a direct role in channel modulation, thereby demonstrating a mode of action for those D-peptides analogous to that of CARPs, or if the penta-arginine stretch primarily enhances the BBB-permeability of the D-peptides, or potentially both. Future studies will evaluate the inhibitory capacity, as well as the BBB permeation efficacy of D-peptides lacking the C-terminal penta-arginine sequence, employing suitable *in vitro* models.

To summarize, while the exact contribution of the cationic properties and the respective arginine residues to the neuroprotective effects of CARPs remains unclear, the overall findings point towards a role for cell-penetrating CARPs as general effectors in the context of neuroprotection, rather than this effect being only mediated by respectively fused cargo proteins. Due to their similar characteristics, RD2 and RD2-derived D-peptides are likely to act in a comparable neuroprotective way as described for CARPs. This provides an interesting hypothesis for their mode of action on Cav2.2 channels, which could include direct or indirect inhibition of Ca^{2+} fluxes through the channel but may not present the mutually exclusive mechanism by which these compounds act neuroprotective.

4.5 Concluding Remarks and Future Perspectives

Previous studies and first results from this work suggested a role for $Ca_V2.2$ channels in the context of neurodegenerative diseases such as AD, which is potentially mediated, at least in part, by upregulated channel density leading to Ca^{2+} dysregulation, as demonstrated in this study, and subsequent excitotoxicity. The here presented findings highlight $Ca_V2.2$ as an interesting therapeutic target for a general neuroprotection approach. This study further aimed to optimize our lead compound RD2, an all D-enantiomeric 12-mer peptide, towards improved inhibition capacity on $Ca_V2.2$-mediated Ca^{2+} fluxes.

Specific emphasis was laid on functional expression of the channel with subsequent purification in its native three-dimensional conformation. Due to the complex structure of the multidomain channel $Ca_V2.2$ and further challenges due to its integral membrane protein characteristics, establishment of a suitable protocol for the complete purification of the protein remains a challenging future need, although first protocols achieved improved separation and recovery for the generation of partial purified $Ca_V2.2$ protein samples.

Furthermore, *in vitro* proof of concept of the inhibitory capacity of RD2 on Ca^{2+} fluxes, mediated by $Ca_V2.2$, was confirmed in *in vivo* experiments using wide-field Ca^{2+} imaging. Here, RD2 was observed to not only inhibit signal transmission from the periphery to the brain, but was further found to influence intracortical signaling, putatively involved in information perception and processing. It remains to be analyzed how this effect may influence other higher-order cognitive or behavioral skills and its effect in disease context.

A first lead-derived candidate, namely RD2C, was obtained via rational design and demonstrated to show enhanced inhibitory effects on $Ca_V2.2$-mediated currents. RD2C was able to inhibit $Ca_V2.2$-mediated currents in a dose-dependent way with fast recovery observed afterwards. Compared with RD2, a significantly increased percentage of inhibited $Ca_V2.2$-mediated currents could be detected, presenting this D-peptide as a promising new candidate. Additional work will deal with the evaluation of the inhibitory capacity with regard to voltage dependence, subtype and isoform specificity as well as subsequently *in vivo* proof of concept.

Lastly, peptide docking modeling was employed to gain more insights into the underlying mode of action of the inhibition of $Ca_V2.2$ channels by RD2 and RD2C. The lack of a clear binding mode of the D-peptides on $Ca_V2.2$ channels as observed in the docking modeling approach might indicate a rather flexible binding mode of both D-peptides inside the electronegative cavity of $Ca_V2.2$ channels that forms the entrance of the ion selectivity filter above the Ca^{2+}-permeable pore. Electrostatic interactions of the positively charged arginine-rich C-terminal region of RD2 and RD2C, associated with negatively charged residues of $Ca_V2.2$, possibly leads to the blocking of Ca^{2+} entrance due to charge neutralization or direct steric occlusion of the Ca^{2+}-permeable pore. By this, RD2 and RD2C may inhibit $Ca_V2.2$-mediated Ca^{2+} fluxes through a pore-blocking mechanism. More work is needed to analyze the binding mode on a higher level of complexity, including total channel structures and further auxiliary subunits, plasma membrane components, or using molecular dynamics simulation to analyze the stability of the association of the complex over time. Experimental structural data will finally be needed for the confirmation of the obtained *in silico* identified binding mode of the compounds on $Ca_V2.2$ channels.

To summarize, the here presented study not only identified the $Ca_V2.2$ channel as a promising therapeutic target for the treatment of neurodegenerative diseases, following a general neuroprotection approach, but further presented the lead compound RD2 as well as an improved lead-derived D-peptide, namely RD2C, as a putative novel therapeutic compound. Additional work has to overall deal with further improvement of the lead candidate as well as final verification with regard to its therapeutic capacity, and will follow up this study.

I. Appendix

Table I.1: Effects of different Aβ species on VGCCs

	Subtype (CCB)	Aβ species	Effect	Model	Reference
Expression	L-type	Aβ oligomers (Endogenously expressed Aβ)	Increased expression of $Ca_V1.2$ after Aβ production	Human neuroblastoma/ MC65 cells	(Anekonda, Quinn et al. 2011)
	L-type	$Aβ_{25-35}$ (25 nM)	Increased transcription and expression levels of $Ca_V1.2$ and surface levels of $Ca_V1.3$	Primary hippocampal rat neurons	(Kim and Rhim 2011)
	L-type	Aggregated $Aβ_{25-35}$ (20 µM)	Increased transcription and expression levels	Human SK-N-SH neuroblastoma	(Chiou 2006)
	L-type	Amyloid plaques	Associated with increased $Ca_V1.2$ expression	Reactive astrocytes in hAβPP751 mice	(Daschil, Obermair et al. 2013)
	P/Q-type	Aggregated $Aβ_{25-35}$ (20 µM)	Increased transcription and expression levels	Human SK-N-SH neuroblastoma	(Chiou 2006)
	N-type	Aggregated $Aβ_{25-35}$ (20 µM)	Increased transcription and expression levels	Human SK-N-SH neuroblastoma	(Chiou 2006)
Modulation	L-type (nifedipine)	$Aβ_{25-35}$ (25 nM)	Increased Ca^{2+} influx (blocked by CCB)	Transfected HEK293 cells ($Ca_V1.2$ and 1.3)	(Kim and Rhim 2011)
	L-type (nifedipine)	Oligomeric (6-8 mer) $Aβ_{25–35}$ (200 nM)	Increased amplitude (blocked by CCB)	CA1 hippocampal neurons (slice culture)	(Rovira, Arbez et al. 2002)
	L-type (nimodipine (and Gas6))	$Aβ_{25-35}$ (10 µM)	Increased Ca^{2+} influx (blocked by CCB)	Primary cortical rat neurons	(Yagami, Ueda et al. 2002)
	L-type (nimodipine)	Aggregated $Aβ_{25-35}$ (10 µM)	Increased Ca^{2+} influx (blocked by CCB)	Primary cortical rat neurons	(Ueda, Shinohara et al. 1997)
	L-type (S-312-d, nimodipine)	Aggregated $Aβ_{25-35}$ (10 µM)	Increased amplitude (blocked by CCB)	Primary cortical rat neurons	(Yagami, Ueda et al. 2004)
	L-type (nimodipine)	Monomeric $Aβ_{25-35}$ (23 µM)	Cnc to amplitude or kinetics	N1E-115 neuroblastoma	(Davidson, Shajenko et al. 1994)

	Subtype (CCB)	Aβ species	Effect	Model	Reference
Modulation	L-type (verapamil, nifedipine, diltiazem)	$A\beta_{25-35}$ (40 µM)	Increased Ca^{2+} influx (blocked by CCB)	Human microglial cells	(Silei, Fabrizi et al. 1999)
	L-type (nimodipine (and bis(7)-tacrine))	-Fibrillar $A\beta_{25-35}$ (20 µM) -Fibrillar $A\beta_{1-42}$ (10 µM) -sOligomeric $A\beta_{1-42}$ (1 µM)	Increased Ca^{2+} influx (blocked by CCB)	Primary cortical rat neurons	(Fu, Li et al. 2006)
	L-type (nifedipine)	-Oligomeric (4-6 mer) $A\beta_{1-40}$ (200 nM)	Cnc (overall increased amplitude, not blocked by CCB) → Act through non-L-type VGCC	CA1 hippocampal neurons (slice culture)	(Rovira, Arbez et al. 2002)
	L-type (nifedipine)	$A\beta_{1-40}$ (1 µM)	Increased Ca^{2+} influx (blocked by CCB)	Rat cortical synaptosomes	(MacManus, Ramsden et al. 2000)
	L-type (nimodipine)	Monomeric $A\beta_{1-40}$ (23 µM)	-Increased Ca^{2+} influx, blocked by CCBs -Shift V_{act} to more positive potentials	N1E-115 neuroblastoma	(Davidson, Shajenko et al. 1994)
	P/Q-type (ω-Aga-IVA, ω-CgTx-MVIIC)	Aggregated $A\beta_{25-35}$ (10 µM)	P/Q-type block: cnc in Aβ-induced Ca^{2+} influx	Primary cortical rat neurons	(Yagami, Ueda et al. 2004)
	P/Q-type (ω-Aga-IVA)	Monomeric $A\beta_{1-40}$ (1 µM)	Increased current	Primary cortical rat neurons	(Ramsden, Henderson et al. 2002)
	P/Q-type (ω-Aga-IVA)	$A\beta_{1-40}$ (1 µM)	Increased amplitude (blocked by CCB)	Cortical neurons	(MacManus, Ramsden et al. 2000)
	P/Q-type (roscovitine)	$A\beta_{1-42}$ globulomer (8 nM)	Inhibition current, reversed by enhancement of P/Q VGCC	Primary hippocampal rat neurons	(Nimmrich, Grimm et al. 2008)
	P/Q-type	$A\beta_{1-42}$ globulomer (20-200 nM)	-Reduced channel opening threshold (leftward shift in current-voltage curve) -Increased current	*Xenopus laevis* oocytes	(Mezler, Barghorn et al. 2012)

	Subtype (CCB)	Aβ species	Effect	Model	Reference
Modulation	P/Q-type	$A\beta_{1-42}$ globulomer (830 nM)	-Half-activation voltage (V_{half}): Shift to more hyperpolarized values -Decreased amplitude (reversed by CCB)	Transfected HEK293	(Hermann, Mezler et al. 2013)
	N-type (ω-CgTx-GVIA)	Aggregated $A\beta_{25-35}$ (10 µM)	N-type block: cnc in Aβ-induced Ca^{2+} influx	Primary cortical rat neurons	(Yagami, Ueda et al. 2004)
	N-type (ω-CgTx-GVIA)	$A\beta_{1-40}$ (1 µM)	-Increased current (blocked by CCB) -Increased channel deactivation rate (blocked by CCB) -Shift in current activation curve (pos) (not blocked by CCB)	Rat cerebellar granule neurons	(Price, Held et al. 1998)
	N-type (ω-CgTx-GVIA)	Monomeric $A\beta_{1-40}$ (1 µM)	Increased current	Primary cortical rat neurons	(Ramsden, Henderson et al. 2002)
	N-type (ω-CgTx-GVIA)	Aggregated $A\beta_{1-40}$ (1 µM)	Decreased current	Primary cortical rat neurons	(Ramsden, Henderson et al. 2002)
	N-type (ω-CgTx-GVIA)	$A\beta_{1-40}$ (1 µM)	-Increased Ca^{2+} influx (blocked by CCB) -Increased amplitude (blocked by CCB)	Rat cortical synaptosomes, Cortical neurons	(MacManus, Ramsden et al. 2000)
	N-type	$A\beta_{1-42}$ globulomer (830 nM)	-Half-activation voltage: Shift to more hyperpolarized values -Decreased amplitude (reversed by CCB)	Transfected HEK293	(Hermann, Mezler et al. 2013)
	N-type (ω-CgTx-GVIA)	Protofibrillar $A\beta_{1-42}$ (1 µM)	Inhibitory decrease in current density and max conductance	Transfected HEK293	(Kaisis, Thei et al. 2022)
	HVA VGCC	-Oligomeric (4-6 mer) $A\beta_{1–40}$ (200 nM) -Oligomeric (6-8 mer) $A\beta_{25-35}$ (200 nM)	Increased amplitude	CA1 hippocampal neurons (slice culture)	(Rovira, Arbez et al. 2002)
	LVA/HVA-VGCC ($CdCl_2$)	Fibrillar $A\beta_{25-35}$ (2 µM)	-Increased Ca^{2+} influx -Increased $[Ca^{2+}]_i$	Rat dorsal root ganglion neurons	(He, Chen et al. 2002)

	Subtype (CCB)	Aβ species	Effect	Model	Reference
Survival	L-type (verapamil, diltiazem, isradipine and nimodipine)	Aβ oligomers (Endogenously expressed Aβ)	L-type block: Increased survival after Aβ-oligomer-induced cytotoxicity by decreasing $[Ca^{2+}]_i$ (partially with diltiazem, isradipine, and nimodipine)	Human neuroblastoma/ MC65	(Anekonda, Quinn et al. 2011)
	L-type (verapamil, nifedipine and diltiazem)	$A\beta_{25-35}$ (40 µM)	L-type block: Rescued Aβ-induced decrease in proliferation	Human microglial cells	(Silei, Fabrizi et al. 1999)
	L-type (nimodipine)	Aggregated $A\beta_{25-35}$ (10 µM)	L-type block: prevented Aβ-induced apoptosis	Primary cortical rat neurons	(Ueda, Shinohara et al. 1997)
	L-type (S-312-d)	Aggregated $A\beta_{25-35}$ (10 µM)	L-type block: prevented Aβ-induced apoptosis	Primary cortical rat neurons	(Yagami, Ueda et al. 2004)
	L-type (nimodipine)	-$A\beta_{25-35}$ (10 µM) -$A\beta_{1-42}$ (25 µM)	L-type block: prevented Aβ-induced apoptosis	Primary murine cortical cells	(Weiss, Pike et al. 1994)
	L-type (nimodipine)	-Fibrillar $A\beta_{25-35}$ (20 µM) -sOligomeric $A\beta_{1-42}$ (1 µM)	L-type block: prevented Aβ-induced apoptosis	Primary cortical rat neurons	(Fu, Li et al. 2006)
	L-type (verapamil, diltiazem, nifedipine)	$A\beta_{1-40}$ (20 µM)	N-type block: cnc in Aβ-induced apoptosis	Primary cortical rat neurons	(Whitson and Appel 1995)
	P/Q-type (ω-Aga-IVA, ω-CgTx-MVIIC)	Aggregated $A\beta_{25-35}$ (10 µM)	P/Q-type block: cnc in Aβ-induced apoptosis	Primary cortical rat neurons	(Yagami, Ueda et al. 2004)
	P/Q-type (ω-Aga-IVA)	Aggregated $A\beta_{25-35}$ (10 µM)	P/Q-type block: cnc in Aβ-induced apoptosis	Primary cortical rat neurons	(Ueda, Shinohara et al. 1997)
	P/Q-type (ω-Aga-IVA)	-Fibrillar $A\beta_{25-35}$ (20 µM) -sOligomeric $A\beta_{1-42}$ (1 µM)	P/Q-type block: cnc in Aβ-induced apoptosis	Primary cortical rat neurons	(Fu, Li et al. 2006)
	N-type (ω-CgTx-GVIA)	-Aggregated $A\beta_{25-35}$ (10 µM)	N-type block: cnc in Aβ-induced apoptosis	Primary cortical rat neurons	(Yagami, Ueda et al. 2004)
	N-type (ω-CgTx-GVIA)	Aggregated $A\beta_{25-35}$ (10 µM)	N-type block: cnc in Aβ-induced apoptosis	Primary cortical rat neurons	(Ueda, Shinohara et al. 1997)

	Subtype (CCB)	Aβ species	Effect	Model	Reference
Survival	N-type (ω-CgTx-GVIA)	-Fibrillar $A\beta_{25-35}$ (20 µM) -sOligomeric $A\beta_{1-42}$ (1 µM)	N-type block: cnc in Aβ-induced apoptosis	Primary cortical rat neurons	(Fu, Li et al. 2006)
	N-type (ω-CgTx-GVIA)	$A\beta_{1-40}$ (20 µM)	N-type block: cnc in Aβ-induced apoptosis	Primary cortical rat neurons	(Whitson and Appel 1995)
	R-type (SNX-482)	-Fibrillar $A\beta_{25-35}$ (20 µM) -sOligomeric $A\beta_{1-42}$ (1 µM)	R-type block: cnc in Aβ-induced apoptosis	Primary cortical rat neurons	(Fu, Li et al. 2006)

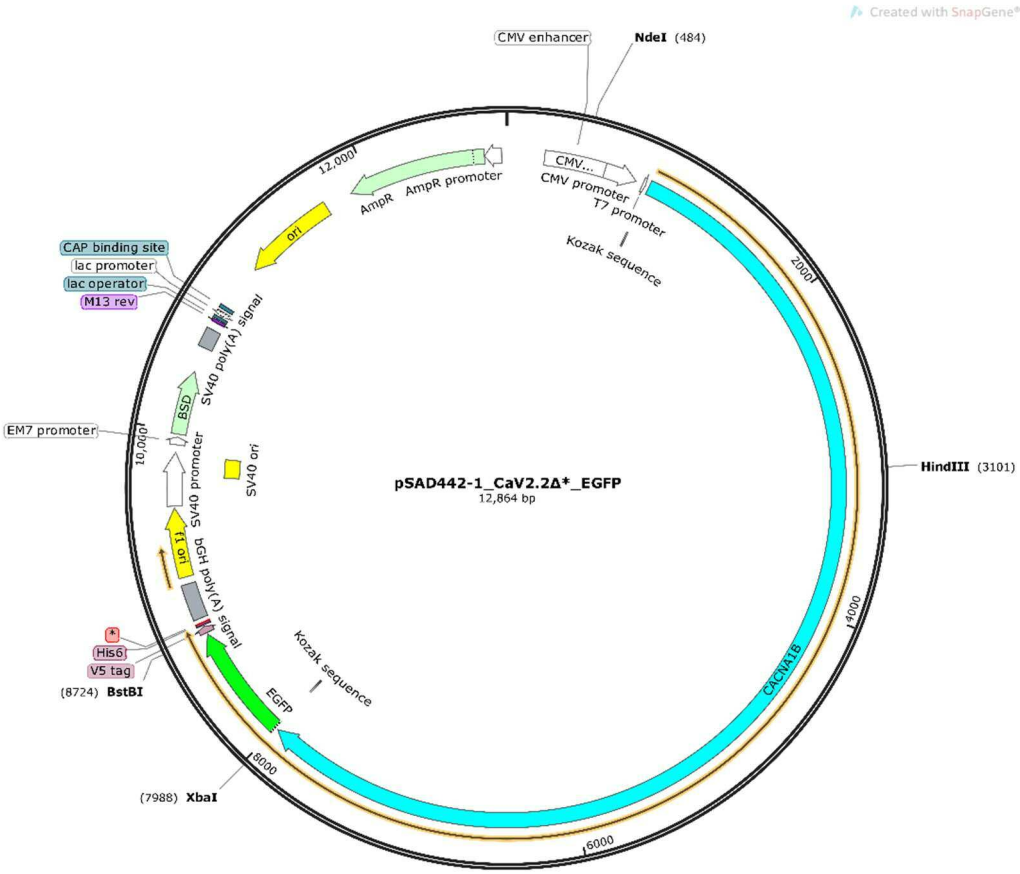

Figure I.1: Plasmid map of pSAD442-1_Cav2.2Δ*_EGFP

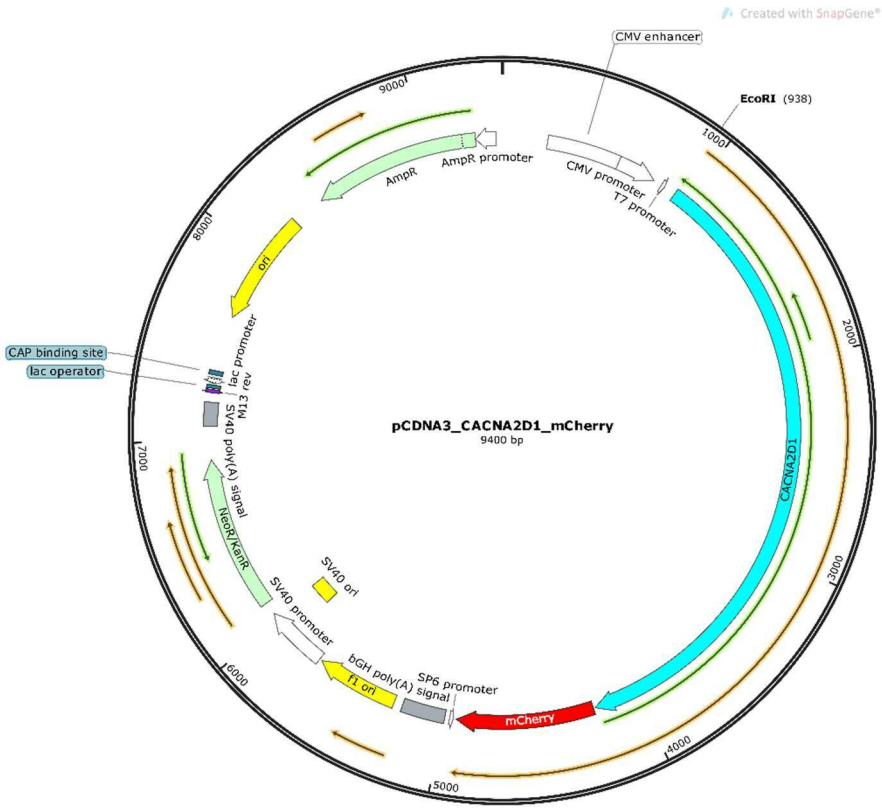

Figure I.2: Plasmid map of pCDNA3_*CACNA2D1*_mCherry

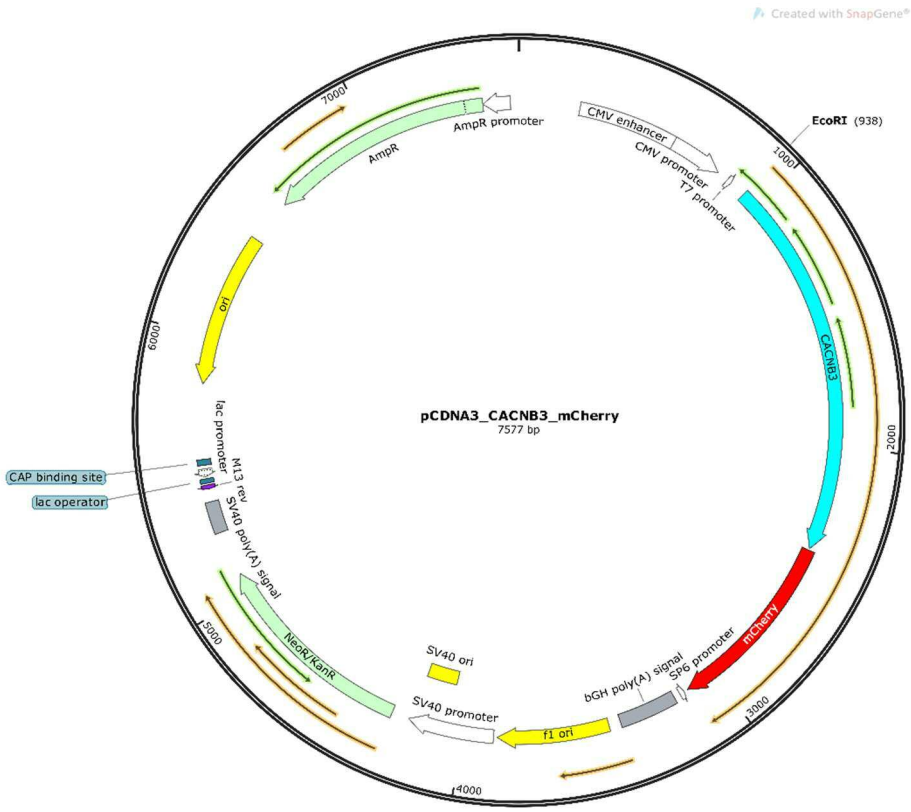

Figure I.3: Plasmid map of pCDNA3_*CACNB3*_mCherry

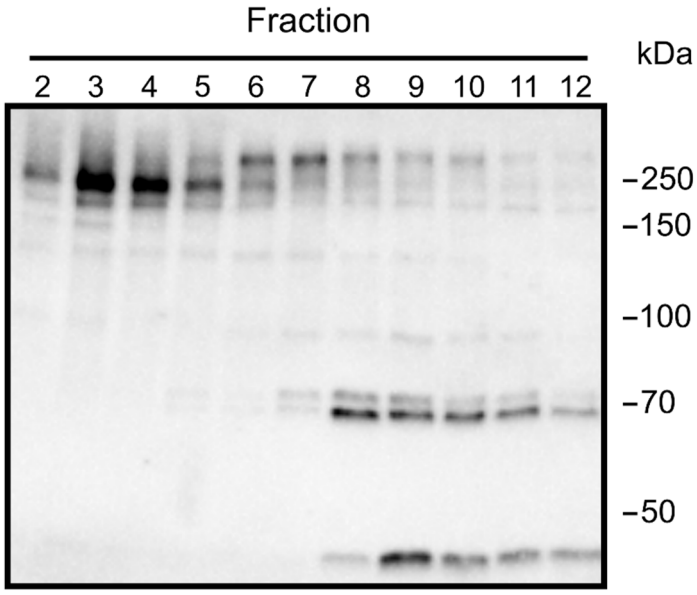

Figure I.4: Western blot visualizing $Ca_V2.2$ purification via size exclusion chromatography by HPLC

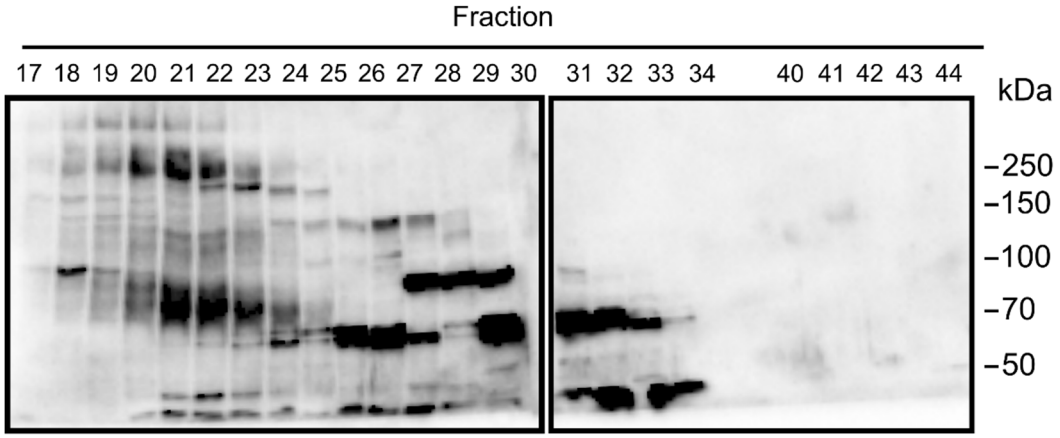

Figure I.5: Western blot visualizing $Ca_V2.2$ purified via size exclusion chromatography by FPLC

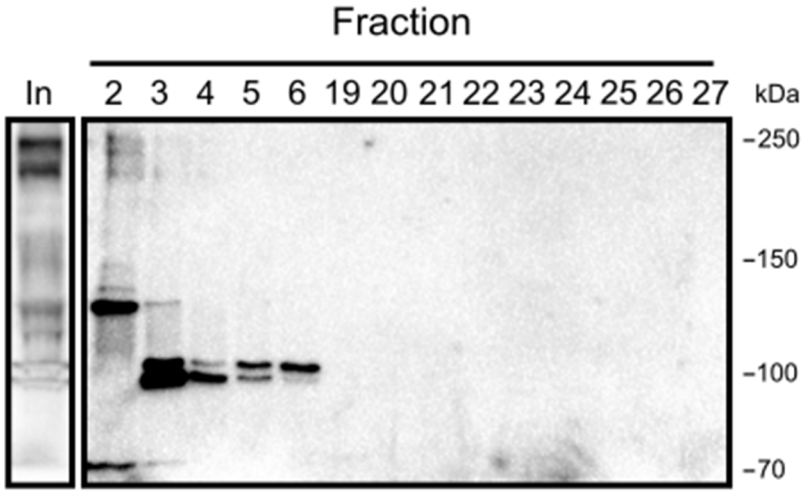

Figure I.6: Western blot visualizing $Ca_V2.2$ purified via cation anion exchange chromatography by HPLC

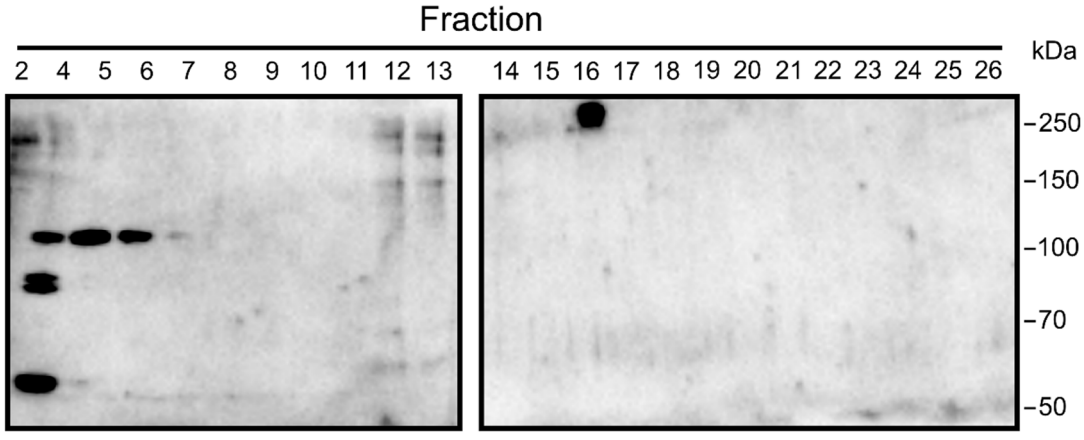

Figure I.7: Western blot visualizing $Ca_V2.2$ purified via hydrophobic interaction chromatography by FPLC

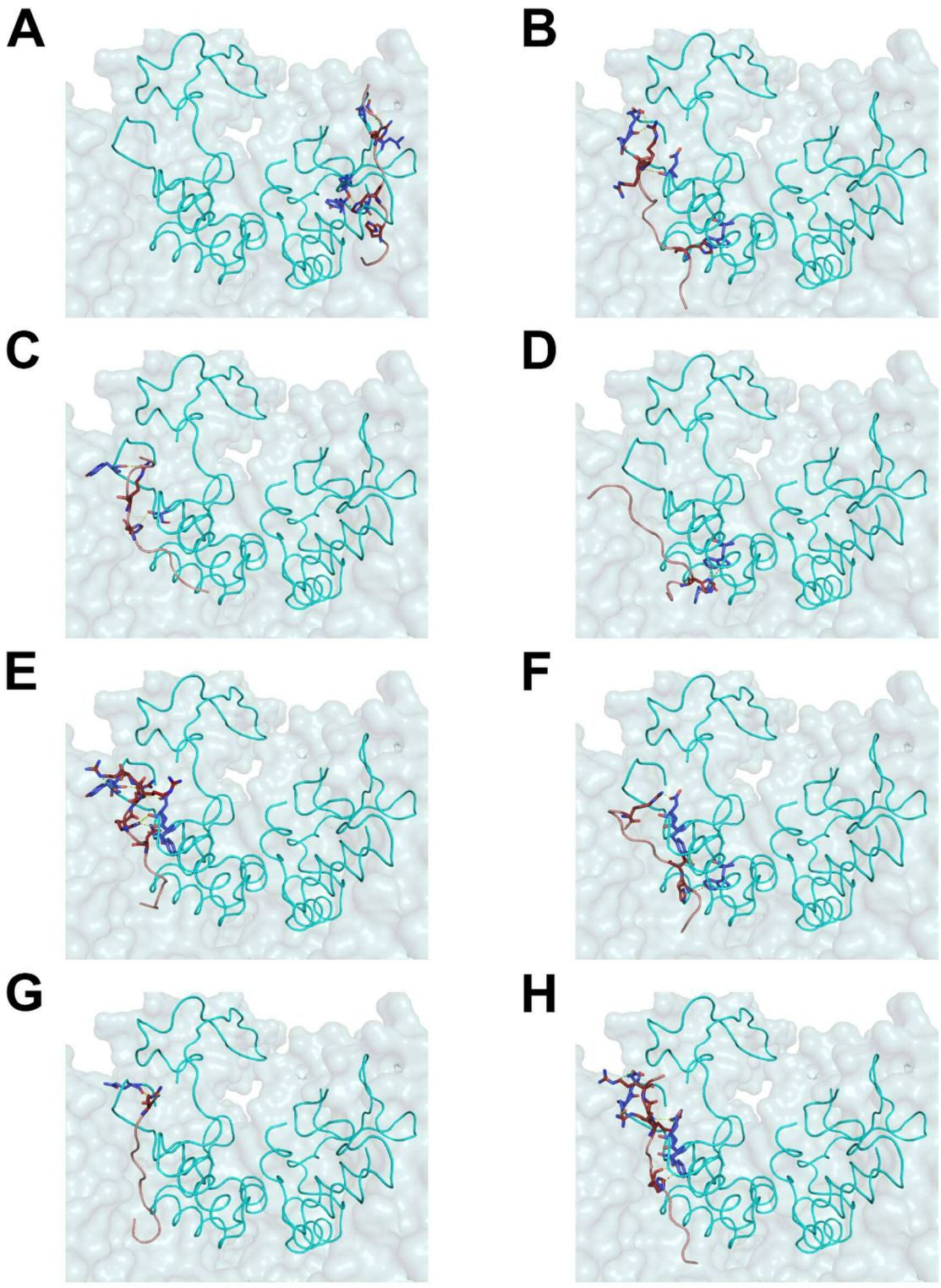

Figure I.8: Peptide docking modeling showing allosteric binding mode of RD2 on $Ca_V2.2$ ω-CgTx binding groove

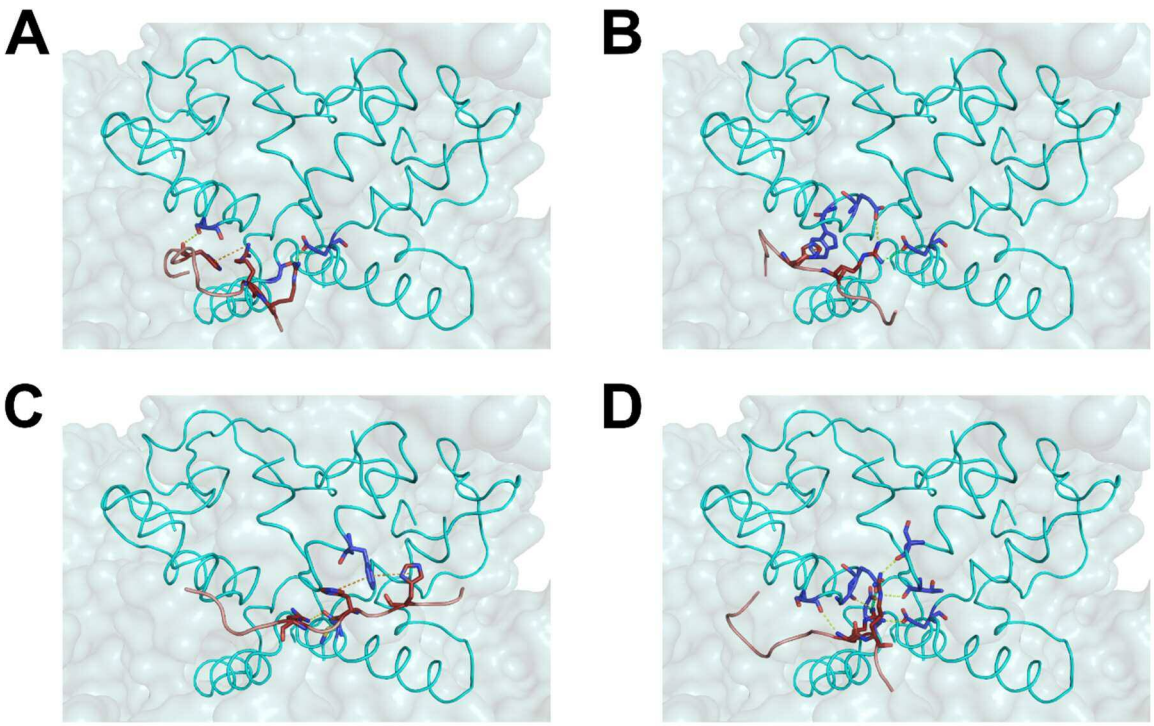

Figure I.9: Peptide docking modeling showing binding modes of RD2 on $Ca_V2.2$ ω-CgTx binding groove under the Ca^{2+} pore

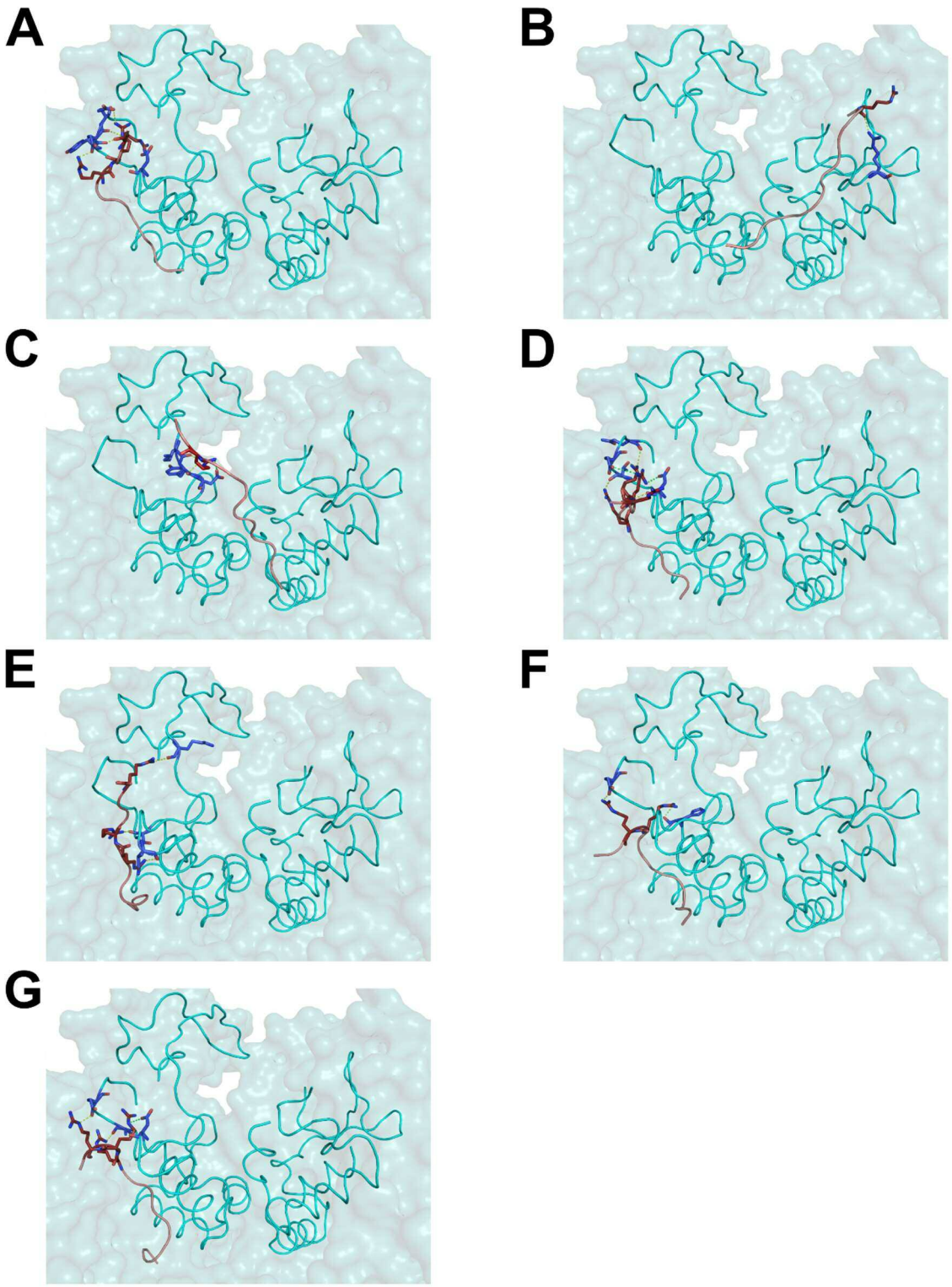

Figure I.10: Peptide docking modeling showing allosteric binding mode of RD2C on $Ca_V2.2$ ω-CgTx binding groove

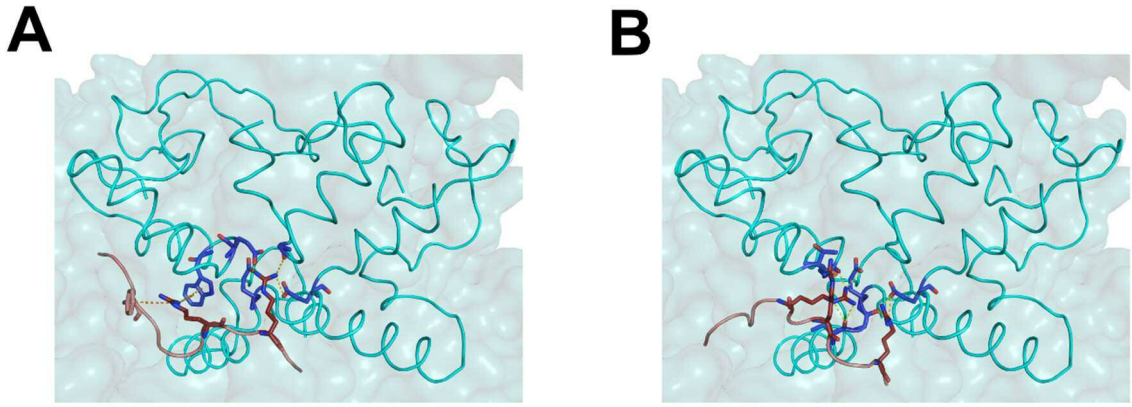

Figure I.11: Peptide docking modeling showing binding modes of RD2 on $Ca_V2.2$ ω-CgTx binding groove under the Ca^{2+} pore

II. Literature

Abbadie, C., O. B. McManus, S. Y. Sun, R. M. Bugianesi, G. Dai, R. J. Haedo, J. B. Herrington, G. J. Kaczorowski, M. M. Smith, A. M. Swensen, V. A. Warren, B. Williams, S. P. Arneric, C. Eduljee, T. P. Snutch, E. W. Tringham, N. Jochnowitz, A. Liang, D. Euan MacIntyre, E. McGowan, S. Mistry, V. V. White, S. B. Hoyt, C. London, K. A. Lyons, P. B. Bunting, S. Volksdorf and J. L. Duffy (2010). "Analgesic effects of a substituted N-triazole oxindole (TROX-1), a state-dependent, voltage-gated calcium channel 2 blocker." J Pharmacol Exp Ther **334**(2): 545-555.

Afrashteh, N., S. Inayat, E. Bermudez-Contreras, A. Luczak, B. L. McNaughton and M. H. Mohajerani (2021). "Spatiotemporal structure of sensory-evoked and spontaneous activity revealed by mesoscale imaging in anesthetized and awake mice." Cell Rep **37**(10): 110081.

Aguado, C., S. Garcia-Madrona, M. Gil-Minguez and R. Lujan (2016). "Ontogenic Changes and Differential Localization of T-type Ca^{2+} Channel Subunits Cav3.1 and Cav3.2 in Mouse Hippocampus and Cerebellum." Front Neuroanat **10**: 83.

Albillos, A., E. Neher and T. Moser (2000). "R-Type Ca^{2+} channels are coupled to the rapid component of secretion in mouse adrenal slice chromaffin cells." J Neurosci **20**(22): 8323-8330.

Allen, S. E., C. P. Toro, A. Andrade, E. J. Lopez-Soto, S. Denome and D. Lipscombe (2017). "Cell-Specific RNA Binding Protein Rbfox2 Regulates $Ca_V2.2$ mRNA Exon Composition and $Ca_V2.2$ Current Size." eNeuro **4**(5).

Altier, C., C. S. Dale, A. E. Kisilevsky, K. Chapman, A. J. Castiglioni, E. A. Matthews, R. M. Evans, A. H. Dickenson, D. Lipscombe, N. Vergnolle and G. W. Zamponi (2007). "Differential role of N-type calcium channel splice isoforms in pain." J Neurosci **27**(24): 6363-6373.

Altier, C., A. Garcia-Caballero, B. Simms, H. You, L. Chen, J. Walcher, H. W. Tedford, T. Hermosilla and G. W. Zamponi (2011). "The Cavβ subunit prevents RFP2-mediated ubiquitination and proteasomal degradation of L-type channels." Nat Neurosci **14**(2): 173-180.

Andrell, J. and C. G. Tate (2013). "Overexpression of membrane proteins in mammalian cells for structural studies." Mol Membr Biol **30**(1): 52-63.

Andronache, Z., D. Ursu, S. Lehnert, M. Freichel, V. Flockerzi and W. Melzer (2007). "The auxiliary subunit γ_1 of the skeletal muscle L-type Ca^{2+} channel is an endogenous Ca^{2+} antagonist." Proc Natl Acad Sci U S A **104**(45): 17885-17890.

Anekonda, T. S., J. F. Quinn, C. Harris, K. Frahler, T. L. Wadsworth and R. L. Woltjer (2011). "L-type voltage-gated calcium channel blockade with isradipine as a therapeutic strategy for Alzheimer's disease." Neurobiol Dis **41**(1): 62-70.

Antunes, F. T. T., A. H. de Souza, E. S. Caminski, S. Greggio, G. T. Venturin, J. C. da Costa, M. Taffarel, I. N. Rebelo, M. V. Gomez, D. S. Correa, F. N. Vilanova, A. P. Regner

and E. Dallegrave (2021). "Neuroprotective effects of the CTK 01512-2 toxin against neurotoxicity induced by 3-nitropropionic acid in rats." Neurotoxicology **87**: 30-42.

Ariel, P., M. B. Hoppa and T. A. Ryan (2012). "Intrinsic variability in Pv, RRP size, Ca^{2+} channel repertoire, and presynaptic potentiation in individual synaptic boutons." Front Synaptic Neurosci **4**: 9.

Arispe, N., E. Rojas and H. B. Pollard (1993). "Alzheimer disease amyloid beta protein forms calcium channels in bilayer membranes: blockade by tromethamine and aluminum." Proc Natl Acad Sci U S A **90**(2): 567-571.

Armstrong, C. T., P. E. Mason, J. L. Anderson and C. E. Dempsey (2016). "Arginine side chain interactions and the role of arginine as a gating charge carrier in voltage sensitive ion channels." Sci Rep **6**: 21759.

Arnot, M. I., S. C. Stotz, S. E. Jarvis and G. W. Zamponi (2000). "Differential modulation of N-type α_{1B} and P/Q-type α_{1A} calcium channels by different G protein subunit isoforms." J Physiol **527 Pt 2**(Pt 2): 203-212.

Artalejo, C. R., M. E. Adams and A. P. Fox (1994). "Three types of Ca^{2+} channel trigger secretion with different efficacies in chromaffin cells." Nature **367**(6458): 72-76.

Arundine, M. and M. Tymianski (2003). "Molecular mechanisms of calcium-dependent neurodegeneration in excitotoxicity." Cell Calcium **34**(4-5): 325-337.

Asakura, K., Y. Matsuo, T. Kanemasa and M. Ninomiya (1997). "P/Q-type Ca^{2+} channel blocker omega-agatoxin IVA protects against brain injury after focal ischemia in rats." Brain Res **776**(1-2): 140-145.

Bading, H. (2013). "Nuclear calcium signalling in the regulation of brain function." Nat Rev Neurosci **14**(9): 593-608.

Bano, D. and M. Ankarcrona (2018). "Beyond the critical point: An overview of excitotoxicity, calcium overload and the downstream consequences." Neurosci Lett **663**: 79-85.

Bano, D. and P. Nicotera (2007). "Ca^{2+} signals and neuronal death in brain ischemia." Stroke **38**(2 Suppl): 674-676.

Barghorn, S., V. Nimmrich, A. Striebinger, C. Krantz, P. Keller, B. Janson, M. Bahr, M. Schmidt, R. S. Bitner, J. Harlan, E. Barlow, U. Ebert and H. Hillen (2005). "Globular amyloid β-peptide$_{1-42}$ oligomer - a homogenous and stable neuropathological protein in Alzheimer's disease." J Neurochem **95**(3): 834-847.

Barthas, F. and A. C. Kwan (2017). "Secondary Motor Cortex: Where 'Sensory' Meets 'Motor' in the Rodent Frontal Cortex." Trends Neurosci **40**(3): 181-193.

Baskys, A. and J. X. Cheng (2012). "Pharmacological prevention and treatment of vascular dementia: approaches and perspectives." Exp Gerontol **47**(11): 887-891.

Bauer, C. S., M. Nieto-Rostro, W. Rahman, A. Tran-Van-Minh, L. Ferron, L. Douglas, I. Kadurin, Y. Sri Ranjan, L. Fernandez-Alacid, N. S. Millar, A. H. Dickenson, R. Lujan and A. C. Dolphin (2009). "The increased trafficking of the calcium channel subunit $\alpha_2\delta$-1 to

presynaptic terminals in neuropathic pain is inhibited by the $\alpha_2\delta$ ligand pregabalin." J Neurosci **29**(13): 4076-4088.

Baynes, B. M., D. I. Wang and B. L. Trout (2005). "Role of arginine in the stabilization of proteins against aggregation." Biochemistry **44**(12): 4919-4925.

Bean, B. P. (1989). "Neurotransmitter inhibition of neuronal calcium currents by changes in channel voltage dependence." Nature **340**(6229): 153-156.

Belgard, T. G., A. C. Marques, P. L. Oliver, H. O. Abaan, T. M. Sirey, A. Hoerder-Suabedissen, F. Garcia-Moreno, Z. Molnar, E. H. Margulies and C. P. Ponting (2011). "A transcriptomic atlas of mouse neocortical layers." Neuron **71**(4): 605-616.

Bell, T. J., C. Thaler, A. J. Castiglioni, T. D. Helton and D. Lipscombe (2004). "Cell-specific alternative splicing increases calcium channel current density in the pain pathway." Neuron **41**(1): 127-138.

Bergquist, F., J. Jonason, E. Pileblad and H. Nissbrandt (1998). "Effects of local administration of L-, N-, and P/Q-type calcium channel blockers on spontaneous dopamine release in the striatum and the substantia nigra: a microdialysis study in rat." J Neurochem **70**(4): 1532-1540.

Berkefeld, H., C. A. Sailer, W. Bildl, V. Rohde, J. O. Thumfart, S. Eble, N. Klugbauer, E. Reisinger, J. Bischofberger, D. Oliver, H. G. Knaus, U. Schulte and B. Fakler (2006). "BK_{Ca}-Cav channel complexes mediate rapid and localized Ca^{2+}-activated K^+ signaling." Science **314**(5799): 615-620.

Berman, R. F., B. H. Verweij and J. P. Muizelaar (2000). "Neurobehavioral protection by the neuronal calcium channel blocker ziconotide in a model of traumatic diffuse brain injury in rats." J Neurosurg **93**(5): 821-828.

Bermudez-Contreras, E., A. G. Schjetnan, A. Luczak and M. H. Mohajerani (2023). "Sensory experience selectively reorganizes the late component of evoked responses." Cereb Cortex **33**(6): 2626-2640.

Berntson, A., W. R. Taylor and C. W. Morgans (2003). "Molecular identity, synaptic localization, and physiology of calcium channels in retinal bipolar cells." J Neurosci Res **71**(1): 146-151.

Berridge, M. J. (2010). "Calcium hypothesis of Alzheimer's disease." Pflugers Arch **459**(3): 441-449.

Berridge, M. J., M. D. Bootman and P. Lipp (1998). "Calcium--a life and death signal." Nature **395**(6703): 645-648.

Berridge, M. J., M. D. Bootman and H. L. Roderick (2003). "Calcium signalling: dynamics, homeostasis and remodelling." Nat Rev Mol Cell Biol **4**(7): 517-529.

Berridge, M. J., P. Lipp and M. D. Bootman (2000). "The versatility and universality of calcium signalling." Nat Rev Mol Cell Biol **1**(1): 11-21.

Bers, D. M. (2002). "Cardiac excitation-contraction coupling." Nature **415**(6868): 198-205.

Beyreuther, K. and C. L. Masters (1991). "Amyloid precursor protein (APP) and beta A4 amyloid in the etiology of Alzheimer's disease: precursor-product relationships in the derangement of neuronal function." Brain Pathol **1**(4): 241-251.

Bezprozvanny, I. and M. P. Mattson (2008). "Neuronal calcium mishandling and the pathogenesis of Alzheimer's disease." Trends Neurosci **31**(9): 454-463.

Bezprozvanny, I., P. Zhong, R. H. Scheller and R. W. Tsien (2000). "Molecular determinants of the functional interaction between syntaxin and N-type Ca^{2+} channel gating." Proc Natl Acad Sci U S A **97**(25): 13943-13948.

Bichet, D., V. Cornet, S. Geib, E. Carlier, S. Volsen, T. Hoshi, Y. Mori and M. De Waard (2000). "The I-II loop of the Ca^{2+} channel α_1 subunit contains an endoplasmic reticulum retention signal antagonized by the β subunit." Neuron **25**(1): 177-190.

Bill, R. M., P. J. Henderson, S. Iwata, E. R. Kunji, H. Michel, R. Neutze, S. Newstead, B. Poolman, C. G. Tate and H. Vogel (2011). "Overcoming barriers to membrane protein structure determination." Nat Biotechnol **29**(4): 335-340.

Birnbaumer, L., K. P. Campbell, W. A. Catterall, M. M. Harpold, F. Hofmann, W. A. Horne, Y. Mori, A. Schwartz, T. P. Snutch, T. Tanabe and et al. (1994). "The naming of voltage-gated calcium channels." Neuron **13**(3): 505-506.

Bishop, G. M. and S. R. Robinson (2004). "Physiological roles of amyloid-β and implications for its removal in Alzheimer's disease." Drugs Aging **21**(10): 621-630.

Bleakman, D., D. Bowman, C. P. Bath, P. F. Brust, E. C. Johnson, C. R. Deal, R. J. Miller, S. B. Ellis, M. M. Harpold, M. Hans and et al. (1995). "Characteristics of a human N-type calcium channel expressed in HEK293 cells." Neuropharmacology **34**(7): 753-765.

Bobich, J. A., Q. Zheng and A. Campbell (2004). "Incubation of nerve endings with a physiological concentration of $A\beta_{1-42}$ activates CaV2.2(N-Type)-voltage operated calcium channels and acutely increases glutamate and noradrenaline release." J Alzheimers Dis **6**(3): 243-255.

Bock, G., M. Gebhart, A. Scharinger, W. Jangsangthong, P. Busquet, C. Poggiani, S. Sartori, M. E. Mangoni, M. J. Sinnegger-Brauns, S. Herzig, J. Striessnig and A. Koschak (2011). "Functional properties of a newly identified C-terminal splice variant of $Ca_V1.3$ L-type Ca^{2+} channels." J Biol Chem **286**(49): 42736-42748.

Bornschein, G., J. Eilers and H. Schmidt (2019). "Neocortical High Probability Release Sites Are Formed by Distinct Ca^{2+} Channel-to-Release Sensor Topographies during Development." Cell Rep **28**(6): 1410-1418 e1414.

Bourinet, E., A. Francois and S. Laffray (2016). "T-type calcium channels in neuropathic pain." Pain **157 Suppl 1**: S15-S22.

Bourinet, E., T. W. Soong, K. Sutton, S. Slaymaker, E. Mathews, A. Monteil, G. W. Zamponi, J. Nargeot and T. P. Snutch (1999). "Splicing of α_{1A} subunit gene generates phenotypic variants of P- and Q-type calcium channels." Nat Neurosci **2**(5): 407-415.

Bourinet, E. and G. W. Zamponi (2005). "Voltage gated calcium channels as targets for analgesics." Curr Top Med Chem **5**(6): 539-546.

Bozorgi, H., T. Budde and M. Nankali (2020). "Antidepressant-like and memory-enhancing effects of the N-type calcium channel blocker ziconotide in rats." Behav Brain Res **390**: 112647.

Brehm, P. and R. Eckert (1978). "Calcium entry leads to inactivation of calcium channel in Paramecium." Science **202**(4373): 1203-1206.

Brewer, L. D., O. Thibault, J. Staton, V. Thibault, J. T. Rogers, G. Garcia-Ramos, S. Kraner, P. W. Landfield and N. M. Porter (2007). "Increased vulnerability of hippocampal neurons with age in culture: temporal association with increases in NMDA receptor current, NR2A subunit expression and recruitment of L-type calcium channels." Brain Res **1151**: 20-31.

Brini, M., T. Cali, D. Ottolini and E. Carafoli (2014). "Neuronal calcium signaling: function and dysfunction." Cell Mol Life Sci **71**(15): 2787-2814.

Buchan, A. M., S. Z. Gertler, H. Li, D. Xue, Z. G. Huang, K. E. Chaundy, K. Barnes and H. J. Lesiuk (1994). "A selective N-type Ca^{2+}-channel blocker prevents CA1 injury 24 h following severe forebrain ischemia and reduces infarction following focal ischemia." J Cereb Blood Flow Metab **14**(6): 903-910.

Bucurenciu, I., A. Kulik, B. Schwaller, M. Frotscher and P. Jonas (2008). "Nanodomain coupling between Ca^{2+} channels and Ca^{2+} sensors promotes fast and efficient transmitter release at a cortical GABAergic synapse." Neuron **57**(4): 536-545.

Budde, T., S. Meuth and H. C. Pape (2002). "Calcium-dependent inactivation of neuronal calcium channels." Nat Rev Neurosci **3**(11): 873-883.

Buraei, Z. and J. Yang (2010). "The β subunit of voltage-gated Ca^{2+} channels." Physiol Rev **90**(4): 1461-1506.

Buraei, Z. and J. Yang (2013). "Structure and function of the β subunit of voltage-gated Ca^{2+} channels." Biochim Biophys Acta **1828**(7): 1530-1540.

Busquet, P., A. Hetzenauer, M. J. Sinnegger-Brauns, J. Striessnig and N. Singewald (2008). "Role of L-type Ca^{2+} channel isoforms in the extinction of conditioned fear." Learn Mem **15**(5): 378-386.

Camandola, S. and M. P. Mattson (2011). "Aberrant subcellular neuronal calcium regulation in aging and Alzheimer's disease." Biochim Biophys Acta **1813**(5): 965-973.

Canti, C., M. Nieto-Rostro, I. Foucault, F. Heblich, J. Wratten, M. W. Richards, J. Hendrich, L. Douglas, K. M. Page, A. Davies and A. C. Dolphin (2005). "The metal-ion-dependent adhesion site in the Von Willebrand factor-A domain of $\alpha_2\delta$ subunits is key to trafficking voltage-gated Ca^{2+} channels." Proc Natl Acad Sci U S A **102**(32): 11230-11235.

Canti, C., K. M. Page, G. J. Stephens and A. C. Dolphin (1999). "Identification of residues in the N terminus of α1B critical for inhibition of the voltage-dependent calcium channel by Gβγ." J Neurosci **19**(16): 6855-6864.

Cao, S., D. W. Fisher, T. Yu and H. Dong (2019). "The link between chronic pain and Alzheimer's disease." J Neuroinflammation **16**(1): 204.

Carabelli, V., A. Marcantoni, V. Comunanza, A. de Luca, J. Diaz, R. Borges and E. Carbone (2007). "Chronic hypoxia up-regulates α_{1H} T-type channels and low-threshold catecholamine secretion in rat chromaffin cells." J Physiol **584**(Pt 1): 149-165.

Carbone, E. and H. D. Lux (1984). "A low voltage-activated, fully inactivating Ca channel in vertebrate sensory neurones." Nature **310**(5977): 501-502.

Casagrande, C. C., A. I. Wiesman, M. Schantell, H. J. Johnson, S. L. Wolfson, J. O'Neill, C. M. Johnson, P. E. May, S. Swindells, D. L. Murman and T. W. Wilson (2022). "Signatures of somatosensory cortical dysfunction in Alzheimer's disease and HIV-associated neurocognitive disorder." Brain Commun **4**(4): fcac169.

Cassidy, J. S., L. Ferron, I. Kadurin, W. S. Pratt and A. C. Dolphin (2014). "Functional exofacially tagged N-type calcium channels elucidate the interaction with auxiliary $\alpha_2\delta$-1 subunits." Proc Natl Acad Sci U S A **111**(24): 8979-8984.

Cassinelli, S., C. Vinola-Renart, A. Benavente-Garcia, M. Navarro-Perez, J. Capera and A. Felipe (2022). "Palmitoylation of Voltage-Gated Ion Channels." Int J Mol Sci **23**(16).

Castiglioni, A. J., J. Raingo and D. Lipscombe (2006). "Alternative splicing in the C-terminus of $Ca_V2.2$ controls expression and gating of N-type calcium channels." J Physiol **576**(Pt 1): 119-134.

Cataldi, M. (2013). "The changing landscape of voltage-gated calcium channels in neurovascular disorders and in neurodegenerative diseases." Curr Neuropharmacol **11**(3): 276-297.

Catterall, W. A. (1999). "Interactions of presynaptic Ca^{2+} channels and snare proteins in neurotransmitter release." Ann N Y Acad Sci **868**: 144-159.

Catterall, W. A. (2000). "Structure and regulation of voltage-gated Ca2+ channels." Annu Rev Cell Dev Biol **16**: 521-555.

Catterall, W. A. (2010). "Ion channel voltage sensors: structure, function, and pathophysiology." Neuron **67**(6): 915-928.

Catterall, W. A., E. Perez-Reyes, T. P. Snutch and J. Striessnig (2005). "International Union of Pharmacology. XLVIII. Nomenclature and structure-function relationships of voltage-gated calcium channels." Pharmacol Rev **57**(4): 411-425.

Cawley, J. (2023). "Hydroxyapatite Chromatography (HAC)." Methods Mol Biol **2699**: 179-192.

Chad, J. E. and R. Eckert (1986). "An enzymatic mechanism for calcium current inactivation in dialysed Helix neurones." J Physiol **378**: 31-51.

Chakroborty, S., C. Briggs, M. B. Miller, I. Goussakov, C. Schneider, J. Kim, J. Wicks, J. C. Richardson, V. Conklin, B. G. Cameransi and G. E. Stutzmann (2012). "Stabilizing ER Ca^{2+} channel function as an early preventative strategy for Alzheimer's disease." PLoS One **7**(12): e52056.

Chan, C. S., T. S. Gertler and D. J. Surmeier (2009). "Calcium homeostasis, selective vulnerability and Parkinson's disease." Trends Neurosci **32**(5): 249-256.

Chan, S. L., M. Mayne, C. P. Holden, J. D. Geiger and M. P. Mattson (2000). "Presenilin-1 mutations increase levels of ryanodine receptors and calcium release in PC12 cells and cortical neurons." J Biol Chem **275**(24): 18195-18200.

Chang, Q. and L. J. Martin (2016). "Voltage-gated calcium channels are abnormal in cultured spinal motoneurons in the G93A-SOD1 transgenic mouse model of ALS." Neurobiol Dis **93**: 78-95.

Chang, S. Y., T. F. Yong, C. Y. Yu, M. C. Liang, O. Pletnikova, J. Troncoso, J. M. Burgunder and T. W. Soong (2007). "Age and gender-dependent alternative splicing of P/Q-type calcium channel EF-hand." Neuroscience **145**(3): 1026-1036.

Charlton, A. and M. Zachariou (2008). "Immobilized metal ion affinity chromatography of native proteins." Methods Mol Biol **421**: 25-35.

Chen, R. S., T. C. Deng, T. Garcia, Z. M. Sellers and P. M. Best (2007). "Calcium channel γ subunits: a functionally diverse protein family." Cell Biochem Biophys **47**(2): 178-186.

Chen, S., C. Yu, L. Rong, C. H. Li, X. Qin, H. Ryu and H. Park (2018). "Altered Synaptic Vesicle Release and Ca^{2+} Influx at Single Presynaptic Terminals of Cortical Neurons in a Knock-in Mouse Model of Huntington's Disease." Front Mol Neurosci **11**: 478.

Cheung, K. H., L. Mei, D. O. Mak, I. Hayashi, T. Iwatsubo, D. E. Kang and J. K. Foskett (2010). "Gain-of-function enhancement of IP3 receptor modal gating by familial Alzheimer's disease-linked presenilin mutants in human cells and mouse neurons." Sci Signal **3**(114): ra22.

Cheung, K. H., D. Shineman, M. Muller, C. Cardenas, L. Mei, J. Yang, T. Tomita, T. Iwatsubo, V. M. Lee and J. K. Foskett (2008). "Mechanism of Ca^{2+} disruption in Alzheimer's disease by presenilin regulation of InsP3 receptor channel gating." Neuron **58**(6): 871-883.

Cheung, W. Y. (1980). "Calmodulin plays a pivotal role in cellular regulation." Science **207**(4426): 19-27.

Chevalier, M., P. Lory, C. Mironneau, N. Macrez and J. F. Quignard (2006). "T-type $Ca_V3.3$ calcium channels produce spontaneous low-threshold action potentials and intracellular calcium oscillations." Eur J Neurosci **23**(9): 2321-2329.

Chi, C. H., C. Y. Tang and C. Y. Pan (2017). "Calmodulin modulates the Ca^{2+}-dependent inactivation and expression level of bovine $Ca_V2.2$ expressed in HEK293T cells." IBRO Rep **2**: 63-71.

Chien, A. J., K. M. Carr, R. E. Shirokov, E. Rios and M. M. Hosey (1996). "Identification of palmitoylation sites within the L-type calcium channel β_{2a} subunit and effects on channel function." J Biol Chem **271**(43): 26465-26468.

Chien, A. J., T. Gao, E. Perez-Reyes and M. M. Hosey (1998). "Membrane targeting of L-type calcium channels. Role of palmitoylation in the subcellular localization of the β_{2a} subunit." J Biol Chem **273**(36): 23590-23597.

Chiou, W. F. (2006). "Effect of Aβ exposure on the mRNA expression patterns of voltage-sensitive calcium channel α_1 subunits (α_{1A}-α_{1D}) in human SK-N-SH neuroblastoma." Neurochem Int **49**(3): 256-261.

Choi, D. W. (1988). "Calcium-mediated neurotoxicity: relationship to specific channel types and role in ischemic damage." Trends Neurosci **11**(10): 465-469.

Choi, D. W. (1988). "Glutamate neurotoxicity and diseases of the nervous system." Neuron **1**(8): 623-634.

Chopra, A., W. G. Willmore and K. K. Biggar (2019). "Protein quantification and visualization via ultraviolet-dependent labeling with 2,2,2-trichloroethanol." Sci Rep **9**(1): 13923.

Chu, P. J., J. K. Larsen, C. C. Chen and P. M. Best (2004). "Distribution and relative expression levels of calcium channel β subunits within the chambers of the rat heart." J Mol Cell Cardiol **36**(3): 423-434.

Cizkova, D., J. Marsala, N. Lukacova, M. Marsala, S. Jergova, J. Orendacova and T. L. Yaksh (2002). "Localization of N-type Ca^{2+} channels in the rat spinal cord following chronic constrictive nerve injury." Exp Brain Res **147**(4): 456-463.

Colbourne, F., H. Li, A. M. Buchan and J. A. Clemens (1999). "Continuing postischemic neuronal death in CA1: influence of ischemia duration and cytoprotective doses of NBQX and SNX-111 in rats." Stroke **30**(3): 662-668.

Cole, R. L., S. M. Lechner, M. E. Williams, P. Prodanovich, L. Bleicher, M. A. Varney and G. Gu (2005). "Differential distribution of voltage-gated calcium channel alpha-2 delta ($\alpha_2\delta$) subunit mRNA-containing cells in the rat central nervous system and the dorsal root ganglia." J Comp Neurol **491**(3): 246-269.

Coon, A. L., D. R. Wallace, C. F. Mactutus and R. M. Booze (1999). "L-type calcium channels in the hippocampus and cerebellum of Alzheimer's disease brain tissue." Neurobiol Aging **20**(6): 597-603.

Copenhaver, P. F., T. S. Anekonda, D. Musashe, K. M. Robinson, J. M. Ramaker, T. L. Swanson, T. L. Wadsworth, D. Kretzschmar, R. L. Woltjer and J. F. Quinn (2011). "A translational continuum of model systems for evaluating treatment strategies in Alzheimer's disease: isradipine as a candidate drug." Dis Model Mech **4**(5): 634-648.

Courderot-Masuyer, C., F. Dalloz, V. Maupoil and L. Rochette (1999). "Antioxidant properties of aminoguanidine." Fundam Clin Pharmacol **13**(5): 535-540.

Crochet, S. and C. C. Petersen (2015). "Cortical Sensorimotor Reverberations." Neuron **86**(5): 1116-1118.

Crook, R., A. Verkkoniemi, J. Perez-Tur, N. Mehta, M. Baker, H. Houlden, M. Farrer, M. Hutton, S. Lincoln, J. Hardy, K. Gwinn, M. Somer, A. Paetau, H. Kalimo, R. Ylikoski, M. Poyhonen, S. Kucera and M. Haltia (1998). "A variant of Alzheimer's disease with spastic paraparesis and unusual plaques due to deletion of exon 9 of presenilin 1." Nat Med **4**(4): 452-455.

Cummins, P. M., K. D. Rochfort and B. F. O'Connor (2017). "Ion-Exchange Chromatography: Basic Principles and Application." Methods Mol Biol **1485**: 209-223.

Curra, A., L. Marinelli, F. Cotellessa, L. Mori, C. Avanti, D. Greco, M. Gorini, P. Missori, F. Fattapposta and C. Trompetto (2021). "Habituation of Somatosensory Evoked Potentials

in Patients with Alzheimer's Disease and Those with Vascular Dementia." Medicina (Kaunas) **57**(12).

Dahimene, S., K. M. Page, M. Nieto-Rostro, W. S. Pratt and A. C. Dolphin (2024). "The Interplay Between Splicing of Two Exon Combinations Differentially Affects Membrane Targeting and Function of Human $Ca_V2.2$." Function (Oxf) **5**(1): zqad060.

Dalton, S., S. X. Takahashi, J. Miriyala and H. M. Colecraft (2005). "A single $Ca_V\beta$ can reconstitute both trafficking and macroscopic conductance of voltage-dependent calcium channels." J Physiol **567**(Pt 3): 757-769.

Dao, D. T., P. B. Mahon, X. Cai, C. E. Kovacsics, R. A. Blackwell, M. Arad, J. Shi, P. P. Zandi, P. O'Donnell, C. Bipolar Genome Study, J. A. Knowles, M. M. Weissman, W. Coryell, W. A. Scheftner, W. B. Lawson, D. F. Levinson, S. M. Thompson, J. B. Potash and T. D. Gould (2010). "Mood disorder susceptibility gene CACNA1C modifies mood-related behaviors in mice and interacts with sex to influence behavior in mice and diagnosis in humans." Biol Psychiatry **68**(9): 801-810.

Daschil, N., G. J. Obermair, B. E. Flucher, N. Stefanova, B. Hutter-Paier, M. Windisch, C. Humpel and J. Marksteiner (2013). "$Ca_V1.2$ calcium channel expression in reactive astrocytes is associated with the formation of amyloid-β plaques in an Alzheimer's disease mouse model." J Alzheimers Dis **37**(2): 439-451.

Davare, M. A. and J. W. Hell (2003). "Increased phosphorylation of the neuronal L-type Ca^{2+} channel $Ca_v1.2$ during aging." Proc Natl Acad Sci U S A **100**(26): 16018-16023.

Davidson, M. and R. G. Stern (1991). "The treatment of cognitive impairment in Alzheimer's disease: beyond the cholinergic approach." Psychiatr Clin North Am **14**(2): 461-482.

Davidson, R. M., L. Shajenko and T. S. Donta (1994). "Amyloid beta-peptide (AβP) potentiates a nimodipine-sensitive L-type barium conductance in N1E-115 neuroblastoma cells." Brain Res **643**(1-2): 324-327.

Davies, A., J. Hendrich, A. T. Van Minh, J. Wratten, L. Douglas and A. C. Dolphin (2007). "Functional biology of the $\alpha_2\delta$ subunits of voltage-gated calcium channels." Trends Pharmacol Sci **28**(5): 220-228.

De Waard, M., H. Liu, D. Walker, V. E. Scott, C. A. Gurnett and K. P. Campbell (1997). "Direct binding of G-protein βγ complex to voltage-dependent calcium channels." Nature **385**(6615): 446-450.

Decker, J. M., L. Kruger, A. Sydow, S. Zhao, M. Frotscher, E. Mandelkow and E. M. Mandelkow (2015). "Pro-aggregant Tau impairs mossy fiber plasticity due to structural changes and Ca^{++} dysregulation." Acta Neuropathol Commun **3**: 23.

Deer, T. R., J. E. Pope, M. C. Hanes and G. C. McDowell (2019). "Intrathecal Therapy for Chronic Pain: A Review of Morphine and Ziconotide as Firstline Options." Pain Med **20**(4): 784-798.

Degtiar, V. E., R. H. Scheller and R. W. Tsien (2000). "Syntaxin modulation of slow inactivation of N-type calcium channels." J Neurosci **20**(12): 4355-4367.

Demuro, A., E. Mina, R. Kayed, S. C. Milton, I. Parker and C. G. Glabe (2005). "Calcium dysregulation and membrane disruption as a ubiquitous neurotoxic mechanism of soluble amyloid oligomers." J Biol Chem **280**(17): 17294-17300.

Demuro, A. and I. Parker (2013). "Cytotoxicity of intracellular $A\beta_{42}$ amyloid oligomers involves Ca^{2+} release from the endoplasmic reticulum by stimulated production of inositol trisphosphate." J Neurosci **33**(9): 3824-3833.

Demuro, A., I. Parker and G. E. Stutzmann (2010). "Calcium signaling and amyloid toxicity in Alzheimer disease." J Biol Chem **285**(17): 12463-12468.

Deshpande, A., E. Mina, C. Glabe and J. Busciglio (2006). "Different conformations of amyloid beta induce neurotoxicity by distinct mechanisms in human cortical neurons." J Neurosci **26**(22): 6011-6018.

Deyo, R. A., K. T. Straube and J. F. Disterhoft (1989). "Nimodipine facilitates associative learning in aging rabbits." Science **243**(4892): 809-811.

Dick, I. E., M. R. Tadross, H. Liang, L. H. Tay, W. Yang and D. T. Yue (2008). "A modular switch for spatial Ca^{2+} selectivity in the calmodulin regulation of Ca_V channels." Nature **451**(7180): 830-834.

Diochot, S., S. Richard, M. Baldy-Moulinier, J. Nargeot and J. Valmier (1995). "Dihydropyridines, phenylalkylamines and benzothiazepines block N-, P/Q- and R-type calcium currents." Pflugers Arch **431**(1): 10-19.

Dolphin, A. C. (2003). "β subunits of voltage-gated calcium channels." J Bioenerg Biomembr **35**(6): 599-620.

Dolphin, A. C. (2012). "Calcium channel auxiliary $\alpha_2\delta$ and β subunits: trafficking and one step beyond." Nat Rev Neurosci **13**(8): 542-555.

Dolphin, A. C. (2013). "The $\alpha_2\delta$ subunits of voltage-gated calcium channels." Biochim Biophys Acta **1828**(7): 1541-1549.

Dolphin, A. C. (2016). "Voltage-gated calcium channels and their auxiliary subunits: physiology and pathophysiology and pharmacology." J Physiol **594**(19): 5369-5390.

Dolphin, A. C. (2018). "Voltage-gated calcium channel α2δ subunits: an assessment of proposed novel roles." F1000Res **7**.

Domene, C., D. A. Doyle and C. Venien-Bryan (2005). "Modeling of an ion channel in its open conformation." Biophys J **89**(1): L01-03.

Dong, X. X., Y. Wang and Z. H. Qin (2009). "Molecular mechanisms of excitotoxicity and their relevance to pathogenesis of neurodegenerative diseases." Acta Pharmacol Sin **30**(4): 379-387.

Dong, Y., Y. Gao, S. Xu, Y. Wang, Z. Yu, Y. Li, B. Li, T. Yuan, B. Yang, X. C. Zhang, D. Jiang, Z. Huang and Y. Zhao (2021). "Closed-state inactivation and pore-blocker modulation mechanisms of human $Ca_V2.2$." Cell Rep **37**(5): 109931.

Dooley, D. J., A. Lupp and G. Hertting (1987). "Inhibition of central neurotransmitter release by ω-conotoxin GVIA, a peptide modulator of the N-type voltage-sensitive calcium channel." Naunyn Schmiedebergs Arch Pharmacol **336**(4): 467-470.

Dooley, D. J., A. Lupp, G. Hertting and H. Osswald (1988). "ω-conotoxin GVIA and pharmacological modulation of hippocampal noradrenaline release." Eur J Pharmacol **148**(2): 261-267.

Dreyfus, F. M., A. Tscherter, A. C. Errington, J. J. Renger, H. S. Shin, V. N. Uebele, V. Crunelli, R. C. Lambert and N. Leresche (2010). "Selective T-type calcium channel block in thalamic neurons reveals channel redundancy and physiological impact of $I_{Twindow}$." J Neurosci **30**(1): 99-109.

DuBreuil, D. M., E. J. Lopez Soto, S. Daste, R. Meir, D. Li, B. Wainger, A. Fleischmann and D. Lipscombe (2021). "Heat But Not Mechanical Hypersensitivity Depends on Voltage-Gated $Ca_V2.2$ Calcium Channel Activity in Peripheral Axon Terminals Innervating Skin." J Neurosci **41**(36): 7546-7560.

Dunlap, K., J. I. Luebke and T. J. Turner (1995). "Exocytotic Ca^{2+} channels in mammalian central neurons." Trends Neurosci **18**(2): 89-98.

Duran-Riveroll, L. M. and A. D. Cembella (2017). "Guanidinium Toxins and Their Interactions with Voltage-Gated Sodium Ion Channels." Mar Drugs **15**(10).

Eckert, A. (2005). "[The importance of nimodipine in treatment of dementia]." Pharm Unserer Zeit **34**(5): 392-398.

Edwards, A. B., R. S. Anderton, N. W. Knuckey and B. P. Meloni (2017). "Characterisation of neuroprotective efficacy of modified poly-arginine-9 (R9) peptides using a neuronal glutamic acid excitotoxicity model." Mol Cell Biochem **426**(1-2): 75-85.

Eggermann, E., I. Bucurenciu, S. P. Goswami and P. Jonas (2011). "Nanodomain coupling between Ca^{2+} channels and sensors of exocytosis at fast mammalian synapses." Nat Rev Neurosci **13**(1): 7-21.

Ellinor, P. T., J. Yang, W. A. Sather, J. F. Zhang and R. W. Tsien (1995). "Ca^{2+} channel selectivity at a single locus for high-affinity Ca^{2+} interactions." Neuron **15**(5): 1121-1132.

Ellinor, P. T., J. F. Zhang, W. A. Horne and R. W. Tsien (1994). "Structural determinants of the blockade of N-type calcium channels by a peptide neurotoxin." Nature **372**(6503): 272-275.

Emilsson, L., P. Saetre and E. Jazin (2006). "Alzheimer's disease: mRNA expression profiles of multiple patients show alterations of genes involved with calcium signaling." Neurobiol Dis **21**(3): 618-625.

Emptage, N. J., C. A. Reid and A. Fine (2001). "Calcium stores in hippocampal synaptic boutons mediate short-term plasticity, store-operated Ca^{2+} entry, and spontaneous transmitter release." Neuron **29**(1): 197-208.

Enders, M., T. Heider, A. Ludwig and S. Kuerten (2020). "Strategies for Neuroprotection in Multiple Sclerosis and the Role of Calcium." Int J Mol Sci **21**(5).

Ernst, W. L., Y. Zhang, J. W. Yoo, S. J. Ernst and J. L. Noebels (2009). "Genetic enhancement of thalamocortical network activity by elevating α1G-mediated low-voltage-activated calcium current induces pure absence epilepsy." J Neurosci **29**(6): 1615-1625.

Esposito, Z., L. Belli, S. Toniolo, G. Sancesario, C. Bianconi and A. Martorana (2013). "Amyloid β, glutamate, excitotoxicity in Alzheimer's disease: are we on the right track?" CNS Neurosci Ther **19**(8): 549-555.

Esteras, N., F. Kundel, G. F. Amodeo, E. V. Pavlov, D. Klenerman and A. Y. Abramov (2021). "Insoluble tau aggregates induce neuronal death through modification of membrane ion conductance, activation of voltage-gated calcium channels and NADPH oxidase." FEBS J **288**(1): 127-141.

Etheredge, J. A., D. Murchison, L. C. Abbott and W. H. Griffith (2007). "Functional compensation by other voltage-gated Ca^{2+} channels in mouse basal forebrain neurons with $Ca_V2.1$ mutations." Brain Res **1140**: 105-119.

Fan, M. M. and L. A. Raymond (2007). "N-methyl-D-aspartate (NMDA) receptor function and excitotoxicity in Huntington's disease." Prog Neurobiol **81**(5-6): 272-293.

Fatt, P. and B. L. Ginsborg (1958). "The ionic requirements for the production of action potentials in crustacean muscle fibres." J Physiol **142**(3): 516-543.

Fatt, P. and B. Katz (1953). "The electrical properties of crustacean muscle fibres." J Physiol **120**(1-2): 171-204.

Fedulova, S. A., P. G. Kostyuk and N. S. Veselovsky (1985). "Two types of calcium channels in the somatic membrane of new-born rat dorsal root ganglion neurones." J Physiol **359**: 431-446.

Felix, R., C. A. Gurnett, M. De Waard and K. P. Campbell (1997). "Dissection of functional domains of the voltage-dependent Ca^{2+} channel $\alpha_2\delta$ subunit." J Neurosci **17**(18): 6884-6891.

Felix, R. and N. Weiss (2017). "Ubiquitination and proteasome-mediated degradation of voltage-gated Ca^{2+} channels and potential pathophysiological implications." Gen Physiol Biophys **36**(1): 1-5.

Felizola, S. J., T. Maekawa, Y. Nakamura, F. Satoh, Y. Ono, K. Kikuchi, S. Aritomi, K. Ikeda, M. Yoshimura, K. Tojo and H. Sasano (2014). "Voltage-gated calcium channels in the human adrenal and primary aldosteronism." J Steroid Biochem Mol Biol **144 Pt B**: 410-416.

Ferezou, I., F. Haiss, L. J. Gentet, R. Aronoff, B. Weber and C. C. Petersen (2007). "Spatiotemporal dynamics of cortical sensorimotor integration in behaving mice." Neuron **56**(5): 907-923.

Ferrer-Montiel, A. V., J. M. Merino, S. E. Blondelle, E. Perez-Paya, R. A. Houghten and M. Montal (1998). "Selected peptides targeted to the NMDA receptor channel protect neurons from excitotoxic death." Nat Biotechnol **16**(3): 286-291.

Ferron, L., A. Davies, K. M. Page, D. J. Cox, J. Leroy, D. Waithe, A. J. Butcher, P. Sellaturay, S. Bolsover, W. S. Pratt, F. J. Moss and A. C. Dolphin (2008). "The stargazin-

related protein γ7 interacts with the mRNA-binding protein heterogeneous nuclear ribonucleoprotein A2 and regulates the stability of specific mRNAs, including $Ca_V2.2$." J Neurosci **28**(42): 10604-10617.

Field, M. J., P. J. Cox, E. Stott, H. Melrose, J. Offord, T. Z. Su, S. Bramwell, L. Corradini, S. England, J. Winks, R. A. Kinloch, J. Hendrich, A. C. Dolphin, T. Webb and D. Williams (2006). "Identification of the α_2-δ-1 subunit of voltage-dependent calcium channels as a molecular target for pain mediating the analgesic actions of pregabalin." Proc Natl Acad Sci U S A **103**(46): 17537-17542.

Finkel, L. and S. Koh (2013). "N-type calcium channel antibody-mediated autoimmune encephalitis: An unlikely cause of a common presentation." Epilepsy Behav Case Rep **1**: 92-96.

Fletcher, C. F., C. M. Lutz, T. N. O'Sullivan, J. D. Shaughnessy, Jr., R. Hawkes, W. N. Frankel, N. G. Copeland and N. A. Jenkins (1996). "Absence epilepsy in tottering mutant mice is associated with calcium channel defects." Cell **87**(4): 607-617.

Foehring, R. C. (1996). "Serotonin modulates N- and P-type calcium currents in neocortical pyramidal neurons via a membrane-delimited pathway." J Neurophysiol **75**(2): 648-659.

Forder, J. P. and M. Tymianski (2009). "Postsynaptic mechanisms of excitotoxicity: Involvement of postsynaptic density proteins, radicals, and oxidant molecules." Neuroscience **158**(1): 293-300.

Forette, F., M. L. Seux, J. A. Staessen, L. Thijs, M. R. Babarskiene, S. Babeanu, A. Bossini, R. Fagard, B. Gil-Extremera, T. Laks, Z. Kobalava, C. Sarti, J. Tuomilehto, H. Vanhanen, J. Webster, Y. Yodfat, W. H. Birkenhager and I. Systolic Hypertension in Europe (2002). "The prevention of dementia with antihypertensive treatment: new evidence from the Systolic Hypertension in Europe (Syst-Eur) study." Arch Intern Med **162**(18): 2046-2052.

Forette, F., M. L. Seux, J. A. Staessen, L. Thijs, W. H. Birkenhager, M. R. Babarskiene, S. Babeanu, A. Bossini, B. Gil-Extremera, X. Girerd, T. Laks, E. Lilov, V. Moisseyev, J. Tuomilehto, H. Vanhanen, J. Webster, Y. Yodfat and R. Fagard (1998). "Prevention of dementia in randomised double-blind placebo-controlled Systolic Hypertension in Europe (Syst-Eur) trial." Lancet **352**(9137): 1347-1351.

Foster, T. C. (2007). "Calcium homeostasis and modulation of synaptic plasticity in the aged brain." Aging Cell **6**(3): 319-325.

Foster, T. C., C. Kyritsopoulos and A. Kumar (2017). "Central role for NMDA receptors in redox mediated impairment of synaptic function during aging and Alzheimer's disease." Behav Brain Res **322**(Pt B): 223-232.

Fox, A. P., M. C. Nowycky and R. W. Tsien (1987). "Kinetic and pharmacological properties distinguishing three types of calcium currents in chick sensory neurones." J Physiol **394**: 149-172.

Francois-Moutal, L., Y. Wang, A. Moutal, K. E. Cottier, O. K. Melemedjian, X. Yang, Y. Wang, W. Ju, T. M. Largent-Milnes, M. Khanna, T. W. Vanderah and R. Khanna (2015). "A membrane-delimited N-myristoylated CRMP2 peptide aptamer inhibits $Ca_V2.2$

trafficking and reverses inflammatory and postoperative pain behaviors." Pain **156**(7): 1247-1264.

Freir, D. B., D. A. Costello and C. E. Herron (2003). "Aβ25-35-induced depression of long-term potentiation in area CA1 in vivo and in vitro is attenuated by verapamil." J Neurophysiol **89**(6): 3061-3069.

Fu, H., W. Li, Y. Lao, J. Luo, N. T. Lee, K. K. Kan, H. W. Tsang, K. W. Tsim, Y. Pang, Z. Li, D. C. Chang, M. Li and Y. Han (2006). "Bis(7)-tacrine attenuates β amyloid-induced neuronal apoptosis by regulating L-type calcium channels." J Neurochem **98**(5): 1400-1410.

Funayama, K., G. Minamisawa, N. Matsumoto, H. Ban, A. W. Chan, N. Matsuki, T. H. Murphy and Y. Ikegaya (2015). "Neocortical Rebound Depolarization Enhances Visual Perception." PLoS Biol **13**(8): e1002231.

Furukawa, K., M. Matsuzaki-Kobayashi, T. Hasegawa, A. Kikuchi, N. Sugeno, Y. Itoyama, Y. Wang, P. J. Yao, I. Bushlin and A. Takeda (2006). "Plasma membrane ion permeability induced by mutant α-synuclein contributes to the degeneration of neural cells." J Neurochem **97**(4): 1071-1077.

Furukawa, T., R. Miura, Y. Mori, M. Strobeck, K. Suzuki, Y. Ogihara, T. Asano, R. Morishita, M. Hashii, H. Higashida, M. Yoshii and T. Nukada (1998). "Differential interactions of the C terminus and the cytoplasmic I-II loop of neuronal Ca^{2+} channels with G-protein α and βγ subunits. II. Evidence for direct binding." J Biol Chem **273**(28): 17595-17603.

Gadotti, V. M., C. Bladen, F. X. Zhang, L. Chen, M. G. Gunduz, R. Simsek, C. Safak and G. W. Zamponi (2015). "Analgesic effect of a broad-spectrum dihydropyridine inhibitor of voltage-gated calcium channels." Pflugers Arch **467**(12): 2485-2493.

Gao, S., X. Yao and N. Yan (2021). "Structure of human $Ca_V2.2$ channel blocked by the painkiller ziconotide." Nature **596**(7870): 143-147.

Garcia-Alloza, M., E. M. Robbins, S. X. Zhang-Nunes, S. M. Purcell, R. A. Betensky, S. Raju, C. Prada, S. M. Greenberg, B. J. Bacskai and M. P. Frosch (2006). "Characterization of amyloid deposition in the APPswe/PS1dE9 mouse model of Alzheimer disease." Neurobiol Dis **24**(3): 516-524.

Garcia, M. L., V. F. King, J. L. Shevell, R. S. Slaughter, G. Suarez-Kurtz, R. J. Winquist and G. J. Kaczorowski (1990). "Amiloride analogs inhibit L-type calcium channels and display calcium entry blocker activity." J Biol Chem **265**(7): 3763-3771.

Gholamipour-Badie, H., N. Naderi, F. Khodagholi, F. Shaerzadeh and F. Motamedi (2013). "L-type calcium channel blockade alleviates molecular and reversal spatial learning and memory alterations induced by entorhinal amyloid pathology in rats." Behav Brain Res **237**: 190-199.

Giardino, I., A. K. Fard, D. L. Hatchell and M. Brownlee (1998). "Aminoguanidine inhibits reactive oxygen species formation, lipid peroxidation, and oxidant-induced apoptosis." Diabetes **47**(7): 1114-1120.

Gorman, K. M., E. Meyer, D. Grozeva, E. Spinelli, A. McTague, A. Sanchis-Juan, K. J. Carss, E. Bryant, A. Reich, A. L. Schneider, R. M. Pressler, M. A. Simpson, G. D. Debelle,

E. Wassmer, J. Morton, D. Sieciechowicz, E. Jan-Kamsteeg, A. R. Paciorkowski, M. D. King, J. H. Cross, A. Poduri, H. C. Mefford, I. E. Scheffer, T. B. Haack, G. McCullagh, S. Deciphering Developmental Disorders, U. K. Consortium, N. BioResource, J. J. Millichap, G. L. Carvill, J. Clayton-Smith, E. R. Maher, F. L. Raymond and M. A. Kurian (2019). "Bi-allelic Loss-of-Function CACNA1B Mutations in Progressive Epilepsy-Dyskinesia." Am J Hum Genet **104**(5): 948-956.

Gray, A. C., J. Raingo and D. Lipscombe (2007). "Neuronal calcium channels: splicing for optimal performance." Cell Calcium **42**(4-5): 409-417.

Green, K. N., I. F. Smith and F. M. Laferla (2007). "Role of calcium in the pathogenesis of Alzheimer's disease and transgenic models." Subcell Biochem **45**: 507-521.

Green, W. N. and O. S. Andersen (1991). "Surface charges and ion channel function." Annu Rev Physiol **53**: 341-359.

Greer, P. L. and M. E. Greenberg (2008). "From synapse to nucleus: calcium-dependent gene transcription in the control of synapse development and function." Neuron **59**(6): 846-860.

Gribkoff, V. K. (2006). "The role of voltage-gated calcium channels in pain and nociception." Semin Cell Dev Biol **17**(5): 555-564.

Groen, J. L., A. Andrade, K. Ritz, H. Jalalzadeh, M. Haagmans, T. E. Bradley, A. Jongejan, D. S. Verbeek, P. Nurnberg, S. Denome, R. C. Hennekam, D. Lipscombe, F. Baas and M. A. Tijssen (2015). "CACNA1B mutation is linked to unique myoclonus-dystonia syndrome." Hum Mol Genet **24**(4): 987-993.

Gruner, W. and L. R. Silva (1994). "Omega-conotoxin sensitivity and presynaptic inhibition of glutamatergic sensory neurotransmission in vitro." J Neurosci **14**(5 Pt 1): 2800-2808.

Guillery, R. W. and S. M. Sherman (2002). "Thalamic relay functions and their role in corticocortical communication: generalizations from the visual system." Neuron **33**(2): 163-175.

Guo, Q., W. Fu, B. L. Sopher, M. W. Miller, C. B. Ware, G. M. Martin and M. P. Mattson (1999). "Increased vulnerability of hippocampal neurons to excitotoxic necrosis in presenilin-1 mutant knock-in mice." Nat Med **5**(1): 101-106.

Guo, Q., K. Furukawa, B. L. Sopher, D. G. Pham, J. Xie, N. Robinson, G. M. Martin and M. P. Mattson (1996). "Alzheimer's PS-1 mutation perturbs calcium homeostasis and sensitizes PC12 cells to death induced by amyloid β-peptide." Neuroreport **8**(1): 379-383.

Gurnett, C. A., M. De Waard and K. P. Campbell (1996). "Dual function of the voltage-dependent Ca^{2+} channel $\alpha_2\delta$ subunit in current stimulation and subunit interaction." Neuron **16**(2): 431-440.

Hamid, J., D. Nelson, R. Spaetgens, S. J. Dubel, T. P. Snutch and G. W. Zamponi (1999). "Identification of an integration center for cross-talk between protein kinase C and G protein modulation of N-type calcium channels." J Biol Chem **274**(10): 6195-6202.

Hanyu, H., K. Hirao, S. Shimizu, T. Iwamoto, K. Koizumi and K. Abe (2007). "Favourable effects of nilvadipine on cognitive function and regional cerebral blood flow on SPECT in hypertensive patients with mild cognitive impairment." Nucl Med Commun **28**(4): 281-287.

Hanyu, H., K. Hirao, S. Shimizu, T. Sato, A. Kiuchi and T. Iwamoto (2007). "Nilvadipine prevents cognitive decline of patients with mild cognitive impairment." Int J Geriatr Psychiatry **22**(12): 1264-1266.

Hardy, J. and D. Allsop (1991). "Amyloid deposition as the central event in the aetiology of Alzheimer's disease." Trends Pharmacol Sci **12**(10): 383-388.

Harkins, A. B., A. L. Cahill, J. F. Powers, A. S. Tischler and A. P. Fox (2004). "Deletion of the synaptic protein interaction site of the N-type ($Ca_V2.2$) calcium channel inhibits secretion in mouse pheochromocytoma cells." Proc Natl Acad Sci U S A **101**(42): 15219-15224.

Hartley, D. M., M. C. Kurth, L. Bjerkness, J. H. Weiss and D. W. Choi (1993). "Glutamate receptor-induced 45Ca2+ accumulation in cortical cell culture correlates with subsequent neuronal degeneration." J Neurosci **13**(5): 1993-2000.

Harvey, R. D. and J. W. Hell (2013). "$Ca_V1.2$ signaling complexes in the heart." J Mol Cell Cardiol **58**: 143-152.

He, L. M., L. Y. Chen, X. L. Lou, A. L. Qu, Z. Zhou and T. Xu (2002). "Evaluation of β-amyloid peptide 25-35 on calcium homeostasis in cultured rat dorsal root ganglion neurons." Brain Res **939**(1-2): 65-75.

Heinke, B., E. Gingl and J. Sandkuhler (2011). "Multiple targets of μ-opioid receptor-mediated presynaptic inhibition at primary afferent Aδ- and C-fibers." J Neurosci **31**(4): 1313-1322.

Hell, J. W., R. E. Westenbroek, C. Warner, M. K. Ahlijanian, W. Prystay, M. M. Gilbert, T. P. Snutch and W. A. Catterall (1993). "Identification and differential subcellular localization of the neuronal class C and class D L-type calcium channel alpha 1 subunits." J Cell Biol **123**(4): 949-962.

Herdon, H. and S. R. Nahorski (1989). "Investigations of the roles of dihydropyridine and ω-conotoxin-sensitive calcium channels in mediating depolarisation-evoked endogenous dopamine release from striatal slices." Naunyn Schmiedebergs Arch Pharmacol **340**(1): 36-40.

Herlitze, S., H. Zhong, T. Scheuer and W. A. Catterall (2001). "Allosteric modulation of Ca^{2+} channels by G proteins, voltage-dependent facilitation, protein kinase C, and $Ca_V\beta$ subunits." Proc Natl Acad Sci U S A **98**(8): 4699-4704.

Herman, J. P., K. C. Chen, R. Booze and P. W. Landfield (1998). "Up-regulation of α_{1D} Ca^{2+} channel subunit mRNA expression in the hippocampus of aged F344 rats." Neurobiol Aging **19**(6): 581-587.

Hermann, D., M. Mezler, M. K. Muller, K. Wicke, G. Gross, A. Draguhn, C. Bruehl and V. Nimmrich (2013). "Synthetic Aβ oligomers ($A\beta_{1-42}$ globulomer) modulate presynaptic calcium currents: prevention of Aβ-induced synaptic deficits by calcium channel blockers." Eur J Pharmacol **702**(1-3): 44-55.

Hettiarachchi, N. T., A. Parker, M. L. Dallas, K. Pennington, C. C. Hung, H. A. Pearson, J. P. Boyle, P. Robinson and C. Peers (2009). "α-Synuclein modulation of Ca^{2+} signaling in human neuroblastoma (SH-SY5Y) cells." J Neurochem **111**(5): 1192-1201.

Heyes, S., W. S. Pratt, E. Rees, S. Dahimene, L. Ferron, M. J. Owen and A. C. Dolphin (2015). "Genetic disruption of voltage-gated calcium channels in psychiatric and neurological disorders." Prog Neurobiol **134**: 36-54.

Hillman, D., S. Chen, T. T. Aung, B. Cherksey, M. Sugimori and R. R. Llinas (1991). "Localization of P-type calcium channels in the central nervous system." Proc Natl Acad Sci U S A **88**(16): 7076-7080.

Hirning, L. D., A. P. Fox, E. W. McCleskey, B. M. Olivera, S. A. Thayer, R. J. Miller and R. W. Tsien (1988). "Dominant role of N-type Ca^{2+} channels in evoked release of norepinephrine from sympathetic neurons." Science **239**(4835): 57-61.

Hofmann, F., L. Lacinova and N. Klugbauer (1999). "Voltage-dependent calcium channels: from structure to function." Rev Physiol Biochem Pharmacol **139**: 33-87.

Holden, R., G. Chauhan and T. Emerick (2022). "Intrathecal Administration of Ziconotide as a Potential Treatment for Chronic Migraines." Cureus **14**(3): e23714.

Hoppa, M. B., B. Lana, W. Margas, A. C. Dolphin and T. A. Ryan (2012). "α2δ expression sets presynaptic calcium channel abundance and release probability." Nature **486**(7401): 122-125.

Horne, A. L. and J. A. Kemp (1991). "The effect of ω-conotoxin GVIA on synaptic transmission within the nucleus accumbens and hippocampus of the rat in vitro." Br J Pharmacol **103**(3): 1733-1739.

Hosaka, T., Y. L. Yamamoto and M. Diksic (1991). "Efficacy of retrograde perfusion of the cerebral vein with verapamil after focal ischemia in rat brain." Stroke **22**(12): 1562-1566.

Hu, L. Y., T. R. Ryder, M. F. Rafferty, W. L. Cody, S. M. Lotarski, G. P. Miljanich, E. Millerman, D. M. Rock, Y. Song, S. J. Stoehr, C. P. Taylor, M. L. Weber, B. G. Szoke and M. G. Vartanian (1999). "N,N-dialkyl-dipeptidylamines as novel N-type calcium channel blockers." Bioorg Med Chem Lett **9**(6): 907-912.

Hu, L. Y., T. R. Ryder, M. F. Rafferty, M. R. Feng, S. M. Lotarski, D. M. Rock, M. Sinz, S. J. Stoehr, C. P. Taylor, M. L. Weber, S. S. Bowersox, G. P. Miljanich, E. Millerman, Y. X. Wang and B. G. Szoke (1999). "Synthesis of a series of 4-benzyloxyaniline analogues as neuronal N-type calcium channel blockers with improved anticonvulsant and analgesic properties." J Med Chem **42**(20): 4239-4249.

Hu, L. Y., T. R. Ryder, M. F. Rafferty, K. M. Siebers, T. Malone, A. Chatterjee, M. R. Feng, S. M. Lotarski, D. M. Rock, S. J. Stoehr, C. P. Taylor, M. L. Weber, G. P. Miljanich, E. Millerman and B. G. Szoke (2000). "Neuronal N-type calcium channel blockers: a series of 4-piperidinylaniline analogs with analgesic activity." Drug Des Discov **17**(1): 85-93.

Huang, S. Y. and X. Zou (2008). "An iterative knowledge-based scoring function for protein-protein recognition." Proteins **72**(2): 557-579.

Hulshof, L. A., L. A. Frajmund, D. van Nuijs, D. C. N. van der Heijden, J. Middeldorp and E. M. Hol (2022). "Both male and female APPswe/PSEN1dE9 mice are impaired in spatial memory and cognitive flexibility at 9 months of age." Neurobiol Aging **113**: 28-38.

Hunte, C., G. Von Jagow and H. Schagger (2003). Membrane protein purification and crystallization: a practical guide, Elsevier.

Hunter, A. J. (1997). "Calcium antagonists: their role in neuroprotection." Int Rev Neurobiol **40**: 95-108.

Hurley, J. H., A. L. Cahill, K. P. Currie and A. P. Fox (2000). "The role of dynamic palmitoylation in Ca^{2+} channel inactivation." Proc Natl Acad Sci U S A **97**(16): 9293-9298.

Hussain, S., A. Singh, S. O. Rahman, A. Habib and A. K. Najmi (2018). "Calcium channel blocker use reduces incident dementia risk in elderly hypertensive patients: A meta-analysis of prospective studies." Neurosci Lett **671**: 120-127.

Ifft, J. B. (1976). "Sedimentation equilibrium of proteins in density gradients." Biophys Chem **5**(1-2): 137-157.

Ino, M., T. Yoshinaga, M. Wakamori, N. Miyamoto, E. Takahashi, J. Sonoda, T. Kagaya, T. Oki, T. Nagasu, Y. Nishizawa, I. Tanaka, K. Imoto, S. Aizawa, S. Koch, A. Schwartz, T. Niidome, K. Sawada and Y. Mori (2001). "Functional disorders of the sympathetic nervous system in mice lacking the α_{1B} subunit ($Ca_V2.2$) of N-type calcium channels." Proc Natl Acad Sci U S A **98**(9): 5323-5328.

Irvine, G. B. (2001). "Determination of molecular size by size-exclusion chromatography (gel filtration)." Curr Protoc Cell Biol **Chapter 5**: Unit 5 5.

Jankowsky, J. L., D. J. Fadale, J. Anderson, G. M. Xu, V. Gonzales, N. A. Jenkins, N. G. Copeland, M. K. Lee, L. H. Younkin, S. L. Wagner, S. G. Younkin and D. R. Borchelt (2004). "Mutant presenilins specifically elevate the levels of the 42 residue β-amyloid peptide in vivo: evidence for augmentation of a 42-specific γ secretase." Hum Mol Genet **13**(2): 159-170.

Jarvis, S. E., J. M. Magga, A. M. Beedle, J. E. Braun and G. W. Zamponi (2000). "G protein modulation of N-type calcium channels is facilitated by physical interactions between syntaxin 1A and Gβγ." J Biol Chem **275**(9): 6388-6394.

Jarvis, S. E. and G. W. Zamponi (2001). "Distinct molecular determinants govern syntaxin 1A-mediated inactivation and G-protein inhibition of N-type calcium channels." J Neurosci **21**(9): 2939-2948.

Jensen, T. S., R. Baron, M. Haanpaa, E. Kalso, J. D. Loeser, A. S. C. Rice and R. D. Treede (2011). "A new definition of neuropathic pain." Pain **152**(10): 2204-2205.

Jiang, Y. Q., A. Andrade and D. Lipscombe (2013). "Spinal morphine but not ziconotide or gabapentin analgesia is affected by alternative splicing of voltage-gated calcium channel $Ca_V2.2$ pre-mRNA." Mol Pain **9**: 67.

Joviano-Santos, J. V., P. A. C. Valadao, M. P. S. Magalhaes-Gomes, L. F. Fernandes, D. M. Diniz, T. C. G. Machado, K. B. Soares, M. S. Ladeira, A. R. Massensini, M. V. Gomez, A. S. Miranda, J. C. Tapia and C. Guatimosim (2022). "Neuroprotective effect of CTK

01512-2 recombinant toxin at the spinal cord in a model of Huntington's disease." Exp Physiol **107**(8): 933-945.

Joviano-Santos, J. V., P. A. C. Valadao, M. P. S. Magalhaes-Gomes, L. F. Fernandes, D. M. Diniz, T. C. G. Machado, K. B. Soares, M. S. Ladeira, A. S. Miranda, A. R. Massensini, M. V. Gomez and C. Guatimosim (2021). "Protective effect of a spider recombinant toxin in a murine model of Huntington's disease." Neuropeptides **85**: 102111.

Julius, D. and J. Nathans (2012). "Signaling by sensory receptors." Cold Spring Harb Perspect Biol **4**(1): a005991.

Kaboord, B. and M. Perr (2008). "Isolation of proteins and protein complexes by immunoprecipitation." Methods Mol Biol **424**: 349-364.

Kadurin, I., L. Ferron, S. W. Rothwell, J. O. Meyer, L. R. Douglas, C. S. Bauer, B. Lana, W. Margas, O. Alexopoulos, M. Nieto-Rostro, W. S. Pratt and A. C. Dolphin (2016). "Proteolytic maturation of $\alpha_2\delta$ represents a checkpoint for activation and neuronal trafficking of latent calcium channels." Elife **5**.

Kagan, B. L., Y. Hirakura, R. Azimov, R. Azimova and M. C. Lin (2002). "The channel hypothesis of Alzheimer's disease: current status." Peptides **23**(7): 1311-1315.

Kaisis, E., L. J. Thei, G. J. Stephens and M. L. Dallas (2022). "Protofibrillar Amyloid Beta Modulation of Recombinant hCaV2.2 (N-Type) Voltage-Gated Channels." Pharmaceuticals (Basel) **15**(12).

Kalia, J. and K. J. Swartz (2011). "Elucidating the molecular basis of action of a classic drug: guanidine compounds as inhibitors of voltage-gated potassium channels." Mol Pharmacol **80**(6): 1085-1095.

Kamphuis, W., C. Mamber, M. Moeton, L. Kooijman, J. A. Sluijs, A. H. Jansen, M. Verveer, L. R. de Groot, V. D. Smith, S. Rangarajan, J. J. Rodriguez, M. Orre and E. M. Hol (2012). "GFAP isoforms in adult mouse brain with a focus on neurogenic astrocytes and reactive astrogliosis in mouse models of Alzheimer disease." PLoS One **7**(8): e42823.

Kang, M. G., C. C. Chen, R. Felix, V. A. Letts, W. N. Frankel, Y. Mori and K. P. Campbell (2001). "Biochemical and biophysical evidence for γ_2 subunit association with neuronal voltage-activated Ca^{2+} channels." J Biol Chem **276**(35): 32917-32924.

Kasai, H., T. Aosaki and J. Fukuda (1987). "Presynaptic Ca-antagonist ω-conotoxin irreversibly blocks N-type Ca-channels in chick sensory neurons." Neurosci Res **4**(3): 228-235.

Kasparova, J., V. Lisa, S. Tucek and V. Dolezal (2001). "Chronic exposure of NG108-15 cells to amyloid β peptide (Aβ1-42) abolishes calcium influx via N-type calcium channels." Neurochem Res **26**(8-9): 1079-1084.

Kass, B., S. Schemmert, C. Zafiu, M. Pils, O. Bannach, J. Kutzsche, T. Bujnicki and D. Willbold (2022). "Aβ oligomer concentration in mouse and human brain and its drug-induced reduction *ex vivo*." Cell Rep Med **3**(5): 100630.

Katz, B. and R. Miledi (1967). "Ionic requirements of synaptic transmitter release." Nature **215**(5101): 651.

Kawahara, M. and Y. Kuroda (2000). "Molecular mechanism of neurodegeneration induced by Alzheimer's β-amyloid protein: channel formation and disruption of calcium homeostasis." Brain Res Bull **53**(4): 389-397.

Keimasi, M., K. Salehifard, M. Keimasi, M. Amirsadri, N. M. J. Esfahani, M. Moradmand, F. Esmaeili and M. R. Mofid (2023). "Alleviation of cognitive deficits in a rat model of glutamate-induced excitotoxicity, using an N-type voltage-gated calcium channel ligand, extracted from Agelena labyrinthica crude venom." Front Mol Neurosci **16**: 1123343.

Keimasi, M., K. Salehifard, N. Mirshah Jafar Esfahani, F. Esmaeili, A. Farghadani, M. Amirsadri, M. Keimasi, M. Noorbakhshnia, M. Moradmand and M. R. Mofid (2023). "The synergic effects of presynaptic calcium channel antagonists purified from spiders on memory elimination of glutamate-induced excitotoxicity in the rat hippocampus trisynaptic circuit." Front Mol Biosci **10**: 1243976.

Kerr, L. M. and D. Yoshikami (1984). "A venom peptide with a novel presynaptic blocking action." Nature **308**(5956): 282-284.

Khachaturian, Z. S. (1989). "Calcium, membranes, aging, and Alzheimer's disease. Introduction and overview." Ann N Y Acad Sci **568**: 1-4.

Khachaturian, Z. S. (1994). "Calcium hypothesis of Alzheimer's disease and brain aging." Ann N Y Acad Sci **747**: 1-11.

Kim, C., K. Jun, T. Lee, S. S. Kim, M. W. McEnery, H. Chin, H. L. Kim, J. M. Park, D. K. Kim, S. J. Jung, J. Kim and H. S. Shin (2001). "Altered nociceptive response in mice deficient in the α_{1B} subunit of the voltage-dependent calcium channel." Mol Cell Neurosci **18**(2): 235-245.

Kim, S. and H. Rhim (2011). "Effects of amyloid-beta peptides on voltage-gated L-type $Ca_V1.2$ and $Ca_V1.3$ Ca^{2+} channels." Mol Cells **32**(3): 289-294.

Kimpinski, K., V. Iodice, S. Vernino, P. Sandroni and P. A. Low (2009). "Association of N-type calcium channel autoimmunity in patients with autoimmune autonomic ganglionopathy." Auton Neurosci **150**(1-2): 136-139.

Kinney, J. W., S. M. Bemiller, A. S. Murtishaw, A. M. Leisgang, A. M. Salazar and B. T. Lamb (2018). "Inflammation as a central mechanism in Alzheimer's disease." Alzheimers Dement (N Y) **4**: 575-590.

Kiritani, T., I. R. Wickersham, H. S. Seung and G. M. Shepherd (2012). "Hierarchical connectivity and connection-specific dynamics in the corticospinal-corticostriatal microcircuit in mouse motor cortex." J Neurosci **32**(14): 4992-5001.

Kisilevsky, A. E., S. J. Mulligan, C. Altier, M. C. Iftinca, D. Varela, C. Tai, L. Chen, S. Hameed, J. Hamid, B. A. Macvicar and G. W. Zamponi (2008). "D1 receptors physically interact with N-type calcium channels to regulate channel distribution and dendritic calcium entry." Neuron **58**(4): 557-570.

Kitano, J., M. Nishida, Y. Itsukaichi, I. Minami, M. Ogawa, T. Hirano, Y. Mori and S. Nakanishi (2003). "Direct interaction and functional coupling between metabotropic glutamate receptor subtype 1 and voltage-sensitive $Ca_V2.1$ Ca^{2+} channel." J Biol Chem **278**(27): 25101-25108.

Koschak, A., M. L. Fernandez-Quintero, T. Heigl, M. Ruzza, H. Seitter and L. Zanetti (2021). "Cav1.4 dysfunction and congenital stationary night blindness type 2." Pflugers Arch **473**(9): 1437-1454.

Koschak, A., D. Reimer, I. Huber, M. Grabner, H. Glossmann, J. Engel and J. Striessnig (2001). "α1D (Cav1.3) subunits can form L-type Ca^{2+} channels activating at negative voltages." J Biol Chem **276**(25): 22100-22106.

Koutsilieri, E. and P. Riederer (2007). "Excitotoxicity and new antiglutamatergic strategies in Parkinson's disease and Alzheimer's disease." Parkinsonism Relat Disord **13 Suppl 3**: S329-331.

Krejci, A., T. R. Hupp, M. Lexa, B. Vojtesek and P. Muller (2016). "Hammock: a hidden Markov model-based peptide clustering algorithm to identify protein-interaction consensus motifs in large datasets." Bioinformatics **32**(1): 9-16.

Krissinel, E. and K. Henrick (2007). "Inference of macromolecular assemblies from crystalline state." J Mol Biol **372**(3): 774-797.

Krnjevic, K. and Y. Z. Xu (1989). "Dantrolene suppresses the hyperpolarization or outward current observed during anoxia in hippocampal neurons." Can J Physiol Pharmacol **67**(12): 1602-1604.

Kuchibhotla, K. V., S. T. Goldman, C. R. Lattarulo, H. Y. Wu, B. T. Hyman and B. J. Bacskai (2008). "Aβ plaques lead to aberrant regulation of calcium homeostasis in vivo resulting in structural and functional disruption of neuronal networks." Neuron **59**(2): 214-225.

Kukley, M., E. Capetillo-Zarate and D. Dietrich (2007). "Vesicular glutamate release from axons in white matter." Nat Neurosci **10**(3): 311-320.

Kumaradev, S., A. Fayosse, A. Dugravot, J. Dumurgier, C. Roux, M. Kivimaki, A. Singh-Manoux and S. Sabia (2021). "Timeline of pain before dementia diagnosis: a 27-year follow-up study." Pain **162**(5): 1578-1585.

Kurnellas, M. P., K. C. Donahue and S. Elkabes (2007). "Mechanisms of neuronal damage in multiple sclerosis and its animal models: role of calcium pumps and exchangers." Biochem Soc Trans **35**(Pt 5): 923-926.

Kutzsche, J., G. A. Guzman, A. Willuweit, O. Kletke, E. Wollert, I. Gering, D. Jurgens, J. Breitkreutz, H. Stark, A. G. Beck-Sickinge, N. Klocker, P. Hidalgo and D. Willbold (2023). "An orally available N-type calcium channel inhibitor for the treatment of neuropathic pain." Br J Pharmacol.

Kutzsche, J., D. Jurgens, A. Willuweit, K. Adermann, C. Fuchs, S. Simons, M. Windisch, M. Humpel, W. Rossberg, M. Wolzt and D. Willbold (2020). "Safety and pharmacokinetics of the orally available antiprionic compound PRI-002: A single and multiple ascending dose phase I study." Alzheimers Dement (N Y) **6**(1): e12001.

Kutzsche, J., S. Schemmert, T. Bujnicki, C. Zafiu, S. Halbgebauer, V. Kraemer-Schulien, M. Pils, L. Blomeke, J. Post, A. Kulawik, D. Jurgens, W. M. Rossberg, M. Humpel, O. Bannach, M. Otto, J. A. Araujo, A. Willuweit and D. Willbold (2023). "Oral treatment with

the all-D-peptide RD2 enhances cognition in aged beagle dogs - A model of sporadic Alzheimer's disease." Heliyon **9**(8): e18443.

Kutzsche, J., S. Schemmert, M. Tusche, J. Neddens, R. Rabl, D. Jurgens, O. Brener, A. Willuweit, B. Hutter-Paier and D. Willbold (2017). "Large-Scale Oral Treatment Study with the Four Most Promising D3-Derivatives for the Treatment of Alzheimer's Disease." Molecules **22**(10).

Kwon, S. E., H. Yang, G. Minamisawa and D. H. O'Connor (2016). "Sensory and decision-related activity propagate in a cortical feedback loop during touch perception." Nat Neurosci **19**(9): 1243-1249.

Ladner, C. L., J. Yang, R. J. Turner and R. A. Edwards (2004). "Visible fluorescent detection of proteins in polyacrylamide gels without staining." Anal Biochem **326**(1): 13-20.

LaFerla, F. M. (2002). "Calcium dyshomeostasis and intracellular signalling in Alzheimer's disease." Nat Rev Neurosci **3**(11): 862-872.

Lalonde, R., H. D. Kim, J. A. Maxwell and K. Fukuchi (2005). "Exploratory activity and spatial learning in 12-month-old APP_{695}SWE/co+*PS1*/ΔE9 mice with amyloid plaques." Neurosci Lett **390**(2): 87-92.

Lambert, J. C., F. Wavrant-De Vrieze, P. Amouyel and M. C. Chartier-Harlin (1998). "Association at LRP gene locus with sporadic late-onset Alzheimer's disease." Lancet **351**(9118): 1787-1788.

Lazniewska, J. and N. Weiss (2014). "The "sweet" side of ion channels." Rev Physiol Biochem Pharmacol **167**: 67-114.

Lazniewska, J. and N. Weiss (2017). "Glycosylation of voltage-gated calcium channels in health and disease." Biochim Biophys Acta Biomembr **1859**(5): 662-668.

Lee, A., S. T. Wong, D. Gallagher, B. Li, D. R. Storm, T. Scheuer and W. A. Catterall (1999). "Ca^{2+}/calmodulin binds to and modulates P/Q-type calcium channels." Nature **399**(6732): 155-159.

Lee, S. Y., D. Y. Hwang, Y. K. Kim, J. W. Lee, I. C. Shin, K. W. Oh, M. K. Lee, J. S. Lim, D. Y. Yoon, S. J. Hwang and J. T. Hong (2006). "PS2 mutation increases neuronal cell vulnerability to neurotoxicants through activation of caspase-3 by enhancing of ryanodine receptor-mediated calcium release." FASEB J **20**(1): 151-153.

Leissring, M. A., I. Parker and F. M. LaFerla (1999). "Presenilin-2 mutations modulate amplitude and kinetics of inositol 1,4,5-trisphosphate-mediated calcium signals." J Biol Chem **274**(46): 32535-32538.

Leithold, L. H., N. Jiang, J. Post, T. Ziehm, E. Schartmann, J. Kutzsche, N. J. Shah, J. Breitkreutz, K. J. Langen, A. Willuweit and D. Willbold (2016). "Pharmacokinetic Properties of a Novel D-Peptide Developed to be Therapeutically Active Against Toxic β-Amyloid Oligomers." Pharm Res **33**(2): 328-336.

Leroy, J., M. W. Richards, A. J. Butcher, M. Nieto-Rostro, W. S. Pratt, A. Davies and A. C. Dolphin (2005). "Interaction via a key tryptophan in the I-II linker of N-type calcium

channels is required for β1 but not for palmitoylated β2, implicating an additional binding site in the regulation of channel voltage-dependent properties." J Neurosci **25**(30): 6984-6996.

Letts, V. A., R. Felix, G. H. Biddlecome, J. Arikkath, C. L. Mahaffey, A. Valenzuela, F. S. Bartlett, 2nd, Y. Mori, K. P. Campbell and W. N. Frankel (1998). "The mouse stargazer gene encodes a neuronal Ca^{2+}-channel γ subunit." Nat Genet **19**(4): 340-347.

Leveque, C., O. el Far, N. Martin-Moutot, K. Sato, R. Kato, M. Takahashi and M. J. Seagar (1994). "Purification of the N-type calcium channel associated with syntaxin and synaptotagmin. A complex implicated in synaptic vesicle exocytosis." J Biol Chem **269**(9): 6306-6312.

Leveque, C., T. Hoshino, P. David, Y. Shoji-Kasai, K. Leys, A. Omori, B. Lang, O. el Far, K. Sato, N. Martin-Moutot and et al. (1992). "The synaptic vesicle protein synaptotagmin associates with calcium channels and is a putative Lambert-Eaton myasthenic syndrome antigen." Proc Natl Acad Sci U S A **89**(8): 3625-3629.

Li, Y. J. and S. P. Duckles (1991). "GABA agonists and omega conotoxin GVIA modulate responses to nerve activation of the perfused rat mesentery." Life Sci **48**(24): 2331-2339.

Lifshitz, J. and A. M. Lisembee (2012). "Neurodegeneration in the somatosensory cortex after experimental diffuse brain injury." Brain Struct Funct **217**(1): 49-61.

Lim, D., L. Fedrizzi, M. Tartari, C. Zuccato, E. Cattaneo, M. Brini and E. Carafoli (2008). "Calcium homeostasis and mitochondrial dysfunction in striatal neurons of Huntington disease." J Biol Chem **283**(9): 5780-5789.

Lim, D. H., M. H. Mohajerani, J. Ledue, J. Boyd, S. Chen and T. H. Murphy (2012). "In vivo Large-Scale Cortical Mapping Using Channelrhodopsin-2 Stimulation in Transgenic Mice Reveals Asymmetric and Reciprocal Relationships between Cortical Areas." Front Neural Circuits **6**: 11.

Lin, Y., S. I. McDonough and D. Lipscombe (2004). "Alternative splicing in the voltage-sensing region of N-Type $Ca_V2.2$ channels modulates channel kinetics." J Neurophysiol **92**(5): 2820-2830.

Lin, Z., S. Haus, J. Edgerton and D. Lipscombe (1997). "Identification of functionally distinct isoforms of the N-type Ca^{2+} channel in rat sympathetic ganglia and brain." Neuron **18**(1): 153-166.

Lin, Z., Y. Lin, S. Schorge, J. Q. Pan, M. Beierlein and D. Lipscombe (1999). "Alternative splicing of a short cassette exon in α_{1B} generates functionally distinct N-type calcium channels in central and peripheral neurons." J Neurosci **19**(13): 5322-5331.

Link, S., M. Meissner, B. Held, A. Beck, P. Weissgerber, M. Freichel and V. Flockerzi (2009). "Diversity and developmental expression of L-type calcium channel β2 proteins and their influence on calcium current in murine heart." J Biol Chem **284**(44): 30129-30137.

Lipscombe, D., A. Andrade and S. E. Allen (2013). "Alternative splicing: functional diversity among voltage-gated calcium channels and behavioral consequences." Biochim Biophys Acta **1828**(7): 1522-1529.

Lipscombe, D., T. D. Helton and W. Xu (2004). "L-type calcium channels: the low down." J Neurophysiol **92**(5): 2633-2641.

Lipscombe, D., J. Q. Pan and A. C. Gray (2002). "Functional diversity in neuronal voltage-gated calcium channels by alternative splicing of $Ca_V\alpha_1$." Mol Neurobiol **26**(1): 21-44.

Liu, J., L. Chang, Y. Song, H. Li and Y. Wu (2019). "The Role of NMDA Receptors in Alzheimer's Disease." Front Neurosci **13**: 43.

Liu, X., P. S. Yang, W. Yang and D. T. Yue (2010). "Enzyme-inhibitor-like tuning of Ca^{2+} channel connectivity with calmodulin." Nature **463**(7283): 968-972.

Llinas, R., M. Sugimori and R. B. Silver (1992). "Microdomains of high calcium concentration in a presynaptic terminal." Science **256**(5057): 677-679.

Loane, D. J., P. A. Lima and N. V. Marrion (2007). "Co-assembly of N-type Ca^{2+} and BK channels underlies functional coupling in rat brain." J Cell Sci **120**(Pt 6): 985-995.

Lopez, A. and J. Birks (2001). "Nimodipine for primary degenerative, mixed and vascular dementia." Cochrane Database Syst Rev(1): CD000147.

Lopez, J. R., A. Lyckman, S. Oddo, F. M. Laferla, H. W. Querfurth and A. Shtifman (2008). "Increased intraneuronal resting [Ca^{2+}] in adult Alzheimer's disease mice." J Neurochem **105**(1): 262-271.

Lu, A. T., X. Dai, J. A. Martinez-Agosto and R. M. Cantor (2012). "Support for calcium channel gene defects in autism spectrum disorders." Mol Autism **3**(1): 18.

Lu, Q., M. S. AtKisson, S. E. Jarvis, Z. P. Feng, G. W. Zamponi and K. Dunlap (2001). "Syntaxin 1A supports voltage-dependent inhibition of α_{1B} Ca^{2+} channels by Gβγ in chick sensory neurons." J Neurosci **21**(9): 2949-2957.

Lu, S. G., X. L. Zhang, D. Z. Luo and M. S. Gold (2010). "Persistent inflammation alters the density and distribution of voltage-activated calcium channels in subpopulations of rat cutaneous DRG neurons." Pain **151**(3): 633-643.

Luebke, J. I., K. Dunlap and T. J. Turner (1993). "Multiple calcium channel types control glutamatergic synaptic transmission in the hippocampus." Neuron **11**(5): 895-902.

Lukyanetz, E. A., V. M. Shkryl and P. G. Kostyuk (2002). "Selective blockade of N-type calcium channels by levetiracetam." Epilepsia **43**(1): 9-18.

Luo, H., K. Hasegawa, M. Liu and W. J. Song (2017). "Comparison of the Upper Marginal Neurons of Cortical Layer 2 with Layer 2/3 Pyramidal Neurons in Mouse Temporal Cortex." Front Neuroanat **11**: 115.

MacDougall, G., R. S. Anderton, F. L. Mastaglia, N. W. Knuckey and B. P. Meloni (2019). "Mitochondria and neuroprotection in stroke: Cationic arginine-rich peptides (CARPs) as a novel class of mitochondria-targeted neuroprotective therapeutics." Neurobiol Dis **121**: 17-33.

MacDougall, G., R. S. Anderton, A. Trimble, F. L. Mastaglia, N. W. Knuckey and B. P. Meloni (2020). "Poly-arginine-18 (R18) Confers Neuroprotection through Glutamate

Receptor Modulation, Intracellular Calcium Reduction, and Preservation of Mitochondrial Function." Molecules **25**(13).

MacManus, A., M. Ramsden, M. Murray, Z. Henderson, H. A. Pearson and V. A. Campbell (2000). "Enhancement of $^{45}Ca^{2+}$ influx and voltage-dependent Ca^{2+} channel activity by β-amyloid-(1-40) in rat cortical synaptosomes and cultured cortical neurons. Modulation by the proinflammatory cytokine interleukin-1β." J Biol Chem **275**(7): 4713-4718.

Magga, J. M., S. E. Jarvis, M. I. Arnot, G. W. Zamponi and J. E. Braun (2000). "Cysteine string protein regulates G protein modulation of N-type calcium channels." Neuron **28**(1): 195-204.

Maggi, C. A., S. Giuliani, P. Santicioli, M. Tramontana and A. Meli (1990). "Effect of omega conotoxin on reflex responses mediated by activation of capsaicin-sensitive nerves of the rat urinary bladder and peptide release from the rat spinal cord." Neuroscience **34**(1): 243-250.

Maggi, C. A., M. Tramontana, R. Cecconi and P. Santicioli (1990). "Neurochemical evidence for the involvement of N-type calcium channels in transmitter secretion from peripheral endings of sensory nerves in guinea pigs." Neurosci Lett **114**(2): 203-206.

Mandelbaum, G., J. Taranda, T. M. Haynes, D. R. Hochbaum, K. W. Huang, M. Hyun, K. Umadevi Venkataraju, C. Straub, W. Wang, K. Robertson, P. Osten and B. L. Sabatini (2019). "Distinct Cortical-Thalamic-Striatal Circuits through the Parafascicular Nucleus." Neuron **102**(3): 636-652 e637.

Mangoni, M. E., B. Couette, E. Bourinet, J. Platzer, D. Reimer, J. Striessnig and J. Nargeot (2003). "Functional role of L-type $Ca_V1.3$ Ca^{2+} channels in cardiac pacemaker activity." Proc Natl Acad Sci U S A **100**(9): 5543-5548.

Manita, S., T. Suzuki, C. Homma, T. Matsumoto, M. Odagawa, K. Yamada, K. Ota, C. Matsubara, A. Inutsuka, M. Sato, M. Ohkura, A. Yamanaka, Y. Yanagawa, J. Nakai, Y. Hayashi, M. E. Larkum and M. Murayama (2015). "A Top-Down Cortical Circuit for Accurate Sensory Perception." Neuron **86**(5): 1304-1316.

Mao, T., D. Kusefoglu, B. M. Hooks, D. Huber, L. Petreanu and K. Svoboda (2011). "Long-range neuronal circuits underlying the interaction between sensory and motor cortex." Neuron **72**(1): 111-123.

Marambaud, P., U. Dreses-Werringloer and V. Vingtdeux (2009). "Calcium signaling in neurodegeneration." Mol Neurodegener **4**: 20.

Marangoudakis, S., A. Andrade, T. D. Helton, S. Denome, A. J. Castiglioni and D. Lipscombe (2012). "Differential ubiquitination and proteasome regulation of $Ca_V2.2$ N-type channel splice isoforms." J Neurosci **32**(30): 10365-10369.

Martinez, J., I. Moeller, H. Erdjument-Bromage, P. Tempst and B. Lauring (2003). "Parkinson's disease-associated α-synuclein is a calmodulin substrate." J Biol Chem **278**(19): 17379-17387.

Mattson, M. P. (2004). "Pathways towards and away from Alzheimer's disease." Nature **430**(7000): 631-639.

Mattson, M. P. (2007). "Calcium and neurodegeneration." Aging Cell **6**(3): 337-350.

Mattson, M. P., B. Cheng, D. Davis, K. Bryant, I. Lieberburg and R. E. Rydel (1992). "β-Amyloid peptides destabilize calcium homeostasis and render human cortical neurons vulnerable to excitotoxicity." J Neurosci **12**(2): 376-389.

Mattson, M. P. and T. Magnus (2006). "Ageing and neuronal vulnerability." Nat Rev Neurosci **7**(4): 278-294.

Mattson, M. P., W. A. Pedersen, W. Duan, C. Culmsee and S. Camandola (1999). "Cellular and molecular mechanisms underlying perturbed energy metabolism and neuronal degeneration in Alzheimer's and Parkinson's diseases." Ann N Y Acad Sci **893**: 154-175.

Matyas, F., V. Sreenivasan, F. Marbach, C. Wacongne, B. Barsy, C. Mateo, R. Aronoff and C. C. Petersen (2010). "Motor control by sensory cortex." Science **330**(6008): 1240-1243.

McCleskey, E. W., A. P. Fox, D. Feldman and R. W. Tsien (1986). "Different types of calcium channels." J Exp Biol **124**: 177-190.

McCue, J. T. (2009). "Theory and use of hydrophobic interaction chromatography in protein purification applications." Methods Enzymol **463**: 405-414.

McGivern, J. G. (2007). "Ziconotide: a review of its pharmacology and use in the treatment of pain." Neuropsychiatr Dis Treat **3**(1): 69-85.

McGivern, J. G. and S. I. McDonough (2004). "Voltage-gated calcium channels as targets for the treatment of chronic pain." Curr Drug Targets CNS Neurol Disord **3**(6): 457-478.

Meir, A., D. C. Bell, G. J. Stephens, K. M. Page and A. C. Dolphin (2000). "Calcium channel β subunit promotes voltage-dependent modulation of α1B by Gβγ." Biophys J **79**(2): 731-746.

Meir, A., S. Ginsburg, A. Butkevich, S. G. Kachalsky, I. Kaiserman, R. Ahdut, S. Demirgoren and R. Rahamimoff (1999). "Ion channels in presynaptic nerve terminals and control of transmitter release." Physiol Rev **79**(3): 1019-1088.

Melachroinou, K., M. Xilouri, E. Emmanouilidou, R. Masgrau, P. Papazafiri, L. Stefanis and K. Vekrellis (2013). "Deregulation of calcium homeostasis mediates secreted α-synuclein-induced neurotoxicity." Neurobiol Aging **34**(12): 2853-2865.

Mellstrom, B., M. Savignac, R. Gomez-Villafuertes and J. R. Naranjo (2008). "Ca^{2+}-operated transcriptional networks: molecular mechanisms and in vivo models." Physiol Rev **88**(2): 421-449.

Meloni, B. P., F. L. Mastaglia and N. W. Knuckey (2020). "Cationic Arginine-Rich Peptides (CARPs): A Novel Class of Neuroprotective Agents With a Multimodal Mechanism of Action." Front Neurol **11**: 108.

Meloni, B. P., D. Milani, A. B. Edwards, R. S. Anderton, R. L. O'Hare Doig, M. Fitzgerald, T. N. Palmer and N. W. Knuckey (2015). "Neuroprotective peptides fused to arginine-rich cell penetrating peptides: Neuroprotective mechanism likely mediated by peptide endocytic properties." Pharmacol Ther **153**: 36-54.

Mencacci, N. E., L. R'Bibo, S. Bandres-Ciga, M. Carecchio, G. Zorzi, N. Nardocci, B. Garavaglia, A. Batla, K. P. Bhatia, A. M. Pittman, J. Hardy, A. Weissbach, C. Klein, T. Gasser, E. Lohmann and N. W. Wood (2015). "The CACNA1B R1389H variant is not associated with myoclonus-dystonia in a large European multicentric cohort." Hum Mol Genet **24**(18): 5326-5329.

Meng, E. C., T. D. Goddard, E. F. Pettersen, G. S. Couch, Z. J. Pearson, J. H. Morris and T. E. Ferrin (2023). "UCSF ChimeraX: Tools for structure building and analysis." Protein Sci **32**(11): e4792.

Meng, X. Y., H. X. Zhang, M. Mezei and M. Cui (2011). "Molecular docking: a powerful approach for structure-based drug discovery." Curr Comput Aided Drug Des **7**(2): 146-157.

Messing, L., J. M. Decker, M. Joseph, E. Mandelkow and E. M. Mandelkow (2013). "Cascade of tau toxicity in inducible hippocampal brain slices and prevention by aggregation inhibitors." Neurobiol Aging **34**(5): 1343-1354.

Meuth, S. G., N. Melzer, C. Kleinschnitz, T. Budde and H. Wiendl (2009). "[Multiple sclerosis -- a channelopathy? Targeting ion channels and transporters in inflammatory neurodegeneration]." Nervenarzt **80**(4): 422-429.

Mezler, M., S. Barghorn, H. Schoemaker, G. Gross and V. Nimmrich (2012). "A β-amyloid oligomer directly modulates P/Q-type calcium currents in Xenopus oocytes." Br J Pharmacol **165**(5): 1572-1583.

Michailidis, I. E., K. Abele-Henckels, W. K. Zhang, B. Lin, Y. Yu, L. S. Geyman, M. D. Ehlers, E. A. Pnevmatikakis and J. Yang (2014). "Age-related homeostatic midchannel proteolysis of neuronal L-type voltage-gated Ca^{2+} channels." Neuron **82**(5): 1045-1057.

Milani, D., M. C. Bakeberg, J. L. Cross, V. W. Clark, R. S. Anderton, D. J. Blacker, N. W. Knuckey and B. P. Meloni (2018). "Comparison of neuroprotective efficacy of poly-arginine R18 and R18D (D-enantiomer) peptides following permanent middle cerebral artery occlusion in the Wistar rat and in vitro toxicity studies." PLoS One **13**(3): e0193884.

Mintz, I. M., B. L. Sabatini and W. G. Regehr (1995). "Calcium control of transmitter release at a cerebellar synapse." Neuron **15**(3): 675-688.

Mintz, I. M., V. J. Venema, K. M. Swiderek, T. D. Lee, B. P. Bean and M. E. Adams (1992). "P-type calcium channels blocked by the spider toxin ω-Aga-IVA." Nature **355**(6363): 827-829.

Miranda-Laferte, E., D. Ewers, R. E. Guzman, N. Jordan, S. Schmidt and P. Hidalgo (2014). "The N-terminal domain tethers the voltage-gated calcium channel β_{2e}-subunit to the plasma membrane via electrostatic and hydrophobic interactions." J Biol Chem **289**(15): 10387-10398.

Mo, C. and S. M. Sherman (2019). "A Sensorimotor Pathway via Higher-Order Thalamus." J Neurosci **39**(4): 692-704.

Mochida, S., Z. H. Sheng, C. Baker, H. Kobayashi and W. A. Catterall (1996). "Inhibition of neurotransmission by peptides containing the synaptic protein interaction site of N-type Ca^{2+} channels." Neuron **17**(4): 781-788.

Mohajerani, M. H., A. W. Chan, M. Mohsenvand, J. LeDue, R. Liu, D. A. McVea, J. D. Boyd, Y. T. Wang, M. Reimers and T. H. Murphy (2013). "Spontaneous cortical activity alternates between motifs defined by regional axonal projections." Nat Neurosci **16**(10): 1426-1435.

Mori, Y., M. Nishida, S. Shimizu, M. Ishii, T. Yoshinaga, M. Ino, K. Sawada and T. Niidome (2002). "Ca^{2+} channel α_{1B} subunit ($Ca_V2.2$) knockout mouse reveals a predominant role of N-type channels in the sympathetic regulation of the circulatory system." Trends Cardiovasc Med **12**(6): 270-275.

Mosmann, T. (1983). "Rapid colorimetric assay for cellular growth and survival: application to proliferation and cytotoxicity assays." J Immunol Methods **65**(1-2): 55-63.

Moss, F. J., P. Viard, A. Davies, F. Bertaso, K. M. Page, A. Graham, C. Canti, M. Plumpton, C. Plumpton, J. J. Clare and A. C. Dolphin (2002). "The novel product of a five-exon stargazin-related gene abolishes $Ca_V2.2$ calcium channel expression." EMBO J **21**(7): 1514-1523.

Mota, S. I., I. L. Ferreira and A. C. Rego (2014). "Dysfunctional synapse in Alzheimer's disease - A focus on NMDA receptors." Neuropharmacology **76 Pt A**: 16-26.

Motomura, M., B. Lang, I. Johnston, J. Palace, A. Vincent and J. Newsom-Davis (1997). "Incidence of serum anti-P/O-type and anti-N-type calcium channel autoantibodies in the Lambert-Eaton myasthenic syndrome." J Neurol Sci **147**(1): 35-42.

Moutal, A., Y. Wang, X. Yang, Y. Ji, S. Luo, A. Dorame, S. S. Bellampalli, L. A. Chew, S. Cai, E. T. Dustrude, J. E. Keener, M. T. Marty, T. W. Vanderah and R. Khanna (2017). "Dissecting the role of the CRMP2-neurofibromin complex on pain behaviors." Pain **158**(11): 2203-2221.

Moyer, J. R., Jr., L. T. Thompson, J. P. Black and J. F. Disterhoft (1992). "Nimodipine increases excitability of rabbit CA1 pyramidal neurons in an age- and concentration-dependent manner." J Neurophysiol **68**(6): 2100-2109.

Mullan, M., F. Crawford, K. Axelman, H. Houlden, L. Lilius, B. Winblad and L. Lannfelt (1992). "A pathogenic mutation for probable Alzheimer's disease in the APP gene at the N-terminus of β-amyloid." Nat Genet **1**(5): 345-347.

Muller, C. S., A. Haupt, W. Bildl, J. Schindler, H. G. Knaus, M. Meissner, B. Rammner, J. Striessnig, V. Flockerzi, B. Fakler and U. Schulte (2010). "Quantitative proteomics of the Cav2 channel nano-environments in the mammalian brain." Proc Natl Acad Sci U S A **107**(34): 14950-14957.

Murakami, M., O. Nakagawasai, S. Fujii, K. Kameyama, S. Murakami, S. Hozumi, A. Esashi, R. Taniguchi, T. Yanagisawa, K. Tan-no, T. Tadano, K. Kitamura and K. Kisara (2001). "Antinociceptive action of amlodipine blocking N-type Ca^{2+} channels at the primary afferent neurons in mice." Eur J Pharmacol **419**(2-3): 175-181.

Murali, S. S., I. A. Napier, S. A. Mohammadi, P. F. Alewood, R. J. Lewis and M. J. Christie (2015). "High-voltage-activated calcium current subtypes in mouse DRG neurons adapt in a subpopulation-specific manner after nerve injury." J Neurophysiol **113**(5): 1511-1519.

Murchison, D., L. S. Dove, L. C. Abbott and W. H. Griffith (2002). "Homeostatic compensation maintains Ca^{2+} signaling functions in Purkinje neurons in the leaner mutant mouse." Cerebellum **1**(2): 119-127.

Murchison, D. and W. H. Griffith (2007). "Calcium buffering systems and calcium signaling in aged rat basal forebrain neurons." Aging Cell **6**(3): 297-305.

Nakai, J., N. Sekiguchi, T. A. Rando, P. D. Allen and K. G. Beam (1998). "Two regions of the ryanodine receptor involved in coupling with L-type Ca^{2+} channels." J Biol Chem **273**(22): 13403-13406.

Nakamura, Y., H. Harada, N. Kamasawa, K. Matsui, J. S. Rothman, R. Shigemoto, R. A. Silver, D. A. DiGregorio and T. Takahashi (2015). "Nanoscale distribution of presynaptic Ca^{2+} channels and its impact on vesicular release during development." Neuron **85**(1): 145-158.

Narain, S., L. Al-Khoury and E. Chang (2015). "Resolution of chronic migraine headaches with intrathecal ziconotide: a case report." J Pain Res **8**: 603-606.

Neely, A., J. Garcia-Olivares, S. Voswinkel, H. Horstkott and P. Hidalgo (2004). "Folding of active calcium channel β_{1b}-subunit by size-exclusion chromatography and its role on channel function." J Biol Chem **279**(21): 21689-21694.

Neubarth, N. L., A. J. Emanuel, Y. Liu, M. W. Springel, A. Handler, Q. Zhang, B. P. Lehnert, C. Guo, L. L. Orefice, A. Abdelaziz, M. M. DeLisle, M. Iskols, J. Rhyins, S. J. Kim, S. J. Cattel, W. Regehr, C. D. Harvey, J. Drugowitsch and D. D. Ginty (2020). "Meissner corpuscles and their spatially intermingled afferents underlie gentle touch perception." Science **368**(6497).

Newcomb, R., T. J. Abbruscato, T. Singh, L. Nadasdi, T. P. Davis and G. Miljanich (2000). "Bioavailability of Ziconotide in brain: influx from blood, stability, and diffusion." Peptides **21**(4): 491-501.

Newcomb, R., B. Szoke, A. Palma, G. Wang, X. Chen, W. Hopkins, R. Cong, J. Miller, L. Urge, K. Tarczy-Hornoch, J. A. Loo, D. J. Dooley, L. Nadasdi, R. W. Tsien, J. Lemos and G. Miljanich (1998). "Selective peptide antagonist of the class E calcium channel from the venom of the tarantula Hysterocrates gigas." Biochemistry **37**(44): 15353-15362.

Newton, P. M. and R. O. Messing (2009). "The N-type calcium channel is a novel target for treating alcohol use disorders." Channels (Austin) **3**(2): 77-81.

Newton, P. M., C. J. Orr, M. J. Wallace, C. Kim, H. S. Shin and R. O. Messing (2004). "Deletion of N-type calcium channels alters ethanol reward and reduces ethanol consumption in mice." J Neurosci **24**(44): 9862-9869.

Nieto-Rostro, M., K. Ramgoolam, W. S. Pratt, A. Kulik and A. C. Dolphin (2018). "Ablation of $\alpha_2\delta$-1 inhibits cell-surface trafficking of endogenous N-type calcium channels in the pain pathway in vivo." Proc Natl Acad Sci U S A **115**(51): E12043-E12052.

Niidome, T., M. S. Kim, T. Friedrich and Y. Mori (1992). "Molecular cloning and characterization of a novel calcium channel from rabbit brain." FEBS Lett **308**(1): 7-13.

Nimmrich, V., C. Grimm, A. Draguhn, S. Barghorn, A. Lehmann, H. Schoemaker, H. Hillen, G. Gross, U. Ebert and C. Bruehl (2008). "Amyloid beta oligomers ($A\beta_{1-42}$ globulomer) suppress spontaneous synaptic activity by inhibition of P/Q-type calcium currents." J Neurosci **28**(4): 788-797.

Norris, C. M., E. M. Blalock, K. C. Chen, N. M. Porter, O. Thibault, S. D. Kraner and P. W. Landfield (2010). "Hippocampal 'zipper' slice studies reveal a necessary role for calcineurin in the increased activity of L-type Ca^{2+} channels with aging." Neurobiol Aging **31**(2): 328-338.

Norris, C. M., S. Halpain and T. C. Foster (1998). "Reversal of age-related alterations in synaptic plasticity by blockade of L-type Ca^{2+} channels." J Neurosci **18**(9): 3171-3179.

Nowycky, M. C., A. P. Fox and R. W. Tsien (1985). "Three types of neuronal calcium channel with different calcium agonist sensitivity." Nature **316**(6027): 440-443.

Numa, S., T. Tanabe, H. Takeshima, A. Mikami, T. Niidome, S. Nishimura, B. A. Adams and K. G. Beam (1990). "Molecular insights into excitation-contraction coupling." Cold Spring Harb Symp Quant Biol **55**: 1-7.

Oikonomou, K. D., E. J. Donzis, M. T. N. Bui, C. Cepeda and M. S. Levine (2021). "Calcium dysregulation and compensation in cortical pyramidal neurons of the R6/2 mouse model of Huntington's disease." J Neurophysiol **126**(4): 1159-1171.

Olivera, B. M., L. J. Cruz, V. de Santos, G. W. LeCheminant, D. Griffin, R. Zeikus, J. M. McIntosh, R. Galyean, J. Varga, W. R. Gray and et al. (1987). "Neuronal calcium channel antagonists. Discrimination between calcium channel subtypes using omega-conotoxin from Conus magus venom." Biochemistry **26**(8): 2086-2090.

Olivera, B. M., J. M. McIntosh, L. J. Cruz, F. A. Luque and W. R. Gray (1984). "Purification and sequence of a presynaptic peptide toxin from Conus geographus venom." Biochemistry **23**(22): 5087-5090.

Olivera, B. M., G. P. Miljanich, J. Ramachandran and M. E. Adams (1994). "Calcium channel diversity and neurotransmitter release: the ω-conotoxins and ω-agatoxins." Annu Rev Biochem **63**: 823-867.

Olson, W., P. Dong, M. Fleming and W. Luo (2016). "The specification and wiring of mammalian cutaneous low-threshold mechanoreceptors." Wiley Interdiscip Rev Dev Biol **5**(3): 389-404.

Ophoff, R. A., G. M. Terwindt, M. N. Vergouwe, R. van Eijk, P. J. Oefner, S. M. Hoffman, J. E. Lamerdin, H. W. Mohrenweiser, D. E. Bulman, M. Ferrari, J. Haan, D. Lindhout, G. J. van Ommen, M. H. Hofker, M. D. Ferrari and R. R. Frants (1996). "Familial hemiplegic migraine and episodic ataxia type-2 are caused by mutations in the Ca^{2+} channel gene CACNL1A4." Cell **87**(3): 543-552.

Ortner, N. J. (2021). "Voltage-Gated Ca^{2+} Channels in Dopaminergic Substantia Nigra Neurons: Therapeutic Targets for Neuroprotection in Parkinson's Disease?" Front Synaptic Neurosci **13**: 636103.

Ortner, N. J. and J. Striessnig (2016). "L-type calcium channels as drug targets in CNS disorders." Channels (Austin) **10**(1): 7-13.

Ostacher, M. J., D. V. Iosifescu, A. Hay, S. R. Blumenthal, P. Sklar and R. H. Perlis (2014). "Pilot investigation of isradipine in the treatment of bipolar depression motivated by genome-wide association." Bipolar Disord **16**(2): 199-203.

Page, K. M., C. Canti, G. J. Stephens, N. S. Berrow and A. C. Dolphin (1998). "Identification of the amino terminus of neuronal Ca^{2+} channel α1 subunits α1B and α1E as an essential determinant of G-protein modulation." J Neurosci **18**(13): 4815-4824.

Pan, H. L., Z. Z. Wu, H. Y. Zhou, S. R. Chen, H. M. Zhang and D. P. Li (2008). "Modulation of pain transmission by G-protein-coupled receptors." Pharmacol Ther **117**(1): 141-161.

Pan, J. Q. and D. Lipscombe (2000). "Alternative splicing in the cytoplasmic II-III loop of the N-type Ca channel α_{1B} subunit: functional differences are β subunit-specific." J Neurosci **20**(13): 4769-4775.

Pan, X., Z. Li, X. Huang, G. Huang, S. Gao, H. Shen, L. Liu, J. Lei and N. Yan (2019). "Molecular basis for pore blockade of human Na^+ channel $Na_V1.2$ by the μ-conotoxin KIIIA." Science **363**(6433): 1309-1313.

Pangrsic, T., J. H. Singer and A. Koschak (2018). "Voltage-Gated Calcium Channels: Key Players in Sensory Coding in the Retina and the Inner Ear." Physiol Rev **98**(4): 2063-2096.

Pardo, N. E., R. K. Hajela and W. D. Atchison (2006). "Acetylcholine release at neuromuscular junctions of adult tottering mice is controlled by N-($Ca_V2.2$) and R-type ($Ca_V2.3$) but not L-type ($Ca_V1.2$) Ca^{2+} channels." J Pharmacol Exp Ther **319**(3): 1009-1020.

Paris, D., C. Bachmeier, N. Patel, A. Quadros, C. H. Volmar, V. Laporte, J. Ganey, D. Beaulieu-Abdelahad, G. Ait-Ghezala, F. Crawford and M. J. Mullan (2011). "Selective antihypertensive dihydropyridines lower Aβ accumulation by targeting both the production and the clearance of Aβ across the blood-brain barrier." Mol Med **17**(3-4): 149-162.

Patel, R., C. S. Bauer, M. Nieto-Rostro, W. Margas, L. Ferron, K. Chaggar, K. Crews, J. D. Ramirez, D. L. Bennett, A. Schwartz, A. H. Dickenson and A. C. Dolphin (2013). "$\alpha_2\delta$-1 gene deletion affects somatosensory neuron function and delays mechanical hypersensitivity in response to peripheral nerve damage." J Neurosci **33**(42): 16412-16426.

Perez-Pinzon, M. A., M. A. Yenari, G. H. Sun, D. M. Kunis and G. K. Steinberg (1997). "SNX-111, a novel, presynaptic N-type calcium channel antagonist, is neuroprotective against focal cerebral ischemia in rabbits." J Neurol Sci **153**(1): 25-31.

Perez-Reyes, E., L. L. Cribbs, A. Daud, A. E. Lacerda, J. Barclay, M. P. Williamson, M. Fox, M. Rees and J. H. Lee (1998). "Molecular characterization of a neuronal low-voltage-activated T-type calcium channel." Nature **391**(6670): 896-900.

Perez-Reyes, E., J. H. Lee and L. L. Cribbs (1999). "Molecular characterization of two members of the T-type calcium channel family." Ann N Y Acad Sci **868**: 131-143.

Peterson, B. Z., J. S. Lee, J. G. Mulle, Y. Wang, M. de Leon and D. T. Yue (2000). "Critical determinants of Ca^{2+}-dependent inactivation within an EF-hand motif of L-type Ca^{2+} channels." Biophys J **78**(4): 1906-1920.

Pettersen, E. F., T. D. Goddard, C. C. Huang, G. S. Couch, D. M. Greenblatt, E. C. Meng and T. E. Ferrin (2004). "UCSF Chimera--a visualization system for exploratory research and analysis." J Comput Chem **25**(13): 1605-1612.

Pichler, M., T. N. Cassidy, D. Reimer, H. Haase, R. Kraus, D. Ostler and J. Striessnig (1997). "β subunit heterogeneity in neuronal L-type Ca^{2+} channels." J Biol Chem **272**(21): 13877-13882.

Pieri, M., S. Caioli, N. Canu, N. B. Mercuri, E. Guatteo and C. Zona (2013). "Over-expression of N-type calcium channels in cortical neurons from a mouse model of Amyotrophic Lateral Sclerosis." Exp Neurol **247**: 349-358.

Pierrot, N., P. Ghisdal, A. S. Caumont and J. N. Octave (2004). "Intraneuronal amyloid-β1-42 production triggered by sustained increase of cytosolic calcium concentration induces neuronal death." J Neurochem **88**(5): 1140-1150.

Pierrot, N., S. F. Santos, C. Feyt, M. Morel, J. P. Brion and J. N. Octave (2006). "Calcium-mediated transient phosphorylation of tau and amyloid precursor protein followed by intraneuronal amyloid-β accumulation." J Biol Chem **281**(52): 39907-39914.

Pietrobon, D. (2005). "Function and dysfunction of synaptic calcium channels: insights from mouse models." Curr Opin Neurobiol **15**(3): 257-265.

Pietrobon, D. (2010). "$Ca_V2.1$ channelopathies." Pflugers Arch **460**(2): 375-393.

Pitake, S., L. J. Middleton, I. Abdus-Saboor and S. K. Mishra (2019). "Inflammation Induced Sensory Nerve Growth and Pain Hypersensitivity Requires the N-Type Calcium Channel Cav2.2." Front Neurosci **13**: 1009.

Plant, L. D., J. P. Boyle, I. F. Smith, C. Peers and H. A. Pearson (2003). "The production of amyloid β peptide is a critical requirement for the viability of central neurons." J Neurosci **23**(13): 5531-5535.

Post, J., V. Kogel, A. Schaffrath, P. Lohmann, N. J. Shah, K. J. Langen, D. Willbold, A. Willuweit and J. Kutzsche (2021). "A Novel Anti-Inflammatory D-Peptide Inhibits Disease Phenotype Progression in an ALS Mouse Model." Molecules **26**(6).

Post, J., A. Schaffrath, I. Gering, S. Hartwig, S. Lehr, N. J. Shah, K. J. Langen, D. Willbold, J. Kutzsche and A. Willuweit (2021). "Oral Treatment with RD2RD2 Impedes Development of Motoric Phenotype and Delays Symptom Onset in $SOD1^{G93A}$ Transgenic Mice." Int J Mol Sci **22**(13).

Powers, P. A., S. Liu, K. Hogan and R. G. Gregg (1992). "Skeletal muscle and brain isoforms of a beta-subunit of human voltage-dependent calcium channels are encoded by a single gene." J Biol Chem **267**(32): 22967-22972.

Price, S. A., B. Held and H. A. Pearson (1998). "Amyloid beta protein increases Ca2+ currents in rat cerebellar granule neurones." Neuroreport **9**(3): 539-545.

Prihar, G., A. Verkkoniem, J. Perez-Tur, R. Crook, S. Lincoln, H. Houlden, M. Somer, A. Paetau, H. Kalimo, A. Grover, L. Myllykangas, M. Hutton, J. Hardy and M. Haltia (1999). "Alzheimer disease PS-1 exon 9 deletion defined." Nat Med **5**(10): 1090.

Puri, B. K. (2020). "Calcium Signaling and Gene Expression." Adv Exp Med Biol **1131**: 537-545.

Puzianowska-Kuznicka, M. and J. Kuznicki (2009). "The ER and ageing II: calcium homeostasis." Ageing Res Rev **8**(3): 160-172.

Qian, H., T. Patriarchi, J. L. Price, L. Matt, B. Lee, M. Nieves-Cintron, O. R. Buonarati, D. Chowdhury, E. Nanou, M. A. Nystoriak, W. A. Catterall, M. Poomvanicha, F. Hofmann, M. F. Navedo and J. W. Hell (2017). "Phosphorylation of Ser^{1928} mediates the enhanced activity of the L-type Ca^{2+} channel $Ca_V1.2$ by the β_2-adrenergic receptor in neurons." Sci Signal **10**(463).

Qian, J. and J. L. Noebels (2000). "Presynaptic Ca^{2+} influx at a mouse central synapse with Ca^{2+} channel subunit mutations." J Neurosci **20**(1): 163-170.

Qin, N., D. Platano, R. Olcese, E. Stefani and L. Birnbaumer (1997). "Direct interaction of Gβγ with a C-terminal Gβγ-binding domain of the Ca^{2+} channel α1 subunit is responsible for channel inhibition by G protein-coupled receptors." Proc Natl Acad Sci U S A **94**(16): 8866-8871.

Querfurth, H. W. and D. J. Selkoe (1994). "Calcium ionophore increases amyloid β peptide production by cultured cells." Biochemistry **33**(15): 4550-4561.

Quiquempoix, M., S. L. Fayad, K. Boutourlinsky, N. Leresche, R. C. Lambert and T. Bessaih (2018). "Layer 2/3 Pyramidal Neurons Control the Gain of Cortical Output." Cell Rep **24**(11): 2799-2807 e2794.

Radwani, H., M. J. Lopez-Gonzalez, D. Cattaert, O. Roca-Lapirot, E. Dobremez, R. Bouali-Benazzouz, E. Eiriksdottir, U. Langel, A. Favereaux, M. Errami, M. Landry and P. Fossat (2016). "Cav1.2 and Cav1.3 L-type calcium channels independently control short- and long-term sensitization to pain." J Physiol **594**(22): 6607-6626.

Raghib, A., F. Bertaso, A. Davies, K. M. Page, A. Meir, Y. Bogdanov and A. C. Dolphin (2001). "Dominant-negative synthesis suppression of voltage-gated calcium channel $Ca_V2.2$ induced by truncated constructs." J Neurosci **21**(21): 8495-8504.

Raingo, J., A. J. Castiglioni and D. Lipscombe (2007). "Alternative splicing controls G protein-dependent inhibition of N-type calcium channels in nociceptors." Nat Neurosci **10**(3): 285-292.

Rajagopal, S., H. Fang, C. Lynch, 3rd, J. J. Sando and G. L. Kamatchi (2011). "Effects of isoflurane on the expressed $Ca_V2.2$ currents in *Xenopus* oocytes depend on the activation of protein kinase Cδ and its phosphorylation sites in the $Ca_V2.2\alpha_1$ subunits." Neuroscience **182**: 232-240.

Rajagopal, S., B. L. Fields, B. K. Burton, C. On, A. A. Reeder and G. L. Kamatchi (2014). "Inhibition of protein kinase C (PKC) response of voltage-gated calcium (Ca_V)2.2 channels expressed in *Xenopus* oocytes by $Ca_V\beta$ subunits." Neuroscience **280**: 1-9.

Ramirez, D., W. Gonzalez, R. A. Fissore and I. Carvacho (2017). "Conotoxins as Tools to Understand the Physiological Function of Voltage-Gated Calcium (Ca_V) Channels." Mar Drugs **15**(10).

Ramsden, M., Z. Henderson and H. A. Pearson (2002). "Modulation of Ca^{2+} channel currents in primary cultures of rat cortical neurones by amyloid β protein (1-40) is dependent on solubility status." Brain Res **956**(2): 254-261.

Rash, B. G., J. B. Ackman and P. Rakic (2016). "Bidirectional radial Ca^{2+} activity regulates neurogenesis and migration during early cortical column formation." Sci Adv **2**(2): e1501733.

Raymond, L. A. (2017). "Striatal synaptic dysfunction and altered calcium regulation in Huntington disease." Biochem Biophys Res Commun **483**(4): 1051-1062.

Reep, R. L. and J. V. Corwin (1999). "Topographic organization of the striatal and thalamic connections of rat medial agranular cortex." Brain Res **841**(1-2): 43-52.

Reep, R. L., G. S. Goodwin and J. V. Corwin (1990). "Topographic organization in the corticocortical connections of medial agranular cortex in rats." J Comp Neurol **294**(2): 262-280.

Reid, C. A., J. M. Bekkers and J. D. Clements (2003). "Presynaptic Ca^{2+} channels: a functional patchwork." Trends Neurosci **26**(12): 683-687.

Ren, C. and T. Komiyama (2021). "Wide-field calcium imaging of cortex-wide activity in awake, head-fixed mice." STAR Protoc **2**(4): 100973.

Rettig, J., C. Heinemann, U. Ashery, Z. H. Sheng, C. T. Yokoyama, W. A. Catterall and E. Neher (1997). "Alteration of Ca^{2+} dependence of neurotransmitter release by disruption of Ca^{2+} channel/syntaxin interaction." J Neurosci **17**(17): 6647-6656.

Rettig, J., Z. H. Sheng, D. K. Kim, C. D. Hodson, T. P. Snutch and W. A. Catterall (1996). "Isoform-specific interaction of the α_{1A} subunits of brain Ca^{2+} channels with the presynaptic proteins syntaxin and SNAP-25." Proc Natl Acad Sci U S A **93**(14): 7363-7368.

Ripke, S., C. O'Dushlaine, K. Chambert, J. L. Moran, A. K. Kahler, S. Akterin, S. E. Bergen, A. L. Collins, J. J. Crowley, M. Fromer, Y. Kim, S. H. Lee, P. K. Magnusson, N. Sanchez, E. A. Stahl, S. Williams, N. R. Wray, K. Xia, F. Bettella, A. D. Borglum, B. K. Bulik-Sullivan, P. Cormican, N. Craddock, C. de Leeuw, N. Durmishi, M. Gill, V. Golimbet, M. L. Hamshere, P. Holmans, D. M. Hougaard, K. S. Kendler, K. Lin, D. W. Morris, O. Mors, P. B. Mortensen, B. M. Neale, F. A. O'Neill, M. J. Owen, M. P. Milovancevic, D. Posthuma, J. Powell, A. L. Richards, B. P. Riley, D. Ruderfer, D. Rujescu, E. Sigurdsson, T. Silagadze, A. B. Smit, H. Stefansson, S. Steinberg, J. Suvisaari, S. Tosato, M. Verhage, J. T. Walters, C. Multicenter Genetic Studies of Schizophrenia, D. F. Levinson, P. V. Gejman, K. S. Kendler, C. Laurent, B. J. Mowry, M. C. O'Donovan, M. J. Owen, A. E. Pulver, B. P. Riley, S. G. Schwab, D. B. Wildenauer, F. Dudbridge, P. Holmans, J. Shi, M. Albus, M. Alexander, D. Campion, D. Cohen, D. Dikeos, J. Duan, P. Eichhammer, S. Godard, M. Hansen, F. B. Lerer, K. Y. Liang, W. Maier, J. Mallet, D. A. Nertney, G. Nestadt, N. Norton, F. A. O'Neill, G. N. Papadimitriou, R. Ribble, A. R. Sanders, J. M. Silverman, D. Walsh, N. M. Williams, B. Wormley, C. Psychosis Endophenotypes International, M. J. Arranz, S. Bakker, S. Bender, E. Bramon, D. Collier, B. Crespo-Facorro, J. Hall, C. Iyegbe, A. Jablensky, R. S. Kahn, L. Kalaydjieva, S. Lawrie, C. M. Lewis, K. Lin, D. H. Linszen, I. Mata, A. McIntosh, R. M. Murray, R. A. Ophoff, J. Powell, D. Rujescu, J. Van Os, M. Walshe, M. Weisbrod, D. Wiersma, C. Wellcome Trust Case Control, P. Donnelly, I. Barroso, J. M. Blackwell, E. Bramon, M. A. Brown, J. P. Casas, A. P. Corvin, P. Deloukas,

A. Duncanson, J. Jankowski, H. S. Markus, C. G. Mathew, C. N. Palmer, R. Plomin, A. Rautanen, S. J. Sawcer, R. C. Trembath, A. C. Viswanathan, N. W. Wood, C. C. Spencer, G. Band, C. Bellenguez, C. Freeman, G. Hellenthal, E. Giannoulatou, M. Pirinen, R. D. Pearson, A. Strange, Z. Su, D. Vukcevic, P. Donnelly, C. Langford, S. E. Hunt, S. Edkins, R. Gwilliam, H. Blackburn, S. J. Bumpstead, S. Dronov, M. Gillman, E. Gray, N. Hammond, A. Jayakumar, O. T. McCann, J. Liddle, S. C. Potter, R. Ravindrarajah, M. Ricketts, A. Tashakkori-Ghanbaria, M. J. Waller, P. Weston, S. Widaa, P. Whittaker, I. Barroso, P. Deloukas, C. G. Mathew, J. M. Blackwell, M. A. Brown, A. P. Corvin, M. I. McCarthy, C. C. Spencer, E. Bramon, A. P. Corvin, M. C. O'Donovan, K. Stefansson, E. Scolnick, S. Purcell, S. A. McCarroll, P. Sklar, C. M. Hultman and P. F. Sullivan (2013). "Genome-wide association analysis identifies 13 new risk loci for schizophrenia." Nat Genet **45**(10): 1150-1159.

Ritz, B., S. L. Rhodes, L. Qian, E. Schernhammer, J. H. Olsen and S. Friis (2010). "L-type calcium channel blockers and Parkinson disease in Denmark." Ann Neurol **67**(5): 600-606.

Robitaille, R., M. L. Garcia, G. J. Kaczorowski and M. P. Charlton (1993). "Functional colocalization of calcium and calcium-gated potassium channels in control of transmitter release." Neuron **11**(4): 645-655.

Romo, R. and R. Rossi-Pool (2020). "Turning Touch into Perception." Neuron **105**(1): 16-33.

Ronzitti, G., G. Bucci, M. Emanuele, D. Leo, T. D. Sotnikova, L. V. Mus, C. H. Soubrane, M. L. Dallas, A. Thalhammer, L. A. Cingolani, S. Mochida, R. R. Gainetdinov, G. J. Stephens and E. Chieregatti (2014). "Exogenous α-synuclein decreases raft partitioning of Cav2.2 channels inducing dopamine release." J Neurosci **34**(32): 10603-10615.

Rothbard, J. B., E. Kreider, C. L. VanDeusen, L. Wright, B. L. Wylie and P. A. Wender (2002). "Arginine-rich molecular transporters for drug delivery: role of backbone spacing in cellular uptake." J Med Chem **45**(17): 3612-3618.

Rovira, C., N. Arbez and J. Mariani (2002). "Aβ(25-35) and Aβ(1-40) act on different calcium channels in CA1 hippocampal neurons." Biochem Biophys Res Commun **296**(5): 1317-1321.

Rowland, L. P. and N. A. Shneider (2001). "Amyotrophic lateral sclerosis." N Engl J Med **344**(22): 1688-1700.

Ruth, P., A. Rohrkasten, M. Biel, E. Bosse, S. Regulla, H. E. Meyer, V. Flockerzi and F. Hofmann (1989). "Primary structure of the beta subunit of the DHP-sensitive calcium channel from skeletal muscle." Science **245**(4922): 1115-1118.

Rycroft, B. K., K. S. Vikman and M. J. Christie (2007). "Inflammation reduces the contribution of N-type calcium channels to primary afferent synaptic transmission onto NK1 receptor-positive lamina I neurons in the rat dorsal horn." J Physiol **580**(Pt.3): 883-894.

Sachidhanandam, S., V. Sreenivasan, A. Kyriakatos, Y. Kremer and C. C. Petersen (2013). "Membrane potential correlates of sensory perception in mouse barrel cortex." Nat Neurosci **16**(11): 1671-1677.

Saegusa, H., T. Kurihara, S. Zong, A. Kazuno, Y. Matsuda, T. Nonaka, W. Han, H. Toriyama and T. Tanabe (2001). "Suppression of inflammatory and neuropathic pain symptoms in mice lacking the N-type Ca^{2+} channel." EMBO J **20**(10): 2349-2356.

Saegusa, H., T. Kurihara, S. Zong, O. Minowa, A. Kazuno, W. Han, Y. Matsuda, H. Yamanaka, M. Osanai, T. Noda and T. Tanabe (2000). "Altered pain responses in mice lacking α_{1E} subunit of the voltage-dependent Ca^{2+} channel." Proc Natl Acad Sci U S A **97**(11): 6132-6137.

Saegusa, H., Y. Matsuda and T. Tanabe (2002). "Effects of ablation of N- and R-type Ca^{2+} channels on pain transmission." Neurosci Res **43**(1): 1-7.

Sandoval, A., J. Arikkath, E. Monjaraz, K. P. Campbell and R. Felix (2007). "γ_1-dependent down-regulation of recombinant voltage-gated Ca^{2+} channels." Cell Mol Neurobiol **27**(7): 901-908.

Sandoval, A., N. Oviedo, A. Andrade and R. Felix (2004). "Glycosylation of asparagines 136 and 184 is necessary for the $\alpha_2\delta$ subunit-mediated regulation of voltage-gated Ca^{2+} channels." FEBS Lett **576**(1-2): 21-26.

Sanford, M. (2013). "Intrathecal ziconotide: a review of its use in patients with chronic pain refractory to other systemic or intrathecal analgesics." CNS Drugs **27**(11): 989-1002.

Sarchielli, P., L. Greco, A. Floridi, A. Floridi and V. Gallai (2003). "Excitatory amino acids and multiple sclerosis: evidence from cerebrospinal fluid." Arch Neurol **60**(8): 1082-1088.

Sattler, R., M. P. Charlton, M. Hafner and M. Tymianski (1998). "Distinct influx pathways, not calcium load, determine neuronal vulnerability to calcium neurotoxicity." J Neurochem **71**(6): 2349-2364.

Sattler, R. and M. Tymianski (2000). "Molecular mechanisms of calcium-dependent excitotoxicity." J Mol Med (Berl) **78**(1): 3-13.

Savonenko, A. V., G. M. Xu, D. L. Price, D. R. Borchelt and A. L. Markowska (2003). "Normal cognitive behavior in two distinct congenic lines of transgenic mice hyperexpressing mutant APP_{SWE}." Neurobiol Dis **12**(3): 194-211.

Schampel, A. and S. Kuerten (2017). "Danger: High Voltage-The Role of Voltage-Gated Calcium Channels in Central Nervous System Pathology." Cells **6**(4).

Schartmann, E., S. Schemmert, T. Ziehm, L. H. E. Leithold, N. Jiang, M. Tusche, N. Joni Shah, K. J. Langen, J. Kutzsche, D. Willbold and A. Willuweit (2018). "Comparison of blood-brain barrier penetration efficiencies between linear and cyclic all-D-enantiomeric peptides developed for the treatment of Alzheimer's disease." Eur J Pharm Sci **114**: 93-102.

Scheiffele, P. (2003). "Cell-cell signaling during synapse formation in the CNS." Annu Rev Neurosci **26**: 485-508.

Schlaepfer, W. W. and U. J. Zimmerman (1985). "Mechanisms underlying the neuronal response to ischemic injury. Calcium-activated proteolysis of neurofilaments." Prog Brain Res **63**: 185-196.

Schlick, B., B. E. Flucher and G. J. Obermair (2010). "Voltage-activated calcium channel expression profiles in mouse brain and cultured hippocampal neurons." Neuroscience **167**(3): 786-798.

Schmidt, D., Q. X. Jiang and R. MacKinnon (2006). "Phospholipids and the origin of cationic gating charges in voltage sensors." Nature **444**(7120): 775-779.

Schmidtko, A., J. Lotsch, R. Freynhagen and G. Geisslinger (2010). "Ziconotide for treatment of severe chronic pain." Lancet **375**(9725): 1569-1577.

Schneider, C. A., W. S. Rasband and K. W. Eliceiri (2012). "NIH Image to ImageJ: 25 years of image analysis." Nat Methods **9**(7): 671-675.

Schneider, I., D. Reverse, I. Dewachter, L. Ris, N. Caluwaerts, C. Kuiperi, M. Gilis, H. Geerts, H. Kretzschmar, E. Godaux, D. Moechars, F. Van Leuven and J. Herms (2001). "Mutant presenilins disturb neuronal calcium homeostasis in the brain of transgenic mice, decreasing the threshold for excitotoxicity and facilitating long-term potentiation." J Biol Chem **276**(15): 11539-11544.

Schrodinger, LLC (2015). The PyMOL Molecular Graphics System, Version 1.8.

Schroeder, C. I., C. J. Doering, G. W. Zamponi and R. J. Lewis (2006). "N-type calcium channel blockers: novel therapeutics for the treatment of pain." Med Chem **2**(5): 535-543.

Schwartzkroin, P. A. and C. E. Stafstrom (1980). "Effects of EGTA on the calcium-activated afterhyperpolarization in hippocampal CA3 pyramidal cells." Science **210**(4474): 1125-1126.

Selkoe, D. J. (2000). "Toward a comprehensive theory for Alzheimer's disease. Hypothesis: Alzheimer's disease is caused by the cerebral accumulation and cytotoxicity of amyloid β-protein." Ann N Y Acad Sci **924**: 17-25.

Selkoe, D. J. and J. Hardy (2016). "The amyloid hypothesis of Alzheimer's disease at 25 years." EMBO Mol Med **8**(6): 595-608.

Serrano-Pozo, A., M. P. Frosch, E. Masliah and B. T. Hyman (2011). "Neuropathological alterations in Alzheimer disease." Cold Spring Harb Perspect Med **1**(1): a006189.

Shan, Z., S. Cai, J. Yu, Z. Zhang, T. G. M. Vallecillo, M. J. Serafini, A. M. Thomas, N. Y. N. Pham, S. S. Bellampalli, A. Moutal, Y. Zhou, G. B. Xu, Y. M. Xu, S. Luo, M. Patek, J. M. Streicher, A. A. L. Gunatilaka and R. Khanna (2019). "Reversal of Peripheral Neuropathic Pain by the Small-Molecule Natural Product Physalin F via Block of CaV2.3 (R-Type) and CaV2.2 (N-Type) Voltage-Gated Calcium Channels." ACS Chem Neurosci **10**(6): 2939-2955.

Sharp, A. H., J. L. Black, 3rd, S. J. Dubel, S. Sundarraj, J. P. Shen, A. M. Yunker, T. D. Copeland and M. W. McEnery (2001). "Biochemical and anatomical evidence for specialized voltage-dependent calcium channel γ isoform expression in the epileptic and ataxic mouse, stargazer." Neuroscience **105**(3): 599-617.

Sheng, Z. H., J. Rettig, T. Cook and W. A. Catterall (1996). "Calcium-dependent interaction of N-type calcium channels with the synaptic core complex." Nature **379**(6564): 451-454.

Sheng, Z. H., J. Rettig, M. Takahashi and W. A. Catterall (1994). "Identification of a syntaxin-binding site on N-type calcium channels." Neuron **13**(6): 1303-1313.

Sheng, Z. H., C. T. Yokoyama and W. A. Catterall (1997). "Interaction of the synprint site of N-type Ca^{2+} channels with the C2B domain of synaptotagmin I." Proc Natl Acad Sci U S A **94**(10): 5405-5410.

Sherman, S. M. (2016). "Thalamus plays a central role in ongoing cortical functioning." Nat Neurosci **19**(4): 533-541.

Shistik, E., T. Ivanina, T. Puri, M. Hosey and N. Dascal (1995). "Ca^{2+} current enhancement by α2/δ and βsubunits in Xenopus oocytes: contribution of changes in channel gating and α1 protein level." J Physiol **489 (Pt 1)**(Pt 1): 55-62.

Shukla, D. and B. L. Trout (2010). "Interaction of arginine with proteins and the mechanism by which it inhibits aggregation." J Phys Chem B **114**(42): 13426-13438.

Silei, V., C. Fabrizi, G. Venturini, M. Salmona, O. Bugiani, F. Tagliavini and G. M. Lauro (1999). "Activation of microglial cells by PrP and β-amyloid fragments raises intracellular calcium through L-type voltage sensitive calcium channels." Brain Res **818**(1): 168-170.

Silva, F. R., A. S. Miranda, R. P. M. Santos, I. G. Olmo, G. W. Zamponi, T. Dobransky, J. S. Cruz, L. B. Vieira and F. M. Ribeiro (2017). "N-type Ca^{2+} channels are affected by full-length mutant huntingtin expression in a mouse model of Huntington's disease." Neurobiol Aging **55**: 1-10.

Silva, R. B. M., S. Greggio, G. T. Venturin, J. C. da Costa, M. V. Gomez and M. M. Campos (2018). "Beneficial Effects of the Calcium Channel Blocker CTK 01512-2 in a Mouse Model of Multiple Sclerosis." Mol Neurobiol **55**(12): 9307-9327.

Simen, A. A., C. C. Lee, B. B. Simen, V. P. Bindokas and R. J. Miller (2001). "The C terminus of the Ca channel α_{1B} subunit mediates selective inhibition by G-protein-coupled receptors." J Neurosci **21**(19): 7587-7597.

Simon, R. P., T. Griffiths, M. C. Evans, J. H. Swan and B. S. Meldrum (1984). "Calcium overload in selectively vulnerable neurons of the hippocampus during and after ischemia: an electron microscopy study in the rat." J Cereb Blood Flow Metab **4**(3): 350-361.

Simutis, C. B., J. R. Brosch and A. F. Cunningham (2020). "Autoimmune Encephalitis With Elevated N-Type Calcium Channel Antibodies Presenting as Psychotic Depression." Prim Care Companion CNS Disord **22**(3).

Singer, D., M. Biel, I. Lotan, V. Flockerzi, F. Hofmann and N. Dascal (1991). "The roles of the subunits in the function of the calcium channel." Science **253**(5027): 1553-1557.

Singh, A., D. Hamedinger, J. C. Hoda, M. Gebhart, A. Koschak, C. Romanin and J. Striessnig (2006). "C-terminal modulator controls Ca^{2+}-dependent gating of $Ca_V1.4$ L-type Ca^{2+} channels." Nat Neurosci **9**(9): 1108-1116.

Sinor, J. D., S. Du, S. Venneti, R. C. Blitzblau, D. N. Leszkiewicz, P. A. Rosenberg and E. Aizenman (2000). "NMDA and glutamate evoke excitotoxicity at distinct cellular locations in rat cortical neurons in vitro." J Neurosci **20**(23): 8831-8837.

Smith, H. S. and T. R. Deer (2009). "Safety and efficacy of intrathecal ziconotide in the management of severe chronic pain." Ther Clin Risk Manag **5**(3): 521-534.

Smith, P. K., R. I. Krohn, G. T. Hermanson, A. K. Mallia, F. H. Gartner, M. D. Provenzano, E. K. Fujimoto, N. M. Goeke, B. J. Olson and D. C. Klenk (1985). "Measurement of protein using bicinchoninic acid." Anal Biochem **150**(1): 76-85.

Smith, R. G., F. Kimura, Y. Harati, K. McKinley, E. Stefani and S. H. Appel (1995). "Altered muscle calcium channel binding kinetics in autoimmune motoneuron disease." Muscle Nerve **18**(6): 620-627.

Smith, S. J. and G. J. Augustine (1988). "Calcium ions, active zones and synaptic transmitter release." Trends Neurosci **11**(10): 458-464.

Snutch, T. P. (2005). "Targeting chronic and neuropathic pain: the N-type calcium channel comes of age." NeuroRx **2**(4): 662-670.

Soong, T. W., A. Stea, C. D. Hodson, S. J. Dubel, S. R. Vincent and T. P. Snutch (1993). "Structure and functional expression of a member of the low voltage-activated calcium channel family." Science **260**(5111): 1133-1136.

Stanika, R. I., I. Villanueva, G. Kazanina, S. B. Andrews and N. B. Pivovarova (2012). "Comparative impact of voltage-gated calcium channels and NMDA receptors on mitochondria-mediated neuronal injury." J Neurosci **32**(19): 6642-6650.

Stanley, E. F. (1993). "Single calcium channels and acetylcholine release at a presynaptic nerve terminal." Neuron **11**(6): 1007-1011.

Stephens, G. J., N. L. Brice, N. S. Berrow and A. C. Dolphin (1998). "Facilitation of rabbit α_{1B} calcium channels: involvement of endogenous Gβγ subunits." J Physiol **509 (Pt 1)**(Pt 1): 15-27.

Stotz, S. C., J. Hamid, R. L. Spaetgens, S. E. Jarvis and G. W. Zamponi (2000). "Fast inactivation of voltage-dependent calcium channels. A hinged-lid mechanism?" J Biol Chem **275**(32): 24575-24582.

Stotz, S. C., S. E. Jarvis and G. W. Zamponi (2004). "Functional roles of cytoplasmic loops and pore lining transmembrane helices in the voltage-dependent inactivation of HVA calcium channels." J Physiol **554**(Pt 2): 263-273.

Striessnig, J. and A. Koschak (2008). "Exploring the function and pharmacotherapeutic potential of voltage-gated Ca^{2+} channels with gene knockout models." Channels (Austin) **2**(4): 233-251.

Striessnig, J., A. Pinggera, G. Kaur, G. Bock and P. Tuluc (2014). "L-type Ca^{2+} channels in heart and brain." Wiley Interdiscip Rev Membr Transp Signal **3**(2): 15-38.

Stutzmann, G. E., I. Smith, A. Caccamo, S. Oddo, F. M. Laferla and I. Parker (2006). "Enhanced ryanodine receptor recruitment contributes to Ca^{2+} disruptions in young, adult, and aged Alzheimer's disease mice." J Neurosci **26**(19): 5180-5189.

Stys, P. K. and Q. Jiang (2002). "Calpain-dependent neurofilament breakdown in anoxic and ischemic rat central axons." Neurosci Lett **328**(2): 150-154.

Su, S. C., J. Seo, J. Q. Pan, B. A. Samuels, A. Rudenko, M. Ericsson, R. L. Neve, D. T. Yue and L. H. Tsai (2012). "Regulation of N-type voltage-gated calcium channels and presynaptic function by cyclin-dependent kinase 5." Neuron **75**(4): 675-687.

Sudhof, T. C. (2012). "Calcium control of neurotransmitter release." Cold Spring Harb Perspect Biol **4**(1): a011353.

Sun, Y., A. Savanenin, P. H. Reddy and Y. F. Liu (2001). "Polyglutamine-expanded huntingtin promotes sensitization of N-methyl-D-aspartate receptors via post-synaptic density 95." J Biol Chem **276**(27): 24713-24718.

Sur, S. and V. K. Sinha (2009). "Event-related potential: An overview." Ind Psychiatry J **18**(1): 70-73.

Suzuki, T., S. Futaki, M. Niwa, S. Tanaka, K. Ueda and Y. Sugiura (2002). "Possible existence of common internalization mechanisms among arginine-rich peptides." J Biol Chem **277**(4): 2437-2443.

Swayne, L. A., L. Chen, S. Hameed, W. Barr, E. Charlesworth, M. A. Colicos, G. W. Zamponi and J. E. Braun (2005). "Crosstalk between huntingtin and syntaxin 1A regulates N-type calcium channels." Mol Cell Neurosci **30**(3): 339-351.

Swensen, A. M., J. Herrington, R. M. Bugianesi, G. Dai, R. J. Haedo, K. S. Ratliff, M. M. Smith, V. A. Warren, S. P. Arneric, C. Eduljee, D. Parker, T. P. Snutch, S. B. Hoyt, C. London, J. L. Duffy, G. J. Kaczorowski and O. B. McManus (2012). "Characterization of the substituted N-triazole oxindole TROX-1, a small-molecule, state-dependent inhibitor of Ca_V2 calcium channels." Mol Pharmacol **81**(3): 488-497.

Szabo, Z., G. J. Obermair, C. B. Cooper, G. W. Zamponi and B. E. Flucher (2006). "Role of the synprint site in presynaptic targeting of the calcium channel $Ca_V2.2$ in hippocampal neurons." Eur J Neurosci **24**(3): 709-718.

Szeto, H. H. (2006). "Cell-permeable, mitochondrial-targeted, peptide antioxidants." AAPS J **8**(2): E277-283.

Tai, C. H., Y. C. Yang, M. K. Pan, C. S. Huang and C. C. Kuo (2011). "Modulation of subthalamic T-type Ca^{2+} channels remedies locomotor deficits in a rat model of Parkinson disease." J Clin Invest **121**(8): 3289-3305.

Takahashi, T. and A. Momiyama (1993). "Different types of calcium channels mediate central synaptic transmission." Nature **366**(6451): 156-158.

Takashima, A., K. Noguchi, K. Sato, T. Hoshino and K. Imahori (1993). "Tau protein kinase I is essential for amyloid β-protein-induced neurotoxicity." Proc Natl Acad Sci U S A **90**(16): 7789-7793.

Takeuchi, T. and S. Futaki (2016). "Current Understanding of Direct Translocation of Arginine-Rich Cell-Penetrating Peptides and Its Internalization Mechanisms." Chem Pharm Bull (Tokyo) **64**(10): 1431-1437.

Tanabe, T., K. G. Beam, J. A. Powell and S. Numa (1988). "Restoration of excitation-contraction coupling and slow calcium current in dysgenic muscle by dihydropyridine receptor complementary DNA." Nature **336**(6195): 134-139.

Tanabe, T., H. Takeshima, A. Mikami, V. Flockerzi, H. Takahashi, K. Kangawa, M. Kojima, H. Matsuo, T. Hirose and S. Numa (1987). "Primary structure of the receptor for calcium channel blockers from skeletal muscle." Nature **328**(6128): 313-318.

Tanaka, O., H. Sakagami and H. Kondo (1995). "Localization of mRNAs of voltage-dependent Ca^{2+}-channels: four subtypes of α1- and β-subunits in developing and mature rat brain." Brain Res Mol Brain Res **30**(1): 1-16.

Tang, L., T. M. Gamal El-Din, M. J. Lenaeus, N. Zheng and W. A. Catterall (2019). "Structural Basis for Diltiazem Block of a Voltage-Gated Ca^{2+} Channel." Mol Pharmacol **96**(4): 485-492.

Tang, T. S., E. Slow, V. Lupu, I. G. Stavrovskaya, M. Sugimori, R. Llinas, B. S. Kristal, M. R. Hayden and I. Bezprozvanny (2005). "Disturbed Ca^{2+} signaling and apoptosis of medium spiny neurons in Huntington's disease." Proc Natl Acad Sci U S A **102**(7): 2602-2607.

Tao, H., Y. Zhang and S. Y. Huang (2020). "Improving Protein-Peptide Docking Results via Pose-Clustering and Rescoring with a Combined Knowledge-Based and MM-GBSA Scoring Function." J Chem Inf Model **60**(4): 2377-2387.

Tate, C. G. (2001). "Overexpression of mammalian integral membrane proteins for structural studies." FEBS Lett **504**(3): 94-98.

Tate, C. G. (2010). "Practical considerations of membrane protein instability during purification and crystallisation." Methods Mol Biol **601**: 187-203.

Tedford, H. W. and G. W. Zamponi (2006). "Direct G protein modulation of Ca_V2 calcium channels." Pharmacol Rev **58**(4): 837-862.

Texido, L., M. Martin-Satue, E. Alberdi, C. Solsona and C. Matute (2011). "Amyloid β peptide oligomers directly activate NMDA receptors." Cell Calcium **49**(3): 184-190.

Thaler, C., A. C. Gray and D. Lipscombe (2004). "Cumulative inactivation of N-type $Ca_V2.2$ calcium channels modified by alternative splicing." Proc Natl Acad Sci U S A **101**(15): 5675-5679.

Thibault, O., J. C. Gant and P. W. Landfield (2007). "Expansion of the calcium hypothesis of brain aging and Alzheimer's disease: minding the store." Aging Cell **6**(3): 307-317.

Thibault, O. and P. W. Landfield (1996). "Increase in single L-type calcium channels in hippocampal neurons during aging." Science **272**(5264): 1017-1020.

Tippens, A. L., J. F. Pare, N. Langwieser, S. Moosmang, T. A. Milner, Y. Smith and A. Lee (2008). "Ultrastructural evidence for pre- and postsynaptic localization of $Ca_V1.2$ L-type Ca^{2+} channels in the rat hippocampus." J Comp Neurol **506**(4): 569-583.

Toescu, E. C., A. Verkhratsky and P. W. Landfield (2004). "Ca^{2+} regulation and gene expression in normal brain aging." Trends Neurosci **27**(10): 614-620.

Tran-Van-Minh, A. and A. C. Dolphin (2010). "The $\alpha_2\delta$ ligand gabapentin inhibits the Rab11-dependent recycling of the calcium channel subunit $\alpha_2\delta$-2." J Neurosci **30**(38): 12856-12867.

Trifaro, J. M. and M. L. Vitale (1993). "Cytoskeleton dynamics during neurotransmitter release." Trends Neurosci **16**(11): 466-472.

Trompet, S., R. G. Westendorp, A. M. Kamper and A. J. de Craen (2008). "Use of calcium antagonists and cognitive decline in old age. The Leiden 85-plus study." Neurobiol Aging **29**(2): 306-308.

Tsien, R. W., P. T. Ellinor and W. A. Horne (1991). "Molecular diversity of voltage-dependent Ca^{2+} channels." Trends Pharmacol Sci **12**(9): 349-354.

Tu, H., O. Nelson, A. Bezprozvanny, Z. Wang, S. F. Lee, Y. H. Hao, L. Serneels, B. De Strooper, G. Yu and I. Bezprozvanny (2006). "Presenilins form ER Ca^{2+} leak channels, a function disrupted by familial Alzheimer's disease-linked mutations." Cell **126**(5): 981-993.

Tuluc, P., N. Molenda, B. Schlick, G. J. Obermair, B. E. Flucher and K. Jurkat-Rott (2009). "A $Ca_V1.1$ Ca^{2+} channel splice variant with high conductance and voltage-sensitivity alters EC coupling in developing skeletal muscle." Biophys J **96**(1): 35-44.

Turner, R. W. and G. W. Zamponi (2014). "T-type channels buddy up." Pflugers Arch **466**(4): 661-675.

Turner, T. J., M. E. Adams and K. Dunlap (1993). "Multiple Ca^{2+} channel types coexist to regulate synaptosomal neurotransmitter release." Proc Natl Acad Sci U S A **90**(20): 9518-9522.

Tymianski, M. (1996). "Cytosolic calcium concentrations and cell death in vitro." Adv Neurol **71**: 85-105.

Tymianski, M., M. P. Charlton, P. L. Carlen and C. H. Tator (1993). "Source specificity of early calcium neurotoxicity in cultured embryonic spinal neurons." J Neurosci **13**(5): 2085-2104.

Tymianski, M. and C. H. Tator (1996). "Normal and abnormal calcium homeostasis in neurons: a basis for the pathophysiology of traumatic and ischemic central nervous system injury." Neurosurgery **38**(6): 1176-1195.

Ueda, K., S. Shinohara, T. Yagami, K. Asakura and K. Kawasaki (1997). "Amyloid β protein potentiates Ca^{2+} influx through L-type voltage-sensitive Ca^{2+} channels: a possible involvement of free radicals." J Neurochem **68**(1): 265-271.

Valentino, K., R. Newcomb, T. Gadbois, T. Singh, S. Bowersox, S. Bitner, A. Justice, D. Yamashiro, B. B. Hoffman, R. Ciaranello and et al. (1993). "A selective N-type calcium channel antagonist protects against neuronal loss after global cerebral ischemia." Proc Natl Acad Sci U S A **90**(16): 7894-7897.

van Groen, T., S. Schemmert, O. Brener, L. Gremer, T. Ziehm, M. Tusche, L. Nagel-Steger, I. Kadish, E. Schartmann, A. Elfgen, D. Jurgens, A. Willuweit, J. Kutzsche and D. Willbold (2017). "The Aβ oligomer eliminating D-enantiomeric peptide RD2 improves cognition without changing plaque pathology." Sci Rep **7**(1): 16275.

van Groen, T., K. Wiesehan, S. A. Funke, I. Kadish, L. Nagel-Steger and D. Willbold (2008). "Reduction of Alzheimer's disease amyloid plaque load in transgenic mice by D3, A

D-enantiomeric peptide identified by mirror image phage display." ChemMedChem **3**(12): 1848-1852.

Vaslin, A., C. Rummel and P. G. Clarke (2009). "Unconjugated TAT carrier peptide protects against excitotoxicity." Neurotox Res **15**(2): 123-126.

Verweij, B. H., J. P. Muizelaar, F. C. Vinas, P. L. Peterson, Y. Xiong and C. P. Lee (2000). "Improvement in mitochondrial dysfunction as a new surrogate efficiency measure for preclinical trials: dose-response and time-window profiles for administration of the calcium channel blocker Ziconotide in experimental brain injury." J Neurosurg **93**(5): 829-834.

Viaene, A. N., I. Petrof and S. M. Sherman (2011). "Properties of the thalamic projection from the posterior medial nucleus to primary and secondary somatosensory cortices in the mouse." Proc Natl Acad Sci U S A **108**(44): 18156-18161.

Vivas, O., H. Castro, I. Arenas, D. Elias-Vinas and D. E. Garcia (2013). "PIP_2 hydrolysis is responsible for voltage independent inhibition of $Ca_V2.2$ channels in sympathetic neurons." Biochem Biophys Res Commun **432**(2): 275-280.

von Lewinski, F. and B. U. Keller (2005). "Ca^{2+}, mitochondria and selective motoneuron vulnerability: implications for ALS." Trends Neurosci **28**(9): 494-500.

Vyleta, N. P. and P. Jonas (2014). "Loose coupling between Ca^{2+} channels and release sensors at a plastic hippocampal synapse." Science **343**(6171): 665-670.

Wagner, J. A., A. M. Snowman, A. Biswas, B. M. Olivera and S. H. Snyder (1988). "ω-conotoxin GVIA binding to a high-affinity receptor in brain: characterization, calcium sensitivity, and solubilization." J Neurosci **8**(9): 3354-3359.

Waithe, D., L. Ferron, K. M. Page, K. Chaggar and A. C. Dolphin (2011). "β-subunits promote the expression of $Ca_V2.2$ channels by reducing their proteasomal degradation." J Biol Chem **286**(11): 9598-9611.

Wakamori, M., G. Mikala and Y. Mori (1999). "Auxiliary subunits operate as a molecular switch in determining gating behaviour of the unitary N-type Ca^{2+} channel current in Xenopus oocytes." J Physiol **517 (Pt 3)**(Pt 3): 659-672.

Wallace, A. C., R. A. Laskowski and J. M. Thornton (1995). "LIGPLOT: a program to generate schematic diagrams of protein-ligand interactions." Protein Eng **8**(2): 127-134.

Walsh, D. M., I. Klyubin, J. V. Fadeeva, W. K. Cullen, R. Anwyl, M. S. Wolfe, M. J. Rowan and D. J. Selkoe (2002). "Naturally secreted oligomers of amyloid β protein potently inhibit hippocampal long-term potentiation *in vivo*." Nature **416**(6880): 535-539.

Wang, Q., S. L. Ding, Y. Li, J. Royall, D. Feng, P. Lesnar, N. Graddis, M. Naeemi, B. Facer, A. Ho, T. Dolbeare, B. Blanchard, N. Dee, W. Wakeman, K. E. Hirokawa, A. Szafer, S. M. Sunkin, S. W. Oh, A. Bernard, J. W. Phillips, M. Hawrylycz, C. Koch, H. Zeng, J. A. Harris and L. Ng (2020). "The Allen Mouse Brain Common Coordinate Framework: A 3D Reference Atlas." Cell **181**(4): 936-953 e920.

Watson, C. (2012). Chapter 21 - The Somatosensory System. The Mouse Nervous System. C. Watson, G. Paxinos and L. Puelles. San Diego, Academic Press**:** 563-570.

Weber, A. M., F. K. Wong, A. R. Tufford, L. C. Schlichter, V. Matveev and E. F. Stanley (2010). "N-type Ca^{2+} channels carry the largest current: implications for nanodomains and transmitter release." Nat Neurosci **13**(11): 1348-1350.

Weiss, J. H., C. J. Pike and C. W. Cotman (1994). "Ca^{2+} channel blockers attenuate beta-amyloid peptide toxicity to cortical neurons in culture." J Neurochem **62**(1): 372-375.

Wender, P. A., W. C. Galliher, E. A. Goun, L. R. Jones and T. H. Pillow (2008). "The design of guanidinium-rich transporters and their internalization mechanisms." Adv Drug Deliv Rev **60**(4-5): 452-472.

Weng, X. C., X. D. Gai, J. Q. Zheng and J. Li (2003). "Agmatine blocked voltage-gated calcium channel in cultured rat hippocampal neurons." Acta Pharmacol Sin **24**(8): 746-750.

Wessler, I., D. J. Dooley, J. Werhand and F. Schlemmer (1990). "Differential effects of calcium channel antagonists (ω-conotoxin GVIA, nifedipine, verapamil) on the electrically-evoked release of [^{3}H]acetylcholine from the myenteric plexus, phrenic nerve and neocortex of rats." Naunyn Schmiedebergs Arch Pharmacol **341**(4): 288-294.

Westenbroek, R. E., J. W. Hell, C. Warner, S. J. Dubel, T. P. Snutch and W. A. Catterall (1992). "Biochemical properties and subcellular distribution of an N-type calcium channel α1 subunit." Neuron **9**(6): 1099-1115.

Westenbroek, R. E., L. Hoskins and W. A. Catterall (1998). "Localization of Ca^{2+} channel subtypes on rat spinal motor neurons, interneurons, and nerve terminals." J Neurosci **18**(16): 6319-6330.

Wheeler, D. B., A. Randall and R. W. Tsien (1994). "Roles of N-type and Q-type Ca^{2+} channels in supporting hippocampal synaptic transmission." Science **264**(5155): 107-111.

Wheeler, D. B., A. Randall and R. W. Tsien (1996). "Changes in action potential duration alter reliance of excitatory synaptic transmission on multiple types of Ca^{2+} channels in rat hippocampus." J Neurosci **16**(7): 2226-2237.

Wheeler, D. G., R. D. Groth, H. Ma, C. F. Barrett, S. F. Owen, P. Safa and R. W. Tsien (2012). "Ca_V1 and Ca_V2 channels engage distinct modes of Ca^{2+} signaling to control CREB-dependent gene expression." Cell **149**(5): 1112-1124.

Whitson, J. S. and S. H. Appel (1995). "Neurotoxicity of Aβ amyloid protein in vitro is not altered by calcium channel blockade." Neurobiol Aging **16**(1): 5-10.

Wiesman, A. I., V. M. Mundorf, C. C. Casagrande, S. L. Wolfson, C. M. Johnson, P. E. May, D. L. Murman and T. W. Wilson (2021). "Somatosensory dysfunction is masked by variable cognitive deficits across patients on the Alzheimer's disease spectrum." EBioMedicine **73**: 103638.

Wilkins, M. R., E. Gasteiger, A. Bairoch, J. C. Sanchez, K. L. Williams, R. D. Appel and D. F. Hochstrasser (1999). "Protein identification and analysis tools in the ExPASy server." Methods Mol Biol **112**: 531-552.

Williams, M. E., P. F. Brust, D. H. Feldman, S. Patthi, S. Simerson, A. Maroufi, A. F. McCue, G. Velicelebi, S. B. Ellis and M. M. Harpold (1992). "Structure and functional

expression of an ω-conotoxin-sensitive human N-type calcium channel." Science **257**(5068): 389-395.

Willis, W. D., Jr. and K. N. Westlund (2001). "The role of the dorsal column pathway in visceral nociception." Curr Pain Headache Rep **5**(1): 20-26.

Wilson, S. M., B. S. Schmutzler, J. M. Brittain, E. T. Dustrude, M. S. Ripsch, J. J. Pellman, T. S. Yeum, J. H. Hurley, C. M. Hingtgen, F. A. White and R. Khanna (2012). "Inhibition of transmitter release and attenuation of anti-retroviral-associated and tibial nerve injury-related painful peripheral neuropathy by novel synthetic Ca^{2+} channel peptides." J Biol Chem **287**(42): 35065-35077.

Woodruff, G., J. E. Young, F. J. Martinez, F. Buen, A. Gore, J. Kinaga, Z. Li, S. H. Yuan, K. Zhang and L. S. Goldstein (2013). "The presenilin-1 ΔE9 mutation results in reduced γ-secretase activity, but not total loss of PS1 function, in isogenic human stem cells." Cell Rep **5**(4): 974-985.

Woodward, J. J., S. M. Rezazadeh and S. W. Leslie (1988). "Differential sensitivity of synaptosomal calcium entry and endogenous dopamine release to ω-conotoxin." Brain Res **475**(1): 141-145.

Wu, J., Z. Yan, Z. Li, X. Qian, S. Lu, M. Dong, Q. Zhou and N. Yan (2016). "Structure of the voltage-gated calcium channel $Ca_V1.1$ at 3.6 A resolution." Nature **537**(7619): 191-196.

Wu, L. G., R. E. Westenbroek, J. G. Borst, W. A. Catterall and B. Sakmann (1999). "Calcium channel types with distinct presynaptic localization couple differentially to transmitter release in single calyx-type synapses." J Neurosci **19**(2): 726-736.

Wu, Z. Z., S. R. Chen and H. L. Pan (2004). "Differential sensitivity of N- and P/Q-type Ca^{2+} channel currents to a μ opioid in isolectin B_4-positive and -negative dorsal root ganglion neurons." J Pharmacol Exp Ther **311**(3): 939-947.

Wulff, H. and B. S. Zhorov (2008). "K^+ channel modulators for the treatment of neurological disorders and autoimmune diseases." Chem Rev **108**(5): 1744-1773.

Wycisk, K. A., C. Zeitz, S. Feil, M. Wittmer, U. Forster, J. Neidhardt, B. Wissinger, E. Zrenner, R. Wilke, S. Kohl and W. Berger (2006). "Mutation in the auxiliary calcium-channel subunit CACNA2D4 causes autosomal recessive cone dystrophy." Am J Hum Genet **79**(5): 973-977.

Xie, J. Y., L. A. Chew, X. Yang, Y. Wang, C. Qu, Y. Wang, L. M. Federici, S. D. Fitz, M. S. Ripsch, M. R. Due, A. Moutal, M. Khanna, F. A. White, T. W. Vanderah, P. L. Johnson, F. Porreca and R. Khanna (2016). "Sustained relief of ongoing experimental neuropathic pain by a CRMP2 peptide aptamer with low abuse potential." Pain **157**(9): 2124-2140.

Xu, H. P., J. W. Zhao and X. L. Yang (2002). "Expression of voltage-dependent calcium channel subunits in the rat retina." Neurosci Lett **329**(3): 297-300.

Yagami, T., H. Kohma and Y. Yamamoto (2012). "L-type voltage-dependent calcium channels as therapeutic targets for neurodegenerative diseases." Curr Med Chem **19**(28): 4816-4827.

Yagami, T., K. Ueda, K. Asakura, T. Sakaeda, H. Nakazato, T. Kuroda, S. Hata, G. Sakaguchi, N. Itoh, T. Nakano, Y. Kambayashi and H. Tsuzuki (2002). "Gas6 rescues cortical neurons from amyloid β protein-induced apoptosis." Neuropharmacology **43**(8): 1289-1296.

Yagami, T., K. Ueda, T. Sakaeda, N. Itoh, G. Sakaguchi, N. Okamura, Y. Hori and M. Fujimoto (2004). "Protective effects of a selective L-type voltage-sensitive calcium channel blocker, S-312-d, on neuronal cell death." Biochem Pharmacol **67**(6): 1153-1165.

Yaksh, T. L. (2006). "Calcium channels as therapeutic targets in neuropathic pain." J Pain **7**(1 Suppl 1): S13-30.

Yamaguchi, T., H. Saisu, H. Mitsui and T. Abe (1988). "Solubilization of the ω-conotoxin receptor associated with voltage-sensitive calcium channels from bovine brain." J Biol Chem **263**(19): 9491-9498.

Yamashita, T. and C. Petersen (2016). "Target-specific membrane potential dynamics of neocortical projection neurons during goal-directed behavior." Elife **5**.

Yamawaki, N., J. Radulovic and G. M. Shepherd (2016). "A Corticocortical Circuit Directly Links Retrosplenial Cortex to M2 in the Mouse." J Neurosci **36**(36): 9365-9374.

Yang, J., P. T. Ellinor, W. A. Sather, J. F. Zhang and R. W. Tsien (1993). "Molecular determinants of Ca^{2+} selectivity and ion permeation in L-type Ca^{2+} channels." Nature **366**(6451): 158-161.

Yang, J., M. X. Xie, L. Hu, X. F. Wang, J. Z. Mai, Y. Y. Li, N. Wu, C. Zhang, J. Li, R. P. Pang and X. G. Liu (2018). "Upregulation of N-type calcium channels in the soma of uninjured dorsal root ganglion neurons contributes to neuropathic pain by increasing neuronal excitability following peripheral nerve injury." Brain Behav Immun **71**: 52-65.

Yang, L., A. Katchman, J. P. Morrow, D. Doshi and S. O. Marx (2011). "Cardiac L-type calcium channel ($Ca_V1.2$) associates with γ subunits." FASEB J **25**(3): 928-936.

Yasar, S., M. Corrada, R. Brookmeyer and C. Kawas (2005). "Calcium channel blockers and risk of AD: the Baltimore Longitudinal Study of Aging." Neurobiol Aging **26**(2): 157-163.

Yenari, M. A., J. T. Palmer, G. H. Sun, A. de Crespigny, M. E. Mosely and G. K. Steinberg (1996). "Time-course and treatment response with SNX-111, an N-type calcium channel blocker, in a rodent model of focal cerebral ischemia using diffusion-weighted MRI." Brain Res **739**(1-2): 36-45.

Yokoyama, C. T., Z. H. Sheng and W. A. Catterall (1997). "Phosphorylation of the synaptic protein interaction site on N-type calcium channels inhibits interactions with SNARE proteins." J Neurosci **17**(18): 6929-6938.

Yoshikami, D., Z. Bagabaldo and B. M. Olivera (1989). "The inhibitory effects of omega-conotoxins on Ca channels and synapses." Ann N Y Acad Sci **560**: 230-248.

Younes, K., L. A. Lepow, C. Estrada and P. E. Schulz (2018). "Auto-antibodies against P/Q- and N-type voltage-dependent calcium channels mimicking frontotemporal dementia." SAGE Open Med Case Rep **6**: 2050313X17750928.

Young, W. (1992). "Role of calcium in central nervous system injuries." J Neurotrauma **9 Suppl 1**: S9-25.

Zacharias, N. and D. A. Dougherty (2002). "Cation-π interactions in ligand recognition and catalysis." Trends Pharmacol Sci **23**(6): 281-287.

Zaichick, S. V., K. M. McGrath and G. Caraveo (2017). "The role of Ca^{2+} signaling in Parkinson's disease." Dis Model Mech **10**(5): 519-535.

Zalewski, N. L., V. A. Lennon, D. H. Lachance, C. J. Klein, S. J. Pittock and A. McKeon (2016). "P/Q- and N-type calcium-channel antibodies: Oncological, neurological, and serological accompaniments." Muscle Nerve **54**(2): 220-227.

Zaman, T., K. Lee, C. Park, A. Paydar, J. H. Choi, E. Cheong, C. J. Lee and H. S. Shin (2011). "$Ca_V2.3$ channels are critical for oscillatory burst discharges in the reticular thalamus and absence epilepsy." Neuron **70**(1): 95-108.

Zamponi, G. W. (2003). "Calmodulin lobotomized: novel insights into calcium regulation of voltage-gated calcium channels." Neuron **39**(6): 879-881.

Zamponi, G. W., E. Bourinet, D. Nelson, J. Nargeot and T. P. Snutch (1997). "Crosstalk between G proteins and protein kinase C mediated by the calcium channel α_1 subunit." Nature **385**(6615): 442-446.

Zamponi, G. W., R. J. Lewis, S. M. Todorovic, S. P. Arneric and T. P. Snutch (2009). "Role of voltage-gated calcium channels in ascending pain pathways." Brain Res Rev **60**(1): 84-89.

Zamponi, G. W., J. Striessnig, A. Koschak and A. C. Dolphin (2015). "The Physiology, Pathology, and Pharmacology of Voltage-Gated Calcium Channels and Their Future Therapeutic Potential." Pharmacol Rev **67**(4): 821-870.

Zhang, H., A. Maximov, Y. Fu, F. Xu, T. S. Tang, T. Tkatch, D. J. Surmeier and I. Bezprozvanny (2005). "Association of $Ca_V1.3$ L-type calcium channels with Shank." J Neurosci **25**(5): 1037-1049.

Zhang, J., J. Yang, C. Zhang, X. Jiang, H. Zhou and M. Liu (2012). "Calcium antagonists for acute ischemic stroke." Cochrane Database Syst Rev(5): CD001928.

Zhang, Y., J. S. Helm, A. Senatore, J. D. Spafford, L. K. Kaczmarek and E. A. Jonas (2008). "PKC-induced intracellular trafficking of Ca_V2 precedes its rapid recruitment to the plasma membrane." J Neurosci **28**(10): 2601-2612.

Zhang, Y., P. Li, J. Feng and M. Wu (2016). "Dysfunction of NMDA receptors in Alzheimer's disease." Neurol Sci **37**(7): 1039-1047.

Zhou, C., H. H. Ye, S. Q. Wang and Z. Chai (2006). "Interleukin-1β regulation of N-type Ca^{2+} channels in cortical neurons." Neurosci Lett **403**(1-2): 181-185.

Zhou, P., B. Jin, H. Li and S. Y. Huang (2018). "HPEPDOCK: a web server for blind peptide-protein docking based on a hierarchical algorithm." Nucleic Acids Res **46**(W1): W443-W450.

Zhu, Y. and S. R. Ikeda (1994). "Modulation of Ca^{2+}-channel currents by protein kinase C in adult rat sympathetic neurons." J Neurophysiol **72**(4): 1549-1560.

Zhuchenko, O., J. Bailey, P. Bonnen, T. Ashizawa, D. W. Stockton, C. Amos, W. B. Dobyns, S. H. Subramony, H. Y. Zoghbi and C. C. Lee (1997). "Autosomal dominant cerebellar ataxia (SCA6) associated with small polyglutamine expansions in the α_{1A}-voltage-dependent calcium channel." Nat Genet **15**(1): 62-69.

Zingg, B., H. Hintiryan, L. Gou, M. Y. Song, M. Bay, M. S. Bienkowski, N. N. Foster, S. Yamashita, I. Bowman, A. W. Toga and H. W. Dong (2014). "Neural networks of the mouse neocortex." Cell **156**(5): 1096-1111.

Zundorf, G. and G. Reiser (2011). "Calcium dysregulation and homeostasis of neural calcium in the molecular mechanisms of neurodegenerative diseases provide multiple targets for neuroprotection." Antioxid Redox Signal **14**(7): 1275-1288.

III. Acknowledgments

Thank you, to all the people that contributed towards the completion of this work, making the success of this doctoral thesis possible. Over the years, numerous people have supported me on my way, and while I cannot name everyone, please be assured I am aware and deeply appreciative of each and every individual who has played a role in my journey!!

First of all, I would like to express my gratitude to Prof. Dieter Willbold and Prof. Colin Masters for the opportunity to work on this research project in such a special collaboration between two universities, labs and countries. I highly appreciate the supervision, scientific advice, and overall support you provided throughout this time.

Many thanks to Dr. Janine Kutzsche as my co-supervisor for not only offering exceptional guidance and encouragement throughout this project but also providing unwavering motivation during challenging times.

I express my gratitude to the JUMPA graduate school for offering me the opportunity to conduct a research period abroad, which has facilitated amazing collaboration and allowed for personal and scientific growth.

Further thanks go to all the supportive people at the Florey Institute in Melbourne, particularly Dr. Luke Miles for the supervision in modeling approaches, Prof. Lucy Palmer and Rosie for their collaboration in conducting *in vivo* Ca^{2+} imaging experiments, and all the wonderful individuals who contributed to organization, specifically Céline and Joelyn, scientific discussion, and support both within and outside the lab.

A heartfelt ‘Danke’ goes to all members, past and present, of the Abeta group of the IBI-7 institute in Jülich - Markus, Dominik, Gustavo, Katharina, Julia, Luana and many others. I want to give a special shoutout to Ian Gering and Dr. Sarah Schemmert, who not only supported me majorly with scientific advice and support but also created an amazing working atmosphere which filled or office with joy and laughter over the years. Further thanks go to all members of the IBI-7 institute for fostering such a special work environment; from the administration- and the order-team to the exceptional management of the lab by the TA-team - without you, the lab would not run a single day. I am further grateful to consider some of my co-workers from the IBI-7 good friends by now - Franzi, Gabriel, Sebastian and Alina. I cannot even put in words how awesome the times with you, both at work and outside it, have been. I am certain our friendship will survive many more years.

However, supportive people are not limited to the lab. I would like to thank all my friends, in Germany and Australia (special thanks to my lovely flatmates), as well as my partner in crime, Leies. Never underestimate the power of friends. Your personal support, willingness to lend an ear to all my PhD-related challenges and worries, and constant motivation were truly invaluable. I genuinely could not have made it through without you all by my side.

Above all, my deepest gratitude is reserved for my family, notably my father Joachim, my mother Birgit, and my sister Hannah. Ihr habt es geschafft aus dem “dokka Mächa” mit den großen Träumen eine erwachsene Frau zu machen, die am Ende wirklich eine echte Wissenschaftlerin geworden ist. Danke, dass ihr immer an mich geglaubt habt, mich ermutigt und mich bei allem unterstützt habt. Ohne euch wäre ich niemals so weit gekommen.

Thank you! Danke! Cheers!